University of Nottingham
UK | CHINA | MALAYSIA

Development of Blood Vessel Segmentation Methods for Clinical Use

Faiza Bukenya

A thesis submitted March 2023, in partial fulfilment of the requirements for the degree of Doctor of Philosophy

in the

School of Computer Science
University of Nottingham

March 2023

Declaration

I declare that this thesis entitled **"Development of Blood Vessel Segmentation Methods for Clinical Use"** is the result of my research except as cited in the references. This thesis has not been accepted for any degree and is not concurrently submitted in the candidature of any other degree.

Signature:.....

Name: Faiza Bukenya

Date: March 2023

Abstract

Blood vessel segmentation is important for diagnosing disease, monitoring treatment response and for treatment planning. However, the performance of the available segmentation techniques is limited by the image artefacts (such as low contrast variation between blood vessel pixels and background, noise, and stain variation) in the medical images and therefore, the available automated segmentation techniques fail to distinguish between blood vessels from non-blood vessels. In addition, the existing segmentation techniques have a challenge of segmenting blood vessels of various sizes especially small vessels, and therefore they cannot be used during diagnosis of small blood vessel diseases (such as stroke and Alzheimer's disease) and cannot be used in medical applications that require monitoring the blood vessel growth. For a more accurate diagnosis, an automated blood vessel segmentation method should segment blood vessel of various sizes in the image. This thesis aims to develop both 3D and 2D hybrid blood vessel segmentation techniques that can overcome the challenges associated with the available methods, coupled with a high accuracy rate when applied to medical images.

Regarding the problem of image artefacts, this thesis presents a blood vessel enhancement filter for the enhancement of blood vessels in medical images referred to as a White top-hat scale-space Bilateral Hessian based Filter. The White top-hat scale-space Bilateral Hessian based Vessel Enhancement Filter (WBHVEF) is designed by integrating the capabilities of White top-hat Morphological Transform and Bilateral convolution into the Frangi Vessel Enhancement Filter to correct illumination, enhance contrast and address noise of the image while maintaining strong sharp edged blood vessels. Analysis of the blood vessel enhancement filter on the publicly available retina fundus image dataset shows that its performance is comparable to existing blood vessel enhancement filters. Moreover, the

capabilities of the White top-hat scale-space Bilateral Hessian based Filter are exploited during the image enhancement stage to demonstrate its potential for improving the performance of the 3D hybrid blood vessel segmentation method and the 2D hybrid blood vessel segmentation method. Furthermore, to address the problem of lack of methods that can segment blood vessels of various sizes (especially small vessels) from 3D medical images, a 3D hybrid blood vessel segmentation method that is easily parallelizable is developed. A White top-hat scale-space Bilateral Hessian based Vessel Enhancement Filter combined with hysteresis thresholding is used during the segmentation of the small to medium blood vessels, hysteresis thresholding is used during segmentation of the medium to big vessels, image addition is utilised to combine segmentation results from the two processes, and Matlab bwareaopen operation is used to enhance the segmentation results. Evaluation of the 3D hybrid blood vessel segmentation framework on private image dataset achieved the highest average (sensitivity = 91.06%, specificity = 99.49%, accuracy = 99.41%, DICE = 74.53%, and Jaccard index = 59.40%) on the Magnetic Resonance Angiography (MRA) carotid dataset, average (sensitivity = 89.96%, specificity = 99.76%, accuracy = 99.70%, DICE = 78.93%, and jaccard index = 65.20%) on the Computerised Tomography (CT) pelvic arteriogram image dataset dataset, and average (sensitivity = 82.76%, specificity = 99.62%, accuracy = 99.47%, DICE = 73.43%, and jaccard index = 58.02%) on Computed Tomography Angiography (CTA) femeral artery and veins dataset. The capabilities of White top-hat scale-space Bilateral Hessian based Vessel Enhancement Filter, hysteresis thresholding and MATLAB bwareaopen operation are further exploited during the extraction of blood vessels from 2D retina fundus images. Evaluation of the 2D hybrid blood vessel segmentation framework on DRIVE dataset yielded state of art performance with the accuracy of 95.4%, the sensitivity of 74.9%, and specificity of 97.4%. On the STARE dataset, it yielded state of art performance with the accuracy of 95.3%, the sensitivity of 79.2%, and specificity of 96.5%.

In addition, this thesis presents a hybrid morphological method for the segmentation of blood vessels from the Haematoxylin and Diaminobenzidine (H&DAB) images. The morphological method involves three steps including stain normalisation for the image enhancement, classification of pixels into blood vessel pixels and non-blood vessel pixels for seg-

mentation and blood vessel diameter quantification for blood vessel quantification. Blood vessel diameter quantification results obtained using the proposed automated are compared to blood vessel diameter quantification results obtained using the manual method. Test results indicate that the automated is capable of achieving better results.

Regarding the issue of applicability, this thesis presents a new morphological tool for the segmentation of blood vessels from histology images to facilitate research in complex diseases such as breast cancer and Alzheimer disease.

Acknowledgements

In the name of God, the Most Gracious and the Most Merciful. All praise be upon God.
Being a multi-disciplinary programme, a lot of people from different disciplines contributed in different ways. First and foremost, I would like to thank my sponsor Islamic Development Bank group for the support and effort they put in to see that I finish my PhD program successfully. Secondly, I acknowledge all my supervisors Dr Li Bai, Prof. Tony Pridmore, and Prof. Robert John, and the director of postgraduate studies, Ass. Prof. Dario Landa-Silva for being so helpful and encouraging in seeing me through this PhD Program. My sincere thanks go out to the medical experts, I worked with during the two projects. Thank you so much, Dr Marie-Christine Pardon. I cannot forget to thank you Amir Awwad. I am grateful for the help.
My warm thanks go out to PhD colleagues, Jinming Duan, Ding Yuchun, Aaron Jackson, Thomas Smith, Luke Sibbet, and Wil Ward for always being there whenever I needed them in matters to do with my research. I cannot forget to thank Imo, Osman, Suzan, Elissa, Joy, Norah, Wen, Raras, Pingu, and Simon. I was always aware of what is going on within the school. Thank you.
Lastly but not least, I cannot forget to thank the School of Computer Science staff members, Associate Professor Rong Qu, Associate Professor Gail Hopkins, Viktor Huddleston, Deborah Pitchfork and Christine Fletcher, and Joseph Best for their help and support. Lastly, I am so grateful to my husband, mother, father, sisters and brothers for the love, support and encouragement they have given me throughout my studies. Thank you so much my husband for being understanding.

Dedication

First and foremost I dedicate this thesis

To my sponsor IDB,

My husband,

My beloved parents, my dad and mum

My sisters and brothers

And

To my dear friends

Thank you for the support you gave me throughout this research.

List of Abbreviations

MRI	Magnetic Resonance Imaging
MR	Magnetic Resonance
CT	Computerised Tomography
CTA	Computed Tomography Angiography
MRA	Magnetic Resonance Angiography
CE-MRI	Contrast Enhanced Magnetic Resonance Imaging
CFP	Colour Fundus Photography
WHVEF	White top-hat scale-space Hessian based Vessel Enhancement Filter
WBHVEF	White top-hat scale-space Bilateral Hessian based Vessel Enhancement Filter
IUWT	Isotropic Undecimated Wavelet Transform
ACM	Active Contour Model
LBF	Local Binary Fitted
RGB	Red Green Blue
HSV	Hue Saturation Value
H&DAB	Haematoxylin and Diaminobenzidine
L	Longitudinal
T	Traverse
ISODATA	Iterative Self Organising Data Analysis.

Contents

List of Tables

List of Figures

Chapter 1

Overview and Problem Identification

Blood vessel segmentation plays an important role in different clinical fields, such as diagnostic radiology [152, 119, 68, 245, 92, 236, 220, 70], pathology [211, 234], oncology [45], and neurosurgery [63], both for diagnosis, treatment planning and execution, and for treatment outcome evaluation and follow up. The techniques used to extract blood vessels from medical images are categorised into classes including manual segmentation techniques, semi-automated segmentation techniques and automated segmentation techniques. Manual segmentation is done in a slice by slice manner, with an expert (such as a radiologist, specialised clinician) either encircling the region of interest or annotating the region of interest. Manual segmentation is extremely slow and tedious, and an expert physician can make errors due to fatigue [155, 32]. To solve these problems, semi-automated segmentation is employed. In semi-automated segmentation, an expert makes use of segmentation tools to label the region of interest during segmentation [32]. However, user interaction still exists, as the manual part of the segmentation and the settings of the algorithm influence the result. Compared to semi-automated segmentation, automated segmentation doesn't or require less human intervention during segmentation. Automatic blood vessel segmentation could assist clinicians and, therefore, is a topic of great interest in medical research. Indeed, an extensive research already exists on blood vessel segmentation and in the past years, a high amount of papers is annually published on blood vessel segmentation e.g on aorta segmentation [131, 162, 81, 168], retina vessel segmentation [98, 29, 99, 82], coronary artery segmentation [206, 124, 46], limb segmentation [49], colony segmentation [147, 65],

carotid segmentation [214, 237, 129, 91], brain blood vessel segmentation [7, 251, 119, 68], liver blood vessel segmentation [92, 134, 236], and heart blood vessel segmentation [220, 70]. However, these techniques struggle to distinguish blood vessels from non-blood vessels due to the image artefacts in the medical images. The characteristics of the medical images have a major obstacle to developing segmentation methods that are usable [155]. The noise present in medical images and tiny contrast variation between blood vessel pixels and background pixels cause problems such as false detections (detecting non-blood vessels as blood vessels) and missed detections (skipping blood vessels of various sizes during segmentation) that in-turn result in a poor diagnosis. In addition, the existing segmentation techniques have a challenge of segmenting blood vessels of various sizes especially small vessels [142, 4, 231, 96, 155, 58], and therefore they cannot be used during diagnosis of small blood vessel diseases (such as stroke and Alzheimer's disease) and cannot be used in medical applications that require monitoring the blood vessel growth. Naturally, blood vessel varies in size and shape. Moreover, laminar flow within blood vessels causes blood flow velocity variations, which leads to highly varying contrast distribution across different blood vascular structures [58, 254]. For a more accurate diagnosis, an automated blood vessel segmentation method should segment blood vessel of various sizes in the image. Furthermore, most of the blood vessel segmentation techniques are developed for only 2D images, whilst some that claim to be 3D based, segment 2D image planes and then later reconstruct 2D image planes into a 3D image [123, 66]. 3D segmentation is important during diagnosis. Although 2D blood vessel segmentation is easy to carry out, it doesn't provide full information about the anatomic structure of the blood vessels for proper diagnosis. Additionally, 2D leads to inconsistencies in the segmentation results and non-smooth vessel surfaces, due to omission of important anatomical information in 3D space. Therefore, 3D segmentation techniques are required for more accurate segmentation of volumetric imagery [123, 66]. The main difference between 2D and 3D image segmentation is in the processing elements. In 2D image segmentation, image pixels are processed, whilst, in 3D image segmentation, image voxels are processed. Given the above limitations of blood vessel segmentation research, (i) There is a need to develop image enhancement methods to improve the quality of the image to enable effective segmentation. (ii) There is a need to develop automated segmentation

methods that can extract the blood vessels of various sizes from medical images of different modalities. (iii) There is a need for 3D blood vessel segmentation techniques to provide full information about the anatomic structure of the blood vessels for proper diagnosis, ensure consistencies in the segmentation results and to produce smooth vessel surfaces.

This thesis addresses the aforementioned problems by proposing both 3D and 2D hybrid blood vessel segmentation techniques that can overcome the challenges associated with the available methods, coupled with a high accuracy rate when applied to medical images. The proposed methods are tested on both public and private datasets to show their viability in comparison with state-of-the-art methods. In addition, a morphological tool for enhancing and segmenting blood vessels is developed to facilitate clinical research.

1.1 Research Aim and Objectives

1. To develop a method that can enhance the blood vessels and medical images to enable effective extraction of vessels.

2. To develop 3D hybrid blood vessel segmentation methods that can extract the whole vasculature from 3D medical images.

3. To develop 2D hybrid blood vessel segmentation methods that can extract the blood vessels from medical images.

4. To develop a morphological tool that can extract blood vessels from medical images to facilitate research in a variety of clinical fields.

1.2 Contributions

The key contributions of this thesis are:

1.2.1 A new blood vessel enhancement filter

The performance of segmentation techniques in radiology images is limited by the image artefacts (such as presence of intensity inhomogeneity, noise, and low contrast in images) in medical images. Frangi vessel enhancement filter is popular and widely during image enhancement due to its robustness to noise and its ability to enhance both dark vessels on

a bright background and bright vessels on a dark background even in presence of noise. However, Frangi vessel enhancement filter fails to work on images with high levels of intensity in-homogeneity (intensity non-uniformity) and causes blurriness around the edges of the blood vessels due to usage of Gaussian convolution [77]. To boost the efficiency of the Frangi vessel enhancement filter, this work first integrates the capabilities of White top-hat morphological transform into Frangi vessel enhancement filter to design a new filter known as White top-hat scale-space Hessian based Vessel Enhancement Filter (WHVEF). A White top-hat scale-space Hessian based Vessel Enhancement Filter is used for enhancing blood vessels in both the STARE dataset and DRIVE dataset. The work shows that White top-hat scale-space Hessian based Vessel Enhancement Filter can correct illumination to uncover the blood vessels rendered absent. However, it fails to maintain the edges of vessels (especially small vessels) in medical images with a high level of noise. To improve the performance of White top-hat scale-space Hessian based Vessel Enhancement Filter, This work integrates Bilateral Convolution into White top-hat scale-space Hessian based Vessel Enhancement Filter to design another vessel enhancement filter known as White top-hat scale-space Bilateral Hessian based Vessel Enhancement Filter (WBHVEF). This work shows that the integration of White top-hat Transform and Bilateral Convolution into Frangi Vessel enhancement Filter significantly boosts the efficiency of Frangi Vessel Enhancement Filter and subsequently improves vessel enhancement interms of correcting illumination, enhancing contrast and addressing noise while maintaining strong sharp edged blood vessels. The White top-hat scale-space Bilateral Hessian based Vessel Enhancement Filter comparable to the former Frangi vessel enhancement filter and other influential vessel enhancement filters. To demonstrate its ability for improving blood vessel segmentation, the White top-hat scale-space Bilateral Hessian based Vessel Enhancement Filter is exploited during the image enhancement stage of the 3D hybrid blood vessel segmentation method and 2D hybrid blood vessel segmentation method proposed in this thesis.

1.2.2 A 3D hybrid blood vessel segmentation framework

The available 3D segmentation techniques face a challenge of extracting blood vessels of various sizes (especially small blood vessels) from 3D radiology images(such as CTA, MRA, MRI and CT images). This work presents a 3D hybrid blood vessel segmentation frame-

work for extraction of the whole organ vasculature. The uniqueness of the 3D hybrid blood vessel segmentation framework is that it is easily parallelizable; segmentation processes occur independently on two identical images, and then an integration step quickly merges both outputs from two identical images into a coherent segmentation result, that is later enhanced using an appropriate image enhancement method. This is in contrast with others that segment blood vessels of various sizes using a single method and one image. In this work, three methods that adopt the same framework are developed. I first developed a 3D Hybrid Method of Multi-threshold Otsu, WHVEF filter combined with Iterative Self Organising Data Analysis (ISODATA) thresholding, Image Addition and Matlab Bwareaopen Operation for segmentation of blood vessels of various sizes. The method is capable of segmenting blood vessels of various sizes. However, it produces weak edged blood vessels and fails to work on images with high levels of noise. To improve the performance of the 3D Hybrid Method of Multi-threshold Otsu, WHVEF filter combined with ISODATA thresholding, Image Addition and Matlab Bwareaopen Operation, a Multi-threshold Otsu is combined with hysteresis thresholding, WHVEF filter is replaced with WBHVEF filter and ISODATA thresholding is replaced with hysteresis thresholding, to form another hybrid method known as a 3D hybrid method of WBHVEF filter combined with Hysteresis Thresholding, Multi-threshold Otsu combined with Hysteresis thresholding, Image Addition and Matlab Bwareaopen Operation. The hybrid method is suitable for segmenting blood vessels from only detailed images such as Magnetic Resonance Imaging (MRI), Magnetic Resonance Angiography (MRA). More vessels of various sizes were detected in the MRI image. On contrary, fewer vessels are detected in Computerised Tomography (CT) scan images after introducing the hysteresis threshold method. MRI and MRA images are naturally detailed as compared to medical images of other modalities (such as CT scan images). To improve the performance of the 3D hybrid method of WBHVEF filter combined with Hysteresis Thresholding, Multi-threshold Otsu combined with Hysteresis thresholding, Image Addition and Matlab Bwareaopen Operation, in the extraction of blood vessels from both detailed and non-detailed images, I then do away with Multi-threshold Otsu, forming a new a method known as a 3D hybrid method of WBHVEF filter combined with Hysteresis Thresholding, Hysteresis Thresholding, Image Addition and Matlab Bwareaopen Opera-

tion. The evaluation shows that the performance of the 3D hybrid method of WBHVEF filter combined with Hysteresis Thresholding, Hysteresis Thresholding, Image Addition and Matlab Bwareaopen Operation is comparable to other methods on the same dataset in terms of accuracy, sensitivity and specificity. In addition, the visual comparison between the segmentation performance of the proposed method and other state-of-the-art methods on the same dataset show that the method can segment blood vessels various sizes from medical images irrespective of the size of the image, and can also detect blood vessel disorders such as blood vessel tortuosity. Although the visual comparison is considered purely subjective, it can still emphasise the positive and negative points of various segmentation approaches in support of quantitative results.

1.2.3 A hybrid method for blood vessel segmentation in 2D medical images

In this work, the capabilities of a White top-hat scale-space Bilateral Hessian based Vessel Enhancement Filter, hysteresis thresholding and MATLAB bwareaopen operation are further exploited during the extraction of blood vessels of various sizes from 2D retina fundus images. Evaluation of the method on both the STARE dataset and the DRIVE dataset shows that its performance is comparable to other 2D blood vessel segmentation methods on the same dataset interms of evaluation metrics such as sensitivity, specificity and the accuracy. In addition, the visual comparison between the segmentation performance of the proposed method and other state-of-the-art methods on the same dataset show that the proposed method can detect blood vessels of various sizes (including small blood vessels) and can easily get rid of the unwanted object tissue (such as the optic disc, fovea) during blood vessel segmentation.

1.2.4 A morphological tool for segmentation and quantification of blood vessels from histology images

The available segmentation techniques face a challenge of extracting blood vessels of various sizes (especially small blood vessels) from Histology images. This is mainly due to image artefacts (such as stain variation problem, specks and stain leakage problem). Stain nor-

malisation is performed during image pre-processing and before blood vessel segmentation to standardise the appearance of the image to facilitate segmentation and quantification of blood vessels. In this work, Haemotoxylin and Diaminobenzidine (H&DAB) images are first normalised following two steps including the stain separation stage and colour transfer stage. Octree colour quantisation algorithm combined with Beer-Lambert law and a modified blind source separation algorithm are exploited during the stain separation stage to computationally estimate the amount of stain in the histology images based on the chromatic and luminous response. A modified colour transfer algorithm is exploited during the colour transfer stage to minimise the effect of varying stain and illumination. To the best of my knowledge, this is the first work to demonstrate that Beer-Lambert law applies to histology images with stains (such as Diaminobenzidine (DAB)) that are non-absorbers of light. In addition, compared to the original blind source separation method, the blind source separation method used in this work makes use of the Spatial-Spectral Schrodinger Eigenvectors and Eigenvalues rather than the ordinary Eigenvalues and Eigenvectors to incorporate texture and spatial information. The method can address the stain variation problem without distorting image tissue while maintaining brightness in the H&DAB images. After stain normalisation, only saturation channel of the normalised image and methods such as ISODATA thresholding, MATLAB bwareaopen operation, and Matlab dilation operation are exploited during segmentation of vessels to group image pixels in to blood vessels and non blood vessels. To the best of my knowledge, this method uses only saturation channel during the segmentation of the whole blood vessel. Lastly, unlike other methods, this work quantifies the blood vessel diameter of the blood vessel traverse section and the blood vessel longitudinal sections separately to create a better understanding of the image data, following MATLAB region props operation steps. The performance of the morphological method is assessed by comparing the automatically obtained blood vessel diameters against the manually obtained blood vessel diameter on the private H&DAB dataset. The evaluation shows that the method is capable of producing better segmentation and quantification results in 120 seconds on a 250GB CPU.

1.3 Research Importance

The output of this research could potentially result in an improved vascular diagnosis and therapy. The blood vessel enhancement filter improve the quality of the image to improve both the human visual analysis and computer system analysis. In advanced medical image analysis, the 3D and 2D segmented vasculature trees can be used during classification to discriminating veins from arteries and to calculate the number of blood vessels, and blood vessel diameter. In addition, the 3D hybrid blood vessel segmentation method can be used during early diagnosis as it can detect blood vessel abnormality during segmentation. Furthermore, segmented blood vessels can be utilised as features for blood vessel disease classification and systematic disease (such as diabetes, stroke or hypertension) identification systems.

The morphological tool developed can be used by clinical researchers to aid with research in histopathology and cytology. The stain normalisation module standardises the appearance of the images to improve both visual analysis and computer analysis. The blood vessels produced by the blood vessel segmentation module can be used to quantify the number of blood vessels to know the blood vessel growth rate. By quantifying the blood vessel diameter of the blood vessel traverse section and blood vessel longitudinal section separately, the user can measure the plaque in the blood vessels.

1.4 Structure of Blood Vessel Segmentation System

In summary, the primary goal of this thesis is to present both 3D and 2D hybrid blood vessel segmentation techniques that can overcome the challenges associated with the available methods, coupled with a high accuracy rate when applied to medical images. Three major parts will be needed for this. The first part is image pre-processing, from which the image and the blood vessels will be enhanced at various scales for better segmentation. The second step will be to classify voxels or pixels into blood vessel voxels (or pixels) and non-blood vessels voxels (or pixels) using an appropriate method. The last step will be to enhance the resulting whole vasculature by removing unwanted objects using an appropriate image enhancement method.

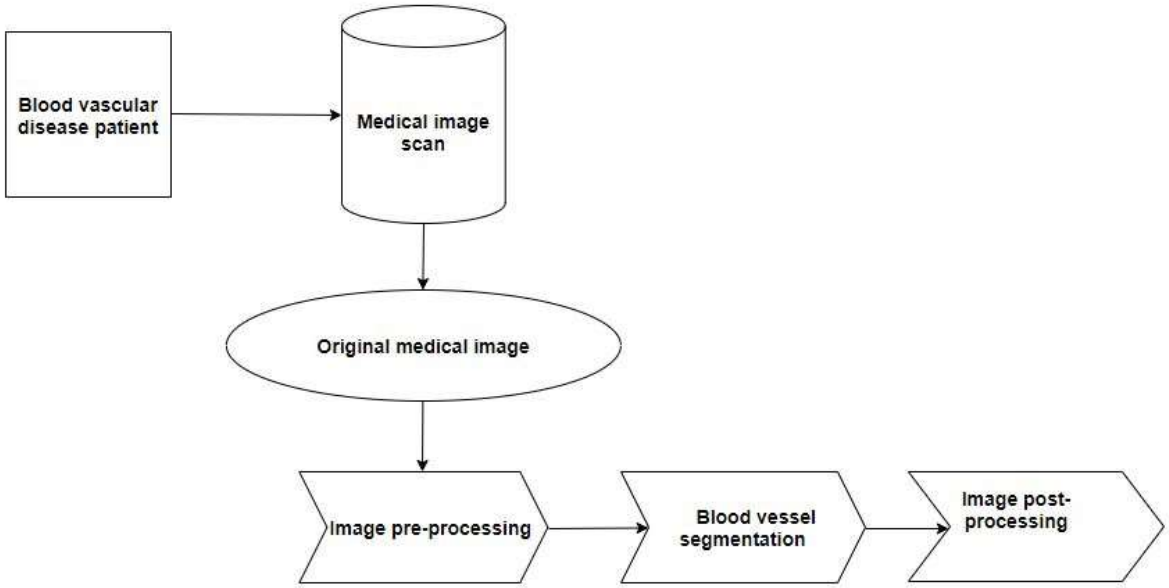

Figure 1.1: Structure of blood vessel segmentation system

1.5 Thesis Outline

This section describes the structure of the thesis and highlights the themes presented in each of the chapters. The main contributions of this work are described in Chapter 4, 5, 6 and 7. The relevant medical image theoretical framework which forms the methods used in this work are discussed in detail in Chapters 3 and Chapter 2.

(a) Chapter 2, This chapter presents the image dataset used to evaluate the proposed methods. Chapter 2 describes the data collection protocol for the radiology image dataset, histology image dataset and the retina image dataset. It describes the methodology used in creating ground-truth dataset for radiology image dataset.

(b) Chapter 3, introduces the subject of blood vessels from an anatomical and physiological perspective with the focus on the mechanism involved in the generation of blood vessel disorders. It discusses the structure of the blood vessel, different classes of blood vessels, blood vessel abnormalities, and the genetic and environmental factors that have been identified to be indicative of blood vessel disorders. It reviews existing work on automatic image segmentation with emphasis on the image enhancement techniques, and segmentation techniques. Finally, it discusses the limitations of the existing segmentation methods and how this work addresses the problems.

(c) Chapter 4, introduces a new vessel enhancement filter for enhancement of the image and blood vessels developed to deal with problems (such as failure to work on images with high levels of intensity variations, blood vessel blurriness problem) associated with the Frangi vessel enhancement filter. Related work on vessel enhancement is discussed. It outlines the blood vessel enhancement process. It shows how the integration of bilateral convolution and White top-hat Transform into Frangi vessel enhancement filter, improves the performance of Frangi vessel enhancement filter in enhancing both the image and the blood vessels. A new vessel enhancement filter known as a White top-hat scale-space Bilateral Hessian based Vessel Enhancement Filter is presented. A comparison of a White top-hat scale-space Bilateral Hessian based Vessel Enhancement Filter with the most influential vessel enhancement filters is also presented. To demonstrate its potential for improving blood vessel segmentation, the White top-hat scale-space Bilateral Hessian based Vessel Enhancement Filter is exploited during the image enhancement stage of the 3D hybrid blood vessel segmentation method and 2D hybrid blood vessel segmentation method proposed in chapter 5 and chapter 6.

(d) Chapter 5, focuses on the 3D hybrid blood vessel segmentation framework to segment blood vessels of various sizes from 3D medical images. Related work on 3D blood vessel segmentation is discussed. It outlines the blood vessel segmentation process. It shows how the 3D WHVEF filter, a 3D WBHVEF filter, Multi-threshold Otsu, hysteresis thresholding, ISODATA thresholding and MATLAB bwareaopen operation are exploited to form three blood vessel segmentation methods. The three 3D blood vessel segmentation methods are presented; (i) A 3D Hybrid Method of Multi-threshold Otsu, WHVEF filter combined with ISODATA, Image Addition and Matlab Bwareaopen Operation. (ii) A 3D hybrid method of White top-hat scale-space Bilateral Hessian based Vessel Enhancement Filter combined with Hysteresis Thresholding, Multi-threshold Otsu combined with Hysteresis thresholding, Image Addition and Matlab Bwareaopen Operation, and (iii) A 3D hybrid method of White top-hat scale-space Bilateral Hessian based Vessel Enhancement Filter combined with Hysteresis Thresholding, Hysteresis Thresholding, Image Addition and Matlab Bwareaopen Op-

eration. It shows the performance of the three methods in segmenting blood vessels of various sizes on a private image dataset from Queen medical centre and consequently advances the state of art. A visual comparison of the three methods that adopt the same hybrid blood vessel segmentation framework is presented. The best method, in this case, the 3D hybrid method of White top-hat scale-space Bilateral Hessian based Vessel Enhancement Filter combined with Hysteresis Thresholding, Hysteresis Thresholding, Image Addition and Matlab Bwareaopen Operation, is compared to the existing 3D segmentation methods.

(e) Chapter 6, focuses on a 2D hybrid blood vessel segmentation method for 2D retina fundus images. Related work on 2D blood vessel segmentation is discussed. It outlines the blood vessel segmentation process. It shows how the 2D White top-hat scale-space Bilateral Hessian based Vessel Enhancement Filter (WBHVEF), Hysteresis Thresholding and Matlab Bwareaopen Operation are exploited to segment blood vessels of various sizes. It shows the performance of the 2D hybrid blood vessel segmentation framework in segmenting blood vessels of various sizes on a publicly available image dataset and consequently advances the state of art.

(f) Chapter 7, presents a fully automated morphological tool for segmentation and quantification of vessels in H&DAB stained histology mice brain image slides. It outlines the stain normalisation process, blood vessel segmentation process and blood vessel diameter quantification process. Test results indicate that the automated morphological can achieve better results.

(g) Chapter 8, presents a summary of this research, identifies open challenges and provides recommendations on how they can be addressed. It also highlights future research directions.

1.6 Academic Publication

The following publications were produced as a direct result of the work undertaken during the course of conducting this research.

1. F. Bukenya, L. Bai and A. Kiweewa, "A Review of Blood Vessel Segmentation Tech-

niques," 2018 1st International Conference on Computer Applications Information Security (ICCAIS), Riyadh, 2018, pp. 1-10. doi: 10.1109/CAIS.2018.8441989.

2. F. Bukenya, J. Ehling, A. K. Kalema, I. Eyoh, J. Robert and L. Bai, "3D segmentation of the whole heart vasculature using improved multi-threshold Otsu and white top-hat scale-space hessian based vessel filter," 2016 IEEE Symposium Series on Computational Intelligence (SSCI), Athens, 2016, pp. 1-7. doi: 10.1109/SSCI.2016.7850137.

3. F. Bukenya, A. Awwad, J. Duan, J. Ehling, H. Faas and L. Bai, "Three-dimensional Segmentation of Blood Vessels from Intensity In-homogeneous Medical Images," 2018 IEEE Symposium Series on Computational Intelligence (SSCI), Bangalore, India, 2018, pp. 1508-1514. doi: 10.1109/SSCI.2018.8628675.

4. Bukenya, F., Nerissa, C., Serres, S., Pardon, M.-C., and Bai, L, "An automated method for segmentation and quantification of blood vessels in histology images". Microvascular Research(2019), 103928. https://doi.org/10.1016/j.mvr.2019.103928.

5. F. Bukenya, "Automated method for stain for normalisation of histology images". Multimedia Tools and Applications, 2019, pp:1-24, doi:10.1007/s11042-019-08262-0.

Chapter 2

Medical Image Data Collection

2.1 Chapter Overview

This chapter describes the data collection process for the medical image dataset used during the PhD research. The purpose of collecting this data was to assess the merits of the White Top-Hat scale space Bilateral Hessian based Vessel Enhancement Filter, 3D hybrid blood vessel segmentation method, 2D hybrid blood vessel segmentation method and the automated morphological tool for segmentation and quantification of blood vessels proposed in this thesis, (i.e. in chapters 4, 5, 6, 7). The dataset consists of three categories: the radiology image dataset, histology image dataset and the retina image dataset. The categorisation is based on the differences in the medical procedures. The radiology image dataset consist of the CTA common femoral artery and veins dataset, MRA-scan carotid and aotic arc dataset, CT pelvic arteriogram image dataset dataset, MRI heart images, CTA scan rat head dataset that were obtained from sir peter mansfield imaging centre, Nottingham. The radiology image dataset are original medical recordings of routine patients' investigation. The radiology imaging data were anonymised and cleared from any individual or identifiable personal data before being further processed or meta-analysed by the study methodology.

The histology image dataset consists of H&DAB (Haematoxylin and Diaminobenzidine) mouse brain dataset that was prepared in the laboratory of School of Life Science at Queen Medical Centre, Nottingham. The image dataset was created from 4.5-month-old APP-swe/PS1de9 mice obtained from Jackson laboratory.

Retina image dataset is a publicly available dataset that consists of Digital Retinal Images for Vessel Extraction (DRIVE) image dataset and the Structured Analysis of the Retina (STARE) image dataset.

Lastly, the methodology used and the challenges faced when creating groundtruth dataset for CTA, MRA image dataset is described. Details of the data collection protocol and dataset-specific characteristics will now be discussed in subsequent sections.

2.2 Radiology image dataset

2.2.1 Overview

This section describes an observational study of radiology image dataset recording for adults that took place at sir peter mansfield imaging centre, Nottingham. Sir peter mansfield imaging centre is an interdisciplinary, cross-faculty centre for innovative imaging in experimental and translational medicine, bringing together researchers who develop new medical imaging techniques with clinicians and scientists who use them. Instead of the researcher, QMC research staff was used to perform the data collection as the researcher needed to do a CRDB check which take about 6 months to complete, which cause delay to the project. Data output from the sir peter mansfield imaging centre included (a) CTA common femoral artery and veins images recorded using CT-scan, (b) MRA carotid and aotic arc images recorded using MRI scan, (c) CT pelvic arteriogram image dataset recorded using a CT scan, (d) MRI heart images recorded using MRI scan, and (e) CT scan rat head dataset recorded using CT scan.

2.2.2 Data collection protocol

2.2.2.1 Ethics

The original medical recordings were part of routine patients' investigation (not treatment). The medical imaging data were first anonymised and cleared from any individual or identifiable personal data prior to being further processed or meta-analysed by the study methodology. The original medical imaging subset of data used in the study methodology are courtesy of Queen Medical Centre, Nottingham University Hospitals NHS Trust.

2.2.2.2 Sample size

A total of 354 unique radiology images were recorded. 101 3D CTA femoral artery and veins image dataset, 124 3D CT pelvic arteriogram image dataset, 122 3D MRA-scan carotid and aotic arc image dataset, 5 3D MRI heart image dataset, and 2 3D CT-scan Rat head dataset were recorded at sir peter mansfield imaging centre, Nottingham.

2.2.2.3 Recruitment protocol

Before receiving a scan, a patient fill out a questionnaire. A patient may continue any medication her doctor has prescribed unless the technician has informed the patient otherwise. A patient can also eat normally, if he wont have a contrast agent injection.

2.2.3 Data acquisition and storage

This section describes the procedure and equipment used for the collection of 3D MRA-scan carotid and aotic arc image dataset, 3D CTA External Iliac and Common Femoral Artery and veins image dataset, CT pelvic arteriogram image dataset, 3D MRI heart image dataset and 3D CT scan Rat head dataset.

2.2.3.1 MRI image acquisition

Magnetic Resonance Imaging (MRI) is a medical imaging technique that uses a magnetic field and computer-generated radio waves to create detailed images of the organs and tissues in the body Figure 2.1.

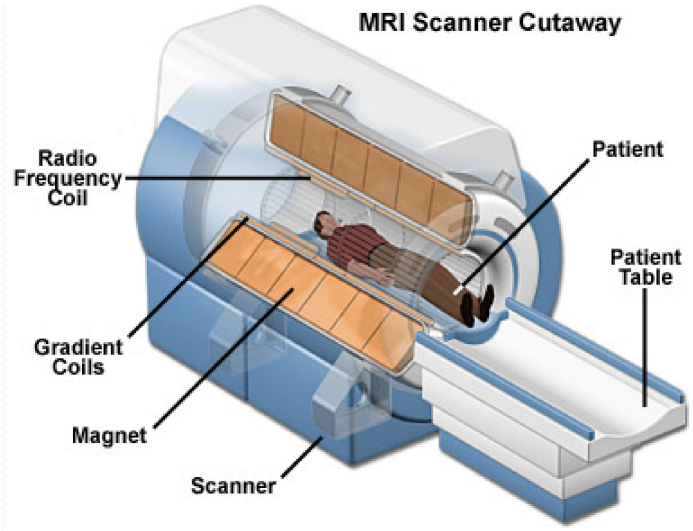

Figure 2.1: Illustration of MRI scan machine

During the test, the patient lay on a padded table that moves into an open magnet that creates a strong magnetic field around his body. The patient remains relaxed during the scan and doesn't move, as this will cause blurry images. The patient will hear thumping and humming noises, along with the occasional knock. The patient will be able to speak with the technician and see the control room during the procedure so there is no need to panic. To capture the images, the MRI scanners (Figure 2.1) uses magnets and radio frequencies which are completely harmless. Hydrogen is the most abundant element in the universe. There are two hydrogen atoms in every water molecule and water makes up around 70% of your body. Hydrogen has a single positively charged proton as its nucleus. These protons have what's known as a 'magnetic moment'-north and south pole and a tendency to spin on an axis, just like the Earth. The magnetic field generated by an MRI scan causes these protons to line up and spin at a particular frequency. A secondary magnet turns the molecules to face new directions and when it's switched off they realign. The rate at which they realign depends on the type of tissue the molecule resides in. The radio frequencies are detected by coils placed over the patients body, and this information allows a computer to visualise everything from soft tissue to bone and organs like the heart and brain. Most MRI tests take anywhere from 30 to 45 minutes.

2.2.3.2 CT image acquisition

A computed tomography scan (formerly known as a computed axial tomography) is a medical imaging technique that uses computer-processed combinations of multiple X-ray measurements taken from different angles to produce tomographic images (virtual slices) of a body, allowing the user to see inside the body without cutting. Compared to MRI scans, CT scans produce less detailed images.

Figure 2.2: Illustration of CT scan machine

During a CT scan, the patient lies on a table that moves through a doughnut-like ring known as a gantry. The gantry has an X-ray tube that rotates around the patient while shooting narrow beams of X-rays through the body. The X-rays are picked up by digital detectors directly opposite the source. After the X-ray source completes a full rotation, a sophisticated computer creates a 2D image of that slice of the body, which typically ranges from 0.04 to 0.4 inches (1 to 10 millimetres) thick. The computer then stacks up several 2D slices to create a 3D image of the organ, making it easier for a doctor to pinpoint where the patient's problem exists. The scan itself typically takes less than 15 minutes depending on the area of the body being imaged.

2.2.3.3 3D MRA-scan carotid and aotic arc image acquisition

MR angiography (MRA) uses a powerful magnetic field, radio waves and a computer to evaluate blood vessels and help identify abnormalities. This exam does not use radiation and may require an injection of contrast material. Compared to MRI, MRA (magnetic resonance angiography) focuses more on the blood vessels than the tissue surrounding it. This section presents a 3D MRA-scan carotid and aotic arc image acquisition process.

- **Patients:** MRA examinations of the neck vessels were carried out during a 2-year period from January 1, 2016, to December 31, 2017. Patients who had undergone MRA within 1 month of each other were included in the study. In addition, 4 subjects were excluded because not all required images were available; and one subject was excluded because of a poor signal intensity-to-noise ratio (SNR). This resulted in a cohort of 50 patients (23 men, 27 women; age range, 21–96 years; mean age, 52 ± 18 years, 5 months) and this formed the study group.
- **MRA image acquisition technique:** MRA studies were performed on a 1.5T Magnetom Symphony (Siemens Medical Systems, Iselin, NJ). Before positioning the patient, a 20-gauge cannula was inserted into an antecubital vein and connected via extendable tubing to a power injector (Medrad, Indianola, PA) containing 20 mL of gadopenetate dimeglumine (Magnevist; Berlex Laboratories, Montvale, NJ) and 40 mL of normal saline. Patients were placed in a supine position on the scan table, and a single circularly polarized standard neck coil was connected. They were then entered headfirst into the magnet bore.

A preliminary 2-dimensional (2D) timing-bolus acquisition was obtained in the coronal plane, to include the aortic arch up to the intracerebral circulation. Two milliliters of gadopenetate dimeglumine was injected at 2 mL/s followed by a 20-mL bolus of normal saline. The transit time was recorded as the time between the start of the injection and initial enhancement of the carotid bifurcation. Patients were asked to hyperventilate before scanning began and to hold their breath on inspiration during image acquisition. All patients held their breath successfully. Pre and post contrast breath-held 3D volumes were acquired in a coronal orientation, extending from the aortic arch up through the intracerebral circulation. In-line digital subtraction was carried out, yielding one subtracted 3D set, as shown in Figure 2.8.

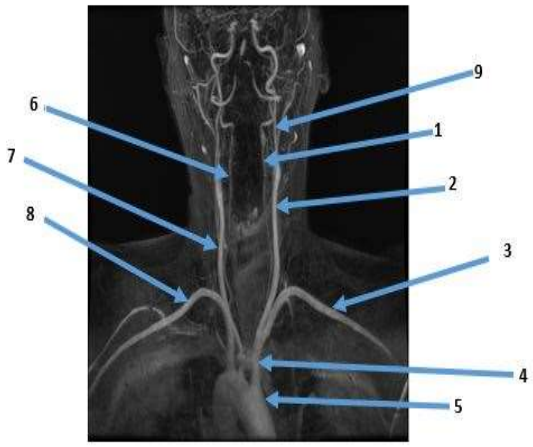

Figure 2.3: Maximum Intensity Projection (MIP) images of randomly selected MRA carotid and aortic arc image. 1 and 6 are vertebral arteries; 2 and 7 are common carotid arteries; 3 and 8 are subclavian arteries; 5. Aortic arc; 9. internal carotid artery

2.2.3.4 CT pelvic arteriogram image acquisition

Computed tomography angiography (CTA) uses an injection of contrast material into your blood vessels and CT scanning to help diagnose and evaluate blood vessel disease or related conditions, such as blockages. This section and section 2.2.3.5 presents a CT pelvic arteriogram image acquisition process and the CTA femoral artery and veins image acquisition process.

(a) **Patients** Between January 2016 and December 2017, 60 patients referred for CT pelvic arteriogram for clinical suspicion or evaluation of artery stenosis, pre-interventional evaluation, and post-operative follow-up were included in this study. General exclu-

sion criteria for CTA examination applied (hemodynamic instability, pregnancy, and iodine allergy).

(b) **CT pelvic arteriogram technique:** During CT pelvic arteriogram image acquisition, the Images were obtained with 120 kV, effective mAs of 250, slice thickness of 2 mm, and reconstruction increments of 1 mm after intravenous administration of iodinated contrast material, ioversol injection 74% (Optiray 350; Mallinckrodt, St. Louis, MO). The injection rate of $4-5mL/s$ with total contrast volume of $95-125mL$ was utilised. Bolus tracking is utilized. Tracking begins after a $15s$ fixed delay and image acquisition $7s$ after reaching the trigger value of 150 Hounsfield units. However, the start position for CT pelvic arteriogram scanning is the above the kidney, and finish position is the middle of the thighs. After successful image acquisition, maximum intensity projections (Figure 2.4), and other 3-dimensional reconstructions such as volume-rendered images are created by the technologist and/or radiologist on a separate workstation.

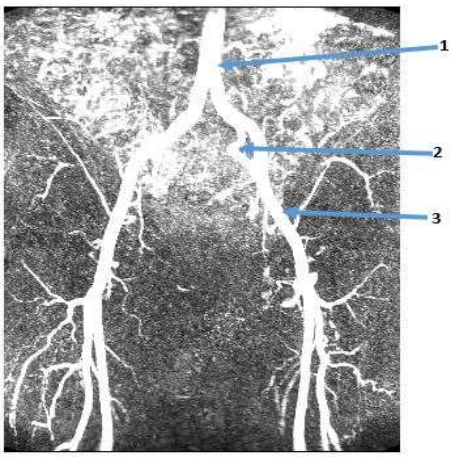

Figure 2.4: Maximum Intensity Projection (MIP) images of randomly chosen CT pelvic arteriogram. 1. abnorminal aorta; 2. internal iliac artery; 3. external iliac artery

2.2.3.5 CTA femoral artery and veins image acquisition

(a) **Patients:** Between January 2016 and December 2017, 60 patients referred for CTA of the femoral arteries and veins for clinical suspicion or evaluation of lower extremity artery stenosis, pre-interventional evaluation, post-operative follow-up were included in this study. General exclusion criteria for CTA examination applied (hemodynamic instability, pregnancy, and iodine allergy). Patients with a history of lower extremity

joint replacement received a dual energy (DE) scan protocol and were therefore also excluded from this study.

(b) **CTA technique:** Like in the CT pelvic arteriogram acquisition, CTA External Iliac and Common femoral artery and veins images were obtained with 120 kV, effective mAs of 250, slice thickness of 2 mm, and reconstruction increments of $1mm$ after intravenous administration of iodinated contrast material, ioversol injection 74% (Optiray 350; Mallinckrodt, St. Louis, MO). The injection rate of $4-5mL/s$ with total contrast volume of $95-125mL$ was utilised. Bolus tracking is utilized. Tracking begins after a $15s$ fixed delay and image acquisition $7s$ after reaching the trigger value of 150 Hounsfield units. Start position for CTA scanning is beginning of the thighs, and finish position is below the knees. After successful image acquisition, maximum intensity projections (MIP) (Figure 2.5), and other 3-dimensional reconstructions such as volume-rendered images are created by the technologist and/or radiologist on a separate workstation.

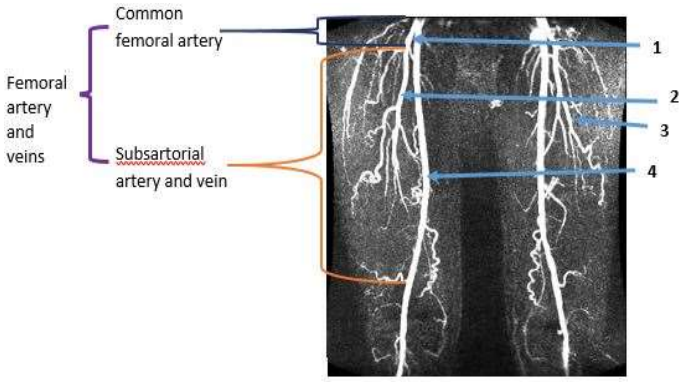

Figure 2.5: Maximum Intensity Projection (MIP) images of randomly selected CTA image from femoral artery and veins image datasets. 1. Common femoral vein; 2. subsartorial vein; 3. deep femoral vein; 4. great saphenous vein.

2.2.4 Radiology image quality and artefacts

Image quality depends on the quality of the scanner, the skills of the radiographer, and the cooperation of the patient. Artefacts are features in radiology images produced by various complications of the imaging process. They result in an image that doesnot portray (in the simple visual sense) an accurate representation of a slice of tissue. Image artefacts affect both human visual analysis and analysis by the computer system. Examples of image artefacts include chemical shift, noise, varying contrast among the blood vessels, low varying

contrast between the non blood vessels and blood vessels, and motion artefact.

2.2.4.1 Highly varying contrast distribution among blood vessels

The highly varying contrast distribution across different blood vascular structures occur due to the laminar flow within blood vessels that causes blood flow velocity variations. This section presents the most common artefacts encountered in MRI (Figure 2.6), MRA (Figure 2.8), and CT (Figure 2.7) images.

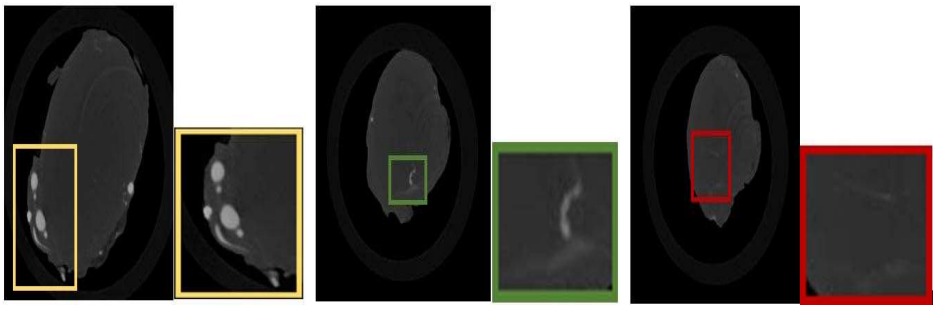

(a) (b) (c)

Figure 2.6: Illustration of randomly selected MRI heart image slices interms of the quality of the MRI image. (a) Yellow in image 1 show that the all the blood vessels are bright on the background and therefore more likely to be detected by the system; (b) Green in image 2 blood vessels with different intensity. One is brighter and the other is blur and darker; (c) Red in image 3 shows the blood vessels that are blur and have the intensity similar to background. Mostly likely not be detected by the system.

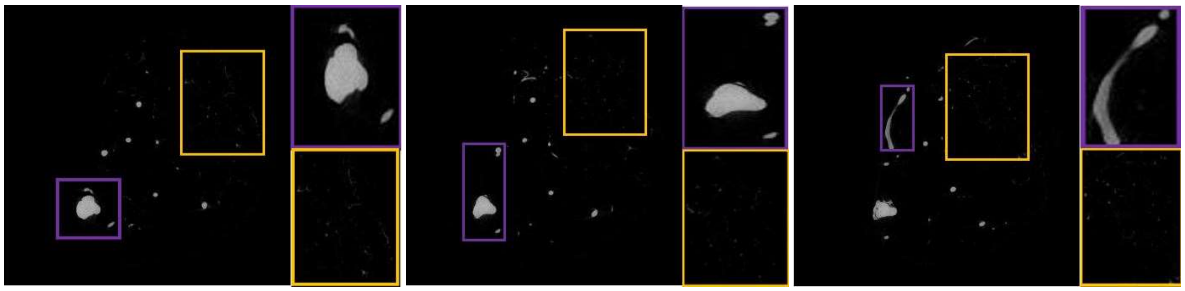

Figure 2.7: Illustration of CT image plane interms of image quality. Purple are large blood vessels that are brighter on the background. Yellow are small blood vessels that appear dark on the background.

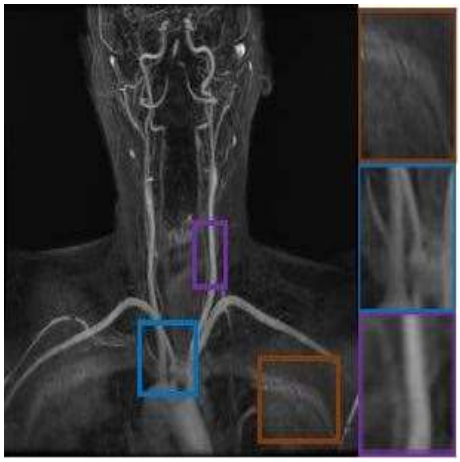

Figure 2.8: Illustration of a randomly selected MRA carotid and aortic arc image in-terms of the image quality. Orange shows the non- blood vessels that have a similar shape and colour as the blood vessels. Blue shows the conglutination tissue surrounding the blood vessels. Purple shows vessels of different contrast (Note: the bigger vessel is brighter than the small vessels).

2.2.4.2 Motion artefact

Any movement of the patient can cause this artefact. The patient motion during the imaging sequence generally results in a blurring of the entire image with ghost images in the phase encoding direction. Movement of a part of the patient results in a blurring of the corresponding part across the image. Red and green in Figure 2.6 shows blur blood vessels due to the patients movement during image acquisition.

2.2.4.3 Noise

Image noise refers to random uncertainties in medical images. Gaussian noise is noticeable in CTA images.

Gaussian noise: Gaussian noise is statistical noise having a probability density function (PDF) equal to that of the normal distribution. Gaussian noise is caused by the random fluctuation in the signal.

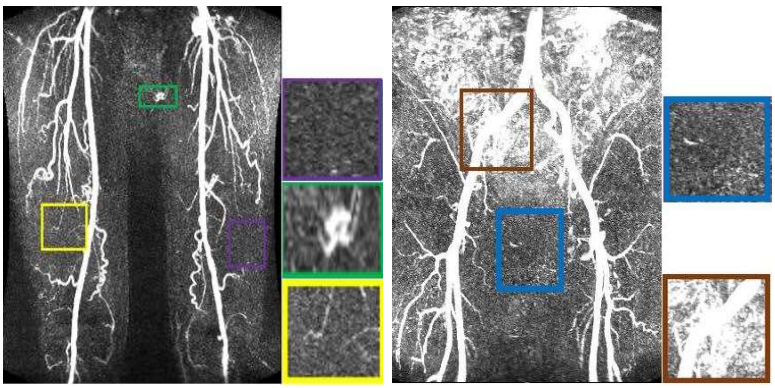

(a) (b)

Figure 2.9: Illustration of image artefacts in MIP images of randomly selected CTA femoral artery and veins image and CT pelvic arteriogram interms of image quality; (a) CTA femoral artery and veins image; (b) CT pelvic arteriogram. Yellow shows small vessels covered with noise, green is the non blood vessels that appear as blood vessel, purple is the noise in the image, brown shows that blood vessels have similar intensity as the background, and blue shows the image noise surrounding the blood vessels

2.3 Histology Image Dataset

2.3.1 Overview

In histopathology, tissue samples are examined during the diagnosis of diseases. Image staining is performed to increase the contrast between different structures for manual examination. This upcoming sections describe an observational study of histology image dataset recording for mice that took place at laboratory of School of Life Science at Queen Medical Centre, Nottingham.

2.3.2 Data collection protocol

2.3.2.1 Ethics

The study protocol was approved by the Research Ethics Committee of the University of Nottingham, United Kingdom. Ethics approval was gotten from the Nottingham University Hospitals Research and Innovation department (REF: 15CS007). All animal procedures were carried out in accordance with the animal's scientific procedures Act 1986.

2.3.2.2 Sample size

A total of 40000 unique H&DAB cortical images of size 1920×1080 pixels were used during the study.

2.3.3 H&DAB image data acquisition and storage

This section describes the image acquisition and preparation procedure used for the collection.

2.3.3.1 Animals

Examinations of the mouse brain blood vessels was carried during a 1-year period from January 1, 2017, to December 31, 2017. Nine 4.5-month-old APPswe/PS1de9 mice (breeding stock obtained from Jackson laboratory) infected with the wild type Alzheimer disease were included in the study.

2.3.3.2 Image Preparation in Laboratory

This section presents the image preparation process before the segmentation process.

1. **Animal model and immunohistochemistry:** All animal procedures were carried out following the animal's scientific procedures Act 1986. The mice were sacrificed and their brains removed. The brains were fixed in 4% PFA for 6 hours before being transferred into 70% ethanol. The brains were processed and embedded into wax, from which 7μm slices were cut using a microtome. The brain slices were then placed onto adhesive slides ready to be stained via immunohistochemistry for blood vessels. The paraffin fixed brain sections were deparaffinised and antigen retrieval was conducted for 20 minutes at 98 °C using a Tris-EDTA buffer $pH9.0$. Sections were incubated with an endogenous peroxidase block for 10 minutes at room temperature, followed by a species-specific blocking serum for 30 minutes at room temperature. The sections were then incubated with a rabbit anti-mouse collagen IV polyclonal antibody (1:1000, Millipore - Darmstadt, Germany) overnight at 4°C. Secondary biotinylated goat anti-rabbit antibody (1 : 200, Vector - Burlingame, CA, USA) was then applied for 1 hour at room temperature. Avidin biotin complex (Vector - Orton Southgate, Peterborough, UK) was then applied for 30 minutes at room temperature to amplify the immune signal which was recognised by DAB (Vector - Burlingame, CA, USA). Positive staining for vessels appears brown against a blue/purple background that is produced via counter staining for nuclei with haematoxylin staining.

2. **Image digitisation:** High-resolution images were captured using a nano-zoomer digital slide scanner (HamamatsuHertfordshire, UK). The images were viewed using the software NDP. View 2 (Hamamatsu), which is used to extract images of regions of interest. Images slides were extracted at a magnification of 15x. Cortical images extracted from the cortex, contained 1920×1080 pixels. Figure 2.10 shows a randomly selected H&DAB image.

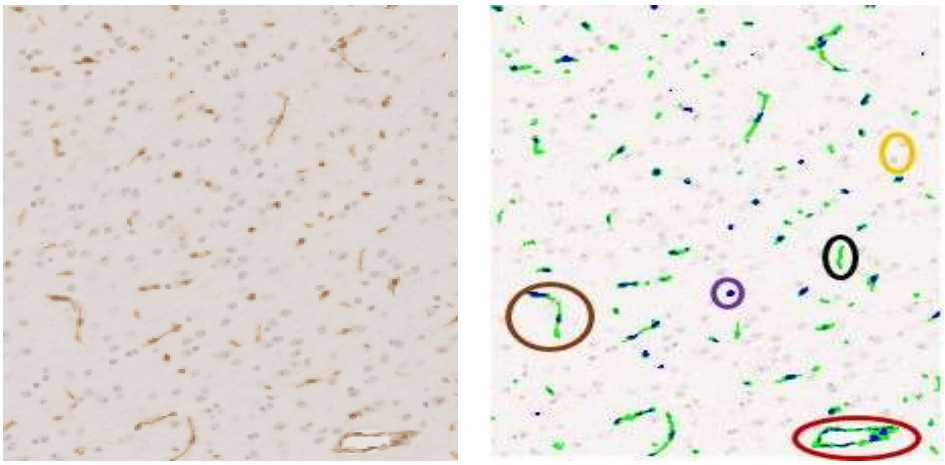

(a) (b)

Figure 2.10: Illustration of the randomly selected H&DAB image slide. (a) original H&DAB image; (b) image showing vessel traverse sections, vessel longitudinal sections, cells and pericytes. Brown are vessel longitudinal sections (green) with pericytes (blue), black are vessel longitudinal sections (green) without pericytes on it, maroon are vessel traverse sections with pericytes on it, purple are pericytes (blue), yellow are the background cells.

2.3.4 H&DAB Image Artefacts

Artefacts are features in histology images produced by various complications of the imaging process. The mostly common artefact in histology images is stain variation (colour variation problem). The next section presents describe the image artefacts.

2.3.4.1 Stain variation

Staining of tissue samples is affected by undesirable stain variation arising from use of different scanners, different staining topology, usage of stains from different manufacturers and also staining image at different times or on different dates. Stain variation artefact affect the visual analysis and further analysis during segmentation and quantification. Figure 2.11 illustrates the stain variation problem.

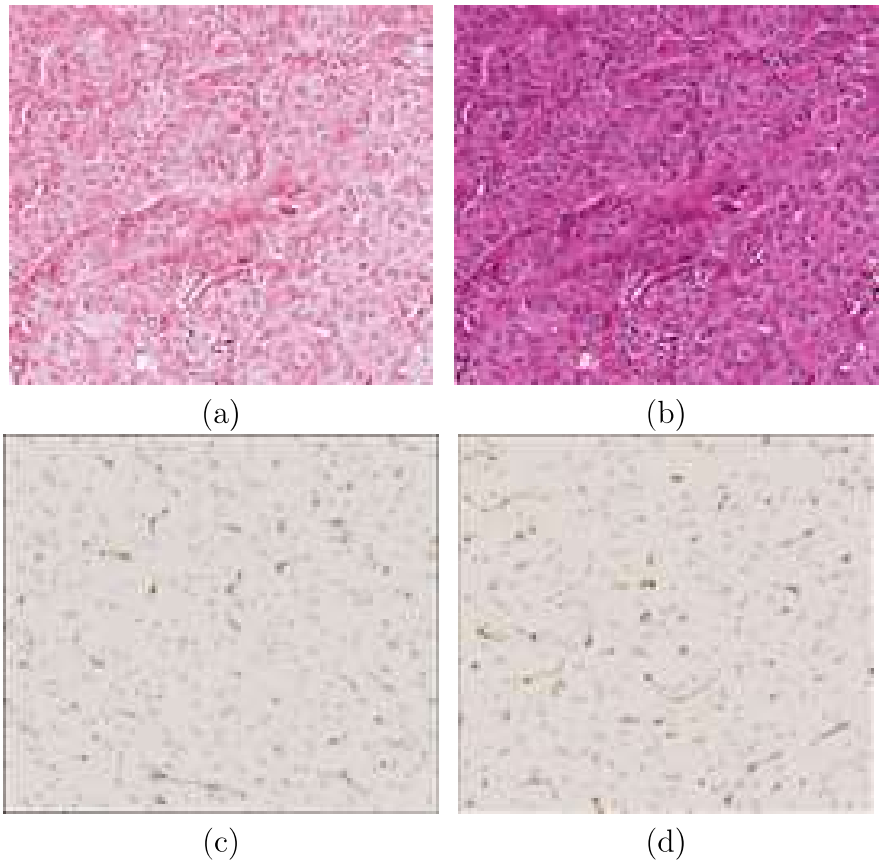

Figure 2.11: (a) and (b) are the same H&E histology images captured using Aperio scanner and Hamamatsu scanner respectively. (c) and (d) are different H&DAB histology images from the same batch stained at different time.

2.4 Publicly Available Retina Fundus Image Dataset

2.4.1 Overview

This section describes an observational study of retina fundus image dataset for adult that took part in the diabetic retinopathy screening program at Netherland and at Tokyo, Japan. Note: these retina images are publicly available.

2.4.2 Data collection protocol

2.4.2.1 Sample size

1. **DRIVE dataset:** This dataset consists of a total of 40 colour retinal images (size 768 by 584 pixels), obtained in the course of a diabetic retinopathy screening program in the Netherlands. The set of 40 images was divided into a test and a training set, each containing 20 images. All of the 40 images come with ground-truth data.
2. **STARE dataset:** This dataset contains 400 colour retinal images (size 605 by 700 pixels), 20 of these come with ground-truth data, 10 of which show evidence of pathology.

2.4.3 Data acquisition and storage

This section describes the procedure and equipment used for the collection of both DRIVE image dataset and the STARE dataset.

2.4.3.1 DRIVE dataset

The images were acquired using a Canon CR5 non-mydriatic 3-CCD camera with a 45-degree field of view.

2.4.3.2 STARE dataset

The images were captured by a TopCon TRV-50 fundus camera (Topcon, Tokyo, Japan), and the photos were digitised to 605 by 700 pixels.

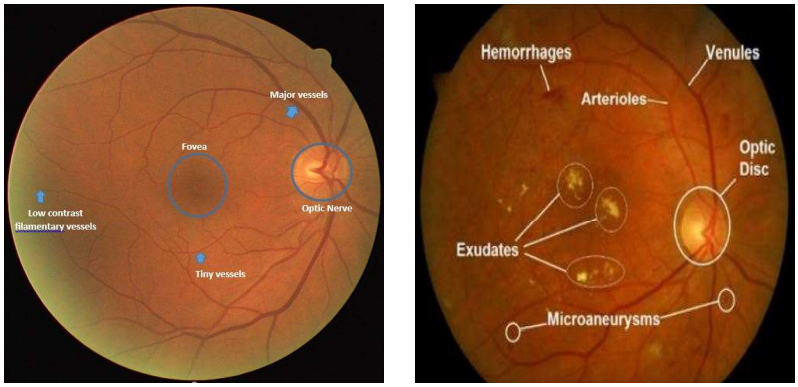

(a) (b)

Figure 2.12: Illustration of randomly selected retina images. (a) retina image showing the low contrast filamentary vessels and other parts of the retina image. (b) diseased image showing blood vessels and none blood vessels. Note: it is hard to detect the low contrast small blood vessels in (a). It may be hard to distinguish the blood vessels from the none blood vessels.

Artefacts in retina images are produced by various complications of the imaging process. Examples of image artefacts include low contrast filament blood vessels. The upcoming sections describe the image artefacts.

2.5 Manual Annotation

The researcher used the open source software ITK-SNAP (Insight segmentation toolkit-Snake automatic partitioning; Penn Image Computing and Science Laboratory, University of Pennsylvania, Philadelphia, Yushkevich et al. 2006) to create 3D groundtruth data. The open source medical imaging program ITK-SNAP is based upon geodesic active contour and region competition methods, and thus offers manual and semiautomatic tools to approximate the volumes of anatomical regions of interest. To create the ground truth volumes, the DICOM data sets were imported into ITK-SNAP and were demonstrated in sagittal, coronal and axial slices (Figure 2.13). The lesions were identified and delineated with the means of semi-automatic segmentation. Afterwards, manual segmentation was performed to control and ensure correct segmentation. Figure 2.14 shows the groundtruth data.

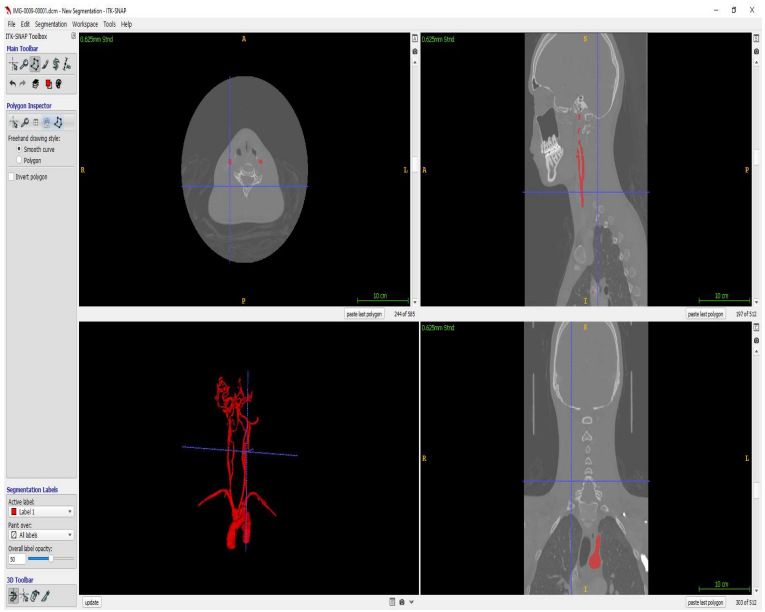

Figure 2.13: Illustration of the ITK-SNAP window showing the manual section, sagittal, coronal and axial sagittal sub-windows. The sagittal window contains the sagittal section of the neck and the label, the coronal window contains the coronal section of the neck and label, the axial window contains the axial section of the neck and the label, and Manual section contains a resulting 3D manual segmentation of carotid and the aortic arc.

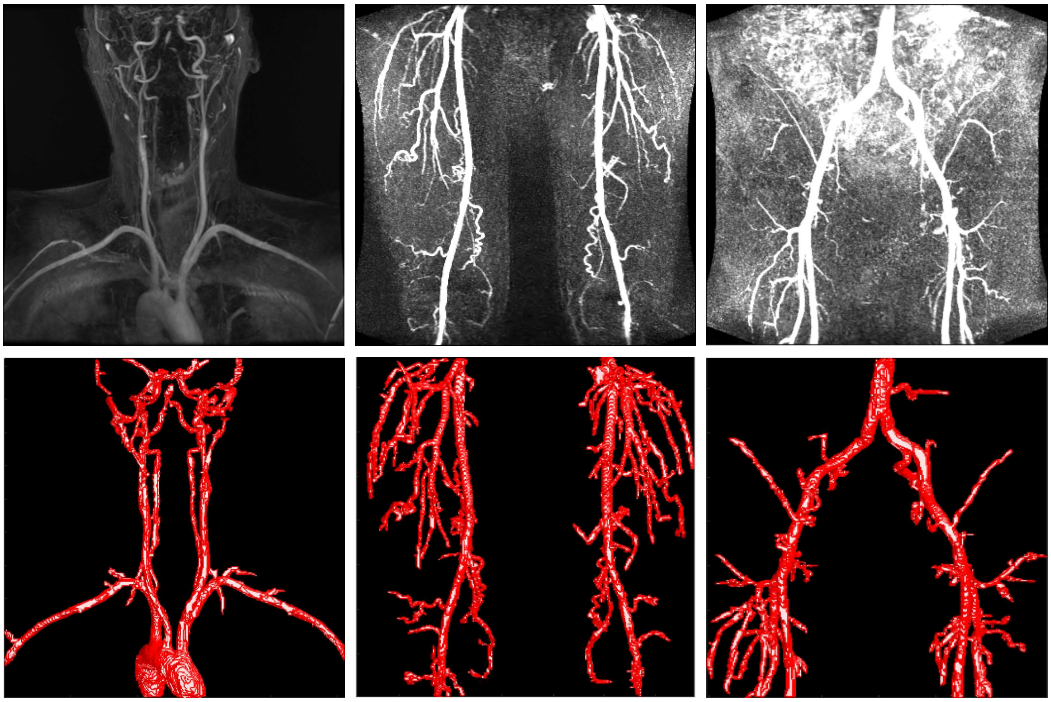

Figure 2.14: Illustration of the MIP and groundtruth data. First row is the MIP images of random selected original MRA carotid image, CTA femoral artery and veins image and the CT pelvic arteriogram image; second row is the 3D view of manually segmented blood vessels created using the random selected MRA carotid image, CTA femoral artery and veins image and the CT pelvic arteriogram image

2.5.1 Challenges faced during manual segmentation of blood vessels

The challenges faced during aortic segmentation include the following:-

1. In most cases, the blood vessels are close to other organs whose grayscale is so similar to that of blood vessels. The non-blood vessel with similar grey scale as blood vessels may be detected as blood vessels, especially if they are of a similar shape as the blood vessels.
2. Some non-blood vessels have a similar shape as blood vessels (see figure 2.8. They cab be mistakenly segmented as blood vessels.
3. In most medical images, more blood vessels are small, dark and blur. They can be missed.
4. The contrast distribution across different blood vascular structures vary. Brighter blood vessels.

2.5.2 How the research overcame the challenges

The ground truth segmentation process was supported by two clinical experts with the same level of experience in segmentation.

2.6 Chapter Conclusion

This chapter has described the methodology used for the medical image data collection at the sir peter mansfield imaging centre Nottingham, Queens Medical Center, Nottingham and online. Lastly, the manual segmentation scheme used and the challenges faced when manually segmenting blood vessels in the radiology images is also presented.

Chapter 3

Blood vessel segmentation

3.1 Chapter Overview

This chapter also introduces the subject of blood vessels from an anatomical and physiological perspective to the mechanism involved in the generation of blood vessel disorders. It discusses different classes of blood vessels, blood vessel disorders that indicate the presence of vascular diseases, and the genetic and environmental factors that have been identified to be indicative of blood vessel disorders. It also reviews the current methods used during the blood vessel segmentation process in medical images. Finally, the current challenges faced by blood vessel segmentation techniques are introduced and the need for automatic blood vessel segmentation methods is discussed.

3.2 Blood Vessels Anatomy and Physiology

Blood vessels refer to tubular structures responsible for supplying the body organs with rich oxygenated blood and vital nutrients [76]. The body requires oxygen and nutrients and needs to eliminate waste products to maintain metabolic stability. The blood vascular system has an important role in supplying oxygen and nutrients to every organ and removing waste products, via a series of blood vessels. In conjunction with the heart, which acts as a pump, it forms the cardiovascular system (Jarvis and Saman, 2018). Arteries and arterioles leaving the heart with oxygenated blood provide oxygen, nutrients, hormones and other substances throughout the body. Veins and venules leaving the organs and tissues return to the heart carrying metabolic waste. The exchange of gases and the transfer of nutrients

between blood and tissues take place in the capillaries.

Any disruption in the normal flow of blood leads to the build-up of plaque inside the inner lining of the walls of the blood vessels which in turn causes blood disorders such as blood vessel tortuosity, and blood vessel malformation. blood vessel disorders signal the presence of blood vascular diseases [76, 56].

Blood vascular diseases are seen as the most claimers of lives with cardiovascular diseases (such as coronary heart disease, cerebrovascular diseases, stroke, rheumatic heart diseases) ranked as the leading cause of death in the world, accounting for 17.9 million death per year. In addition, it poses a burden to the economy. The overall costs to society amount to billions of pounds per annum. Between 2020 and 2030, the annual costs of cardiovascular diseases (CVD) are estimated to range between £19-35 billion. Furthermore, CVD has a drastic effect on those living with the disease as well as the family members that serve as caregivers for the people with the diseases. The financial costs and social costs are devastating. For people who have had the misfortune of watching family members with vascular diseases such as stroke, it is emotionally draining to witness a gradual loss of everything that makes us human. This goes to show the significance and multifaceted consequences of blood vessel diseases and the need for stringent alleviation measures.

3.3 Classification of Blood Vessels

This section present the classes of blood vessels that circulate the body with blood (Figure 3.1). It also presents the functions of each blood vessel class (Table 3.1).

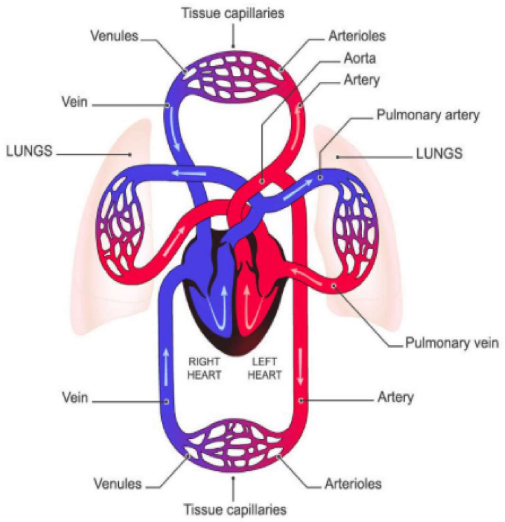

Figure 3.1: Classes of blood vessels

3.3.1 Arterial system

The arteries are the blood vessels that transport oxygen-rich blood from the heart to the tissues of the body. Blood travels from the arteries to the arterioles and onto the capillaries, where gaseous exchange takes place. Arteries can be divided into three types including elastic arteries, muscular arteries and arterioles.

(i) The elastic arteries are the largest (1-2.5cm in diameter) and comprise large amounts of elastin as well as smooth muscle. They have a large lumen with a low resistance to blood flow and can expand and recoil to accommodate changes in blood volume.

(ii) Muscular arteries regulate local blood flow and deliver blood to individual organs. They measure 0.3mm-1cm in diameter and possess more smooth muscle but less elastin than elastic arteries.

(iii) Arterioles are small-diameter blood vessel in the micro-circulation that are considered as the primary resistance vessels as they distribute blood flow into capillary beds. The arterioles are the smallest arteries with a diameter ranging between 0.01 and 0.3mm.

3.3.2 Venous system

Veins transport deoxygenated blood from the tissues back to the heart and there onwards to the lungs. In nature, the veins are thin, elastic vessels that act as a reservoir of blood. They do not need large amounts of elastin and smooth muscle, since they transport low-pressure blood back to the heart. They have a large lumen, as well as valves that ensure a one-way flow of blood to the heart. The veins can be divided into three categories including venules, Inferior venae cavae, and superior vena cava (SVC).

(i) Venule - A venule is a small blood vessel in the microcirculation that allows deoxygenated blood to return from capillary beds to larger blood vessels called veins. Venules range from 8 to 100μm in diameter.

(ii) Inferior venae cavae - Inferior venae cavae is a large vein that carries the deoxygenated blood from the lower and middle body into the right atrium of the heart. The diameter of the Inferior Venae Cavae ranges from 1.5cm to 2.5cm.

(iii) The superior vena cava (SVC) - is the superior of the two venae cavae, the great venous trunks that return deoxygenated blood from the systemic circulation to the right atrium of the heart. It has a large diameter (24 mm) short length vein that receives a venous return from the upper half of the body, above the diaphragm.

The venous system is an irregular network that tends to follow the course of the arteries.

3.3.3 Capillaries

Capillaries are small enough to penetrate body tissues, allowing oxygen, nutrients, and waste products to be exchanged between tissues and the blood. The capillaries are the smallest branches of a tree that connect arterioles to venules. Capillaries can be divided into three categories including continuous, fenestrated and sinusoidal.

(i) Continuous -the uninterrupted lining of endothelial cells with tight junctions between the cells limiting the passage of solutes. Usually found in the skin and muscles.

(ii) Fenestrated capillaries- These Fenestrated capillaries are similar to continuous only that some endothelial cells have pores usually found at filtration sights. Usually found in the intestines and kidney.

(iii) Sinusoidal capillaries - Sinusoidal capillaries are modified capillaries with large fenestrations and less tight junctions, allowing large molecules and cells to pass. Usually found in endocrine tissue, bone marrow and liver.

Blood vessel classes	Function
Arterial system	Transport high-pressure blood that is oxygenated from the heart to smaller arteries and arterioles
Venous system	Act as a reservoir of blood and transport low-pressure blood that is de-oxygenated to the heart.
Capillaries	Allows oxygen, nutrients, and waste products to be exchanged between tissues and the blood

Table 3.1: Classes of blood vessels and their functions

3.4 Structure of a Blood Vessel

Apart from the smallest vessels, blood vessels are made of three layers including the tunica interna, tunica media and tunica externa (or adventitia)(Figure 3.2). The three layers are described in the next section.

3.4.1 Tunica interna

The tunica interna (innermost layer) is a single layer of squamous (flat) epithelial cells called the endothelium. The endothelium regulates blood flow and prevents clotting; The endothelial cells can easily be damaged by hypertension, toxins such as cigarette smoke, or hyperglycaemia. This damage eventually results in atherosclerosis (plaque that blocks the blood flow).

3.4.2 Tunica media

The tunica media (middle layer) takes up most of the arterial vessel wall and is composed of smooth muscle fibres and elastin. This is where an activated sympathetic nervous system can stimulate the smooth muscle fibres to contract, provoking blood vessel narrowing (vasoconstriction) and decreasing blood flow. When the sympathetic nerves are inhibited, the muscle fibres of the tunica media relax, the blood vessels increase in diameter (vasodilation) and blood flow increases.

3.4.3 Tunica externa

The tunica externa (outer layer) consists mainly of connective tissue fibres that protect the blood vessels and attach them to any surrounding tissues.

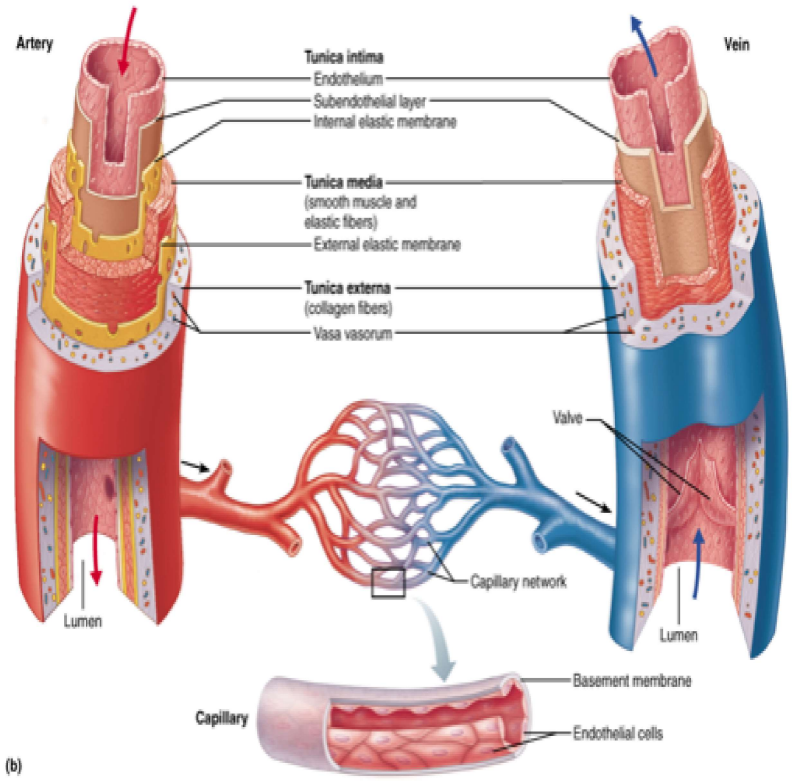

Figure 3.2: Structure of the blood vessel

3.5 Blood Vessel Disorder

Blood vessel disorders refer to malformed, entangled, or ruptured areas in a blood vessel. Examples of blood vessel disorders include blood vessel stenosis, blood vessel tortuosity and vascular malformations. The next upcoming describes each of the blood vessel disorder.

3.5.0.1 Blood vessel stenosis

Stenosis, refers to abnormal narrowing of the blood vessels that occur when the flow of blood is constricted by atherosclerotic plaque. It may occur any where in the body. The narrowing reduce blood flow to the different organs of the body.

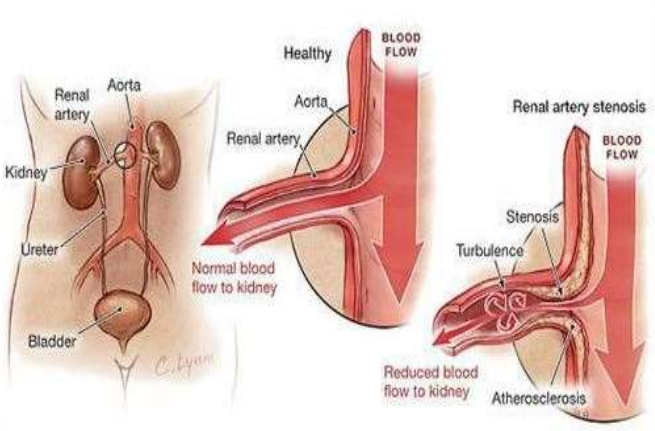

Figure 3.3: Illustration of blood vessel stenosis

3.5.0.2 Blood vessel tortuosity

Blood vessel tortuosity is an extremely rare genetic disorder characterised by lengthening (elongation) and twisting or distortion (tortuosity) of arteries throughout the body. Tortuosity may be caused by multiple factors including genetic factors, degenerative vascular diseases and an alteration in blood flow and pressure.

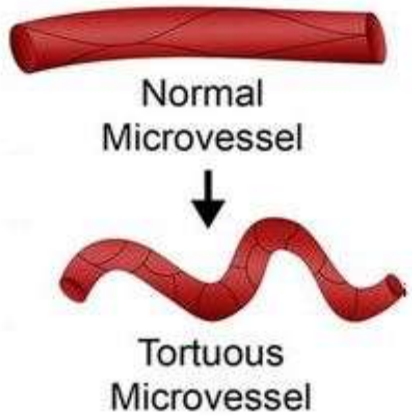

Figure 3.4: Illustration of blood vessel tortuosity

3.5.0.3 Vascular malformations

A vascular malformation is an abnormal development of blood vessels. These are found in the large arteries and veins, in smaller vessels called arterioles and venules, in microscopic capillaries. Examples of malformations include venous malformations and arteriovenous malformations

1. **Venous malformations:** They affect the veins, which carry blood from organs back into the heart and lungs for re-oxygenation. They can occur anywhere in the body.

Figure 3.5 shows a child with a venous malformation on her face.

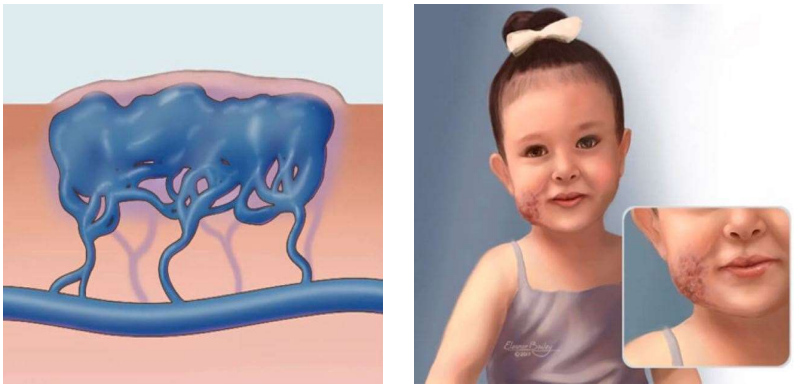

(a) (b)

Figure 3.5: Illustration of venous malformations. (a) venous malformation with macrocystic spaces, meaning with debris separated by septa; (b) child with venous malformation on her face;

2. **Arteriovenous malformations:** Arteriovenous malformations develop as the result of an abnormal connection between arteries that supply the body's organs, and the veins, which drain them. Figure 3.6 illustrates arteriovenous malformations.

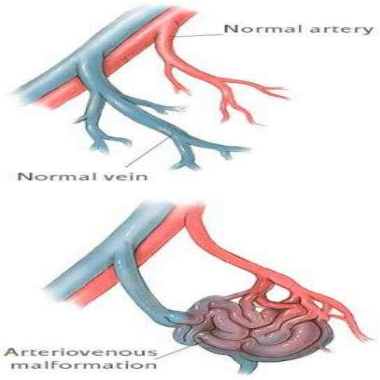

Figure 3.6: Illustration of Arteriovenous malformations

3.6 Blood Vessel Segmentation Process

In the blood vessel segmentation process, a medical image first undergoes through the image pre-processing (also known as image enhancement) step to improving the quality of the image, which typically concerns image denoising, contrast enhancement and blood vessel enhancement, before finally extracting and enhancing the resulting blood vessel structure during the segmentation and post-processing stage respectively (Figure 3.7). The major applications of image segmentation include monitoring patient's response to treatment, treatment planning (including angioplasty and emergency stent placement) and disease

diagnosis, done to save lives, therefore, better blood vessel segmentation techniques that can distinguish blood vessels from non-blood vessels with high accuracy are necessary. In this section, I review recently proposed image pre-processing techniques and segmentation techniques to develop appropriate 2D and 3D segmentation methods for extraction of blood vessels of various sizes.

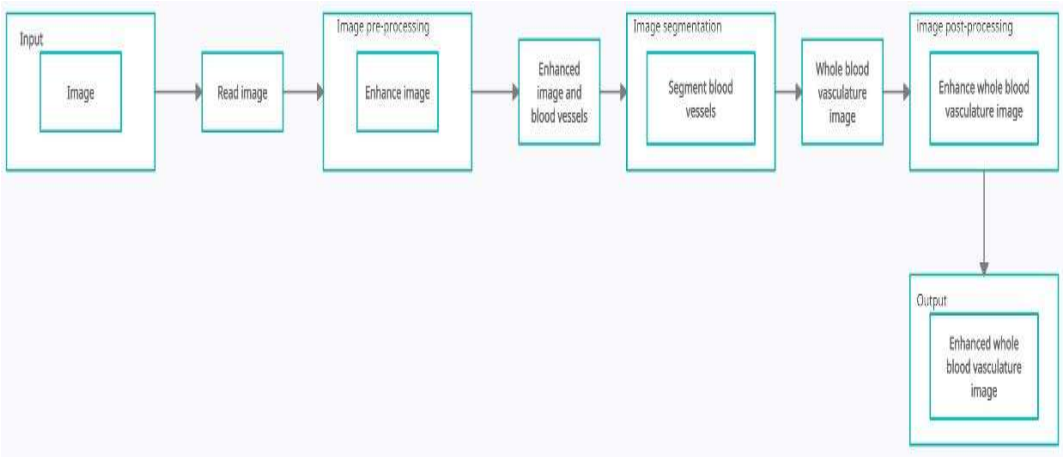

Figure 3.7: Blood vessel segmentation process

Based on the Figure 3.7, images are read from the database then later enhanced to improve the quality of the image during the image pre-processing stage, Image voxels of the enhanced medical image are then grouped in to blood vessel voxels and non-blood vessel voxels during blood vessel segmentation, Finally, the resulting organ vasculature is then enhanced to remove the unwanted objects during the post processing stage. The resulting blood vasculature is enhanced using an appropriate enhancement method. The next upcoming steps describes image enhancement techniques and the segmentation techniques.

3.6.1 Image Enhancement Techniques

Image enhancement (also known as image pre-processing) is performed to improve the quality of the medical image using an appropriate image enhancement method. Image enhancement methods can be classified into three categories including noise removal methods, contrast enhancement methods and vessel enhancement methods. The three categories are described below. Note: These techniques can also be used during post-processing to enhance the resulting blood vasculature.

3.6.1.1 Noise removal methods

Noise removal (also known as image denoising) is an important step in image pre-processing performed to eliminate noise from medical images, to restore the true image. The noise removal step has a strong influence on the quality of the image and other image analysis step. A method that can remove noise while preserving the edges of the image is necessary to improve the quality of the image and the image segmentation results. The next section presents the commonly use noise removal methods.

(a) **Gaussian filter:** is a low pass filter used to remove noise and blur the regions of an image. The filter is implemented as an Odd sized symmetric kernel which is passed through each image pixel of the Region of Interest, replacing the centre pixel with a local average of intensities. Gaussian blur (G) filtered image can be expressed as:

$$G[I_p] = \sum_{q \in S} G_\sigma(\|p - q\|) I_q \tag{3.1}$$

Where $G_\sigma(x)$ denotes the two-dimensional Gaussian kernel

$$G_\sigma(x) = \frac{1}{2\pi\sigma^2}.exp\left(-\frac{x^2}{2\sigma^2}\right) \tag{3.2}$$

So, Gaussian filtering is a weighted average of the intensity of the adjacent positions with a weight decreasing with the spatial distance to the center position p. The weight for pixel q is defined by the Gaussian $G_\sigma(\|p - q\|)$, where σ is a parameter defining the extension of the neighbourhood.

Gaussian filter is easy to implement and is good for removing Gaussian noise. However, it over smoothens the edges of the blood vessels. According to the investigation carried out in [14], over smoothing changes the size and shape of the object hence affecting further analysis. Over smoothing can be avoided by using non-linear filters such as Anisotropic filter and a Bilateral filter [50]. Besides the over smoothing problem, the Gaussian filter blurs the edges of the blood vessels which in turn reduces the contrast of the image.

(b) **Mean filter:** Mean filter removes noise by using a simple sliding window that replaces the centre value with the average of all pixel values in the window (Figure 3.8). The

window or kernel is usually a square but it can be of any shape. Mean filter is easy to implement and is suitable for removing poison noise. However, Like the Gaussian filter, it blurs the image and fails to preserve the details of the image [205].

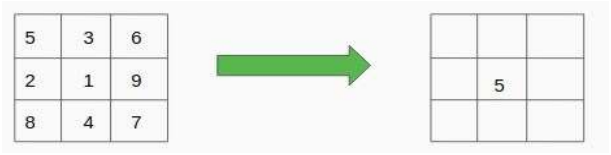

Figure 3.8: Illustration of mean filter

(c) **Median filter:** The median filter is a non-linear filtering technique, used to remove noise from an image. The median filter eliminates noise by using a simple sliding window that replaces the centre value with the Median of all pixel values in the window (Figure 3.9). The window or kernel is usually a square but it can be of any shape. Median particularly effective in presence of salt and pepper noise. Compared to the Gaussian filter and mean filter, the median filter provides excellent noise reduction capabilities with less blurring. furthermore, It also preserves and sharpens the edges of the image. However, It cannot eliminate all types of noise [202].

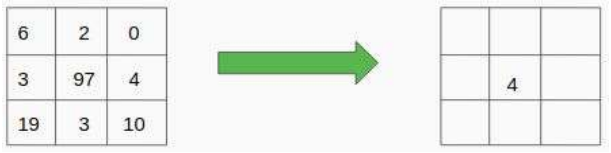

Figure 3.9: Illustration of median filter

(d) **Wiener filter:** The Wiener filter is a filter used to produce an estimate of a desired random process by linear time-invariant filtering an observed noisy process, assuming known stationary signal and noise spectra, and additive noise. The Wiener filter minimizes the mean square error between the estimated random process and the desired process in the process of inverse filtering and noise smoothing. The Wiener filter is suitable for removing additive noise. Like a median filter, a Wiener filter can preserve the edges of the image. However, unlike the mean filter, median and Gaussian filter, the Wiener filter can also invert the blurring simultaneously. But, Wiener filter has the drawback of requiring knowledge of the power spectral density of the image which is unavailable in practice.

(e) **Anisotropic filter:** Anisotropic diffusion is a non-linear diffusion filter that was

proposed by Perona and Malik to address the blurring problem and localisation problems of linear diffusion filtering [169]. The technique applies an in-homogeneous process that reduces the diffusivity at those locations which have a larger likelihood to edge. This likelihood is measured by $|\nabla u|^2$. The Anisotropic filter is based on the equation[169, 228].

$$\partial_t U = div(g(|\nabla u|^2)\nabla u) \tag{3.3}$$

and it uses scalar valued diffusivity (Equation 3.4) during enhancement.

$$g(s^2) = \frac{1}{1 + \frac{s^2}{\lambda^2}} (\lambda > 0) \tag{3.4}$$

Where λ is the contrast parameter. Compared to Gaussian filter, Anisotropic diffusion can smoothen the edges, preserve the edges and remove random noise from the image without blurring edges [169]. However, it cannot work on images with high levels of noise, and reduces the resolution of the image.

(f) **Bilateral filter:** Bilateral filtering is a non-local diffusion process that was proposed by Tomasi and Maduchi [208], [50]. Similarly to the Gaussian convolution, the bilateral filter is also defined as a weighted average of pixels. The difference is that the bilateral filter takes into account the variation of intensities to preserve edges. The rationale of bilateral filtering is that two pixels are close to each other not only if they occupy nearby spatial locations but also if they have some similarity in the photometric range. The bilateral filter B of an image I can be expressed as below [50]:-

$$B[I]_p = \frac{1}{W_p} \sum_{q \in S} G_{\sigma_s}(\|p - q\|) G_{\sigma_r}(I_p - I_q) I_q \tag{3.6}$$

where W_p is a normalization factor:

$$W_p = \sum_{q \in S} G_{\sigma_s}(\|p - q\|) G_{\sigma_r}(I_p - I_q) \tag{3.7}$$

Parameters σ_s and σ_r measure the amount of filtering for the image I. As the range parameter σ_r increases, the bilateral filter becomes closer to Gaussian blur because

the range Gaussian is flatter. Increasing the spatial parameter σ_s smooths larger features. G_{σ_s} is a spatial Gaussian that that decreases the influence of distant pixels. G_{σ_s} ensures that only pixels in a spatial neighbourhood are considered. G_{σ_r} is a range Gaussian that decreases the influence of pixels q with an intensity value different from I_p. G_{σ_r} ensures that only pixels of similar intensities are considered to compute the blurred intensity value to avoid blurriness and also preserves size and shape of edges of vessels [239]. **Note:** that the term range r qualifies quantities related to pixel values, by opposition to space s which refers to pixel location.

Like anisotropic filter, bilateral can remove the noise, smoothen edges, preserve the edges without blurring the edges of the image [14, 146, 105, 118, 184]. Despite the similarity, the Bilateral filter has an advantage over anisotropic diffusion, it caters for intensity in-homogeneity in images while removing noise [50].

(g) **MATLAB bwareaopen operation:** MATLAB bwareaopen operation is a MATLAB operation that removes small objects including noise and other unwanted objects from the image of a certain size [200]. It removes all connected components (objects) that have fewer than P pixels from the binary image, producing another binary image, BW2. The default connectivity is 8 for two dimensions, 26 for three dimensions, and conndef (ndims (BW), 'maximal') for higher dimensions.

MATLAB bwareaopen operation involves three steps that include (i) Determining connected components using Matlab bwconncomp operation. Matlab bwconncomp operation returns connected components (with connectivity of 8 in the binary image), (ii) Computing the area of each component using Matlab regionprops operation. (iii) Removing small objects. All connected objects are labelled. ismember operation is used to remove all unwanted objects of a particular number of pixels. The method is capable of getting rid of noise (such as salt and pepper noise) and unwanted objects while preserving the image details. However, it can only be applied on a binary image [200].

3.6.1.2 Summary of noise removal methods

A method that can denoise the image, smoothen the edges of the image, preserve the edges of the image and address the intensity variations in the image is considered ideal. Generally,

no method can remove all types of noise. Among the denoising methods, the Gaussian filter can remove Gaussian noise and can smoothen the edges of the image. However, the Gaussian filter tends to blur and over smooth the edges of the image which changes the size and shape of the object hence affecting the further analysis. Like Gaussian filter, mean filter blurs the image and fails to preserve the details of the image [205]. Although median filter can remove noise and preserve and sharpen the edges of the image, it doesn't cater for intensity variation in the image while denoising the image. Unlike the mean filter, median and Gaussian filter, the Wiener filter can invert the blurring simultaneously. However, it doesn't smoothen the edges and it also requires knowledge of the power spectral density of the image which is unavailable in practice. An alternative would be to use MATLAB bwareaopen operation as it can remove noise and unwanted objects from the image while preserving the edges of the image. However, it doesn't smoothen the edges of the image and only work on binary images. Although an anisotropic filter can remove noise, smoothen the edges of the image, and preserve the edges of the image, it fails to work on images with high levels of noise and reduces the resolution of the image. Compared to all the methods, a Bilateral filter can remove noise, smoothen edges, and preserve the edges of the image even in the presence of intensity inhomogeneity without reducing the resolution of the image.

3.6.1.3 Image contrast enhancement techniques

Image contrast enhancement is another important image preprocessing step done to enhance the contrast of the image. The next section presents the methods used to enhance the contrast of the image.

(a) **Histogram Equalization (HE):** Histogram equalization is an image contrast enhancement technique that adjusts image intensities to improve contrast. It accomplishes this by stretching out the intensity range of the image. HE increases the global contrast of images when its user data is represented by close contrast values which allow for areas of lower local contrast to gain a higher contrast. HE is simple to implement and computationally fast [212]. However, it changes the mean brightness of an image significantly as a consequence of histogram flattening and sometimes this is not a desirable property when preserving the original mean brightness of a given image is necessary.

(b) **Adaptive Histogram Equalization:** Adaptive Histogram Equalization computes many histograms for each of the separate parts of the image and uses them to redistribute the lightness values of the image, hence it differs from Histogram Equalization [164]. Adaptive Histogram Equalization is suitable for bettering the local contrast in images. However, the AHE technique has the drawback of amplifying noise in comparatively homogeneous regions of an image [212]. This problem in the adaptive histogram equalization technique can be solved by using the modified technique called contrast limited adaptive histogram equalization (CLAHE) which prevents the amplification of noise by limiting the amplification process. According to Nungsanginla et al., [164], CLAHE prevents the amplification of noise by limiting the amplification process.

(c) **Contrast Limited Adaptive Histogram Equalization (CLAHE):** Contrast Limited Adaptive Histogram Equalization is a variant of Adaptive Histogram Equalization. CLAHE has one additional step over Adaptive Histogram Equalization and that is a clipping of the histogram [164]. CLAHE enhances the contrast of the image by following the steps including (i) Divide the image into tiny regions. (ii) Decide the mapping functions of a local histogram. (iii) Choose the clipping point of the histogram. (iv) Apply the function to every region. (v) Reduce the noise by the background subtraction method.

CLAHE can remove noise and obtain a high contrast image [135, 226]. However, it does not take the mean brightness of an image into account. it may result in over enhancement and saturation artefacts due to the stretching of the gray levels over the full gray level range [164].

(d) **White Top-Hat Transform Operation:** White top-hat morphological transform is an important kind of top-hat transform used to find and enhance the contrast of the elements and details in the input image that are brighter than their surrounding. White top-hat morphological transform is obtained by subtracting morphological opening from the image. A White top-hat morphological transform is expressed as follows: Assume an image f and a structuring element K. Dilation operation increases the objects in an image using the structuring element of a particular size. Dilation

operation increases the objects in the image by computing the maximum image value over a circular neighbourhood of a given radius [110]. Dilation operation is the complementary operation of the erosion operation. Erosion operation shrinks the foreground and enlarges the background by computing the minimum image value over the neighbourhood [110]. Dilation operation of structuring element of f by K then is the set of all displacements, z, such that $K^{\wedge}$ and f overlap by at least one element is expressed as $f \oplus K = \{z|(K^{\wedge})z \cap f\square \neq \emptyset\}$ and erosion is expressed as $f\Theta K = \{z|(K), \subseteq f\}$. Erosion followed by dilation represents an important morphological transform called an morphological opening, denoted by $f \circ K$. The residual of the opening compared to the original image, i.e., $f - (f \circ K)$ represents the white top-hat transform (WTH). Thus, when the opened image is subtracted from the original, the desired detail is obtained. The white top-hat transform (WTH) is expressed as follows:

$$WTH = f - (f \circ K) \tag{3.8}$$

White top-hat morphological transform is not only capable of correcting illumination to uncover the objects rendered absent in the images but it also able to get rid of the unwanted tissues in MRI image [80, 244]. In addition, it is flexible and can be incorporated in another method to achieve an objective. For example In [26], a top-hat morphological transform is incorporated into the watershed segmentation method to enhance contrast, [53] incorporated top-hat morphological transform in Frangi vessel enhancement filter to boost the efficiency of Frangi Vessel Enhancement filter interms of illumination correction and contrast enhancement.

3.6.1.4 Summary of image contrast enhancement filter methods

A method that can enhance the contrast in the image without changing the image details is considered ideal. Among the methods, the histogram equalisation method increases the global contrast of images when its usable data is represented by close contrast values which allow areas with lower local contrast to gain a higher contrast. However, it changes the mean brightness of an image which is not a desirable property when preserving the original mean brightness of a given image is necessary. Adaptive Histogram Equalization is suitable

for bettering the local contrast in images. However, the AHE technique has a drawback of amplifying noise in a comparatively homogeneous region of an image [212]. Among all methods, CLAHE can remove noise while enhancing the image contrast [135, 226]. However, it does not take the mean brightness of an image into account, and it may result in over enhancement and saturation artefacts due to the stretching of the gray levels over the full gray level range [164]. Unlike all the methods, White top-hat morphological transform is not only capable of enhancing the image contrast, but it can also correct illumination to uncover the objects rendered absent in the images, enhance contrast and also get rid of the unwanted tissues in image [80, 244]. In addition, it is flexible and can be incorporated in another method to achieve an objective.

3.6.1.5 Blood vessel enhancement filters

Blood vessel enhancement filters enhance the blood vessel structures in the medical images prior to their segmentation, to suppress non-blood vessel structures and image noise [185, 77, 113, 59, 253, 133]. In this thesis, the three commonly adopted vessel enhancement filters are reviewed. The three commonly used vessel enhancement filter include Frangi Vessel Enhancement Filter [77, 216], IUWT [22, 253] and local phase-based filter[132, 253]. These filters are commonly used during blood vessel enhancement due to the capability to enhance blood vessels at various sizes using a multi-scale approach [85]. The next section describes vessel enhancement filters.

(a) **Frangi Vessel Enhancement Filter:** One of the most popular and widely used vessel enhancement filter that was introduced by Frangi et al., [77]. This filter aim at enhancing tubular structures by analysing the behaviour of the image using the second-order derivative of the Gaussian convolution. The Hessian matrix in the point x at scale n, $H_n(x)$, can be efficiently computed using Gaussian second derivatives as shown in Equation 4.1.

$$H(I,x) = \frac{\partial^2 I_n}{\partial x^2} = I(x) \times \frac{\partial^2 G_n(x)}{\partial x^2} \tag{3.9}$$

Where I, is the image and G_n is the Gaussian function with standard deviation δ. The decomposition of the local second-order structure of the image extracts the eigenval-

ues.

The Eigen values of the hessian matrix are combined into vesselness measure to extract tubular structures. Three Eigen values are utilised, meaning that dark and bright regions are treated in the same manner. It employs a multi-scale approach which enables the extraction of vessels of various size, and then the vesselness function is given by:

$$f(x) = \begin{cases} 0, & if \lambda_2 > 0 \; or \; \lambda_3 > 0 \\ \Big(1 - exp\Big(-\frac{R_a^2}{2\alpha^2}\Big)\Big) exp\Big(-\frac{R_b^2}{2\beta^2}\Big)\Big(1 - exp\Big(-\frac{S^2}{2C^2}\Big)\Big) \end{cases} \tag{3.10}$$

Where $S = \sqrt{\lambda_1^2 + \lambda_2^2 + \lambda_3^2}$, $R_a = \left|\frac{\lambda_2}{\lambda_3}\right|$, $R_b = \left|\frac{\lambda_1}{\sqrt{|\lambda_2 \lambda_3|}}\right|$

and $\alpha,\ \beta,\ and\ c$ are thresholds that control the sensitivity of the line filter to the dissimilarity measures R_a, R_b and S. R_a is the ratio of the two biggest eigenvalues that indicates whether the local structure is more plate-like or tube-like, the term R_b accounts for blob-like structures and the term S deals with the difference between vessel and background areas. β is a bias value. An ideal tubular structure implies $|\lambda_1| \approx 0,\ |\lambda_1| \leq |\lambda_2|,\ \lambda_2 \approx \lambda_3$ where the sign of λ_2 and λ_3 indicates polarity. The above vesselness measure uses filter responses at different scales taking the maximum response at each point x:-

$$V_F(X) = \max_{\delta_{min} \leq \delta \leq \delta_{max}} f(x) \tag{3.11}$$

The filter shows positive response in tubular structures in the image at various scales. This is the case with vessels in the organs, vessels vary in size. Frangi vessel enhancement filter is robust to noise and can enhance both the dark vessels on a bright background and the bright vessels on a dark background. However, Frangi vessel enhancement filter blurs the edges of the vessels in images and fails to work on images with high levels of intensity in-homogeneity [77, 116].

(b) **Isotropic Undecimated Wavelet Transform (IUWT):** The Isotropic Undeci-

mated Wavelet Transform is a powerful, redundant wavelet transform that enhances the images using the scaling coefficients and wavelet coefficients. The scaling coefficients are used to preserve the mean of the original image, whilst, wavelet coefficients have a zero mean and encode information corresponding to different spatial scales present within the image [22]. At each iteration, scaling coefficients are computed by low pass filtering and wavelet coefficients by subtraction. Reconstruction of the original signal from all wavelet coefficients and the final set of scaling coefficients is straightforward, and requires only addition. After the computation of n wavelet levels. The set of wavelet coefficients generated at each iteration is referred to as a wavelet level. The higher the wavelet level, the better the image contrast. The method is fast and filters used in IUWT, don't need to be orthogonal or bi-orthogonal and therefore, the lack of the need for orthogonality or bi-orthogonality is beneficial for design freedom [195]. However, it fails to enhance small vessels and it creates ringing artefacts around edges of the vessels [195, 195]. Moreover, it is sensitive to noise and intensity inhomogeneity.

(c) **Local Phase-Based Filter:** Local Phase-Based Filter is commonly used during blood vessel enhancement due to its ability to measure structural information(such as lines and edges). The filter enhances the image by using the Local phase and local energy, interchangeably, following convention. Local phase is estimated using quadrature filters that comprise of pairs of odd and even filters with a phase difference of $\pi 2$. Local energy is used to modulate the Local Phase-Based Filter. Compared to other blood vessel enhancement methods, Local Phase-Based Filter exhibits intensity invariant feature enhancement properties [252], and produces clear line structure. Like Isotropic Undecimated Wavelet Transform, Local Phase-Based Filter is sensitive to noise. Moreover, it fails to enhance small vessels in presence of intensity inhomogeneity [93, 94, 197].

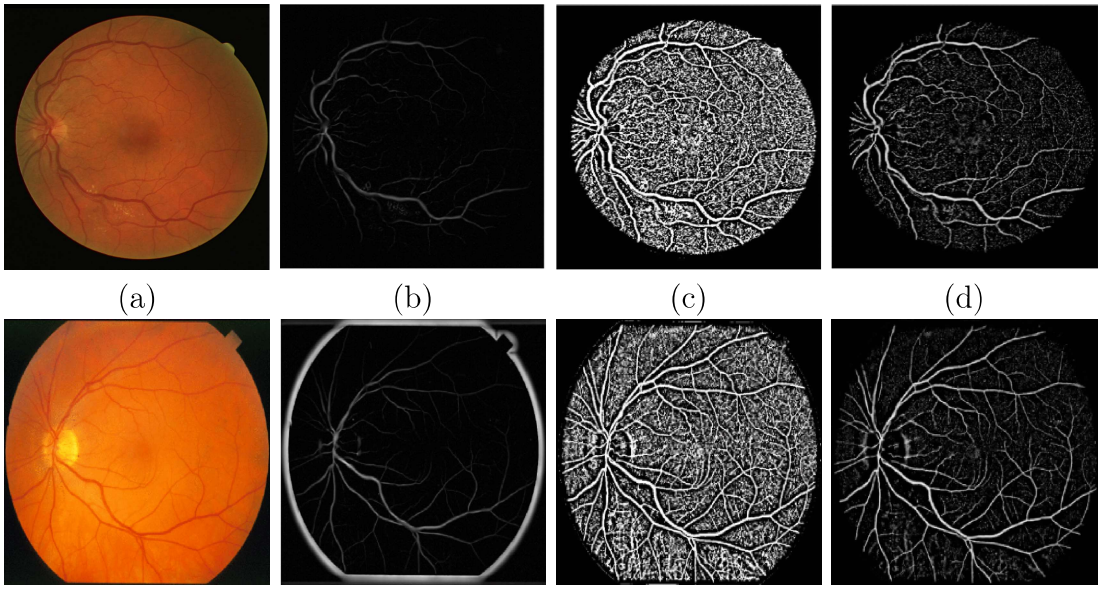

Figure 3.10: Visual comparison of blood vessel enhancement filters on a randomly selected retina image. Column(a) are the original images randomly selected from the DRIVE dataset, and STARE dataset; Column(b) are enhancement results produced by Frangi vessel enhancement filter; Column(c) are enhancement results produced by isotropic undecimated wavelet transform (IUWT); Column(d) are enhancement results produced by local phase-based filter

3.6.1.6 Summary of vessel enhancement filter

Figure 3.10 shows enhancement results using Frangi vessel enhancement filter, isotropic undecimated wavelet transform, and local phase-based filter on a randomly chosen image from the DRIVE dataset and STARE dataset obtained from Zhao et al., [253]. It can be seen from Figure 3.10(b) and 3.10(g) that the Frangi vessel enhancement filter tends to only enhance the larger vessels as does the isotropic undecimated wavelet transform (Figure 3.10(c) and Figure 3.10(h)) and local phase-based filter (Figure 3.10(d) and Figure 3.10(i)). This is because they fail correct illumination in images to detect the thin blood vessels. Compared to isotropic undecimated wavelet transform and local phase-based filter, Frangi vessel enhancement filter is robust to noise. However, by nature, the Frangi vessel enhancement filter fails to enhance vessels in images with high levels of intensity in-homogeneity [77], and it causes blurriness around the edges of the blood vessels due to usage of Gaussian convolution [77]. There is a clear need (i) To address the blurriness problem of the Frangi vessel enhancement filter. (ii) To improve the Frangi Vessel Enhancement Filter to address the problem of blurriness and sensitivity to intensity inhomogeneity problem in Frangi vessel enhancement.

3.6.2 Summary of Image Enhancement Methods

Among image enhancement methods, blood vessel enhancement filters focus on enhancing blood vessels of various sizes using a multiscale approach. Compared to other vessel enhancement filters, Frangi vessel enhancement is robust to noise and can enhance both dark and bright lines in the image. However, by nature, the Frangi vessel enhancement filter fails to enhance vessels in images with high levels of intensity in-homogeneity [77], and it causes blurriness around the edges of the blood vessels due to usage of Gaussian convolution [77]. Further improvement could include replacing Gaussian convolution in Frangi Vessel Enhancement Filter, with either Top Hat Morphological Transform convolution or bilateral convolution or both Top hat morphological transform and bilateral convolution, since Top hat morphological transform is not only capable of correcting illumination to uncover the objects rendered absent in the images but it also able to get rid of the unwanted tissues [80, 244]. Bilateral convolution can prevent blurriness, eliminate the noise, smoothen the edges of the image and also preserve the size and shape of the vessels even in the presence of intensity in-homogeneity [14, 146, 105, 118, 184].

Author	Method	Category	Strength	Weakness
[225][198]	Gaussian filter	noise removal	easy to implement, good for removing Gaussian noise.	blurs the blood vessels, over smoothing
[205]	Mean filter	noise removal	good for removing poison noise, easy to implement	fails to preserve the details of the image
[202]	Median filter	noise removal	easy to implement, it preserves edges of the image,good for removing salt & pepper noise	it is not good for all types of noise.
[23]	Wiener filter	noise removal	it can remove the additive noise,it can also invert the blurring simultaneously, easy to implement	it requires knowledge of the power spectral density of the image
[169]	Anisotropic filter	noise removal	reduces noise, preserving geometry,topology and localisation of the small vessels	sensitivity to the noise,it reduces the image resolution, and it degrades fine structure.
[208],[50]	bilateral filter	noise removal	preserves size and shape of edges of vessel,it eliminates noise, avoid blurriness,good for removing Gaussian noise	high computational costs
[200]	MATLAB bwareaopen operation	noise removal	can remove noise and unwanted objects	it can only work on binary images

Table 3.2: Summary of image pre-processing methods

Author	Method	Category	Strength	Weakness
[164][212]	Histogram equalization	image contrast enhancement	it enhances the overall contrast more effectively	it leads to loss of the original mean brightness of a given image
[164][212]	Adaptive histogram equalization	image contrast enhancement	enhances local contrast in images	amplifies noise in comparatively homogeneous regions of an image
[135][226] [164] [212]	CLAHE	image contrast enhancement	can remove noise, enhances image contrast	loss of brightness in the processed image,saturation artifact.
[80] [244][26] [53]	White top-hat morphological transform	contrast enhancement	it is flexible, enhances contrast image, correct illumination in the image	sensitive to noise
[77][116]	Frangi vessel enhancement filter	blood vessel enhancement	can enhance different sizes of vessels, can enhance both dark and bright tubular structures, robust to noise	sensitive to intensity inhomogeneity, blurs the blood vessels
[22][195]	Isotropic undecimated wavelet transform	blood vessel enhancement	it is fast	creates ringing artefacts around edges of the vessels, sensitive to noise, sensitive to intensity inhomogeneity
[132][252][93] [94][197]	Local phase-based filter	blood vessel enhancement	produces clear line structure	sensitive to noise, sensitive to intensity inhomogeneity

Table 3.3: Summary of image pre-processing methods

3.6.3 Segmentation Methods

Blood vessel segmentation is performed to group medical image voxels in to two blood vessel voxels (also known as foreground) and non-blood vessel voxels (also known as background). The five categories of segmentation methods include model-based method, fuzzy c-means clustering-based method, tracking-based method, Graph cut method, and threshold-based method. The next section presents the model-based approach.

3.6.3.1 Model Based Approach

Methods that employ this approach can be divided in to two categories, namely; Active Contour Models [136, 54, 137, 223, 158, 54, 64, 247, 141, 161, 9], and Surface Fitting Models [106, 219, 218, 227]. Active Contour Model (also known as parametric models), segment vessels by evolving a curve towards the boundary of vessels in the image, whilst, surface fitting model segment vessels by matching a model which contains information about the expected shape and appearance of the structure of interest to new image [106, 219]. Model-based techniques have the advantages of allowing incorporation of prior information about

the considered image structures, having higher flexibility of the shape, and being able to be adapted to fit the given data [229]. However, most of the techniques that employ the model-based method are 2D based. Moreover, most of these utilise global information during segmentation and therefore they cannot segment vessels in images with artefacts. A few model-based techniques that utilise local information or both local and edge-based information during segmentation, produce better segmentation results compared to model based techniques that utilise global information. However, they are sensitive to noise, simply because they are based on the assumption of the Gaussian noise. Methods that adopt Gaussian kennel ignore important details of small vessels during segmentation. Medical images can contain different types of noise (such as salt and pepper noise, poison noise, Gaussian noise, speckle noise and uniform noise). To solve this problem, Niu et al., [161], employed a local similarity factor, which makes use of the bilateral filter. Compared to other methods, the method is more robust to higher noise levels and preserves image details. However, like all other model-based methods, it fails to small vessels and causes vessel leakage. According to HAWAS et al [101] and Qui et al., [171], Fuzzy C-means Clustering Approach can deal with uncertainty and fuzziness in medical image data to accurately segment the blood vessels. The next section presents the Fuzzy C-means Clustering Approach.

3.6.3.2 Fuzzy C-means Clustering Approach

The technique was defined by Dunn [69], [235] in 1973, and later developed by Bezdek et al., [28], [235]. Fuzzy c-means clustering approach segment blood vessels by assigning a fuzzy membership value to each of the data points in the dataset basing proximity to each cluster centroid in the feature space [219]. Like model-based approach, fuzzy c-means clustering methods allows incorporation of information and it mostly applied during 2D image segmentation. However, fuzzy c-means clustering techniques that incorporate spatial information cause blurriness around the edges of the vessels. Furthermore, fuzzy c-means clustering techniques are sensitive to noise and fail to segment vessels of various sizes especially small vessels [6, 171, 5, 86]. Following the Fuzzy C-means Clustering Techniques, various extensions and analysis have been studied to segment blood vessels. For example, in [171], Spatial Fuzzy C-means (SFCM) Clustering is introduced. The method is based on the assumption that the neighbouring pixels highly correlate and that they possess similar

feature values. However, the method is unable to segment much noisy images and consequently blurs finer details of the object. To address that blurriness problem, Adhikar et al., [5], incorporated conditioning effects and local spatial information among adjacent pixels in the fuzzy membership function. The condition describes a level of involvement of the pixel in the constructed clusters. The Conditional Spatial Fuzzy C-means (CSFCM) can work on intensity inhomogeneous images. However, it is sensitive to noise. To address the noise problem in CSFCM, Gharnali et al., [86] proposed a CSKFCM. In this method, an original Euclidean distance in the CSFCM algorithm is replaced with a kernel-induced distance. The method is robust to noise. However, it fails to segment various sizes of vessels, especially small vessels. An alternative would be to track the blood vessels on image planes to easily distinguish blood vessels from non-blood vessels. The next section presents the Tracking Based Segmentation Method.

3.6.3.3 Tracking Based Segmentation Method

The goal of tracking based segmentation method is to extract points of the vessel centerline in medical images [75]. Methods that employ this method, trace vessels using initial position seed, direction seed and radius, to the endpoints of the continuous blood vessel. The direction seed helps in setting the tracking direction by estimating the vector connecting the two positions. Tracking based techniques improve the localisation of the vessels and can estimate the vessel diameter [17, 83]. Tracking based method requires human intervention during segmentation [130, 149], fails to handle vessel crossover points during segmentation and face difficulty in segmenting the vessels especially small vessels [90, 18, 149]. Moreover, the Tracking based Method is mostly applied on 2D[90, 18].

Following, tracking based segmentation techniques, various extensions and analysis have been studied to segment blood vessels. For example, Manniesing et al., [149] tracked the vessel axis using the topologically constrained surface evolution (level set evolution). This method model the topology of the evolving surface rather than its cross-sectional shape which less hinders the vessel tracking process. However, the method involves human intervention in parameter setting at the start point. The method also cannot model bifurcation. In [130], a dynamic programming-based method for automated localisation and segmentation of the thoracic aorta in non-contrast CT images is presented. In this method,

the localisation and segmentation of the aorta are formulated as optimal path detection problems. Although the method improves the localisation of the aorta, it involves human intervention during the tracking process. The method is also based on the assumption that vessels are of circular shape which does not hold. Avila-Montes et al., [18] similarly segmented the blood vessels by formulating localisation, centerline extraction, and segmentation of the aorta as an optimal path detection problem. Although the proposed method does not require any kind of additional input data (such as manually labelled images), it cannot preserve the order of the slices in a volume. Unlike Avila-Montes et al., [18], Guedry et al., [90] proposed a mathematical approach for tracking the centerline curve in retinal vascular images. In this method, the gray level image is first converted into a binary image using the Otsu threshold method to locate blood vessels. Skeletonisation is then performed using a thinning algorithm to obtain a vessel network graph. Pixels in the graph are then classified into endpoint, bifurcation points and the points of the centre line. The method is fast and associated with less error. However, the method does not produce the actual vessel structure.

3.6.3.4 Graph Cut Method

The graph cut method segments blood vessels by first of all binary labelling the image pixels into the foreground and background class, and then later using a cut to partition the image pixels into foreground and background depending on the intensity value, Although Graph cut allows the incorporation of object information (such as edge information, region information, shape information) for effective segmentation, the Graph-based method requires collaboration with other pre-processing techniques to perform better on intensity inhomogeneous images, which make it slow and consume a lot of memory [181, 249, 140, 250]. Moreover, Graph cut fails to segment blood vessels especially thin elongated vessels since the energy minimisation tends to shrink for curvilinear structures [250, 249, 181, 52, 51, 252, 103] and it is mostly applied on 2D image planes.

Following the Graph Cut method, various extensions and analysis have been studied to segment blood vessels. For example, to segment vessels in medical images, Freiman et al., [78] utilised local image intensities during segmentation. In this method, the weighted shortest path between the vessel seed endpoints based on local image and seed intensities

and vessel path geometric characteristics are first computed. then later, a Vessel Region Of Interest (VROI) from the shortest path and the estimated vessel radius is automatically defined. Vessels boundaries are extracted by minimising the energy on a corresponding graph cut. The method slow doesn't segment small vessels and is associated with a shrinkage problem. Chen et al., [51] segmented small vessels by applying quick shift clustering to group spatially neighbouring voxels into local regions and then later, applied Graph cuts basing on regional intensity distribution. The method is slow and cannot distinguish small vessel pixels from noise pixels. Zhao et al. [252] segmented the vessels by first of all addressing intensity in-homogeneity using Retinex based-in-homogeneity correction, then later, enhanced the vessels using the local phase enhancement technique, before finally segmenting the vessels using graph cut-based active contour method. The method is slow and misses small vessels. Sangsefidi et al., [181] adaptively calculated the data term in conventional graph-cuts algorithm locally to reduce memory and run-time requirements of the conventional graph-cuts algorithm, by modelling blood vessel intensities using two Gaussian distributions, then later employed the Maximum Intensity Projection (MIP) of the image in the Expectation-Maximisation algorithm to estimate the parameters of the model. The method leads to over-segmentation and cannot distinguish small vessels pixels from noise [249].

3.6.3.5 Thresholding Approach

Thresholding is the simplest and widely used segmentation method. Pixels in the grayscale image are partitioned into foreground and background depending on their intensity value by using a clip or threshold value. Blood vessels in a grayscale image is segmented by replacing the Pixels in an image with a black pixel if the image intensity I_{ij} is less than threshold value T (That is $I_{ij} < T$) or a white pixel if the image intensity I_{ij} is greater than threshold value T (That is $I_{ij} > T$) using threshold method. The condition used during thresholding to obtain a segmented image is given as follows:- -

$$g(x,y) = \begin{cases} 1 & if\ f(x,y) > T \\ 0 & if\ f(x,y) <= T \end{cases} \tag{3.12}$$

Where (x, y) is the pixels value in the image . T is the threshold.

3.6.3.6 Categories of Thresholding Methods

The three categories of thresholding method include global thresholding algorithms, and local adaptive thresholding. Among the threshold method, the global threshold method is popular because of its simplicity [67], however, it is based on the assumption of a preprocessed image and therefore it fails to work well on poor quality images (images with image artefacts) as it utilises global information. On the other hand, local adaptive thresholding is capable of segmenting vessels from the intensity inhomogeneous images. However, it is region size dependant, time-consuming and dependant on individual image characteristics. The next subsections describe the two thresholding methods.

(a) Global Thresholding

The global threshold method is popular and widely used because of its simplicity. In global thresholding, one threshold is used to separate the background from the foreground. The global threshold method is based on the assumption of a pre-processed image. It assumes that the image beforehand has been pre-processed and therefore it utilises global information during segmentation. Global thresholding doesn't produce better segmentation results when applied to a bad quality image. It requires an image to be pre-processed for it to produce better results. Among global thresholding methods, the Iterative Self-Organizing Data Analysis Technique (ISODATA) threshold method is very effective at identifying spectral clusters in data, there no need for prior knowledge about the image data, it requires little user effort, However, Like other global thresholding methods, it is based on the assumption of intensity homogeneity and therefore it cannot work well on poor quality images.

Compared to global thresholding, thresholding methods that utilise Region information (including local and global information), as well as the edge information, produce better segmentation results. The next section is the Local adaptive thresholding method.

(b) Local Adaptive Thresholding In Local adaptive thresholding, blood vessels are segmented using different threshold values for every pixel in the image based on analysis of its neighbouring pixels.

The threshold value T does not only depend on Gray levels of f(x, y) but also on local image properties of neighbouring pixels such as mean or variance. Local adaptive threshold function T(x, y) is given by

$$g(x,y) = \begin{cases} 1 & if\ f(x,y) >= T(x,y) \\ 0 & if\ f(x,y) < T(x,y) \end{cases} \tag{3.13}$$

Where $g(x,y)$ is the binary image, G(x,y) is gray level image, and T(x,y) is the threshold value. The threshold value T does not only depend on Gray levels of f(x, y) but also on local image properties of neighbouring pixels such as mean or variance. The threshold is calculated for each image pixel based on some local statistics such as variance, mean, and range of the neighbourhood pixels. Compared to the global thresholding, local adaptive thresholding can work on images with artefacts. However, local adaptive thresholding fails to obtain a useful threshold from flat regions, and time consuming [143]. Following local adaptive thresholding, various analysis have been studied to segment blood vessels, Forexample the multithreshold Otsu that was proposed by Otsu [166], The method calculates multiple thresholds for an image and segments the image into certain brightness regions. The method is one of the best methods that select the threshold automatically and stably based on the integration (i.e., a global property) of the histogram. However, the computation time grows exponentially with the number of thresholds. To improve the computational efficiency, another multi-threshold Otsu method based algorithm was proposed by Huang and Wang [107]. The two-stage multi-threshold Otsu method outperformed Otsu's method by reducing the iterations required to compute the between-class variance. For the six class segmentation problem, the computational time increased with an average ratio of about 76 for the conventional Otsu method as compared to 0.463 for the proposed method. In [102], another multi-threshold Otsu is proposed. The method is robust to noise.

In contrast to the multi-threshold Otsu, Hysteresis thresholding segments the image by linking the edge pixels into the curve segments by Starting from the pixel with

the highest gradient magnitude, then grows the curve segment grows at each step by including the most salient edge pixel among the 16 neighbours of the two endpoints of the curve segment. The growing is ended when no more object pixels can be added. Then, a new segment growing starts from the edge pixel with the highest gradient magnitude among the remaining object pixels that have not been included in a curve segment. This process is repeated until no more new curve segment can be generated. The salience value of each curve segment is the sum of the salience values of its edge pixels computed. Hysteresis thresholding has consistently outperformed absolute thresholding methods because of its capability to deal with uncertainty using the two thresholds. In addition, it can detect the absence of pixels in true edges even in presence of intensity in-homogeneity, Furthermore, object boundaries produced by hysteresis thresholding are continuous. However, it fails to detect thin vessels. Among the hysteresis thresholding methods, the hysteresis thresholding in [224] is one of the best methods as thresholding is object-based rather than pixel-based which makes it robust to noise.

Year	Method	Author	Image part	2D	3D	Strength	Weakness
2016	Model based method	Volonghi et al., [218]	thoracic aorta	✓		fast,allows incorporation of image information,it is flexible	cannot distinguish between vessels and non vessels,cannot cope with calcification's
2016	Model based method	Jang et al., [111]	aorta	✓		it is fast,allows incorporation of image information,it is flexible	fails to distinguish vessels from non vessels,cannot cope with calcification's
2017	Model based method	Wang et al., [221]	coronary artery	✓		allows incorporation of image information,flexible	it is not stable,cannot segment small vessels,cannot cope with calcification's
2018	Model based method	Ali et al., [13]	vessel image	✓		allows incorporation of image information,it is flexible	sensitive to noise, cannot segment small vessels,cannot cope with calcification's
2015	Model based method	Li et al., [137]	vessel image	✓		allows incorporation of image information,it is flexible	sensitive to intensity in-homogeneity, sensitive to noise, cannot distinguish vessels from non vessels,cannot cope with calcification's
1999	Fuzzy c-means clustering method	Pham et al., [170]	brain	✓		it is robust to noise,allows incorporation of image information,it is flexible	it involves manual intervention.
2013	Fuzzy c-means clustering method	Qui et al., [171]	brain image	✓		allows incorporation of image information, can deal with uncertainty during segmentation,it is flexible	sensitive to noise, it causes blurriness in the finer details
2015	Fuzzy c-means clustering method	Zhao et al., [255]	blood vessel image	✓		allows incorporation of image information,it is flexible	it is unable to extract small vessels
2015	Fuzzy c-means clustering method	Adhikari et al., [5]	brain	✓		allows incorporation of image information,it is flexible	it causes blurriness in the finer details, it sensitive to noise

Table 3.4: Summary of previous work on automatic blood vessel segmentation

Year	Method	Author	Image part	2D	3D	Strength	Weakness
2018	Fuzzy c-means clustering method	Gharnali et al., [86]	brain	✓		it is robust to noise,allows incorporation of image information,it is flexible	it causes blurriness in the finer details, it misses some vessels especially small brain vessels
2007	Tracking based method	Manniesing et al., [149]	carotid	✓		it is less hindered by vessels with pathology, can estimate the vessel diameter	it involves human intervention, it cannot model vessel bifurcation
2008	Tracking based method	Kurkure et al., [130]	aorta	✓		improves the localisation of the aorta, can estimate the vessel diameter	based on assumption that vessels are of circular shape which does not hold sometimes. it involves human intervation
2017	Tracking based method	Guedri et al., [90]	retina	✓		it is fast,can estimate the vessel diameter	cannot distinguish vessels from non vessels,it involves human intervation
2013	Tracking based method	Chen et al., [54]	blood vessel image	✓		it is fast, can estimate the vessel diameter	cannot segment small vessels, involves human intervation
2012	Threshold based method	Ece et a., [71]	retina	✓		it easy to implement	it is sensitive to noise
2017	Threshold based method	Challoob et al., [48]	retina	✓		it easy to implement,can estimate the vessel diameter	it is applicable on only RGB images
2013	Threshold based method	He et al., [102]	liver		✓	easy to implement	it cuts vessels, cannot segment small vessels
2015	Threshold based method	Mapayi et al., [150]	retina	✓		it easy to implement, it works on intensity in-homogeneous images	cannot segment small vessels,it is sensitive to noise
2017	Threshold based method	Dash et al., [62]	retina	✓		it easy to implement	it does not segment small vessels,it is sensitive to noise
2015	Threshold based method	Boegel et al., [31]	carotid artery	✓		it easy to implement	it does segment small vessels,it is sensitive to noise
2008	Threshold based method	Wang et al., [224]		✓		can detect absence of pixels in true edges even in presence of intensity in-homogeneity, produced object boundaries are continuous, it easy to implement	cannot detect thin vessels, it involves manual intervention

Table 3.5: Summary of previous work on automatic blood vessel segmentation

Year	Method	Author	Image part	2D	3D	Strength	Weakness
2009	Graph based method	Freiman et al., [78]	Carotid		✓	it easy to use, models bifurcations,allows incorporation of image information.	it is slow, doesn't segment small vessels, shrinks for curvilinear structures
2012	Graph based method	Hernandez-Vela et al. [103]	Coronary artery	✓		can segment vessels in presence of complicated Gray-level local distribution,allows incorporation of image information.	it cannot model vessel bifurcation and crossings, cannot segment small vessels,shrink for curvilinear structures
2014	Graph based method	Chen et al., [51]	Liver	✓		allows incorporation of image information.	cannot segment small vessels,sensitive to noise, slow, shrink for curvilinear structures
2015	Graph based method	Zhao et al. [252]	retina image	✓		allows incorporation of image information.	it is slow, fails to segment small vessels, shrink for curvilinear structures
2018	Graph based method	Sangsefidi et al., [181]	retina image	✓		allows incorporation of image information.	it is slow, fails to segment small vessels

Table 3.6: Summary of previous work on automatic blood vessel segmentation

3.6.4 Summary of Segmentation Techniques

A survey of segmentation techniques in medical imaging is presented. In particular, the discussion focused on approaches involving model-based approach, fuzzy c-means clustering, tracking-based approach, graph-based approach, and, threshold-based approach. How these existing approaches segment blood vessels are discussed, their strength and weaknesses in terms of vessel segmentation.

Despite the constant progress and efforts addressed in the field, No single segmentation approach is suitable for segmenting blood vessels of various sizes especially small blood vessels due to the presence of image artefacts (such as the low variation in the contrast between blood vessel pixels and background to successfully segment blood vessels, and the noise) in images. This is evident in [142, 4, 231, 96]. There is a need for methods that can segment blood vessels of various sizes. In addition, most of the methods are 2D based, Whilst, some that claim to be 3D based, segment 2D image planes and then

later reconstruct 2D image planes into a 3D image. 3D segmentation is important during diagnosis. Although 2D blood vessel segmentation is easy to carry out, it doesn't provide full information about the anatomic structure of the blood vessels for proper diagnosis, it leads to inconsistencies in the segmentation results and non-smooth vessel surfaces, due to omitting important anatomical information in 3D space.

An alternative would be to use a Graph cut method as it also allows the incorporation of object information (such as edge information, region information, shape information) for effective segmentation, however, Graph-based methods requires collaboration with other pre-processing techniques to perform better on intensity in-homogeneous images, which make it slow and consume a lot of memory [181, 249, 140, 250]. Like all methods, Graph cut method also fails to segment blood vessels especially thin elongated vessels, since the energy minimisation tends to shrink for curvilinear structures [250, 249, 181, 73, 191, 52, 51, 252, 103]. Among all methods, Tracking based techniques is immune to intensity variations, improve the localisation of the vessels and have the ability to estimate the vessel diameter [17, 83]. However, the tracking-based method requires human intervention during segmentation [130, 149] which is prone to errors, fails to handle vessel crossover points during segmentation and face difficulty in segmenting the vessels especially small vessels [90, 18, 130, 149]. The thresholding method is the easiest and effective method. However, techniques that employ global thresholding utilise global information and therefore can perform well on pre-processed images. Among the global thresholding methods, ISODATA thresholding is popular because it doesn't require prior knowledge about the image data during segmentation. During image acquisition, image artefacts (such as intensity in-homogeneity, noise, low contrast) often manifest in the medical images and therefore, methods that can take image artefacts into consideration during segmentation are necessary. Among thresholding methods, local adaptive thresholding techniques make use of the image local information and global information during segmentation, and therefore they work well on poorly illuminated images. However, they are region size-dependent and time-consuming. Among the local adaptive thresholding methods, Multi-threshold Otsu in [166] is one of the best methods that select the threshold automatically and stably basing on the integration (i.e., a global property) of the histogram. Multi-threshold Otsu is also robust to noise and fully

automated as the threshold are selected automatically [102]. However, the computation time grows exponentially with the number of thresholds. Although hysteresis thresholding requires human intervention during threshold setting, unlike multi-threshold Otsu, hysteresis thresholding can deal with uncertainty using the two thresholds. In addition, it can detect the absence of pixels in true edges even in presence of intensity in-homogeneity. Furthermore, object boundaries produced by hysteresis thresholding are continuous. However, it fails to detect thin vessels. A combination of Hysteresis thresholding with an appropriate pre-processing method would lead to better segmentation results.

3.7 Chapter Discussion and Conclusion

This chapter has introduced the anatomical and physiology of blood vessels, classes of blood vessels, blood vessel disorders that indicate presence of vascular diseases and genetic and environmental factors that have been identified to be indicative of blood vessel disorder. It then drills narrowly to focus on the blood vessel segmentation process in medical images which is the task addressed by this thesis. Although automatic blood vessel segmentation in medical images has witnessed a significant advancement in terms of methodology, The available methods struggle to distinguish blood vessels from non-blood vessels during segmentation. This is mainly because of the image artefacts in the medical images. The characteristics of the medical images have a major obstacle to developing usable segmentation methods. The variation in the contrast between blood vessel pixels and background pixels in medical images is very tiny to successfully segment blood vessels, and the noise present in medical images cause problems such as false detections (detecting non-blood vessels as blood vessels) and missed detections (skipping blood vessels of various sizes during segmentation). Hence, the problem of the image artefacts remains an open challenge that the blood vessel segmentation methods. In addition, the segmentation of blood vessels of various sizes (especially small blood vessels) remains a challenging task due to the complex nature of blood vessels. In nature, blood vessels vary in size, shape and intensity, therefore a method that can segment blood vessels of various is considered ideal. Furthermore, most of the available methods are developed for 2D image planes. Although 2D image segmentation is fast and easy to carry out, it doesn't provide full information about the

anatomic structure of blood vessels, it leads to inconsistencies in the segmentation results and non-smooth blood vessels. There is a need for 3D blood vessel segmentation methods. This thesis addresses the aforementioned problems in the upcoming chapters. The problem of the image artefacts is addressed in chapter 4 by proposing a blood vessel enhancement filter for enhancing the medical images and the blood vessels in medical images to ease blood vessel segmentation. The proposed blood vessel enhancement filter is evaluated on the 2D retina images to show the viability for automatic image enhancement. The capabilities of the White Top-Hat scale-space Bilateral Hessian based Vessel Enhancement Filter are exploited during the image enhancement stage to demonstrate its potential for improving the performance of the 3D hybrid blood vessel segmentation method and 2D hybrid blood vessel segmentation method in chapter 5 and chapter 6. To address the problem of the lack of methods that can segment blood vessels of various sizes (especially small vessels) from 3D medical images, a 3D hybrid blood vessel segmentation method is proposed in chapter 5. The proposed 3D hybrid blood vessel segmentation method is evaluated on the original medical image dataset (containing medical images of different modalities) from Queen medical Centre. To demonstrate its potential in extracting blood vessels from medical images of different modalities. To address the problem of the lack of methods that can segment blood vessels of various sizes (especially small vessels) from 2D medical images, a 2D hybrid blood vessel segmentation method and a 2D morphological tool are proposed in chapter 6 and chapter 7 respectively. The 2D hybrid blood vessel segmentation method is evaluated on the publicly available retina fundus image dataset (DRIVE dataset and STARE dataset). The 2D morphological tool was evaluated on the original H&DAB (Haematoxylin and Diaminobenzidine) medical images from Queen medical centre.

Chapter 4

A 2D Blood Vessel Enhancement Method

4.1 Chapter Overview

The performance of the available segmentation techniques is largely limited by the complex nature of the image. Complex nature means the presence of image artefacts (such as low contrast variation between blood vessel pixels and background, noise) in medical images. One of the main objectives of the thesis is to develop novel methods that can enhance the image to enable effective extraction of vessels from the medical images. In this chapter,a new blood vessel enhancement filter known as the White top-hat scale-space Bilateral Hessian based Vessel Enhancement Filter is developed for enhancement of the blood vessels in medical images. The chapter describes how a White top-hat scale-space Bilateral Hessian based Vessel Enhancement Filter is designed and how the White top-hat scale-space Hessian based Vessel Enhancement Filter and a White top-hat scale-space Bilateral Hessian based Vessel Enhancement Filter enhance the image and blood vessels. This chapter also compares the White top-hat scale-space Bilateral Hessian based Vessel Enhancement Filter to the most influential blood vessel enhancement filters. The chapter shows that the White top-hat scale-space Bilateral Hessian based Vessel Enhancement Filter outperforms the most influential vessel enhancement filters. Finally, limitations of the new vessel enhancement filter are presented.

4.2 Related Work

Automatic blood vessel segmentation methods for both 2D and 3D medical images, still face significant challenge to segment blood vessels of various sizes (especially thin vessels) reliably due to imaging artefacts (such as low contrast variation between blood vessel pixels and background, intensity non-uniformity, and noise etc.). Methods such as Isotropic Undecimated Wavelet Transform (IUWT), local phased based filter, and Frangi vessel enhancement filter, have been applied prior to blood vessel segmentation to suppress non-blood vessel structures and image noise. However, these are sensitive to intensity non-uniformity and they fail to maintain strong edges of blood vessels while suppressing the non-blood vessels. Among these methods, Frangi vessel enhancement filter is the most popular and widely used blood vessel enhancement filter [77] due to its capability to deal with noise and enhance both dark vessels on a bright background and bright vessels on a dark background. Frangi vessel enhancement filter aim at enhancing tubular structures by analysing the behaviour of the image using the second-order derivative of the Gaussian convolution. The Hessian matrix in the point x at scale n, $H_n(x)$, can be efficiently computed using Gaussian second derivatives as shown in Equation 4.1.

$$H(I,x) = \frac{\partial^2 I_n}{\partial x^2} = I(x) \times \frac{\partial^2 G_n(x)}{\partial x^2} \tag{4.1}$$

Where I, is the image and G_n is the Gaussian function with standard deviation δ. The decomposition of the local second-order structure of the image extracts the eigenvalues. The Eigen values of the hessian matrix are combined into vesselness measure to extract tubular structures. It employs a multi-scale approach which enables the extraction of vessels of various size, and then the vesselness function is given by:

$$f(x) = \begin{cases} 0, & ;\lambda_2 > 0 \\ \left(exp\left(-\frac{R_a^2}{2\alpha^2}\right)\right)\left(1 - exp\left(-\frac{S^2}{2\beta^2}\right)\right) & ;\lambda_2 \leqslant 0 \end{cases} \tag{4.2}$$

where

$S = \sqrt{\lambda_1^2 + \lambda_2^2}$, $R_a = \left|\frac{\lambda_1}{\lambda_2}\right|$

Where α and β are thresholds that control the sensitivity of the line filter to the dissimilarity measures R_a and S. R_a is the ratio of the two eigenvalues that indicates whether the local structure is more plate-like or tube-like, and the term S deals with the difference between vessel and background areas. An ideal tubular structure implies $|\lambda_1| \leq |\lambda_2|$. The filter shows positive response in tubular structures in the image at various scales. This is the case with vessels in the organs, vessels vary in size. The above vesselness measure (Equation 4.2) uses filter responses at different scales taking the maximum response at each point x:-

$$V_F(X) = \max_{\delta_{min} \leq \delta \leq \delta_{max}} f(x) \tag{4.3}$$

The filter shows positive response in tubular structures in the image at various scales. This is the case with vessels in the organs, vessels vary in size. Although the Frangi vessel enhancement filter is robust to noise, it blurs the edges of the vessels in images and fails to work on medical images with high levels of intensity in-homogeneity [77, 116]. Following Frangi vessel enhancement filter, several extensions have been made, such as the Weingarten matrix [148], vessel enhancement diffusion [115], offset medialness filter [121], and the Vessel enhancement top-hat transform [53]. However, these methods fail to work on images with high levels of intensity inhomogeneity. Moreover, most of these still utilise Gaussian to model intensities in images during blood vessel enhancement and therefore they are subject to the blurriness problem and over smoothing. Over smoothing especially in cases where noise is much [50], leads to a change in shape and size of an object during segmentation [14]. Over smoothing can be avoided by using non-linear diffusion [50]. This is because the quantum of smoothing is controlled using image features [50]. Non-linear diffusion techniques include the PDE (partial differential equation) based techniques such as Anisotropic diffusion of Perona Malik [169] and bilateral filter. Both PDE based segmentation techniques are capable of reducing noise, preserving geometry, topology and localisation of the small vessels [30, 75]. However, according to investigation in [43], Anisotropic diffusion fails to denoise and preserve edges in images whose noise intensity is equal to or higher than 3% of the maximum image intensity [43]. Among other PDE based segmentation include Bilateral filter. The bilateral filter is the most popular and widely used due to its capability

to eliminate the noise while preserving the size and shape of vessel edges in the presence of intensity variations [14, 146, 105, 118, 184]. Compared to Gaussian, the bilateral filter gives more accurate results and does not blur the edges of the objects [114]. Therefore, usage of bilateral convolution instead of Gaussian convolution would improve the performance of Frangi vessel enhancement especially if combined with a method that addresses or reduce the influence of intensity inhomogeneity.

White top-hat Morphological Transform is not only capable of correcting illumination to uncover the objects rendered absent in the images but it also able to get rid of the unwanted tissues in MRI image [80, 244]. In addition, it is flexible and can be incorporated in another method to achieve an objective. For example In [26], a top-hat morphological transform is incorporated into the watershed segmentation method to enhance contrast, [53] incorporated top-hat morphological transform in Frangi vessel enhancement filter to enhance contrast.

In the following sections, the problems (such as failure to work on images with high levels of intensity, and blood vessel blurriness) associated with the Frangi vessel enhancement filter will be addressed by integrating white top-hat transform and bilateral convolution in Frangi vessel enhancement filter which will subsequently blood vessel enhancement in medical image dataset.

4.3 Methodology

4.3.1 Proposed Blood Vessel Enhancement Filter

I hypothesise that by integrating White top-hat transform and Bilateral convolution in to Frangi vessel enhancement filter would correct illumination and enhance contrast in images to uncover the objects rendered absent in the images, and also address the problems (such as blurriness, over smoothing) associated with Gaussian convolution when enhancing the blood vessels. This work first integrates the capabilities of White top-hat morphological transform into Frangi vessel enhancement filter to design a new filter known as White top-hat scale-space Hessian based Vessel Enhancement Filter (WHVEF). A White top-hat scale-space Hessian based Vessel Enhancement Filter is used for enhancing blood vessels in both the STARE dataset and DRIVE dataset. The work shows that White top-hat scale-space Hes-

sian based Vessel Enhancement Filter can correct illumination to uncover the blood vessels rendered absent. However, it fails to maintain the edges of vessels (especially small vessels) in medical images with a high level of noise. To improve on the performance of White top-hat scale-space Hessian based Vessel Enhancement Filter, This work integrates Bilateral Convolution into White top-hat scale-space Hessian based Vessel Enhancement Filter to design another vessel enhancement filter known as White top-hat scale-space Bilateral Hessian based Vessel Enhancement Filter (WBHVEF). This work shows that the integration of White top-hat Transform and Bilateral Convolution into Frangi Vessel enhancement Filter significantly boosts the efficiency of Frangi Vessel Enhancement Filter and subsequently improves vessel enhancement. The next two subsections present the formulation of the White top-hat scale-space Hessian based Vessel Enhancement Filter (WHVEF) and White top-hat scale-space Bilateral Hessian based Vessel Enhancement Filter (WBHVEF).

4.3.1.1 2D White top-hat scale space Hessian based Vessel Enhancement Filter (WHVEF)

Inspired by the Frangi vessel enhancement filter [77], I propose a novel extension to exploit and integrate the capabilities of White Top-Hat Morphological Transform into the Frangi Vessel Enhancement Filter to correct illumination in medical images and also enhance contrast in medical images during blood vessel enhancement. A multiscale approach is employed to extract detailed information at various scales. The size of a structuring element depends on the scale (scale specified in Frangi vessel enhancement filter). An increase in the scale leads to an increase in the structuring element allowing detailed extraction of information at various scales [110]. Note: Since the Frangi vessel enhancement filter adopts a multiscale approach, White top-hat transform benefits from the scale already specified in the Frangi vessel enhancement filter.

Given Frangi vessel enhancement filter scale space of levels $n = 1, 2, ..., M$. Where a level with index M corresponds to scale. The size of the structuring element depends on the scale, therefore, an increase in the scale leads to an increase in the size of structuring element K_n. The white top-hat morphological transform WTH_n is given by:-

$$WTH_n = I - (I \circ K_n) \tag{4.4}$$

Where I is the image, K_n denote the structuring element used at scale level n. $I \circ K_n$ is the dilation of the erosion of image I by a structuring element K. Dilation operation increases the objects in the image by computing the maximum image value over a circular neighbourhood of a given radius [110]. Dilation operation is the complementary operation of the erosion operation. Erosion operation shrinks the foreground and enlarges the background by computing the minimum image value over the neighbourhood [110].

In White top-hat scale-space Hessian based Vessel Enhancement Filter [37], the local behaviour of an image is analysed using second-order information (Hessian) of white top-hat morphological transform operation rather than Gaussian convolution. The eigenvalues (λ_1, λ_2) obtained from the Hessian matrix are used to extract tubular structures (vessels). The Hessian matrix at point x at scale n is given by:-

$$H(I,x) = \frac{\partial^2 I_n}{\partial x^2} = I(x) \times \frac{\partial^2 WTH_n(x)}{\partial x^2} \tag{4.6}$$

Where I is the image and WTH_n is the white top-hat morphological transform (Equation 4.4).

To distinguish tubular structures from blob-like or plate-like structures and background. A dissimilarity measure below is used.

$$f(x) = \begin{cases} 0, & ;\lambda_2 > 0 \\ \left(exp\left(-\frac{R_a^2}{2\alpha^2}\right)\right)\left(1 - exp\left(-\frac{S^2}{2\beta^2}\right)\right) & ;\lambda_2 \leqslant 0 \end{cases} \tag{4.8}$$

Where $S = \sqrt{\lambda_1^2 + \lambda_2^2}$, $R_a = \left|\frac{\lambda_1}{\lambda_2}\right|$, α and β are thresholds that control the sensitivity of the line filter to the dissimilarity measures R_a and S. R_a is the ratio of the two eigenvalues that indicates whether the local structure is more plate-like or tube-like, and the term S deals with the difference between vessel and background areas. An ideal tubular structure implies $|\lambda_1| \leq |\lambda_2|$. The filter shows positive response in tubular structures in the image at various scales. This is the case with vessels in the organs, vessels vary in size. The above vesselness measure uses filter responses at different scales taking the maximum response:-

$$V_F(X) = \max_{\delta_{min} \leq \delta \leq \delta_{max}} f(x) \tag{4.10}$$

The White top-hat scale space Hessian based Vessel Enhancement Filter can correct illumination to uncover the objects rendered absent in the images and also get rid of the unwanted tissues in medical image. However, it fails to maintain the edges of vessels (especially small vessels) in medical images with a high level of noise (Figure 5.4) [35]. According to Bukenya et al., [35], further improvement could include integration of bilateral convolution to address the noise problem while maintaining strong edges of the blood vessels. The integration of bilateral convolution results in to another vessel enhancement filter known as 2D White top-hat scale-space Bilateral Hessian based Vessel Enhancement Filter. The next section present White top-hat scale space Bilateral Hessian based Vessel Enhancement Filter (WBHVEF).

4.3.1.2 2D White top-hat scale space Bilateral Hessian based Vessel Enhancement Filter (WBHVEF)

The White top-hat scale-space Bilateral Hessian based Vessel Enhancement Filter is designed by integrating the capabilities of White Top-Hat Morphological Transform and Bilateral convolution into the Frangi Vessel Enhancement Filter to correct illumination, enhance contrast and address noise of the image while maintaining strong sharp edged blood vessels.

Given Frangi vessel enhancement filter scale space of levels $n = 1, 2, ..., M$. Where a level with index M corresponds to a white top-hat transform (section 3.6.1.3) with structuring element size F_n. F_n increases with M.

In a 2D WBHVEF filter, the local behaviour of the image is analysed using the second-order information (Hessian) of the White top-hat Morphological Transform and Bilateral filter operation rather than Gaussian. The Eigenvalues are used to segment vessels. The Hessian matrix at point y at scale n is given by:-

$$H(I, y) = \frac{\partial^2 I_n}{\partial y^2} = I(y) \times \frac{\partial^2 WTH_n(y) B_n(y)}{\partial y^2} \tag{4.11}$$

Where WTH_n is a White top-hat scale-space Transform (Equation 4.4), WTH_n is used to correct illumination and also enhance contrast. B_n is a bilateral filter in Equation 3.6, Bilateral Filter operation is used to address the noise problem introduced by White top-hat

Morphological Transform operation during segmentation. The Bilateral Filter is also used to build and preserve strong edges of small to medium-size vessels.

To distinguish tubular structures from blob-like or plate-like structures and background. A dissimilarity measure below is used.

$$f(x) = \begin{cases} 0, & ;\lambda_2 > 0 \\ \left(exp\left(-\frac{R_a^2}{2\alpha^2}\right)\right)\left(1 - exp\left(-\frac{S^2}{2\beta^2}\right)\right) & ;\lambda_2 \leqslant 0 \end{cases} \tag{4.13}$$

where

$S = \sqrt{\lambda_1^2 + \lambda_2^2}$, $R_a = \left|\frac{\lambda_1}{\lambda_2}\right|$

Where α and β are thresholds that control the sensitivity of the line filter to the dissimilarity measures R_a and S. R_a is the ratio of the two eigenvalues that indicates whether the local structure is more plate-like or tube-like, and the term S deals with the difference between vessel and background areas. An ideal tubular structure implies $|\lambda_1| \leq |\lambda_2|$. The filter shows positive response in tubular structures in the image at various scales. This is the case with vessels in the organs, vessels vary in size. The above vesselness measure uses filter responses at different scales taking the maximum response:-

$$V_F(X) = \max_{\delta_{min} \leq \delta \leq \delta_{max}} f(x) \tag{4.15}$$

4.3.2 Blood Vessel Enhancement Process

To enhance the 2D images, steps taken during image enhancement are presented. As shown in Figure 4.1, the image is first input into the system. If the blood vessels are dark in the background, image inversion is performed so as the dark change to bright. The image and the blood vessels are then enhanced using the proposed blood vessel enhancement filter. If the blood vessels are bright in the background, no image inversion is carried out.

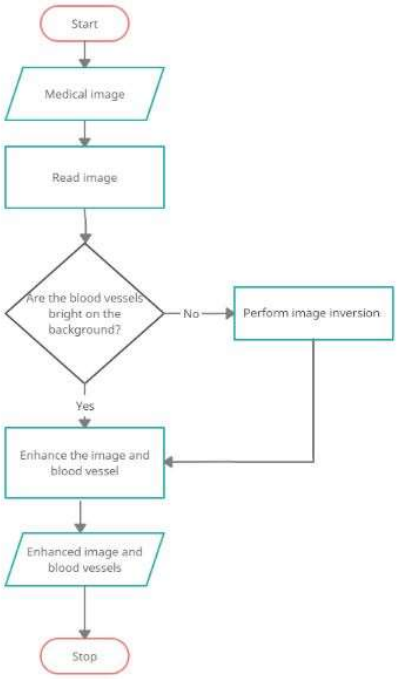

Figure 4.1: Flow chart diagram of the image enhancement process

4.4 Experimental Evaluation

This section describes the evaluation of the proposed White top-hat scale-space Hessian based Vessel Enhancement Filter and White top-hat scale-space Bilateral Hessian based Vessel Enhancement Filter on a publicly available image dataset. The image dataset used in this study includes retina images.

4.4.1 Evaluation Datasets

Two public retinal image datasets were employed for the evaluation of the proposed segmentation method. In this section, a brief introduction to these datasets is presented, followed by an introduction to the evaluation metrics used in our experiments.

4.4.1.1 Digital Retinal Images for Vessel Extraction(DRIVE) dataset

This dataset consists of a total of 40 colour retinal images, obtained in the course of a diabetic retinopathy screening program in the Netherlands. Each image resolution is 768 by 584 pixels. All of the 40 images came with ground-truth data.

4.4.1.2 Structured Analysis of the Retina (STARE)

This dataset contains 400 colour retinal images, 20 of these come with ground-truth data, 10 of which show evidence of pathology. Each image resolution is 605 by 700 pixels.

4.4.1.3 Parameter selection for retina dataset

These free parameters used in this work may be adjusted to produce better results according to the nature of the images. All of the parameters used on the aforementioned filters are shown as follows:

1. The WHVEF parameters used for enhancement of retina vessels include $\alpha = 16$, $\beta = 0.48$. The scale size used in White top-hat scale space Hessian based Vessel Enhancement Filter during the enhancement of blood vessels in STARE image dataset and DRIVE image dataset ranges from 1 and 8. The White top-hat Morphological Transform parameters include the square structuring element, the structuring element size depends on the scale used.
2. The WBHVEF filter parameters used for enhancement of retina vessels include $\alpha = 16$, $\beta = 0.48$. The scale size used in WBHVEF filter during the enhancement of blood vessels in STARE image dataset and DRIVE image dataset ranges from 1 and 8. White top-hat morphological operation parameters include the square structuring element. The structuring element size depends on the scale used. Bilateral parameters that were used include: $G_{\sigma_r} = 2$, $eps = 1e-3$ and $G_{\sigma_s} = 10$. Where G_{σ_s} is a spatial Gaussian ensures that only pixels in a spatial neighbourhood are considered, and, G_{σ_r} is a range Gaussian that ensures that only pixels of similar intensities are considered to compute the blurred intensity value to avoid blurriness.
3. Frangi Vessel Enhancement Filter scales: 1–8, scale ratio: 2.
4. Isotropic Undecimated Wavelet Transform (IUWT) scales: 2–3.
5. Local Phase-Based Filter scales: 2–3.

4.5 Experiments and Results

4.5.1 Experimental Comparison of WBHVEF filter with other Methods on both the DRIVE dataset and the STARE dataset

The performance of the vessel enhancement filters (WHVEF filter and WBHVEF filter) on two datasets (STARE dataset and DRIVE dataset) is compared alternative blood vessel enhancement filters in the literature: results of the method proposed by Frangi et al., [77], Bankhead et al. [22], and Lathen et al., [132] are from Zhao et al., [253].

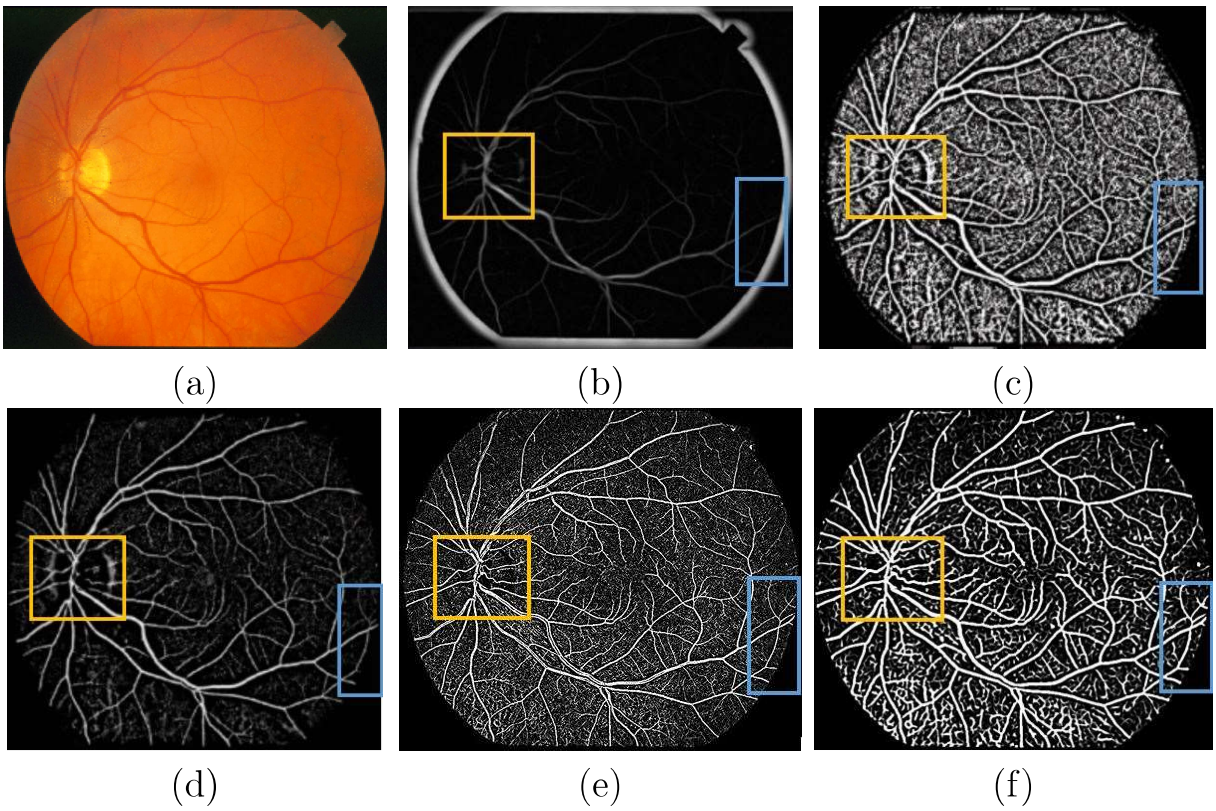

Figure 4.2: Visual comparison of vessel enhancement filters on a image 162 of STARE dataset. (a) is the original retina fundus image; (b) Image enhancement results produced by F [77]; (c) Image enhancement results produced by IUWT [22]; (d) Image enhancement results produced by LPF [132]; (e) Image enhancement results produced by WHVEF filter; (f) Image enhancement results produced by WBHVEF filter. Note: yellow shows that the proposed methods can get rid of non-blood vessels (such as optic disc). Blue shows the proposed methods can detect low contrast filamentary vessels

Compared to other vessel enhancement filters, WHVEF filter and WBHVEF filter are superior to other blood vessel enhancement filters as they are resistant to intensity non-uniformity and can faithfully enhance blood vessels with different widths (Figure 4.2f, Figure 4.3f, Figure 4.2e, and Figure 4.3e). Moreover, both WHVEF filter and WBHVEF filter can get can get rid of the unwanted tissue, an optical disc is removed and vessels in the optic disc are detected. However, Figure 4.2 and Figure 4.3 shows that WBHVEF filter is robust to noise and produces strong edged blood vessels compared to WHVEF filter. Given the efficiency, the proposed blood vessel enhancement filters can applied as a vascular structure enhancement method before vessel segmentation. Although the visual comparison is considered purely subjective, it can still emphasise the positive and negative points of various segmentation approaches. Figure 4.4 shows White top-hat scale-space Bilateral Hessian based Vessel Enhancement Filter can work under different conditions.

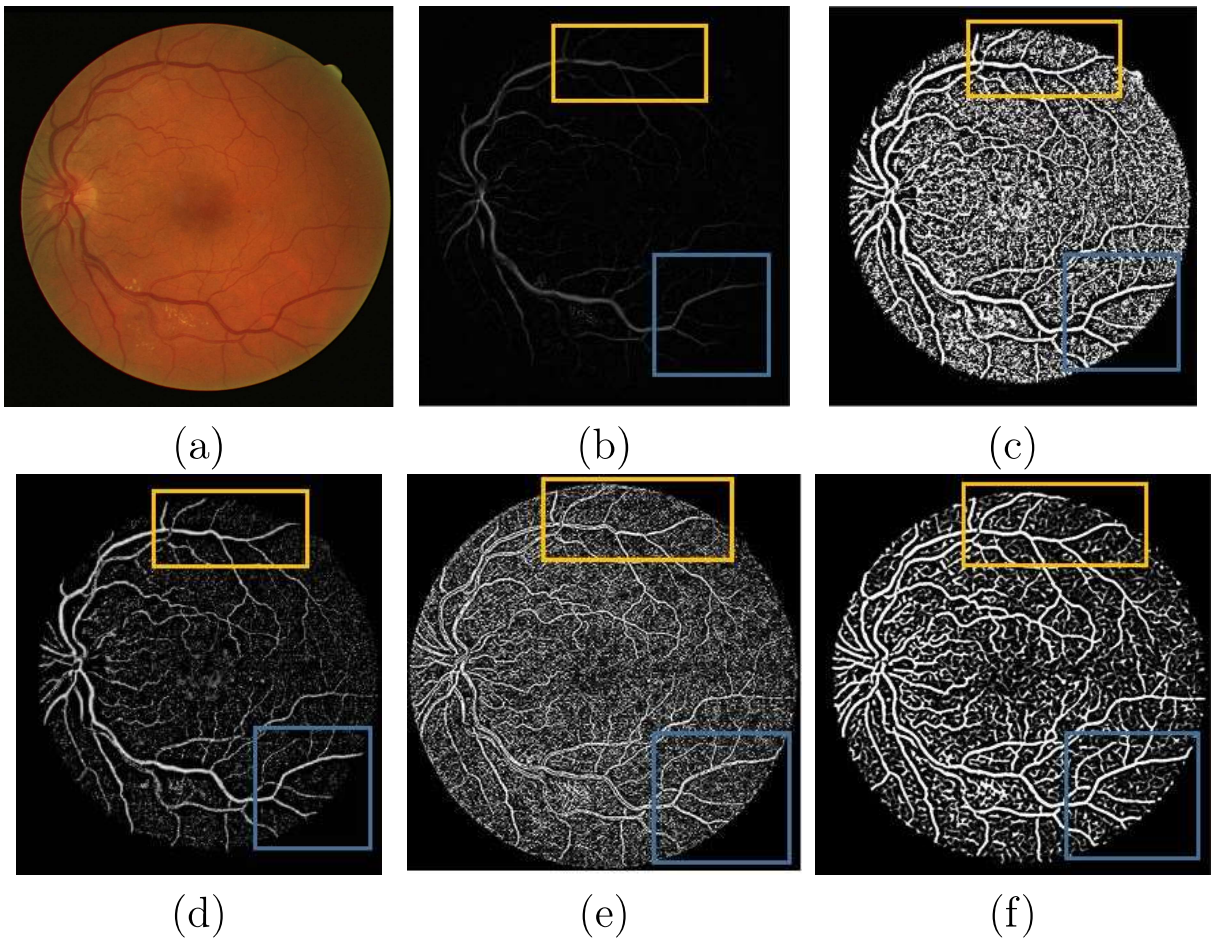

Figure 4.3: Visual comparison of vessel enhancement filters on image 3 of DRIVE dataset. (a) is an original retina fundus image 3; (b) Image enhancement results produced by F [77]; (c) Image enhancement results produced by IUWT [22]; (d) Image enhancement results produced by LPF [132]; (e) Image enhancement results produced by WHVEF; (f) Image enhancement results produced by WBHVEF. Yellow shows that the proposed method can low contrast blood vessels in poor quality images. Blue shows that the proposed method is robust to noise and can maintain strong edged blood vessels

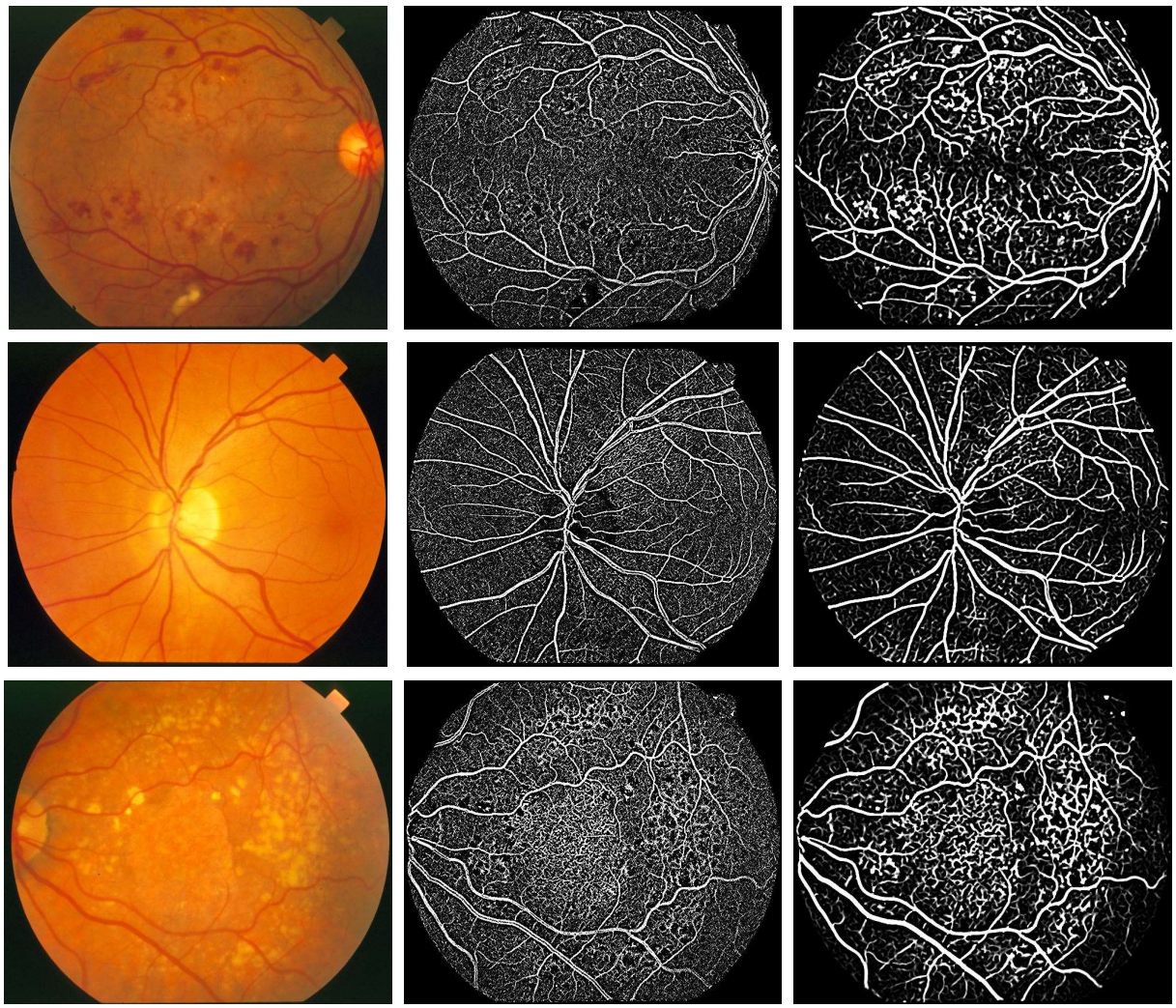

Figure 4.4: Visual comparison of a White top-hat scale space Hessian based Vessel Enhancement Filter and a White top-hat scale space Bilateral Hessian based Vessel Enhancement Filter on randomly selected images from STARE dataset. Column (a) Original images randomly selected from the STARE dataset; column (b) Image enhancement results from WHVEF; column (c) Image enhancement results from WBHVEF.

4.6 Conclusion and Discussion

This chapter presents novel blood vessel enhancement filter, the so called White top-hat scale-space Bilateral Hessian based Vessel Enhancement Filter, for enhancement of blood vessels and the image during image processing stage.

The performance of the White top-hat scale-space Bilateral Hessian based Vessel Enhancement Filter is evaluated against four vessel enhancement filters on both the STARE dataset and the DRIVE dataset. Figure 4.2 and Figure 4.3 show the visual comparison of the White top-hat scale-space Bilateral Hessian based Vessel Enhancement Filter with other

vessel enhancement filters. It can be seen from Figure 4.2b and 4.3b, that the Frangi vessel enhancement filter tends to only enhance the larger vessels as does the IUWT (Figure 4.2c, 4.3c). The IUWT also enhances the non-vessels (such as optic disc, fovea etc.). Like IUWT, LPF enhances non blood vessels (such as optic disc) and it fails to enhance the edges of the low contrast small blood vessels (Figure 4.2d). Compared to LPF, WHVEF can enhance the edges of the low contrast small blood vessels (Figure 4.2e). However, it amplifies noise. WBHVEF filter outperforms all blood vessel enhancement filters interms of enhancing blood vessels at various scales (Figure 4.2f,Figure 4.3f). Blood vessels of various sizes stand out more from the background. Therefore, the White top-hat scale-space Bilateral Hessian based Vessel Enhancement Filter addresses one of the main issues in medical image analysis "image artefacts problem". Although the visual comparison is considered purely subjective, it can still emphasise the positive and negative points of various segmentation approaches. All of the experiments were performed in Matlab version 2016a (Mathworks, Natick, CA) on a PC with a $3.1GHz$ Intel Core system and $8GB$ RAM. The next chapter extends the two filter (White top-hat scale-space Hessian based Vessel Enhancement Filter and White top-hat scale-space Bilateral Hessian based Vessel Enhancement Filter) to 3D and demonstrates the potential of the two filters for improving 3D blood vessel segmentation.

Chapter 5

3D Hybrid Blood Vessel Segmentation Framework

5.1 Chapter Overview

Despite the advances in blood vessel segmentation that attain impressive results, there is a need for 3D blood vessel segmentation methods that can segment blood vessel of various sizes. In this chapter, a 3D hybrid framework for blood vessel segmentation from 3D medical images has been developed. The 3D hybrid blood vessel segmentation framework presented in this chapter is easily parallelizable; segmentation processes occur independently on two individual images, and then an integration step quickly merges both outputs from two individual images into a coherent segmentation result, which is later enhanced using an appropriate method. This chapter describes how the two identical 3D medical images (image A and image B) are input in the system, how 3D medical image A is enhanced to facilitate segmentation of thin to medium vessels, how the voxels are classified into blood vessels (foreground) and non-blood vessels (background) in both the enhanced image A and image B, simultaneously, and how the resulting blood vasculature is enhanced. In the framework, a 3D White top-hat scale-space Hessian based Vessel Enhancement Filter (WHVEF) and a 3D White top-hat scale-space Bilateral Hessian based Vessel Enhancement Filter (WBHVEF) were exploited during image enhancement to improve the quality of image A to enable the extraction of small vessels. Multi-threshold Otsu, hysteresis thresholding and the Iterative Self-Organizing Data Analysis Technique (ISODATA) thresholding are

exploited during the segmentation of blood vessels. MATLAB bwareaopen operation is explored during post-processing to enhance the blood vessel mask. The results show that the proposed 3D hybrid blood vessel segmentation framework outperforms other methods. Finally, a discussion of the limitations of the current blood vessel segmentation framework is presented.

5.2 Related Work

Automatic blood vessel segmentation from 3D medical images, still face difficulty in extracting blood vessels of various sizes (especially small blood vessel). This is mainly due to the image artefact problem in the images and the complex nature of the blood vessels (blood vessel vary in size, shape and in contrast distribution).

Methods such as model-based method, fuzzy c-means clustering method, tracking-based method, graph cut method, and thresholding method segmentation method, have been applied to extract blood vessel of various sizes. Among the methods, a model-based method is popular because of its ability to address image artefacts (such as intensity in-homogeneity) during segmentation. Model-based method segment blood vessels by matching a model which contains information about the expected shape and appearance of the structure of interest to a new image. The method allows the incorporation of prior information about the considered image structures, have higher flexibility of the shape, and a model can be adapted to fit the given data [229]. However, the method is sensitive to noise, it struggles to determine the right parameters for model fitting, and cannot cope with vessel calcifications. Similar methods have been proposed to deal with problems, For-example Xie et al., [232] used the original non-contrast CT scan images and their pre-computed anatomy label maps to locate the aorta and identify its surface. The aorta is segmented by first of all locating a seed point inside the aortic lumen. Then, later progressively fit a cylindrical model on a 3D image space to track the aorta centerline. The method provides promising results, however, it struggles to discriminate between tissue. In [218], a fast matching level set algorithm is used to extract the rough surface. The surface is not able to reach the vessel edges due to insufficient velocity contrast meaning the method could not effectively discriminate the vessel from the background. The model-based method causes vessel leakage [221].

According to Ahmed et al., [101], a method that can deal with uncertainty in medical data would lead to better segmentation results. Fuzzy C-means Clustering Approach is widely used for its capability to deal with uncertainty during segmentation to prevent false detections (non-blood vessels being detected as blood vessels).

The fuzzy c-means clustering method segments blood vessels by assigning a fuzzy membership value to each of the data points in the dataset basing proximity to each cluster centroid in the feature space. Like the model-based method, the Fuzzy c-means clustering method allows the incorporation of image information. The method is also flexible with distance used, and it provides the best result for the overlapped data set, however, it is sensitive to noise, it fails to work intensity in homogeneous images and it is slow as it requires several iterations to produce better results. To address the problems associated with the method, similar methods were proposed. For example, in [171], spatial information is incorporated to reduce the influence of intensity in-homogeneity on segmentation. The method is unable to segment much noisy images and it blurs finer details of the object. To address that blurriness and intensity in-homogeneity, Adhikar et al., [5] incorporated conditioning effects and local spatial information among adjacent pixels in the fuzzy membership function. The method is sensitive to noise. To address the noise and blurriness problem, Gharnali et al., [86] replaced the original Euclidean distance with a kernel-induced distance. The method is robust to noise. However, it misses some vessels, especially small brain vessels. The alternative would be to use the graph cut method.

Graph cut method segments blood vessels, by first of all binary labelling the image pixels into the foreground and background class and then later using a cut to partition the image pixels into foreground and background depending on the intensity value, and then later utilise a threshold to partition image pixels into foreground and background. Although the method allows incorporation of object information (such as edge information, region information, shape information), it fails to segment blood vessels especially thin elongated vessels, since the energy minimisation tends to shrink for curvilinear structures [250, 249, 181, 51, 252]. Similar methods have been proposed to address the problems. For-example, in [103], vesselness, geodesic paths, and a new multi-scale edginess map are combined to the segmentation of tubular structures, utilizing a global optimisation of the Graph-cuts energy

function. The method cannot model vessel bifurcation and crossings. Chen et al., [51] segmented small vessels by applying quick shift clustering to group spatially neighbouring voxels into local regions and then later, applied Graph cuts basing on regional intensity distribution. The method is slow and cannot distinguish small vessel pixels from noise pixels. To ensure accurate segmentation of blood vessels, Flasque et al., [75] proposed to trace blood vessels.

Tracking based method segment blood vessels by tracing blood vessels using initial position seed, direction seed and radius, to the endpoints of the continuous blood vessel. In this method, the direction seed helps in setting the tracking direction by estimating the vector connecting the two positions. The method improves the localisation of the vessels and can estimate the vessel diameter [17]. However, it requires human intervention, which is prone to errors, cannot model blood vessel bifurcation and face difficulty in segmenting the vessels especially small vessels [90, 18]. Similar methods have been proposed such as Avila-Montes et al., [18] segmented the aorta by formulating localisation, centerline extraction, and segmentation of the aorta as an optimal path detection problem. Although the proposed method does not require any kind of additional input data, it cannot preserve the order of the slices in a volume. In 2017, Guedri et al., [90] proposed a mathematical approach for tracking the centerline curve in retinal vascular images. The method is fast and associated with less error. However, it does not produce the actual vessel structure. An alternative would be to use the Thresholding method.

Thresholding method segment blood vessels by using either using threshold or dual threshold or multiple thresholds to distinguish the blood vessels from non-blood vessels. Methods the employ one threshold during segmentation work well on pre-processed or good quality images and fail to work well on the poor quality image (images with artefacts) [238]. All medical images have image artefacts, therefore, methods that can deal with image artefacts are ideal for segmentation. Methods that utilise more than one threshold to separate foreground (blood vessels) from the background (non-blood vessels) achieve better segmentation results. For example, in 2016, Kotte et al. [128] segmented the image by divide image pixels into more than two classes, then later, use more than two thresholds to segment the image[128]. The method consumes less storage space, is easy to manipulate and capable of

incorporating spatial information to detect abnormalities in vessels [102, 128]. In [256], the image is segmented in a different way to incorporate spatial information into the thresholding process. Pixel's Gray level is first of all transferred to a fuzzy set through a fuzzy membership function, then later, the local fuzzy entropy of each image pixel is computed. In the following sections, the blood vessel of various sizes will be distinguished following the 3D hybrid blood vessel segmentation framework, that simultaneously segments blood vessels from two images (enhanced image A and image B) using different methods, then later quickly merges both outputs from two images into a coherent segmentation result, that is later enhanced using an appropriate method.

5.3 Methodology

The new 3D hybrid blood vessel segmentation framework proposes that two identical images (image A and image B) should be used during the segmentation process, that one image should be enhanced before segmentation, that blood vessels of various sizes should be segmented simultaneously from the two images (enhanced image A and image B) using different methods, that image addition should be used to combine the segmentation results from each of the segmentation processes to obtain a whole vasculature, and that the resulting image should be enhanced to remove unwanted objects such as noise. Note: The enhanced image is used during the extraction of thin to medium blood vessels. In the framework, a 3D White top-hat scale-space Hessian based Vessel Enhancement Filter (WHVEF) and a 3D White top-hat scale-space Bilateral Hessian based Vessel Enhancement Filter (WBHVEF) were exploited during image enhancement to improve the quality of image A to enable the extraction of small vessels. Multi-threshold Otsu, hysteresis thresholding and ISODATA thresholding are exploited during the segmentation of blood vessels. MATLAB bwareaopen operation is explored during post-processing to enhance the blood vessel mask.

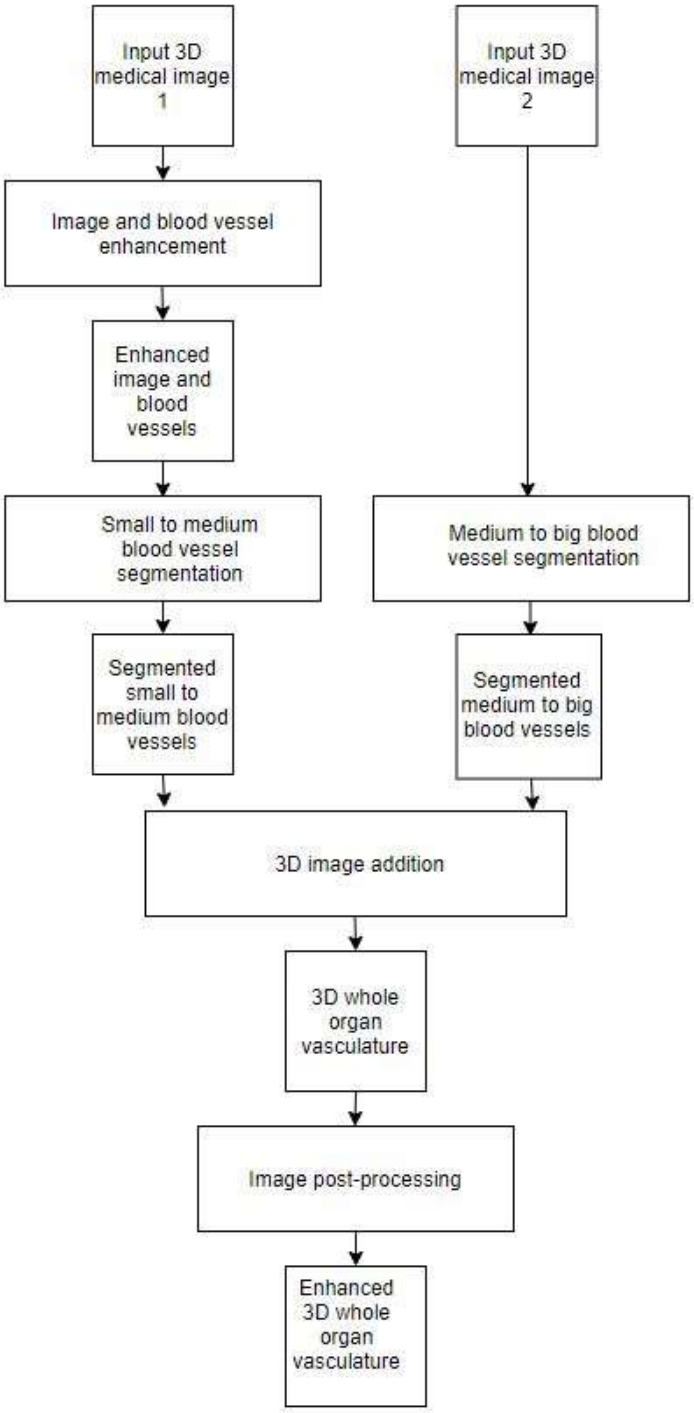

Figure 5.1: A block diagram of the proposed 3D hybrid blood vessel segmentation framework

The proposed 3D hybrid blood vessel segmentation framework consists of four steps including image enhancement, segmentation, 3D blood vessel structure addition, blood vessel mask enhancement. The four steps are described below.

- Image and blood vessel enhancement:- Illumination in the medical image is corrected and noise is removed during this step to prepare the image for segmentation of hard

to extract vessels (small to medium vessels). Note: This process is performed on the image from which the small to medium blood vessels are to be extracted.

- Blood vessel segmentation:- The pre-processed image and unprocessed images are segmented independently to extract small to medium blood vessels and medium to large blood vessels respectively.
- 3D blood vessel structure addition:-The two-segmented images are then combined to form one whole vasculature.
- Blood vessel mask enhancement:- Unwanted small objects are eliminated to obtain a clean image.

In this 3D hybrid blood vessel segmentation framework, a 3D White top-hat scale-space Hessian based Vessel Enhancement Filter (WHVEF) and a 3D White top-hat scale-space Bilateral Hessian based Vessel Enhancement Filter (WBHVEF) are exploited during image enhancement, Multi-threshold Otsu, hysteresis thresholding and ISODATA thresholding are exploited during the segmentation of blood vessels to group image voxels in to blood vessel (foreground) and non-blood vessels (background), image addition is employed to integrate the segmentation results from each segmentation process, and MATLAB bwareaopen operation is utilised during post-processing to enhance the blood vessel mask. The next section presents the three methods that adopt the same framework.

5.3.1 A 3D hybrid blood vessel segmentation framework

In this section, three 3D methods that adopt the same approach (Figure 5.1) to segment the blood vessels of various sizes from 3D medical images are described.

5.3.1.1 A 3D Hybrid Method of Multi-threshold Otsu, WHVEF filter combined with ISODATA, Image Addition and Matlab Bwareaopen Operation.

During image segmentation process 1 of this hybrid framework, White top-hat scale-space Hessian based Vessel Enhancement Filter (WHVEF) is used to enhance the blood vessels and the image before extraction of small to medium vessels using ISODATA thresholding. In segmentation process 2, Multi-threshold Otsu is applied on the unprocessed image to extract medium to large vessels. Image addition is performed to combine the two vessel trees from

each segmentation process to obtain a whole organ vasculature. Finally, post-processing is performed using Matlab Bwareaopen Operation to remove the unwanted objects from the whole organ vasculature [37].

5.3.1.2 A 3D hybrid method of WBHVEF filter combined with Hysteresis Thresholding, Multi-threshold Otsu combined with Hysteresis thresholding, Image Addition and Matlab Bwareaopen Operation.

During image segmentation process 1 of this hybrid framework, White top-hat scale-space Bilateral Hessian based Vessel Enhancement Filter is used to enhance the blood vessels and the image before extraction of small to medium vessels using Hysteresis Thresholding. In segmentation process 2, Multi-threshold Otsu combined with Hysteresis Thresholding is applied on the unprocessed image to extract medium to large vessels. Image addition is performed to combine the two vessel trees from each segmentation process to obtain a whole organ vasculature. Finally, post-processing is performed using Matlab Bwareaopen Operation to remove the unwanted objects from the whole organ vasculature [35].

5.3.1.3 A 3D hybrid method of WBHVEF filter combined with Hysteresis Thresholding, Hysteresis Thresholding, Image Addition and Matlab Bwareaopen Operation.

During image segmentation process 1 of this hybrid framework, White top-hat scale-space Bilateral Hessian based Vessel Enhancement Filter is used to enhance the blood vessels and the image before extraction of small to medium vessels using Hysteresis Thresholding. In segmentation process 2, Hysteresis Thresholding is applied on the unprocessed image to extract medium to large vessels. Image Addition is performed to combine the two vessel trees from each segmentation process to obtain a whole organ vasculature. Finally, post-processing is performed using Matlab Bwareaopen Operation to remove the unwanted objects from the whole organ vasculature.

5.3.2 Image pre-processing/Image enhancement

One of the challenges faced by researchers is segmenting blood vessels in presence of image artefacts (such as non-uniform illumination, noise, low contrast) in images. In this section, two-vessel enhancement filters that were exploited during image enhancement to improve

the quality of the image to enable the extraction of small vessels, are presented. The two novel vessel enhancement filters include a White top-hat scale-space Hessian based Vessel Enhancement Filter and the White top-hat scale-space Bilateral Hessian based Vessel Enhancement Filter. The two vessel enhancement are an extension of the Frangi vessel enhancement filter. A White top-hat scale-space Hessian based Vessel Enhancement Filter is used because of its capability to correct illumination to uncover the objects rendered absent in the images, enhance the blood vessels at various scale, whilst, White top-hat scale-space Bilateral Hessian based Vessel Enhancement Filter is used because of its capability to separate different vessels, enhance blood vessels at various scales, correct illumination to uncover the objects rendered absent in the images and also get rid of unwanted tissues in medical image. The next section presents White top-hat scale-space Hessian based Vessel Enhancement Filter.

5.3.2.1 3D White top-hat scale space Hessian based Vessel Enhancement Filter (WHVEF)

Inspired by the Frangi Vessel Enhancement Filter [77], This work proposes a novel extension to exploit and integrate the capabilities of White top-hat Morphological Transform into the Frangi Vessel Enhancement Filter to correct illumination in medical images, enhance contrast.

A multiscale method is employed to extract detailed information at various scales. The size of a structuring element depends on the scale (scale specified in Frangi Vessel Enhancement Filter). An increase in the scale size leads to an increase in the structuring element allowing detailed extraction of information at various scales [110]. Note: Since Frangi Vessel Enhancement Filter adopts a multiscale method, White top-hat Transform benefits from the scale already specified in Frangi Vessel Enhancement Filter.

Given Frangi Vessel Enhancement Filter scale space of levels $n = 1, 2, ..., M$. Where a level with index M corresponds to scale. the size of the structuring element depends on the scale, therefore, an increase in the scale leads to an increase in the size of the structuring element K_n. A White top-hat morphological transform WTH_n is given by:-

$$WTH_n = I - (I \circ K_n) \tag{5.1}$$

Where I is the image, K_n denote the structuring element used at level n, $I \circ K_n$ is the dilation of the erosion of image I by a structuring element K. Dilation operation increases the objects in the image by computing the maximum image value over a circular neighbourhood of a given radius [110]. Dilation operation is the complementary operation of the erosion operation. Erosion operation shrinks the foreground and enlarges the background by computing the minimum image value over the neighbourhood [110].

In White top-hat scale-space Hessian based Vessel Enhancement Filter [37], the local behaviour of an image is analysed using second-order information (Hessian) of White top-hat Morphological Transform operation rather than Gaussian convolution. The eigenvalues obtained from the Hessian matrix are used to extract tubular structures (vessels). The Hessian matrix at point x at scale n is given by:-

$$H(I,x) = \frac{\partial^2 I_n}{\partial x^2} = I(x) \times \frac{\partial^2 WTH_n(x)}{\partial x^2} \tag{5.3}$$

where $WTH_n = I - M(I)$.

To distinguish tubular structures from blob-like or plate-like structures and background. A dissimilarity measure below is used.

$$f(x) = \begin{cases} 0, \quad if \lambda_2 > 0 \; or \; \lambda_3 > 0 \\ \Big(1 - exp\Big(-\frac{R_a^2}{2\alpha^2}\Big)\Big) exp\Big(-\frac{R_b^2}{2\beta^2}\Big)\Big(1 - exp\Big(-\frac{S^2}{2C^2}\Big)\Big) \end{cases} \tag{5.5}$$

where

$S = \sqrt{\lambda_1^2 + \lambda_2^2 + \lambda_3^2}$, $R_a = \Big|\frac{\lambda_2}{\lambda_3}\Big|$,$R_b = \Big|\frac{\lambda_1}{\sqrt{|\lambda_2 \lambda_3|}}\Big|$

Where α, β, *and* c are thresholds which control the sensitivity of the line filter to the dissimilarity measures R_a, R_b and S. R_a is the ratio of the two biggest eigenvalues that indicates whether the local structure is more plate-like or tube-like, the term R_b accounts for blob-like structures and the term S deals with the difference between vessel and background areas. β is a bias value. An ideal tubular structure implies $|\lambda_1| \approx 0$, $|\lambda_1| \leq |\lambda_2|$, $\lambda_2 \approx \lambda_3$ where the sign of λ_2 and λ_3 indicates polarity. The filter shows positive response in tubular

structures in the image at various scales. This is the case with vessels in the organs, vessels vary in size. The above vesselness measure uses filter responses (Equation 5.12) at different scales taking the maximum response:-

$$V_F(X) = \max_{\delta_{min} \leq \delta \leq \delta_{max}} f(x) \tag{5.7}$$

The White top-hat scale-space Hessian based Vessel Enhancement Filter can address intensity in-homogeneity problem associated with Frangi vessel enhancement filter. However, it fails to maintain the edges of vessels (especially small vessels) in medical images with a high level of noise (Figure 5.4) [35]. According to [35], further improvement could include integration of bilateral convolution to address the noise problem while maintaining strong edges of the blood vessels. The integration of bilateral convolution results in to another vessel enhancement filter Known as 3D White top-hat scale space Bilateral Hessian based Vessel Enhancement Filter. The next section present White top-hat scale space Bilateral Hessian based Vessel Enhancement Filter (WBHVEF).

5.3.2.2 3D White top-hat scale space Bilateral Hessian based Vessel Enhancement Filter (WBHVEF)

The White top-hat scale-space Bilateral Hessian based Vessel Enhancement Filter (WBHVEF) integrates the capabilities of White top-hat Morphological Transform and Bilateral convolution into the Frangi Vessel Enhancement Filter to correct illumination, enhance contrast and address noise of the image while maintaining strong sharp edged blood vessels.
Given Frangi Vessel Enhancement Filter scale space of levels $n = 1, 2, ..., M$. Where a level with index M corresponds to a White top-hat transform (section 3.6.1.3) with structuring element size F_n. F_n increases with M.
In WBHVEF filter, the local behaviour of the image is analysed using the second-order information (Hessian) of the White top-hat Morphological Transform and Bilateral convolution rather than Gaussian. The Eigenvalues are used to segment vessels. The Hessian matrix at point y at scale n is given by:-

$$H(I, y) = \frac{\partial^2 I_n}{\partial y^2} = I(y) \times \frac{\partial^2 WTH_n(y) B_n(y)}{\partial y^2} \tag{5.8}$$

where WTH_n is a White top-hat scale space (Equation 5.1), WTH_n is used to correct illumination. B_n is a bilateral filter in Equation 3.6, bilateral filter operation is used to address the noise problem introduced by top-hat morphological transform operation during segmentation. The bilateral filter is also used to build and preserve strong edges of small to medium-size vessels.

To distinguish tubular structures from blob-like or plate-like structures and background. A dissimilarity measure below is used.

$$f(x) = \begin{cases} 0, & if \lambda_2 > 0 \; or \; \lambda_3 > 0 \\ \Big(1 - exp\Big(-\frac{R_a^2}{2\alpha^2}\Big)\Big) exp\Big(-\frac{R_b^2}{2\beta^2}\Big)\Big(1 - exp\Big(-\frac{S^2}{2C^2}\Big)\Big) \end{cases} \tag{5.10}$$

$S = \sqrt{\lambda_1^2 + \lambda_2^2 + \lambda_3^2}$, $R_a = \Big|\frac{\lambda_2}{\lambda_3}\Big|$,$R_b = \Big|\frac{\lambda_1}{\sqrt{|\lambda_2 \lambda_3|}}\Big|$

Where α, β, *and* c are thresholds that control the sensitivity of the line filter to the dissimilarity measures R_a, R_b and S. R_a is the ratio of the two biggest eigenvalues that indicates whether the local structure is more plate-like or tube-like, the term R_b accounts for blob-like structures and the term S deals with the difference between vessel and background areas. β is a bias value. An ideal tubular structure implies $|\lambda_1| \approx 0$, $|\lambda_1| \leq |\lambda_2|$, $\lambda_2 \approx \lambda_3$ where the sign of λ_2 and λ_3 indicates polarity. The filter shows positive response in tubular structures in the image at various scales. This is the case with vessels in the organs, vessels vary in size. The above vessels measure uses filter responses at different scales taking the maximum response:-

$$V_F(X) = \max_{\delta_{min} \leq \delta \leq \delta_{max}} f(x) \tag{5.12}$$

5.3.3 Image segmentation

After enhancing the blood vessels and the image, segmentation is performed to classify the voxels into two classes (namely: blood vessels and non-blood vessels). A method that can maintain edges of the blood vessels of various sizes in presence of noise and low contrast is considered ideal. This work chooses to segment two images (enhanced image A and image

B) simultaneous using different methods to enable extraction of blood vessels of various sizes [104, 117, 157, 215, 126]. This enables us to focus more on the extraction of the hard to extract blood vessels (such as small blood vessels). Methods such as multi-threshold Otsu, ISODATA, hysteresis thresholding are used to classify voxels into blood vessels and non-blood vessels. The upcoming subsection presents some of the methods used in this thesis to classify voxels into blood vessels and non-blood vessels.

5.3.3.1 Multi-threshold Otsu Method

Spatial information is an important aspect as it can improve outbreak detection performance[33]. This work utilizes a 3D multi-threshold Otsu method, which uses spatial information during segmentation. By using multi-threshold Otsu method, This work benefits from other advantages such as it is fast [241], [37], [222], [36], consumes less storage space [242], [196], ease of implementation [188], [196], [2], [222], [102], [207], [172], [179], [55], [120] and noise resistance [120].

The Multi-threshold Otsu method is an adaptive threshold segmentation method that divides the grayscale image into two classes (namely background and foreground) basing on the image characteristics. The class error is used to show the difference between the classes. The higher the error the more the objects are unlikely to belong to the same class, whilst on the other hand the lower error the more the objects are likely to belong to a different class [102], [37].

5.3.3.2 Iterative Self Organising Data Analysis (ISODATA) Thresholding

In medical imaging analysis, a method that requires less human effort are considered ideal. This work uses ISODATA because it doesnot require knowledge about the image data and requires less human intervention. The Iterative Self-Organizing Data Analysis Technique (Isodata) is an iterative technique that was developed in 1978 by [1]. ISODATA algorithm aims at splitting non-homogeneous regions into two sub-regions (objects and background). According to Gonzalebarron et al., [89], initially a guess is made at a possible value of a threshold. Then, the mean values of the two categories (objects and background) produced with this threshold are estimated. The threshold is moved to the middle of the distance between the two mean values. The procedure is repeated again and a new threshold is

obtained. The process continues until the threshold stops changing its value.

5.3.3.3 Hysteresis Thresholding

In blood vessel segmentation, a method that can detect and maintain edges of blood vessels of various sizes is prefered as it helps during diagnosis in cases where angiogenesis is involved to determine the patients response to treatment. This work therefore employ hysteresis thresholding to ensure accurate extraction of blood vessels of various sizes. Hysteresis Thresholding has consistently outperformed absolute thresholding methods because of its capability to deal with uncertainty using the two thresholds. In addition, it can detect the absence of pixels in true edges even in presence of intensity in-homogeneity [72, 240], Furthermore, object boundaries produced by Hysteresis Thresholding are continuous. In this thesis, the Hysteresis Thresholding method in [224] is used during segmentation.
In Hysteresis Thresholding, the salience value of edge pixels not only depend on the gradient magnitude but also on its spatial distribution measured by supporting range. The hysteresis thresholding method is not based on pixels but on segments/objects. In this method, vessels are segmented following steps. In the first step of the segment-based hysteresis thresholding, edge pixels are linked into curve segments with the following method. Starting from the pixel with the highest gradient magnitude, a curve segment grows at each step by including the most salient edge pixel among the 16 neighbours of the two endpoints (each endpoint has 8 neighbours) of the curve segment. The growing is ended when no more object pixels can be added. Then, a new segment growing starts from the edge pixel with the highest gradient magnitude among the remaining object pixels that have not been included in a curve segment. This process is repeated until no more new curve segment can be generated. The salience value of each curve segment is the sum of the salience values of its edge pixels computed.

5.3.4 Image addition

During this stage, the segmentation results from each of the segmentation process are merged into coherent segmentation result using image addition operation. In Image addition, image pixels of the two input images of the same size are summed up together to obtain an output image. According to Saiyam et al., [178], the addition of two images is

performed straightforwardly in a single pass and that reduces noise without compromising image details. The image addition operation is expressed as follows: Given images I_1 and I_2 of the same size,

$$I_3 = I_1 + I_2 \tag{5.13}$$

Where I_3 is the Output image.

5.3.5 Image post-processing

In post processing stage, a method that can eliminate the unwanted objects such as noise without tampering with the image details is considered ideal. I used MATLAB bwareaopen operation because of its ability to remove unwanted objects of a particular size without tampering with image details. MATLAB bwareaopen operation is well known for eliminating small artefacts without interfering with the region of interest and it has been used in different fields of image analysis. MATLAB bwareaopen morphological operation is used to remove all connected components (objects) that are fewer than 26 pixels from the binary image. MATLAB bwareaopen operation involves three steps that include (i) Determining connected components using Matlab bwconncomp operation. Matlab bwconncomp operation returns connected components (with the connectivity of 8 in the binary image), (ii) Computing the area of each component using Matlab region props operation. (iii) Removing small objects. All connected objects are labelled. MATLAB ismember operation is used to remove all object with less than 26 pixels.

5.4 Experimental Evaluation

This section describes the evaluation of the proposed method on both public and private image dataset. The image dataset used in this study includes MRI and CT scan images.

5.4.1 Evaluation Dataset

The original medical imaging data used in the study methodology was obtained from sir peter mansfield imaging centre, Nottingham. The following sections presents the medical dataset used in this during 3D segmentation.

5.4.1.1 CTA femoral artery and veins image dataset

101 3D medical images of size 1896 X 1626 X 526 voxels are used in this thesis.

5.4.1.2 CT pelvic arteriogram image dataset

124 3D medical images of size 529 X 1259 X 430 voxels are used in this thesis.

5.4.1.3 MRA-scan carotid and aotic arc dataset

122 3D MRA human neck images (size 96 X 512 X 512 voxels) are used in obtained from Queen medical centre in Nottingham (United Kingdom).

5.4.1.4 MRI heart image dataset

5 original MRI images of different sizes obtained from Queen medical centre. The images used in this paper are of size 256 X 256 X 300 voxels.

5.4.1.5 CT-scan Rat head dataset

Three-dimension medical images segmented include 2 CT scan rat brain images (size 337 X 339 X 341 voxels)

5.4.2 Parameter selection

5.4.2.1 Parameter selection for both all the medical image dataset

- Hysteresis threshold parameters used to group voxels in to blood vessel and non-blood vessel in three-dimensional medical images range between 0 and 1.
- The White top-hat scale-space Hessian based Vessel Enhancement Filter (WHVEF) parameters used for enhancement of medical images include $\alpha = 0.2$, $\beta = 50, c = 500$. The scale size used in WHVEF during the enhancement of blood vessels in 3D medical images ranges from 1 to 9. The White top-hat Morphological Transform parameters include the square structuring element, the structuring element size depends on the scale used.
- The White top-hat scale space Bilateral Hessian based Vessel Enhancement Filter (WBHVEF) parameters used for enhancement of retina vessels include $\alpha = 0.2$, $\beta = 50, c = 500$. Scale size used in WBHVEF during the enhancement of blood vessels in three-dimensional medical images ranges from 1 to 9. White top-hat morphological

operation parameters include the square structuring element. The structuring element size depends on the scale used. Bilateral parameters that were used include: $G_{\sigma_r} = 2$, $eps = 1e-3$ and $G_{\sigma_s} = 68$. Where G_{σ_s} is a spatial Gaussian ensures that only pixels in a spatial neighbourhood are considered, and, G_{σ_r} is a range Gaussian that ensures that only pixels of similar intensities are considered to compute the blurred intensity value to avoid blurriness.

5.4.3 Evaluation metrics

In our study, both visual evaluation and quantitative evaluation are carried out to assess the contribution of the three-dimensional hybrid method in the segmentation of vessels from intensity in-homogeneous medical images with noise.

To qualitatively evaluate the method, 354 3D original medical images are used. This work compared the performance of the three 3D hybrid frameworks ([35, 38]). The performance of the three 3D hybrid methods for blood vessel segmentation is evaluated on all dataset. The best 3D hybrid method is compared to existing three-dimensional segmentation methods.

To quantify the effectiveness of the proposed method, three three-dimension original medical images from Queen medical centre are manually segmented using a popular application (itk-snap).

To test the effectiveness of the proposed hybrid method, metrics such as sensitivity, specificity, accuracy, DICE coefficient, and Jaccard Index are utilised. Below is a brief description of each of the similarity measures used.

(a) **Sensitivity:** Sensitivity measures the portion of positive voxels (vessels) in the ground truth that is also detected as positive by the segmentation being evaluated. Sensitivity can be expressed as [201]:-

$$Sensitivity = \frac{TP}{TP + FN} \tag{5.14}$$

where TP is vessel voxels correctly detected by the algorithms, and FN is vessel voxels detected as background voxels.

(b) **Specificity:** Specificity measures the portion of negative voxels (background) in the ground truth segmentation that is also detected as negative by the segmentation being

evaluated. Specificity can be expressed as [201]:-

$$Specificity = \frac{TN}{TN + FP} \tag{5.15}$$

where TN is background voxels correctly detected by method and FP is background voxels detected as vessel voxels.

(c) **Accuracy:** Accuracy is calculated as a degree of closeness between segmentation results and the ground-truth. Accuracy can be expressed as follows:-

$$Accuracy = \frac{TP + TN}{TP + FP + TN + FN} \tag{5.16}$$

where TP is vessel voxels correctly detected by the algorithms, TN is background voxels correctly detected by the method. FP is background voxels detected as vessel voxels, and FN is vessel voxels detected as background voxels.

(d) **Dice coefficient:** Dice coefficient is popular method used in medical segmentation to quantify the similarity between segmentation and the ground truth [201]. Dice coefficient is also commonly known as overlap index. it represents spatial overlap between segmentation and the ground truth [122, 201]. Dice coefficient can be expressed as [44, 201, 176, 204, 108, 144]:-

$$DICE = \frac{2\left|S_g^1 \cap S_t^1\right|}{\left|S_g^1\right| + \left|S_t^1\right|} = \frac{2TP}{2TP + FP + FN} \tag{5.17}$$

where TP are vessels voxels correctly detected by the algorithms, TN are background voxels correctly detected by method. FP are background voxels detected as vessel voxels, and FN are vessel voxels detected as background voxels.

(e) **Jaccard index (JAC):** Jaccard index refers to the intersection between a segmentation and the ground truth divided by the union between a segmentation and the ground truth [44, 109, 201]. Like Dice coefficient, Jaccard index also represents spatial overlap between segmentation and the ground truth [122, 201]. JAC can be expressed [182, 95, 138, 12, 187] as:-

$$JAC = \frac{\left|S_g^1 \cap S_t^1\right|}{\left|S_g^1 \cup S_t^1\right|} = \frac{TP}{TP + FP + FN} \tag{5.18}$$

where TP are vessels voxels correctly detected by the algorithms, TN are background voxels correctly detected by method. FP are background voxels detected as vessel voxels, and FN are vessel voxels detected as background voxels.

5.5 Experiments and Results

This section presents and discusses the results from the three 3D hybrid methods. It also compares the best method with the existing methods.

5.5.1 Experimental results of a 3D Hybrid Method of Multi-threshold Otsu, WHVEF filter combined with ISODATA, image addition and Matlab bwareaopen operation.

The hybrid method is capable of detecting the tumour vessels and abnormalities in the blood vessels (Figure 5.3). However, the hybrid method cuts blood vessels (Figure 5.2) and produces blood vessels with weak edges (Figure 5.4(a)) [35]. An improvement to the method could include integrating bilateral convolution into White top-hat scale-space Hessian based Vessel Enhancement Filter to maintain the strong edges of the thin to medium blood vessels while denoising the image [35]. Further improvement could include combining multi-threshold Otsu with hysteresis thresholding, with hysteresis thresholding used to deal with the multi-threshold Otsu problem of cutting blood vessels. Hysteresis thresholding can detect the absence of pixels in true edges even in presence of intensity inhomogeneity, and the ability to produce continuous blood vessel boundary. Even better segmentation results could be obtained if ISODATA is replaced with Hysteresis thresholding. The next section presents the experimental results from the integration of bilateral convolution and hysteresis thresholding into the 3D Hybrid Method of Multi-threshold Otsu, WHVEF filter combined with ISODATA, Image Addition and Matlab Bwareaopen Operation.

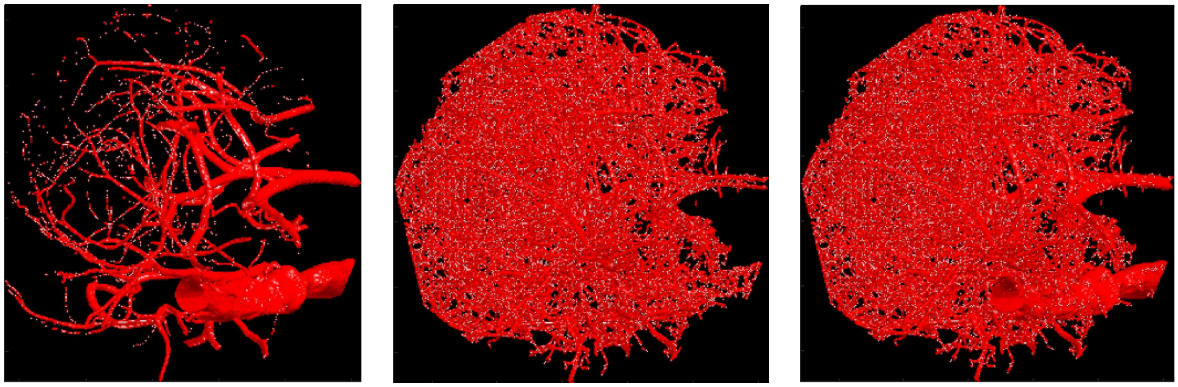

(a) (b) (c)

Figure 5.2: Illustration of a hybrid method of WHVEF combined with ISODATA, multi-threshold Otsu, Image Addition and Matlab Bwareaopen Operation in terms of segmenting different sizes of vessels. (a) Medium to big vessel image using multi-threshold Otsu; (b) Small to medium vessel image using WHVEF combined with ISODATA; (c) A whole rat brain vasculature produced after image addition process.

Figure 5.3: Illustration of the hybrid method of 3D WHVEF filter combined with ISODATA, multi-threshold Otsu and MATLAB bwareaopen in-terms of detecting blood vessel disorders. Note: tumor vessels and tortuous vessels are detected.

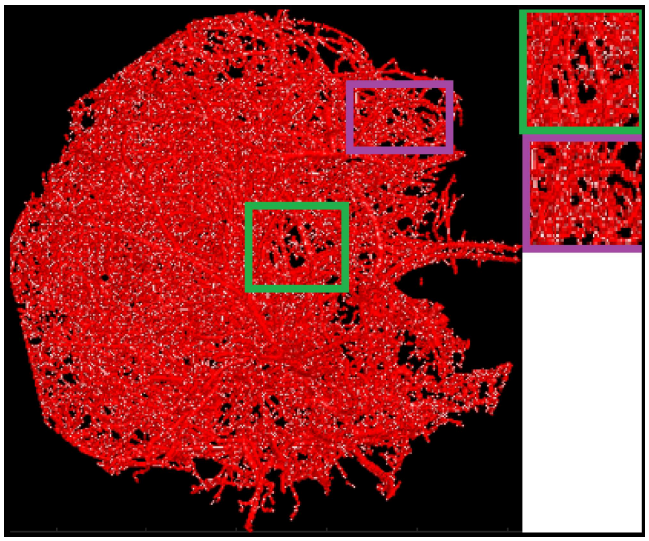

Figure 5.4: A WHVEF combined with ISODATA in-terms of maintaining the edges of the vessels of rat brain.

5.5.2 Experimental results of the 3D Hybrid method of WBHVEF filter combined with Hysteresis Thresholding, Multi-threshold Otsu combined with Hysteresis Thresholding, Image Addition and Matlab Bwareaopen Operation

Compared to the Hybrid method of WHVEF filter combined with ISODATA, Multi-threshold Otsu and Matlab bwareaopen operation, the Hybrid method of WBHVEF combined with hysteresis thresholding, multi-threshold Otsu combined with hysteresis thresholding and Matlab bwareaopen operation is capable of maintaining the blood vessel edges (Figure 5.7(f), Figure 5.6), while segmenting blood vessels of various sizes. The method can get rid of unwanted objects such as skull (Figure 5.5b). However, the hybrid method is suitable for only detailed images such as MRI, MRA (Figure 5.8). Figure 5.8, shows the combination of multi-threshold Otsu method and hysteresis thresholding is suitable for a detailed image such as MRI and MRA and not suitable for less detailed medical images such as CT scan image. Further improvement could include using only hysteresis thresholding to extract medium to large blood vessels to benefit from its capabilities and also reduce the processing time. The next presents the experimental results from this improvement (Figure 5.9).

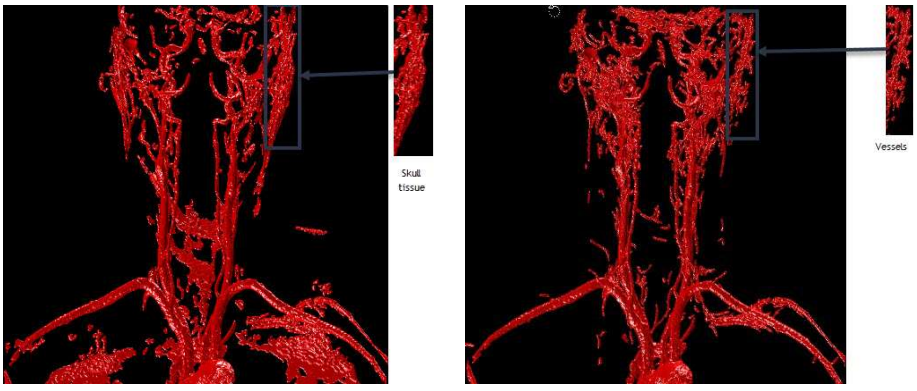

(a) (b)

Figure 5.5: Visual comparison of different segmentation techniques on MRA neck dataset for skull removal. (a) carotid segmentation using multi-threshold Otsu method with respect to skull removal; (b) carotid segmentation using multi-threshold Otsu and hysteresis thresholding method with respect to skull removal.

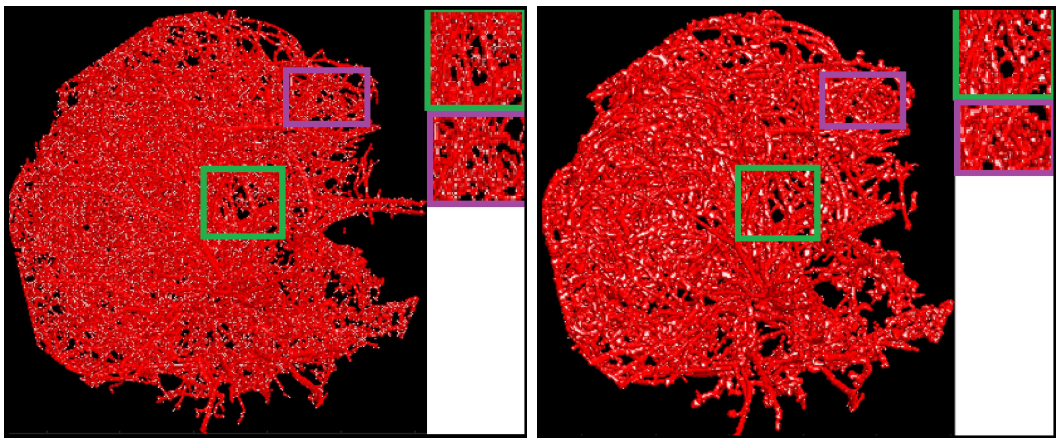

(a) (b)

Figure 5.6: Illustration of segmentation results obtained before and after integrating bilateral convolution in to White top-hat scale space Bilateral Hessian based Vessel Enhancement Filter and after replacing ISODATA with hysteresis thresholding. (a) whole small to medium vessel structure using WHVEF [37]; (b) whole small to medium vessel structure using WBHVEF [35]. **Note:** more strong edged blood vessels are detected after integrating bilateral convolution in to WHVEF and after replacing ISODATA with hysteresis thresholding.

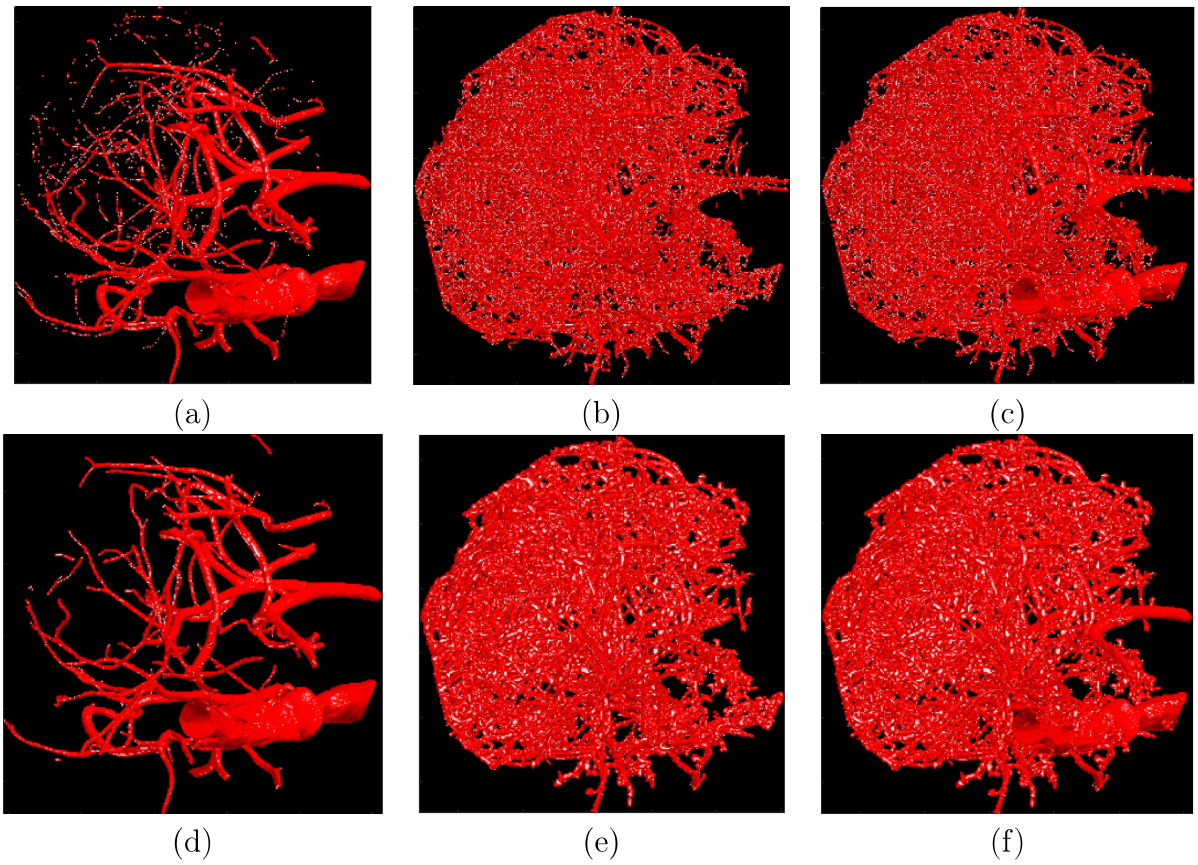

Figure 5.7: Visual comparison of two hybrid segmentation methods in-terms of segmenting different sizes of vessels in CT scan images. (a) medium to big vessels using multi-threshold Otsu method; (b) small to medium vessels using WHVEF in [37]; (c) whole vessel tree after adding the image using multi-threshold Otsu and image using WHVEF combined with ISODATA [37]; (d) medium to big vessels using multi-threshold Otsu method combined with hysteresis thresholding; (e) small to medium vessels using WBHVEF in [35]; (f) whole vessel tree after adding the image using multi-threshold Otsu combined with hysteresis thresholding and image using WBHVEF combined with hysteresis thresholding [35].

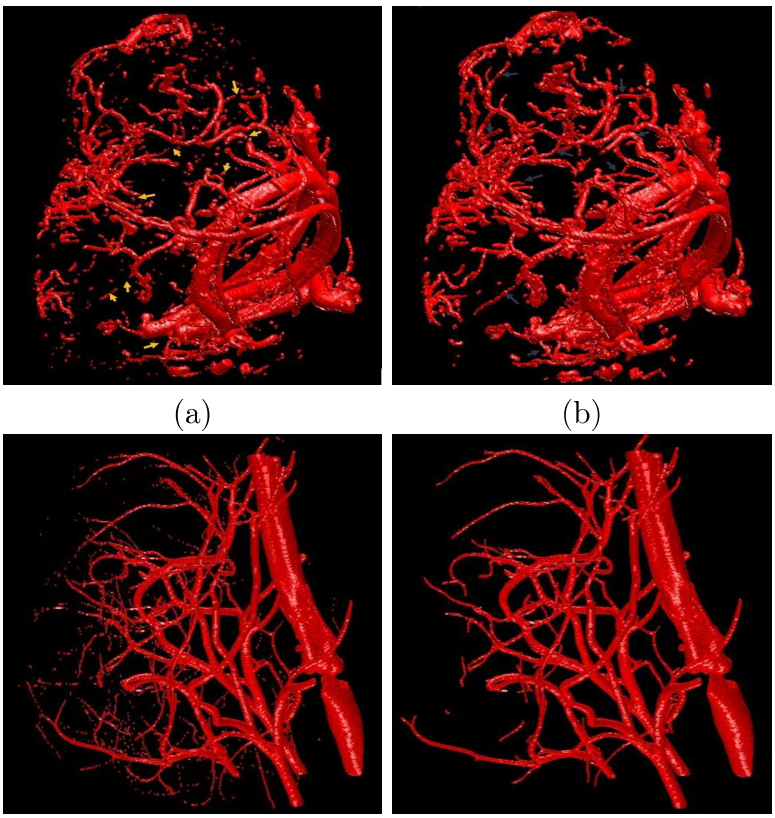

Figure 5.8: Illustration of segmentation results obtained before and after combining multi-threshold Otsu with hysteresis thresholding. (a) multi-threshold Otsu on MRI images; (b) multi-threshold Otsu and hysteresis thresholding on MRI images; (c) multi-threshold Otsu on CT scan image; (d) multi-threshold Otsu method and hysteresis thresholding on CT scan image. **Note:** more blood vessels are detected in MRI image. However, after introducing hysteresis threshold, Less blood vessels are detected in CT scan images.

5.5.3 Experimental results obtained using a 3D hybrid method of WBHVEF filter combined with Hysteresis Thresholding, Hysteresis Thresholding, Image Addition and Matlab Bwareaopen Operation.

Compared to the two proposed methods, the 3D hybrid method of WBHVEF filter combined with Hysteresis Thresholding, Hysteresis Thresholding, Image Addition and Matlab Bwareaopen Operation, outperforms the two hybrid methods as it is capable of extract more strong edged vessels from both detailed and non-detailed images as compared to other methods. Besides detecting more strong edged blood vessels (Figure 5.15), the method can detect abnormalities in the blood vessels and therefore, it can be used during early diagnosis. The next section qualitatively compares the 3D hybrid method of WBHVEF filter com-

bined with Hysteresis Thresholding, Hysteresis Thresholding, Image Addition and Matlab Bwareaopen Operation, with the previous methods.

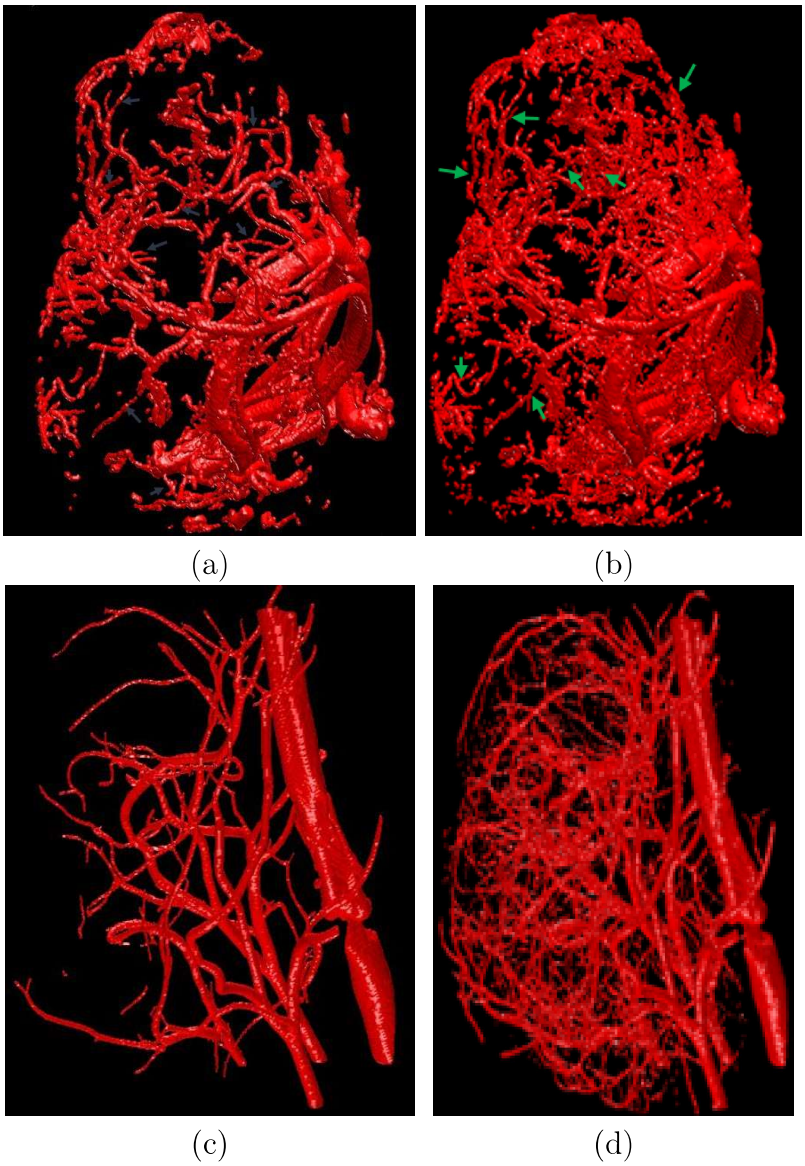

Figure 5.9: Illustration of segmentation results obtained after replacing a combination of multi-threshold Otsu and hysteresis thresholding with hysteresis thresholding. (a) multi-threshold Otsu combined with hysteresis thresholding on MRI images; (b) hysteresis thresholding on MRI image; (c) multi-threshold Otsu combined hysteresis threshold on CT scan image; (d) hysteresis thresholding on CT scan image. Blue arrows show that less vessels are detected in MRI images, after combining multi-threshold Otsu method with hysteresis thresholding. Green arrows show that more vessels are detected after replacing a combination of multi-threshold Otsu and hysteresis thresholding with hysteresis thresholding.

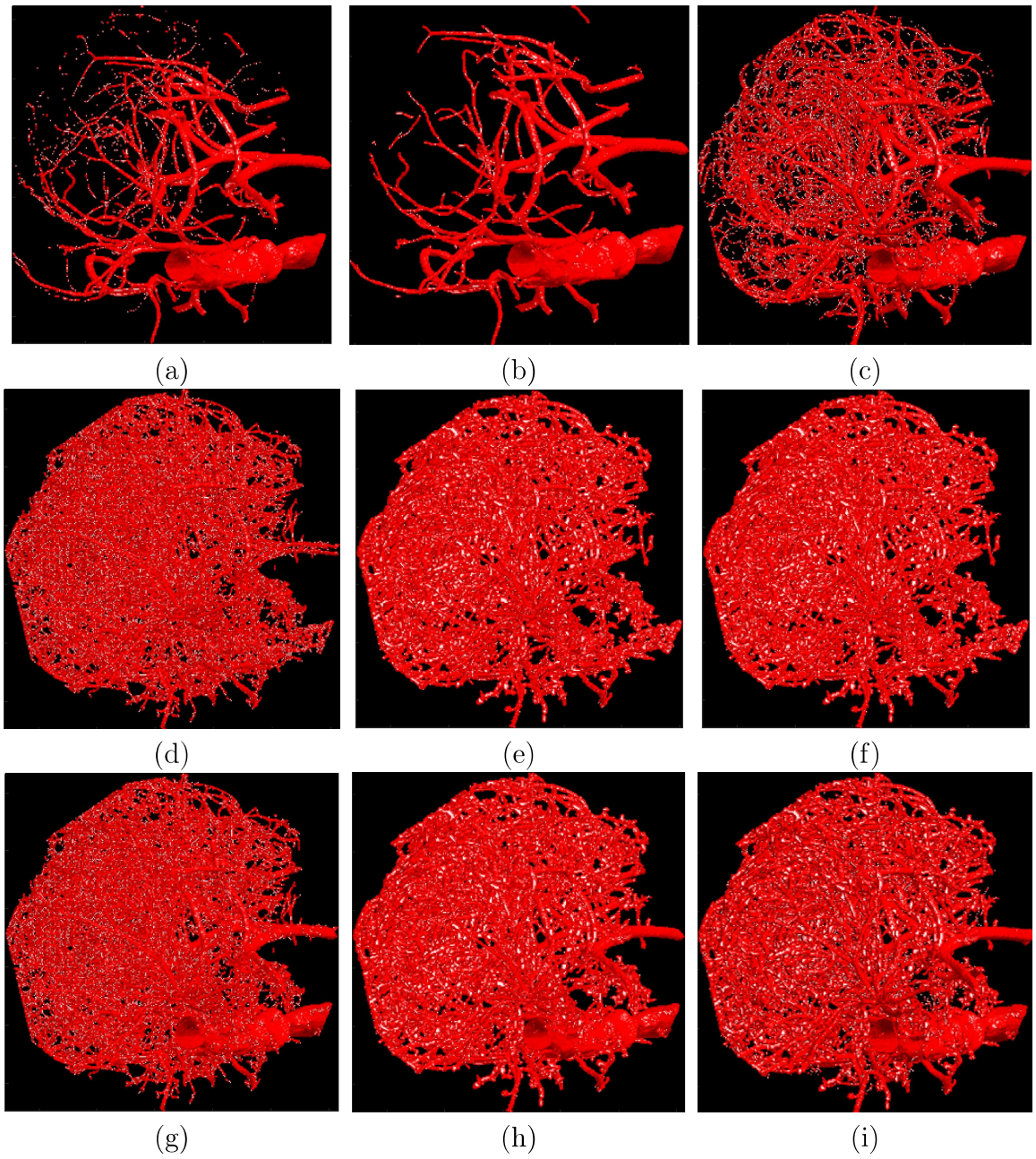

Figure 5.10: Visual comparison of the three developed hybrid segmentation methods on CT scan images. (a) medium to big vessels using multi-threshold Otsu method; (b) medium to big vessels using multi-threshold Otsu method combined with hysteresis thresholding; (c) medium to big vessels using hysteresis thresholding; (d) small to medium vessels using WHVEF in [37]; (e) and (f) small to medium vessels using WBHVEF in [35]; (g) whole vessel tree after adding the image using multi-threshold Otsu and image using WHVEF [37]; (h) whole vessel tree after adding the image using multi-threshold Otsu with hysteresis and image using WBHVEF [35]; (i) whole vessel tree after adding the image using hysteresis and image using WBHVEF.

Note: In this chapter, although three segmentation methods are presented, the best hybrid method is compared to the existing segmentation. In this case, the best method is chosen based on the qualitative analysis. The best method is the 3D hybrid method of WBHVEF filter combined with Hysteresis Thresholding, Hysteresis Thresholding, Image Addition

and Matlab Bwareaopen Operation. The next section presents performance comparison results of the 3D hybrid method of WBHVEF filter combined with Hysteresis Thresholding, Hysteresis Thresholding, Image Addition and Matlab Bwareaopen Operation, with the previous methods on different medical images of different modalities

5.5.4 Performance comparison results of the 3D hybrid blood vessel segmentation method with the previous methods on the CTA femoral dataset

Table 5.1 shows the performance of the proposed method with the previous methods in terms of accuracy, sensitivity, specificity, DICE coefficient, and Jaccard index on the femoral artery & veins dataset. In comparison to other methods, the average (accuracy = 99.47%, sensitivity = 82.76%, DICE = 73.43%, and JAC = 58.02%) achieved with the proposed method on femoral dataset outperforms Bhattacharya et al., [30], Ding et al., [68], Frangi et al., [77]. However, with the average specificity, the proposed method only outperforms Ding et al., [68] and is marginally inferior to the methods presented by Bhattacharya et al., [30] and Frangi et al., [77]. This may be due to the small ground-truth dataset used during the evaluation. An overview of the experimental results on femoral dataset shows that the proposed method offers a reliable and robust segmentation solution for blood vessels. It is clearly observed that the proposed method reaches better performance in terms of the average sensitivity and accuracy.

Method	Sensitivity	Specificity	Accuracy	DICE	JAC
FA [30]	49.50	99.71	98.88	59.27	42.12
FL [68]	61.74	99.57	99.15	61.86	44.78
F [77]	58.60	99.63	99.11	62.45	45.40
proposed method	82.76	99.62	99.47	73.43	58.02

Table 5.1: Results of the blood vessel segmentation method with the previous methods on femeral artery and veins dataset

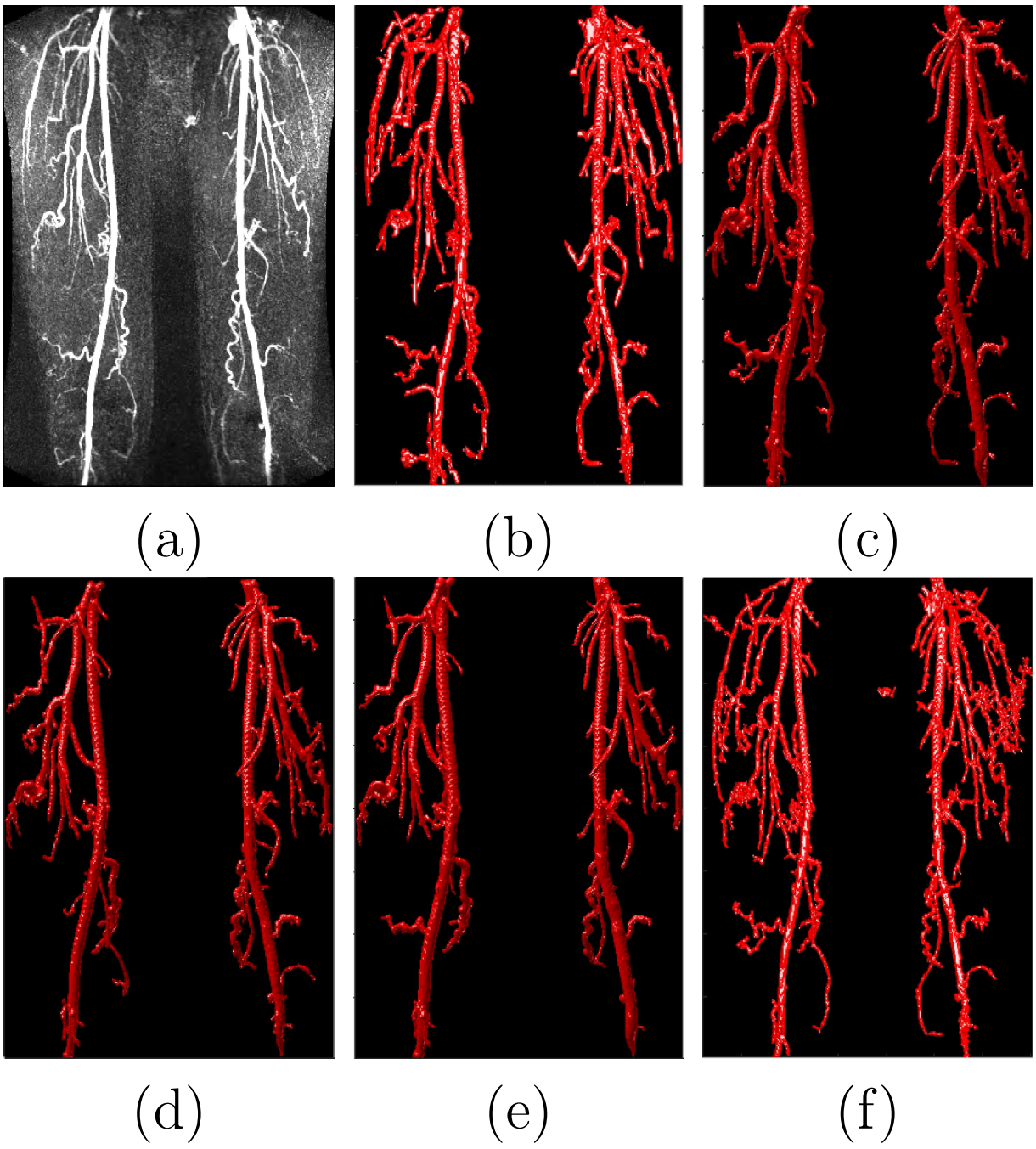

Figure 5.11: Blood vessel segmentation results of the CTA femeral artery and veins images. (a) Maximum Intensity Projection (MIP) images of Original femoral artery and veins images; (b) 3D view of manually segmented blood vessels; (c) segmentation using Frangi vessel enhancement filter and Anisotropic diffusion [30]; (d) segmentation using Frangi vessel enhancement filter and Line filter [68]; (e) segmentation using Frangi vessel enhancement filter [77]; (f) segmentation using the proposed method.

5.5.5 Performance comparison results of the 3D hybrid blood vessel segmentation method with the previous methods on the CT pelvic arteriogram image dataset

The performance results of the proposed method are compared to the method proposed by Bhattacharya et al., [30], the method proposed by Ding et al., [68] and a method proposed by Frangi et al., [77]. The proposed method achieves the highest average accuracy, specificity, DICE and JAC of 99.76%, 99.70%, 78.93%,and 65.20% respectively. However, considering the performance in terms of a sensitivity, the method proposed by Frangi et al., [77] reaches the highest average sensitivity value 99.59% and performs better than all methods including the proposed method. This may due to the small ground-truth dataset used during evaluation. Figure 5.12 shows a visual comparison between the segmentation performance of the proposed method and other state-of-the-art methods for a sample image from the CT pelvic arteriogram image dataset. As it can be seen, the proposed method can segment blood vessels of various sizes including small vessels irrespective of the image condition. Although the visual comparison is considered purely subjective, it can still emphasise the positive and negative points of various segmentation approaches in support of quantitative results. An overview of the experimental results on the CT pelvic arteriogram image dataset shows that the proposed method offers a reliable and robust segmentation solution for blood vessels. It is observed that the proposed method reaches better performance in terms of the average specificity and accuracy. It would produce a better average sensitivity with the application of more ground-truth data.

Method	Sensitivity	Specificity	Accuracy	DICE	JAC
FA	96.16	99.61	99.59	67.19	50.59
FL	97.78	99.46	99.45	49.72	33.08
F	99.59	99.43	99.43	46.20	30.04
proposed method	89.96	99.76	99.70	78.93	65.20

Table 5.2: Results of the blood vessel segmentation method on CT pelvic arteriogram image dataset

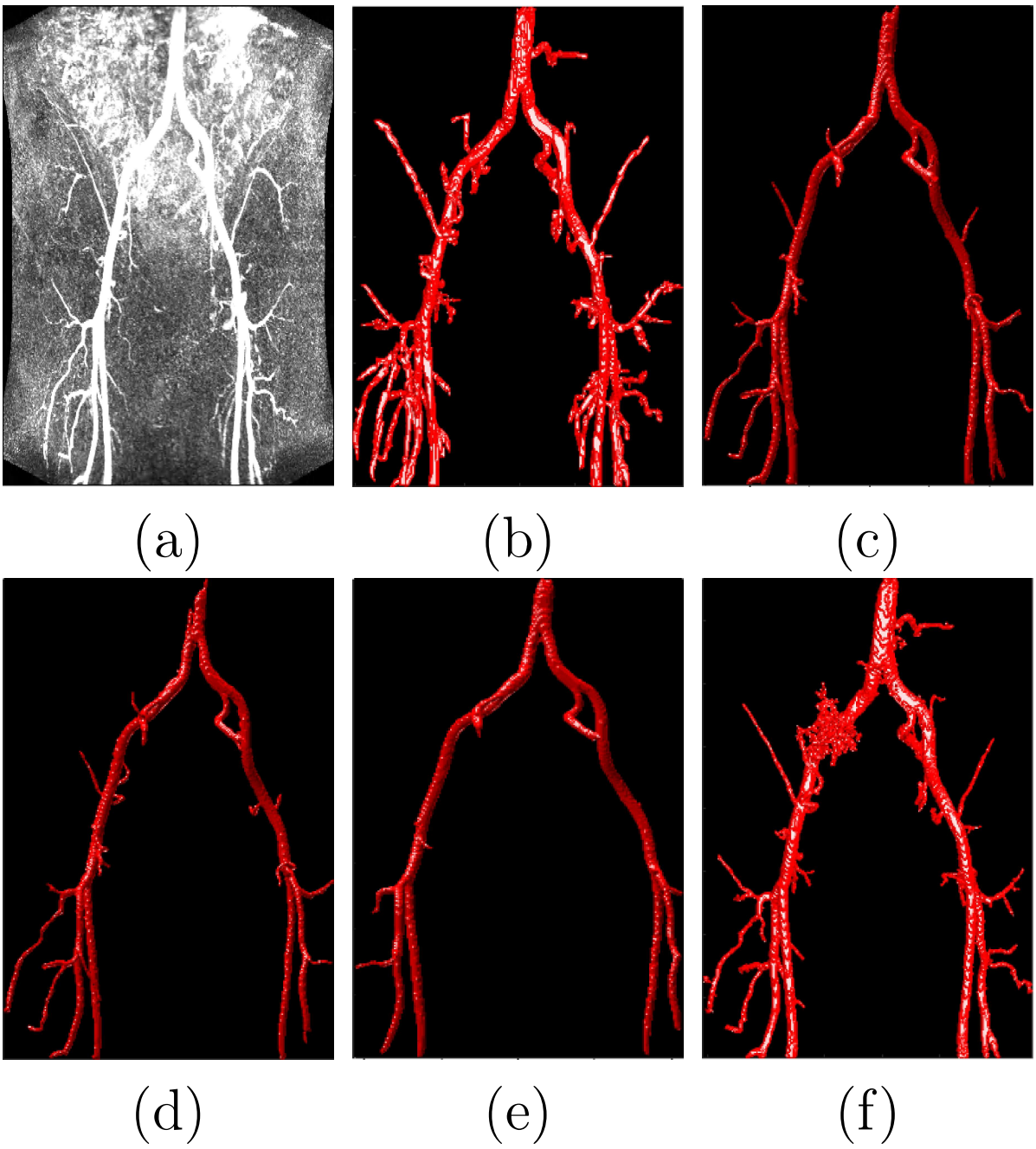

Figure 5.12: Blood vessel segmentation results of the CT pelvic arteriogram image dataset. (a) Maximum Intensity Projection (MIP) images of Original images; (b) 3D view of manually segmented blood vessels; (c) segmentation using FA [30]; (d) segmentation using Frangi vessel enhancement filter and Line filter [68]; (e) segmentation using Frangi vessel enhancement filter [77]; (f) segmentation using the proposed method.

5.5.6 Performance comparison results of the 3D hybrid blood vessel segmentation method with the previous methods on the MRA carotid dataset

Table 5.3 show the performance comparison results of the proposed method with the previous methods in terms of accuracy, sensitivity, specificity, DICE coefficient, and Jaccard index on the MRA carotid dataset. The proposed method outperforms the method proposed by Bhattacharya et al., [30], method proposed by Ding et al., [68] and a method proposed by Frangi et al., [77] with an average (sensitivity = 91.06% , specificity =99.49%, accuracy = 99.41%, DICE = 74.53%, and JAC = 59.40%).

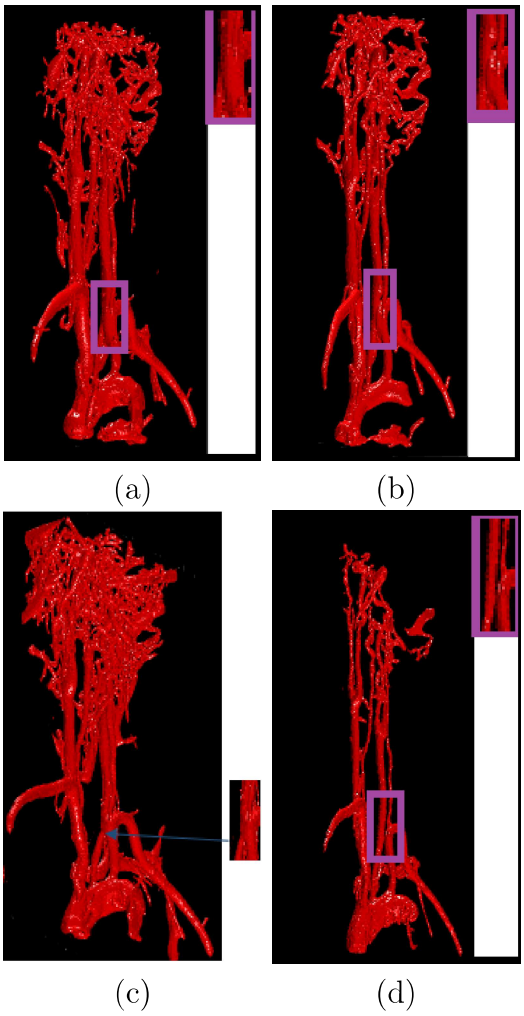

Figure 5.13: Visual comparison of different segmentation techniques on MRA neck dataset for separation of vessels. (a) Frangi vessel enhancement filter [77]; (b) Frangi vessel enhancement filter and line filter [68]; (c) Frangi vessel enhancement filter and Anisotropic diffusion [30]; (d) proposed method

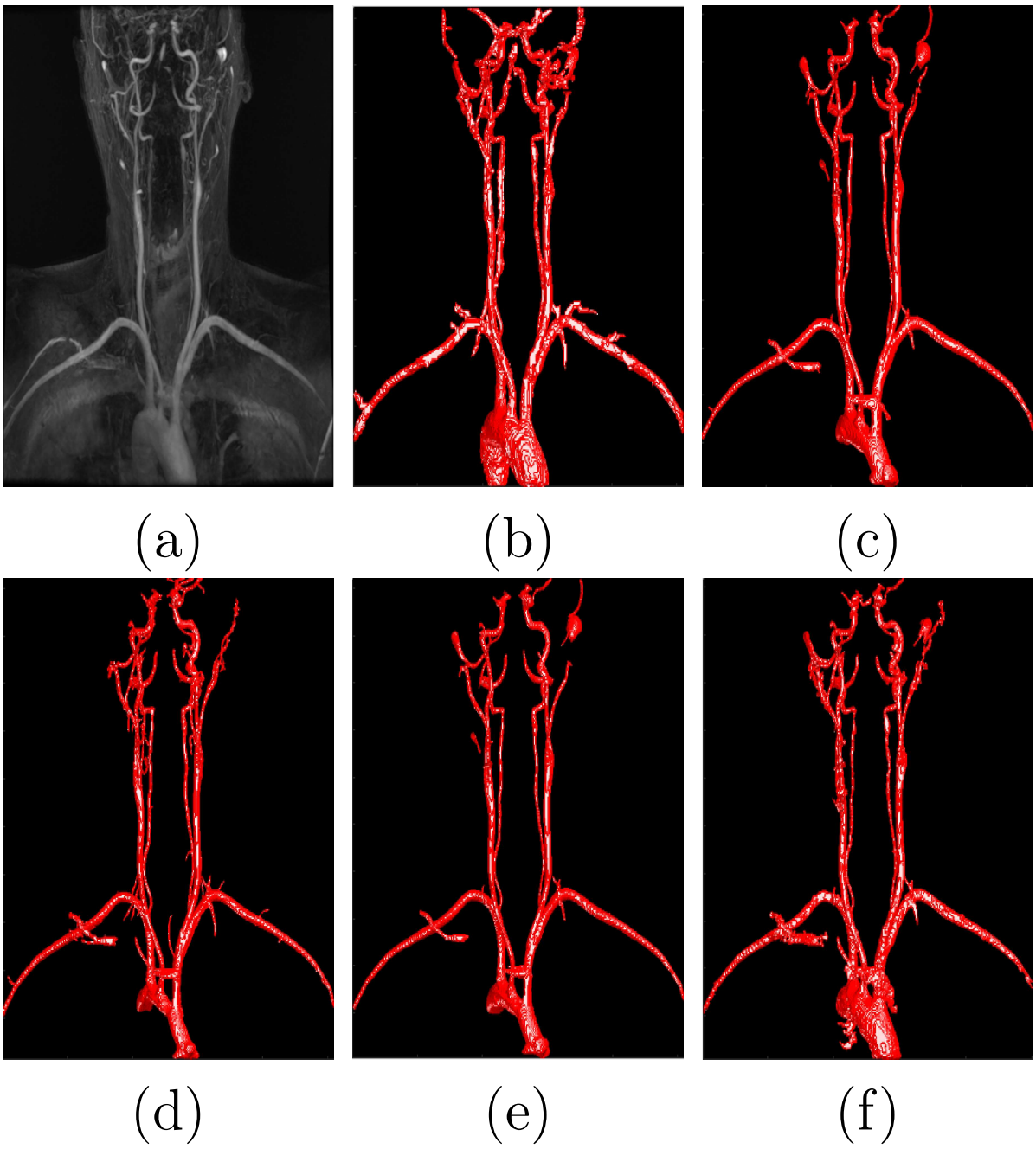

Figure 5.14: Blood vessel segmentation results of the neck image.(a) Maximum Intensity Projection (MIP) images of original neck images; (b) 3D view of manually segmented blood vessels; (c) segmentation using Frangi vessel enhancement filter and Anisotropic diffusion [30]; (d) segmentation using Frangi vessel enhancement filter and Line filter [68]; (e) segmentation using Frangi vessel enhancement filter [77]; (f) segmentation using the proposed method.

Method	Sensitivity	Specificity	Accuracy	DICE	JAC
FA	83.15	99.43	99.28	68.82	52.46
FL	76.12	99.17	99.01	52.05	35.18
F	86.76	99.30	99.20	62.74	45.32
Proposed method	91.06	99.49	99.41	74.53	59.40

Table 5.3: Results of the blood vessel segmentation method on MRA carotid dataset

5.5.7 Performance comparison results of the 3D hybrid blood vessel segmentation method with the previous methods on a MRI heart dataset

For segmentation of blood vessels of various sizes from the MRI images, qualitative results show that the hybrid method is capable of segmenting blood vessels of various sizes from images. More vessels are detected and different sizes are distinguishable to enable further analysis during quantification (Figure 5.16). The method is also able to detect abnormalities in the image. It can be used during early diagnosis. The hybrid method can be applied to both human and pet organ.

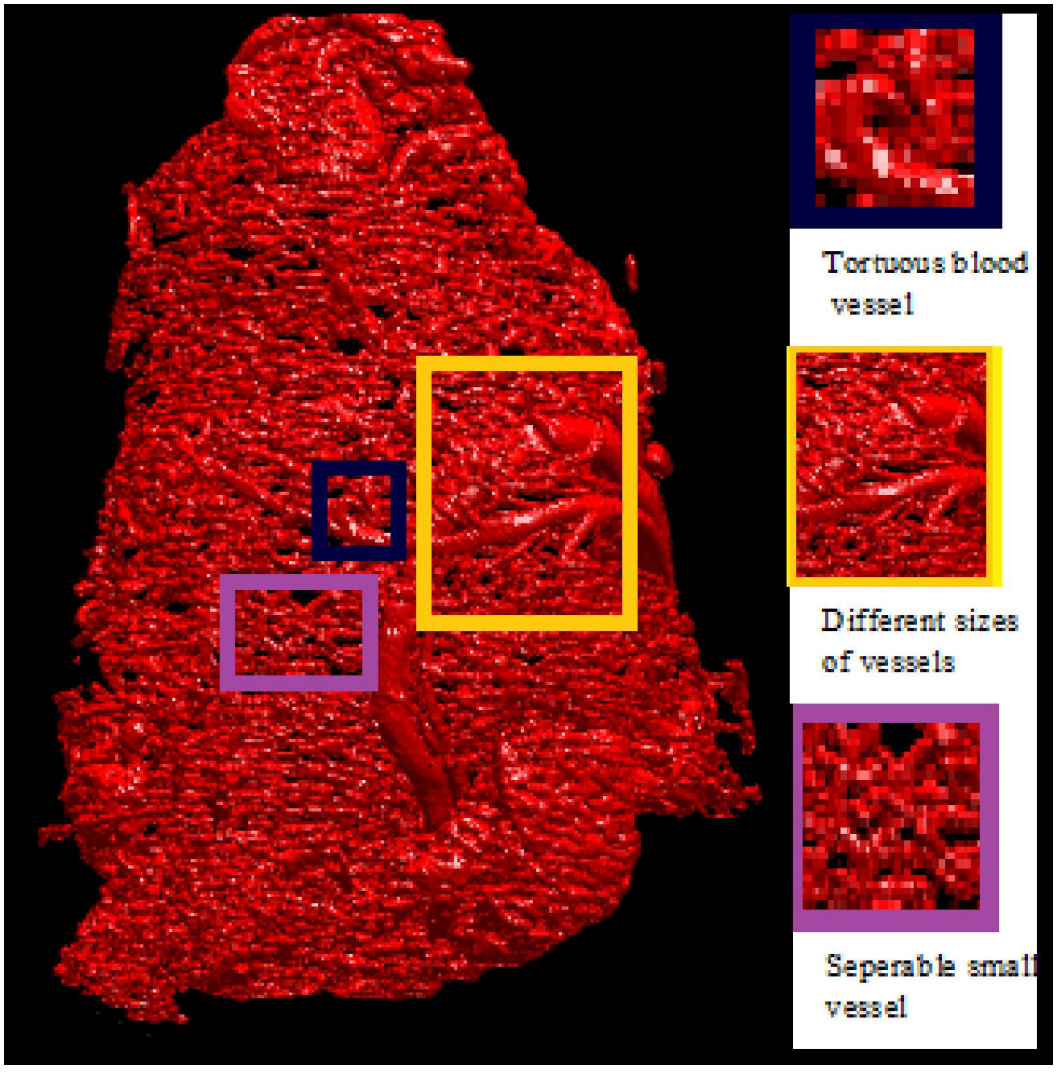

Figure 5.15: Illustration of heart blood vessels after segmentation.

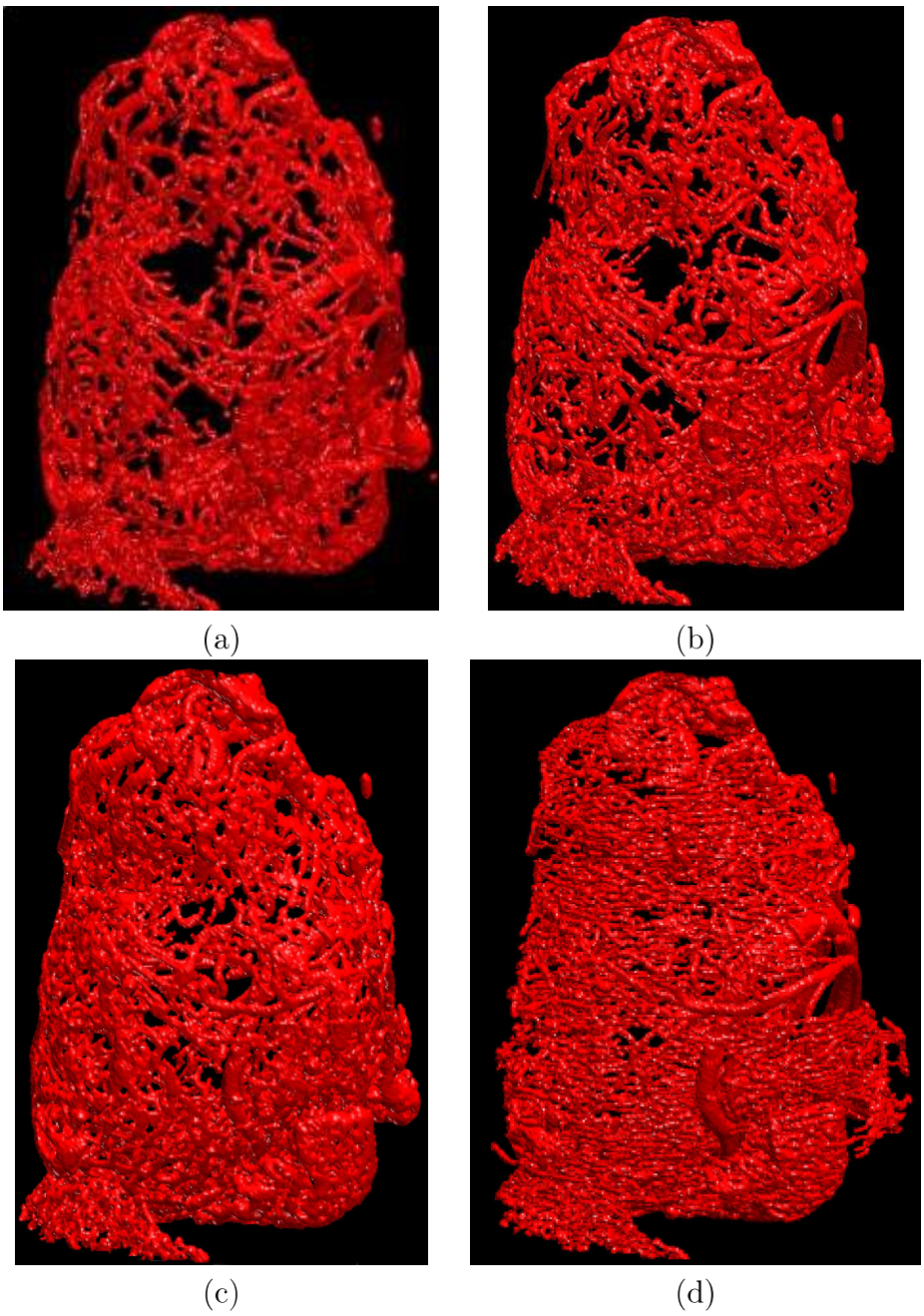

Figure 5.16: Visual comparison of different segmentation techniques on MRI heart dataset. (a) Frangi vessel enhancement filter [77]; (b) Frangi vessel enhancement filter and line filter [68]; (c) Frangi vessel enhancement filter and Anisotropic diffusion [30]; (d) proposed method

5.5.8 Performance comparison results of the proposed method with the previous methods on a CT rat brain image dataset

For segmentation of blood vessels of various sizes from the CT images, qualitative results show that the hybrid method is capable of segmenting blood vessels of various sizes from CT images. More vessels are detected and different sizes are distinguishable to enable further analysis during quantification (Figure 5.17). These results confirm that the method can be

applied to both human and pet.

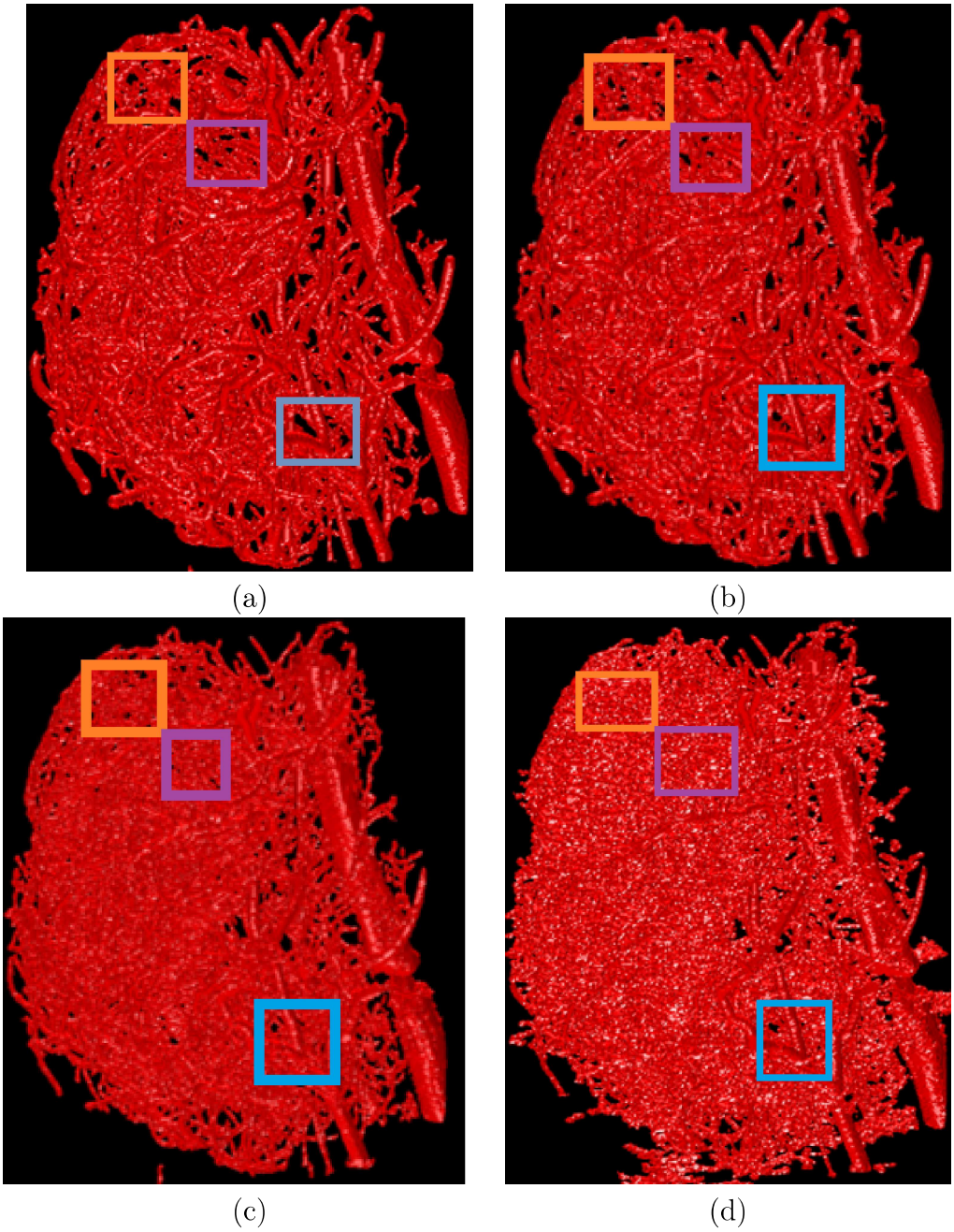

Figure 5.17: Visual comparison of different segmentation techniques on CT scan rat brain dataset. (a) Frangi vessel enhancement filter [77]; (b) Frangi vessel enhancement filter and line filter [68]; (c) Frangi vessel enhancement filter and Anisotropic diffusion [30]; (d) proposed method.

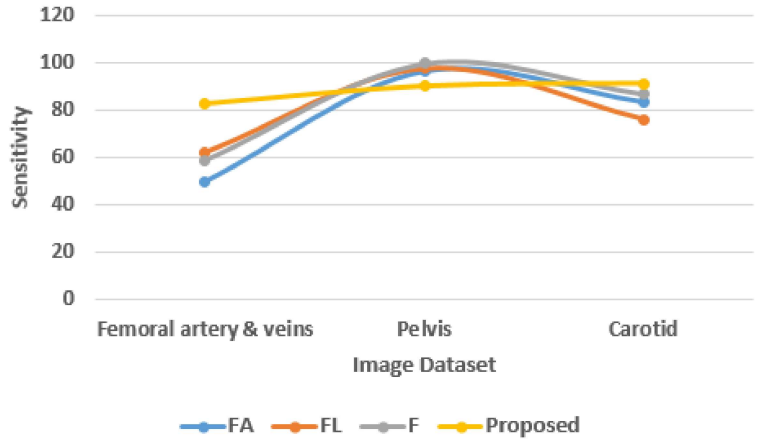

Figure 5.18: A plot of sensitivity for the different methods applied to three datasets

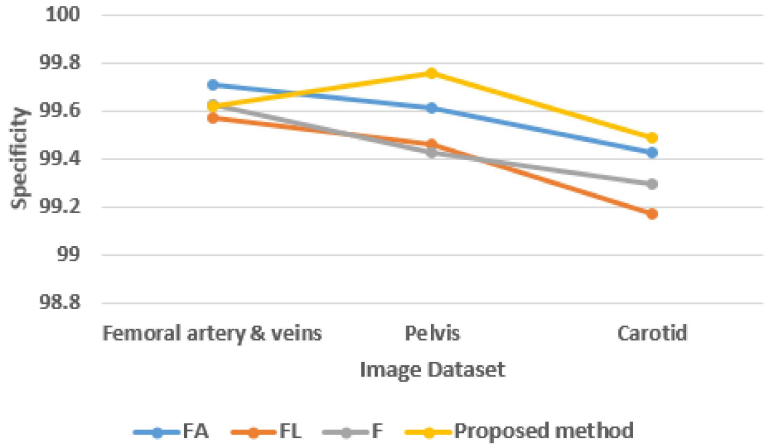

Figure 5.19: A plot of specificity for the different methods applied to three datasets

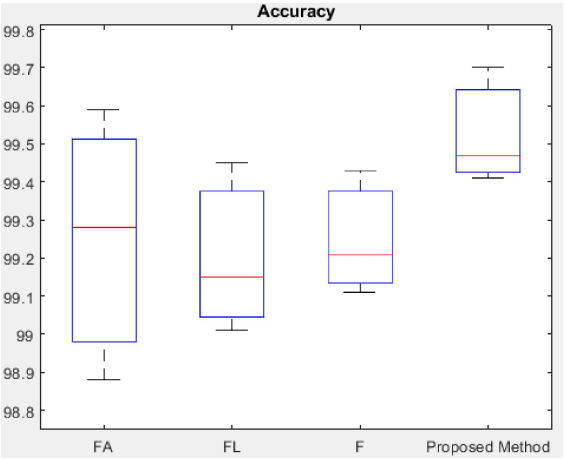

Figure 5.20: A plot of accuracy for the different methods applied to three datasets

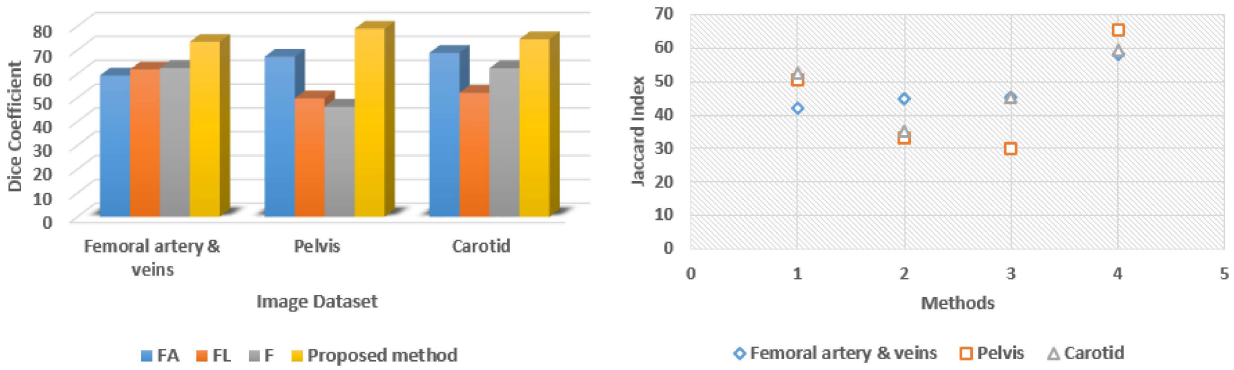

(a) (b)

Figure 5.21: Graph and plot of success measures for the different methods applied to three datasets.(a) Dice coefficient of four methods on all the three images, (b) Jaccard index of four methods (1-FA [30], 2-FL [68], 3-F [77], 4-Proposed method) on all the three images.

5.6 Chapter Discussion and Conclusion

This work has presented a 3D hybrid blood vessel segmentation method based on WBHVEF filter, Hysteresis Thresholding image addition and MATLAB Bwareaopen Operation. In the 3D hybrid blood vessel segmentation framework, segmentation processes occur independently on two individual images, and then an integration step quickly merges both outputs from two individual images into a coherent segmentation result, which is later enhanced using the post-processing method. In the 3D hybrid method, White top-hat scale-space Bilateral Hessian based Vessel Enhancement Filter combined with hysteresis thresholding is used during the segmentation of the small to medium blood vessels, hysteresis thresholding is used during segmentation of the medium to big vessels, Image addition is utilised to combine segmentation results from the two processes, Matlab bwareaopen operation is used to enhance the segmentation results. This work has evaluated the performance of vessel segmentation against three other methods on the CTA femoral dataset, CT pelvic arteriogram image dataset, MRA Carotid dataset, CT mouse brain dataset, and MRI human heart dataset.

Table 5.1, 5.2, 5.3 show performance comparison in terms of the average accuracy, sensitivity, specificity, DICE coefficient, and Jaccard index. According to these results, the 3D hybrid blood vessel segmentation method reaches acceptable results and outperforms all other Bhattacharya et al., [30], Ding et al., [68], Frangi et al., [77] in terms of average accuracy. The proposed method produced the best results with the average (sensitivity =

91.06%, specificity = 99.49%, accuracy = 99.41%, DICE = 74.53%, and JAC = 59.40%) on the MRA carotid dataset. On CTA femoral dataset, the proposed method only achieves the best average (sensitivity = 82.76%, accuracy of 99.47%, DICE = 73.43%, and JAC = 58.02%), and marginally inferior to the methods presented by Bhattacharya et al., [30] and Frangi et al., [77], in terms of the average specificity. This may be due to the small ground-truth dataset used during the evaluation. Surprisingly, the proposed method achieves the best average (specificity = 99.76%, accuracy = 99.70%, DICE = 78.93%, and JAC = 65.20%) on the CT pelvic arteriogram image dataset. But, it is marginally inferior to methods proposed by Bhattacharya et al., [30], Frangi et al., [77] and Ding et al., [68] in terms of sensitivity. This may be due to the small ground-truth dataset used during evaluation as the visual comparison says otherwise. Figure 5.12, show a visual comparison between the segmentation performance of the proposed method and other state-of-the-art methods for a sample image from the CT pelvic arteriogram image dataset. As it can be seen, the proposed method can segment blood vessels of various sizes including small vessels irrespective of the image condition. Although the visual comparison is considered purely subjective, it can still emphasise the positive and negative points of various segmentation approaches in support of quantitative results. Besides detecting the blood vessels of different sizes, the proposed method is capable of detecting blood vessel disorders and therefore it can be used during early diagnosis (Figure 5.15). The method can be used to detect both human and pets. This can be seen in the results achieved by this method on all datasets. The proposed method addresses one of the main issues in medical image analysis, "lack of segmentation methods that can segment blood vessels of various sizes in 3D medical images." Since the blood vessels segmentation method fail to distinguish blood vessels from non-blood vessels. Thus, the proposed method can be used during early diagnosis and during the treatment to monitor patients response to treatment.

Chapter 6

2D Hybrid Blood Vessel Segmentation Method

6.1 Chapter Overview

A substantial amount of work is reported in the literature for detecting blood vessels in 2D retina images. Although remarkable effort has been shown in retinal blood vessel segmentation, there is a need for blood vessel segmentation methods that can segment blood vessel of various sizes, especially small vessels. In this chapter, a White top-hat scale-space Bilateral Hessian based Vessel Enhancement Filter (WBHVEF), Hysteresis Thresholding and Matlab Bwareaopen Operation are utilised during image pre-processing and blood vessel segmentation and post-processing respectively. The chapter describes how the filter enhances the blood vessels to ease segmentation and shows that the blood vessels are extracted and enhanced. The chapter also shows how the new 2D hybrid blood vessel segmentation outperforms other segmentation methods. Finally, limitations of the segmentation are presented.

6.2 Related work

Automatic blood vessel segmentation from 2D medical images, still face difficulty in extracting blood vessels of various sizes (especially small blood vessel). This is because blood vessels naturally vary in size, shape and in contrast distribution, therefore a segmentation method that can extract blood vessels of various sizes from 2D medical images is desirable.

The techniques introduced for vessel segmentation employ model-based approach, tracking-based approach, local adaptive thresholding, and multi-scale approach. Among the methods, the multi-scale approach is popular and widely used due to its ability to extract blood vessel at various scale sizes. Techniques that employ a multi-scale approach, segment blood vessels by representing grey-level data in a way that combines sampling operations with successive smoothing steps conducted by Gaussian kernels with different scales giving rise to a response that is represented by 2D Hessian matrix [203]. Eigenvalues of the Hessian matrix are used to determine the vessel-like structures which, in turn, result in retinal vasculature structure enhancement. Hessian matrix processing through Eigenvalues analysis is used to obtain the principal directions of vessels where the decomposition of local second-order structures in the retinal image can be performed to obtain the direction of the smallest curvature along the retinal vessels [77]. In the multi-scale method, the retinal image size decreases exponentially with scale level, and, as a consequent, the amount of required computation too. The multi-scale approaches can be best suited for structures that have varying width and length in the same image. Similar methods have been proposed such as Abdallah et al. [25] proposed a two-step multi-scale retinal vessel detection algorithm. In this method, the noise-corrupted retina image (grey layer) is first denoised against the additive Gaussian noise using a flux-based anisotropic diffusion technique, then later a multi-scale response of multi-level resolution of retina image is computed. A vessel model is established to analyse the eigenvalues and the Eigen vectors of the Hessian matrix for each scale. The method achieved an area under the ROC curve of 0.94514 on the STARE dataset. Moghimirad et al., [156] segmented the blood vessels by first of all extracting the medial axis of the blood vessels using a two-dimensional Medialness function in multiple scales and sum of smoothed eigenvalues of the image, then later estimated the vessel reconstruction where the centerline of vessels was extracted and radius of vessels was estimated simultaneously to obtain the final segmented results. The method achieved average (accuracy=0.9659, area under ROC = 0.9580) on DRIVE dataset and average (accuracy = 0.9756, area under ROC curve = 0.9678) on STARE dataset.

Active contour models segments vessels by fitting the curve to blood vessel boundaries in the image. It is also known as dynamic contour modelling because during segmentation, it is

initialised at a place in the neighbourhood of the target blood vessel, then the model evolves dynamically to fit the shape of blood vessels by an iterative adaption. The movement of the model used during fitting is controlled by the parameters, which makes it rigid topologically, namely, it does not have the flexibility required to represent blood vessels composed of a variable number of independent parts [61]. Moreover, another drawback associated with the active contour model technique is the incapability of the model to converge to the correct vessel edges in the presence of high-level noise or if the vessels have relatively low contrast levels [246]. Similar segmentation methods have been proposed such as, In 2015, Zhao et al. [253] proposed an infinite perimeter active contour model with hybrid region terms for vessel segmentation. The proposed method uses a combination of intensity information and a local phase-based enhancement map during vessel segmentation. The method can preserve vessel edges. The method achieved an average (sensitivity = 0.780, specificity = 0.978, accuracy = 0.956) on a STARE dataset and an average (sensitivity = 0.7420 , specificity = 0.9820 and accuracy = 0.9540) on DRIVE dataset.

The tracking based method segments the blood vessels by tracking the ridges of the retina image basing on a set of starting points. the ridges of the blood vessels are detected by inspecting the zero crossings of gradient and curvature. However, the "clean-limbed" ridges require a pre-processing step which involves complicated vessel enhancement for all vessels sizes and orientations. Consequently, one of the major drawbacks of vessel tracking is the extreme dependency on the pre-processing steps that proceed with the phase of tracing. Similar methods have been proposed such as Wu et al., [230] proposed a vessel tracking methodology for retinal vasculature structure extraction that combines Hessian and matched filters and an idea of exploiting the edge information at the vessels parallel boundaries, which was first proposed by Sofka and Stewar [192] for retinal vessels extraction. Once the contrast between vessels and other retina tissues are enhanced and the information of sizes and the orientations of enhanced vessels are available, the ridges are used to trace vessels via their centre lines along with ridge seeds that were selected automatically. The method achieves an average (true positive rate = 84.4%, false positive rate = 19.3%) via DRIVE dataset.

Thresholding method segment blood vessels by searching for a global value (level) that opti-

mally maximises the separation between different classes (different tissues in our case) in the image. The effectiveness of thresholding with a global level manifests if the objects in the image under consideration have well-defined areas and if the grey levels can be congregated around values with minimum interference. Uneven illumination, inferior quality of source material, camera artefacts/distortions, and anatomical objects with multi-classes and hybrid features make the global thresholding for the entire retinal image a major source for segmentation errors. Moreover, since retinal image shows a soft transition between different grey levels, uneven illumination or noise distortions, the principal segmentation errors begin to appear due to the pixel-wise approach adopted by global thresholding, namely, the pixels that have the same grey levels (pixel intensity) will be segmented into the same anatomical object, which is considered a long-standing issue of global thresholding with a single hard value. To resolve these issues, several methods have been proposed such as The statistical-based adaptive thresholding method that was used in [10], to segment blood vessels. The method achieved an average accuracy of 0.9469 and an area under the ROC curve approximate value of 0.963. In [160], Adaptive thresholding was used to extract large and medium-sized retinal vessels, Multiscale Tensor Voting Framework (MTVF) was used to extract the smallest ones and morphological cleaning was used to remove the non-vasculature components during the post-processing stage. The method achieved an average (average accuracy = 94.79%, sensitivity = 85.06%, specificity = 95.82%) on Erlangen dataset [165]. Based on the above, there is no best technique to face all performance metrics in high blood vessel segmentation achievement, nor the best mathematical scheme to do so. Deciding whether the methodology is best depends on a set of factors including (1) Achieved accuracy, which depends on the achieved specificity and sensitivity, where segmentation is considered the best if it achieves the highest possible sensitivity value (or shows low false detection to other retinal structures), while also maintaining the specificity at an optimal level. On the other hand, the optimality of the method increases as the detection capability of the method records high performance in pathological retinal images; (2) Time and computational complexity: The time and the computational power required by the methods tend to below, as the accuracy has increased tendency on the condition that high performance of high accuracy has achieved; The accurate detection and segmentation

of the retinal vascular structure form the backbone of a variety of automated computer-aided systems for the screening and diagnosis of cardiovascular diseases. Even though many promising methodologies have been developed and implemented, there is still room for research improvement in blood vessel segmentation methodologies, especially for noisy and pathological retinal images in public datasets. In the following sections, the blood vessel of various sizes will be distinguished using 2D hybrid blood vessel segmentation method, that makes use of 2D White top-hat scale-space Bilateral Hessian based Vessel Enhancement Filter (WBHVEF), hysteresis thresholding and MATLAB bwareaopen operation during image pre-processing, vessel segmentation and post-processing respectively.

6.3 Methodology

This 2D hybrid blood vessel segmentation method takes advantage of WBHVEF, hysteresis thresholding and MATLAB bwareaopen operation during image pre-processing, vessel segmentation and post-processing respectively (Figure 6.1). Image pre-processing is performed to improve the quality of the image to facilitate blood vessel segmentation. Segmentation is performed to distinguish blood vessels from non-blood vessels and post-processing is performed to remove the unwanted objects.

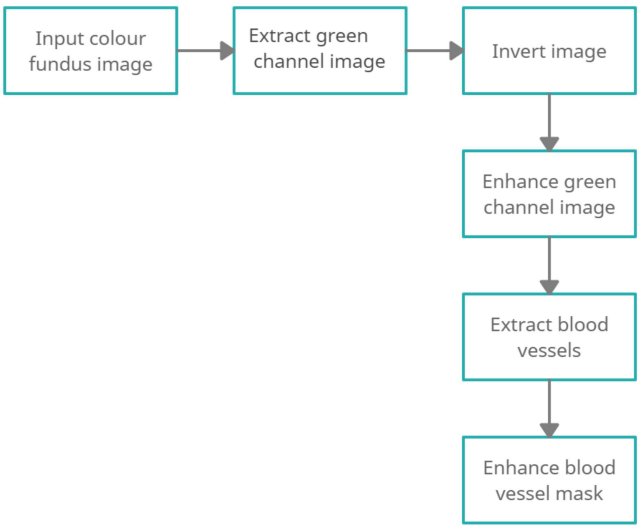

Figure 6.1: Block diagram of the proposed retina vessel segmentation method

6.3.1 Image pre-processing

Blood vessels are tubular structures distributed at different orientations and scales in an image. Blood vessel enhancement filters are applied before blood vessel segmentation to

suppress non-blood vessel structures and image noise to ease the segmentation problem [253, 133]. In this chapter, a White top-hat scale-space Bilateral Hessian based Vessel Enhancement Filter is used to enhance the blood vessels and the image quality before segmenting the blood vessels.

6.3.1.1 White top-hat scale-space Bilateral Hessian based Vessel Enhancement Filter (WBHVEF)

One of the challenges faced by researchers is segmenting and maintaining edges of small vessels especially in presence of image artefacts (such as intensity homogeneity and noise). 2D WBHVEF filter (section 4.3.1.2) is utilised during blood vessel enhancement stage because of its capability to correct illumination, enhance contrast and address noise of the image while maintaining strong sharp edged blood vessels [34].

6.3.2 Blood vessel segmentation

In medical image analysis, a method that can distinguish blood vessels from non-blood vessels and also detect blood vessels of different sizes is considered ideal as it helps during diagnosis to determine the patient's response to treatment. This work, therefore, employ hysteresis thresholding to ensure accurate extraction of vessels.

6.3.2.1 Hysteresis thresholding

Hysteresis thresholding has consistently been able to outperform absolute thresholding methods because of the capability to deal with uncertainties during edge detection. It also detects the absence of pixels in true edges even in presence of intensity in-homogeneity. The hysteresis thresholding method in [224] is used. In Hysteresis Thresholding, the salience value of edge pixels not only depend on the gradient magnitude but also on its spatial distribution measured by supporting range. The hysteresis thresholding method is not based on pixels but on segments/objects. An object (also known as a region) is a group of pixels. In this method, vessels are segmented following steps. In the first step of the segment-based hysteresis thresholding, edge pixels are linked into curve segments with the following method. Starting from the pixel with the highest gradient magnitude, a curve segment grows at each step by including the most salient edge pixel among the 16 neighbours of the two endpoints (each endpoint has 8 neighbours) of the curve segment. The growing is

ended when no more object pixels can be added. Then, a new segment growing starts from the edge pixel with the highest gradient magnitude among the remaining object pixels that have not been included in a curve segment. This process is repeated until no more new curve segment can be generated. The salience value of each curve segment is the sum of the salience values of its edge pixels computed.

6.3.3 Post-processing

In post processing stage, a method that can eliminate the unwanted objects such as noise without tampering with the image details is considered ideal. I used MATLAB bwareaopen operation because of its ability to remove unwanted objects of a particular size without tampering with image details.

6.3.3.1 Matlab bwareaopen operation

MATLAB bwareaopen operation is well known for eliminating small artefacts without interfering with the region of interest and it has been used in different fields of image analysis. MATLAB bwareaopen morphological operation is used to remove all connected components (objects) that are fewer than 26 pixels from the binary image. MATLAB bwareaopen operation involves three steps that include (i) Determining connected components using Matlab bwconncomp operation. Matlab bwconncomp operation returns connected components (with the connectivity of 8 in the binary image), (ii) Computing the area of each component using Matlab region props operation. (iii) Removing small objects. All connected objects are labelled. ismember operation is used to remove all object with less than 26 pixels.

6.4 Experimental Evaluation

This section describes the evaluation of the proposed method on public image dataset. The image dataset used in this study includes DRIVE dataset and STARE dataset.

6.4.1 Evaluation Datasets

Two public retinal image datasets were employed for the evaluation of the proposed segmentation method. In this section, a brief introduction to these datasets is presented, followed by an introduction to the evaluation metrics used in our experiments.

6.4.1.1 Digital Retinal Images for Vessel Extraction(DRIVE) dataset

This dataset consists of a total of 40 colour retinal images, obtained in the course of a diabetic retinopathy screening program in the Netherlands. Each image resolution is 768 by 584 pixels. All of the 40 images came with ground-truth data.

6.4.1.2 Structured Analysis of the Retina (STARE)

This dataset contains 400 colour retinal images, 20 of these come with ground-truth data, 10 of which show evidence of pathology. Each image resolution is 605 by 700 pixels.

6.4.2 Parameter selection for retina dataset

- Hysteresis threshold parameters used to group voxels in to blood vessel and non-blood vessel in three-dimensional medical images range between 0 and 1.
- The White top-hat scale space Bilateral Hessian based Vessel Enhancement Filter parameters used for enhancement of retina vessels include $\alpha = 16$, $\beta = 0.48$. The scale size used in White top-hat scale space Bilateral Hessian based Vessel Enhancement Filter during the enhancement of blood vessels in STARE image dataset and DRIVE image dataset ranges from 1 and 8. White top-hat morphological operation parameters include the square structuring element. The structuring element size depends on the scale used. Bilateral parameters that were used include: $G_{\sigma_r} = 2$, $eps = 1e - 3$ and $G_{\sigma_s} = 10$. Where G_{σ_s} is a spatial Gaussian ensures that only pixels in a spatial neighbourhood are considered, and, G_{σ_r} is a range Gaussian that ensures that only pixels of similar intensities are considered to compute the blurred intensity value to avoid blurriness.

6.4.3 Evaluation metrics

To support comparison with previous work, three commonly used metrics were employed to evaluate the performance of the competing methods in terms of pixels: accuracy, sensitivity, and specificity. Below is a brief description of each of the evaluation Metrics used.

- **Sensitivity:** Sensitivity measures the portion of positive voxels (vessels) in the ground truth that is also detected as positive by the segmentation being evaluated.

Sensitivity is also referred to as True Positive Rate (TPR) and Recall, and can be expressed as [201]:-

$$Sensitivity = Recall = TPR = \frac{TP}{TP + FN} \tag{6.1}$$

where TP is vessel voxels correctly detected by the algorithms, and FN is vessel voxels detected as background voxels.

- **Specificity:** Specificity measures the portion of negative voxels (background) in the ground truth segmentation that is also detected as negative by the segmentation being evaluated. Specificity is also referred to as True Negative Rate (TNR), and can be expressed as [201]:-

$$Specificity = TNR = \frac{TN}{TN + FP} \tag{6.2}$$

where TN is background voxels correctly detected by method and FP is background voxels detected as vessel voxels.

- **Accuracy:** Accuracy is calculated as a degree of closeness between segmentation results and the ground-truth. Accuracy can be expressed as follows:-

$$Accuracy = \frac{TP + TN}{TP + FP + TN + FN} \tag{6.3}$$

where TP is vessel voxels correctly detected by the algorithms, TN is background voxels correctly detected by the method. FP is background voxels detected as vessel voxels, and FN is vessel voxels detected as background voxels.

6.5 Blood Vessel Segmentation Algorithm Experiments

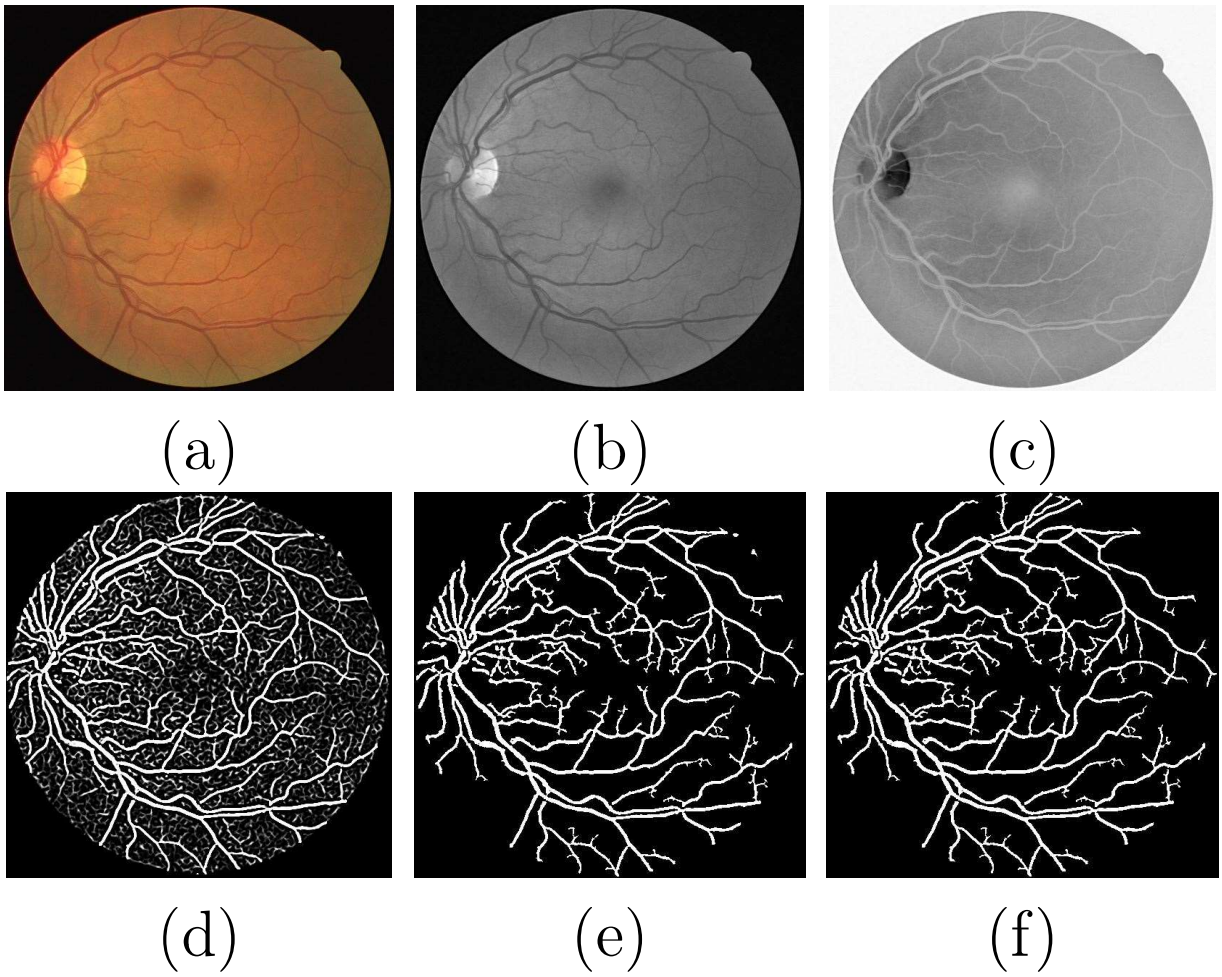

Figure 6.2: Results of proposed segmentation process. (a) colour fundus image; (b) green channel image; (c) image after image inversion; (d) image after image enhancement by White top-hat scale-space Bilateral Hessian based Vessel Enhancement Filter; (e) image after segmentation by hysteresis thresholding; (f) image after post-processing by MATLAB bwareaopen operation

6.5.1 Experimental Results of the Blood Vessel Segmentation Algorithm on the DRIVE Dataset

The performance of the segmentation of the proposed method on the DRIVE dataset is compared with alternative methods: The performance results of second expert hand labelled and the method proposed by Bankhead et al. [22], Dai et al. [60], Bahadarkhan et al., [21], Martinez et al., [151], Zhao et al.[252], and Zhang et al., [248] were obtained from Memari et al., [153]. The results of the method proposed by Zafer et al. [243], Soomro et al. [193], Akhavan et al., [8], Chatraborti et al., [47], and Nugroho et al., [163] are from the original manuscript. The second human expert hand-labeled image [154] is considered

as the target performance level with average (sensitivity = 77.6%, specificity = 97.2% and accuracy = 94.7%). Table 6.1 shows the performance of the proposed method against the aforementioned methods on the DRIVE dataset. The proposed method needs an overall improvement of 2.7% in-terms of sensitivity. On the other hand, with an average sensitivity of 74.9% and average accuracy of 95.4%, the proposed method achieves better performance than all the other methods concerning the average sensitivity value and accuracy value. The average specificity achieved with the proposed method on a DRIVE dataset, outperforms Bankhead et al., [22], Dai et al. [60], Martinez et al., [151], Soomro et al., [193], Akhavan et al., [8], Chatraborti et al., [47], Zhang et al., [248], and Nugroho et al., [163]. But it is marginally inferior to the methods proposed by Zafer et al.[243], and Zhao et al.[252]. An overview of the testing results on DRIVE shows that the proposed method offers a reliable and robust segmentation solution for blood vessels. It is clearly observed that the proposed method reaches better performance in terms of the average sensitivity and accuracy.

Author	Sensitivity	Specificity	Accuracy
Second observer	77.6	97.2	94.7
Soomro et al. [193]	74.5	96.2	94.8
Akhavan et al., [8]	72.5	97.3	95.1
Chatraborti et al., [47]	72.1	95.8	93.7
Nugroho et al., [163]	72.1	96.7	94.5
Dai et al., [60]	73.6	97.2	94.2
Bankhead et al., [22]	70.3	97.1	93.7
Zhao et al.[252]	74.4	97.8	95.3
Zhang et al., [248]	71.2	97.3	93.8
Zafer et al. [243]	67.8	97.9	94.0
Martinez et al., [151]	72.4	96.5	93.4
Proposed method	74.9	97.4	95.4

Table 6.1: A comparison between different retinal vessel segmentation methods evaluated using DRIVE dataset

Image number	Sensitivity	Specificity	Accuracy
1	84.94	96.02	95.03
2	80.09	96.64	94.95
3	74.72	94.80	92.80
4	73.95	97.47	95.3
5	71.33	98.19	95.67
6	70.31	97.6	94.94
7	74.61	96.24	94.27
8	71.19	97.34	95.09
9	71.26	98.32	96.13
10	71.33	98.24	96.03
11	70.44	97.99	95.53
12	75.31	96.92	95.05
13	74.03	96.67	94.46
14	74.93	97.57	95.74
15	77.53	97.47	96.04
16	74.6	98.54	96.38
17	73.32	98.23	96.12
18	77.78	97.63	96.06
19	82.17	98.04	96.73
20	73.17	98.41	96.56
Mean	74.85	97.42	95.39

Table 6.2: Testing results using DRIVE dataset.

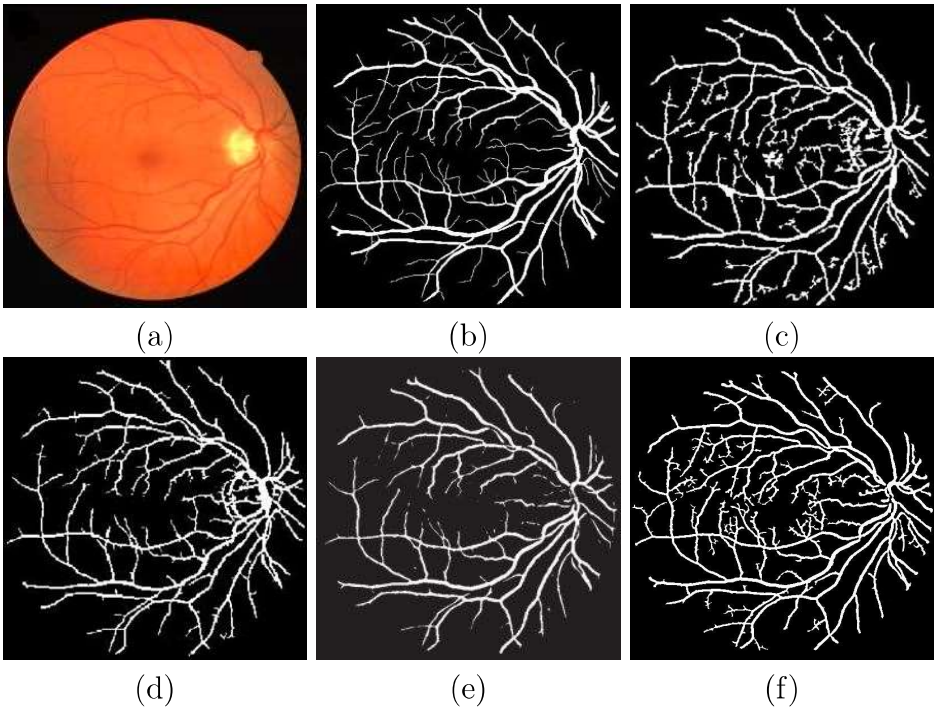

Figure 6.3: Visual comparison of between different retinal vessel segmentation methods evaluated using DRIVE test image 2. (a) colour fundus image; (b) manual segmentation; (c) method by Bankhead et al. [22]; (d) method by Martinez et al. [151]; (e) method by Zafer et al. [243]; (f) proposed method

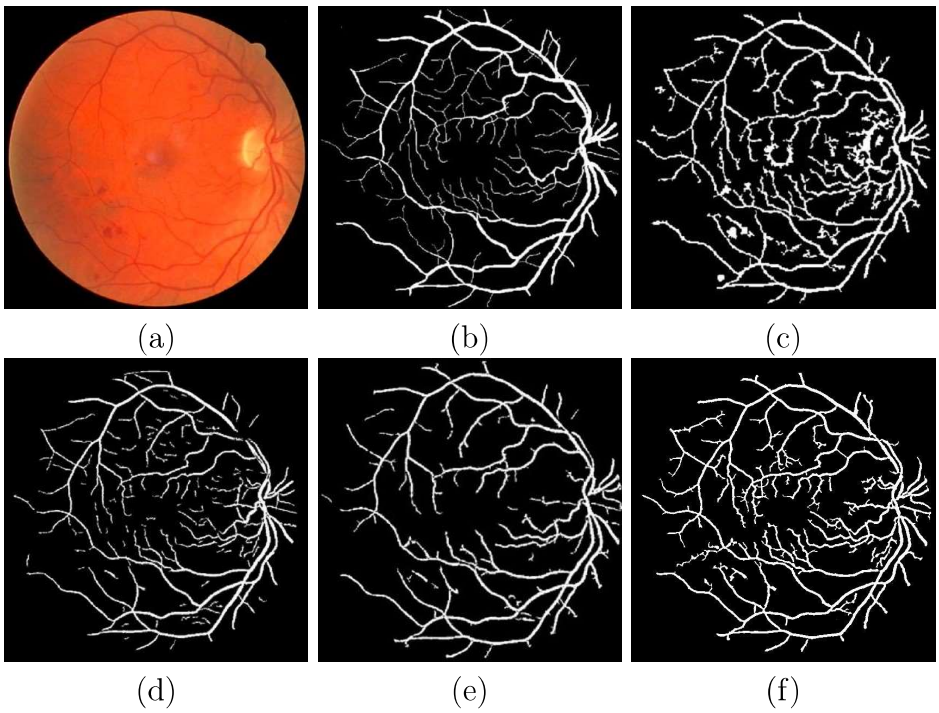

Figure 6.4: Visual comparison of between different retinal vessel segmentation methods evaluated using DRIVE text image 14. (a) colour fundus image; (b) manual segmentation; (c) method by Bankhead et al. [22]; (d) method by Dai et al. [60]; (e) method by Bahadarkhan et al., [21]; (f) proposed method

6.5.2 Results of the blood vessel segmentation algorithm on the STARE dataset

Table 6.4 show performance comparison results of the proposed method with recent alternative methods in terms of sensitivity, specificity, and accuracy on the STARE dataset. The performance results of the second expert hand labelled and the method proposed by Bankhead et al. [22], Dai et al. [60], Bahadarkhan et al., [21], Martinez et al., [151], Zhang et al., [248], Asad and Hassaanien [16], and Azzopardi et al., [19] were obtained from Memari et al., [153]. The results of the method proposed by Memari et al., [153], Chatraborti et al., [47], and Nugroho et al., [163] are taken from the original manuscript. In Tables 6.4, the second human expert hand-labelled image is considered as the target performance level with average (sensitivity = 89.5%, specificity = 93.8% and accuracy = 93.4%). Thus, the proposed method needs an overall improvement of 10.3% in average sensitivity. whereas Chatraborti et al., [47], Nugroho et al., [163], Dai et al. [60], Bankhead et al. [22], Azzopardi et al., [19], Asad and Hassaanien [16], Zhang et al., [248], Bahadarkhan et al., [21], Memari et al., [153], Martinez et al., [151] have a room of improvement

of 21.6%, 14%, 11.8%, 13.7%, 12.3%, 14.7%, 17.8%, 13.7%, 11.3%, and 14.5% respectively. Considering the value of the average sensitivity and the value of the average accuracy as performance measures, the proposed method reaches better performance than all the other methods. However, with the average specificity, the proposed method is only marginally inferior to the method presented by Azzopardi et al., [19]. It has the same value of specificity as Memari et al., [153]. Compared to the results of the second expert hand-labelled and methods proposed by Chatraborti et al., [47], Nugroho et al., [163], Dai et al. [60], Bankhead et al. [22], Asad and Hassaanien [16], Zhang et al., [248], Bahadarkhan et al., [21], Memari et al., [153], and Martinez et al., [151], the proposed method outperforms the average accuracy of these techniques. An overview of the testing results on the STARE dataset shows that the proposed method offers a reliable and robust segmentation solution for blood vessels. It is observed that the proposed method reaches better performance in terms of average sensitivity and accuracy.

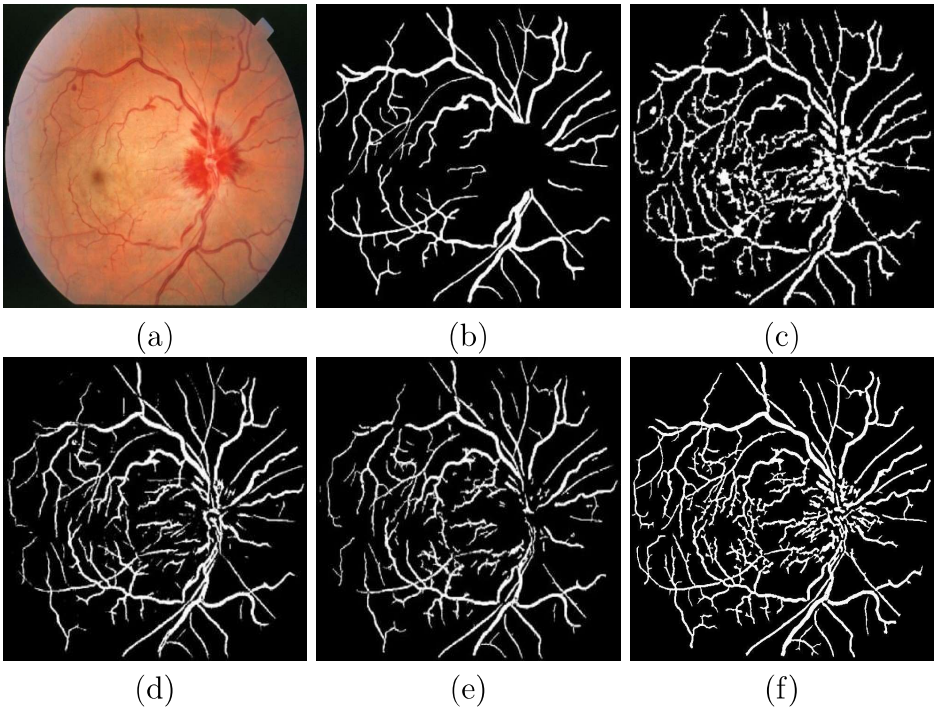

Figure 6.5: Visual comparison of between different retinal vessel segmentation methods evaluated using STARE test image 5. (a) colour fundus image; (b) manual segmentation; (c) method by Bankhead et al. [22]; (d) method by Azzopardi et al. [19]; (e) method by Bahadarkhan et al.[21]; (f) proposed method

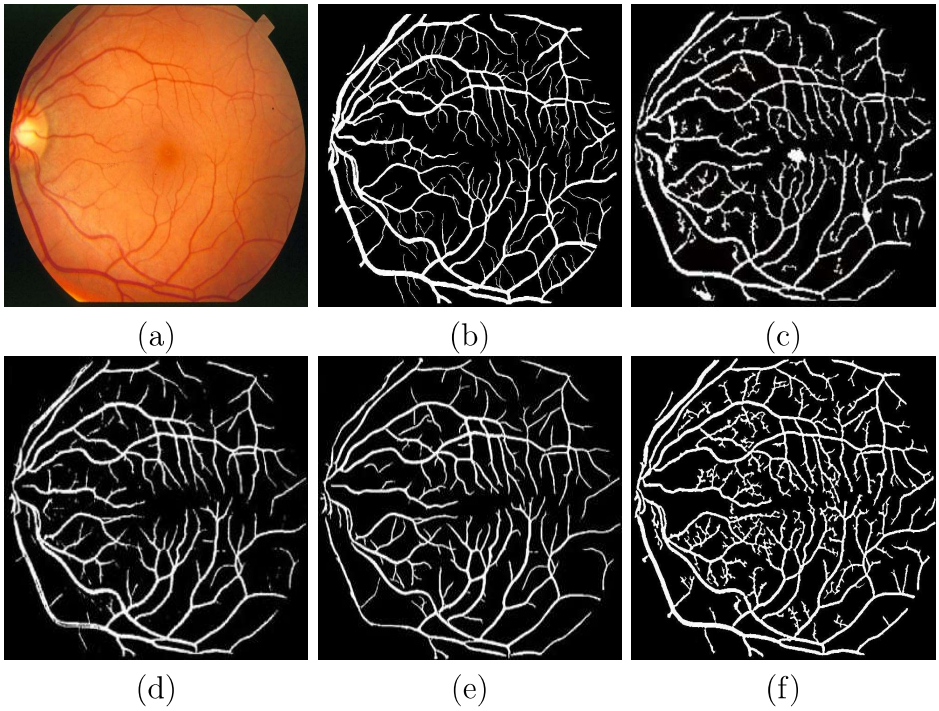

Figure 6.6: Visual comparison of between different retinal vessel segmentation methods evaluated using STARE test image 77. (a) colour fundus image; (b) manual segmentation; (c) method by Bankhead et al. [22]; (d) method by Azzopardi et al. [19]; (e) method by Memari et al. [153]; (f) proposed method

Image number	Sensitivity	Specificity	Accuracy
1	65.23	96.52	94.02
2	70.24	94.33	92.72
3	80.04	94.95	94.05
4	61.33	96.47	93.87
5	74.42	98.05	95.91
6	83.62	97.14	96.20
7	90.24	95.59	95.92
8	91.71	95.11	94.86
9	89.32	95.46	94.97
10	76.26	95.68	94.12
11	87.79	96.32	95.71
12	89.67	97.29	96.71
13	81.47	97.21	95.81
14	82.76	96.64	95.39
15	80.42	97.4	95.93
16	77.12	93.97	92.25
17	87.15	97.12	96.23
18	73.16	99.18	97.87
19	78.51	98.54	97.68
20	63.64	97.12	94.88
Mean	79.21	96.50	95.26

Table 6.3: Testing results using STARE dataset.

Author	Sensitivity	Specificity	Accuracy
Second observer	89.5	93.8	93.4
Chatraborti et al., [47]	67.9	95.9	94.0
Nugroho et al., [163]	75.5	90.4	88.8
Dai et al., [60]	77.7	95.5	93.6
Bankhead et al., [22]	75.8	95.0	93.2
Azzopardi et al., [19]	77.2	97.0	95.0
Asad and Hassaanien [16]	74.8	95.4	94.4
Zhang et al., [248]	71.7	94.8	94.8
Bahadarkhan et al., [21]	75.8	96.3	94.6
Memari et al., [153]	78.2	96.5	95.1
Martinez et al., [151]	75	95.6	94.1
Proposed method	79.2	96.5	95.3

Table 6.4: A comparison between different retinal vessel segmentation methods evaluated using STARE dataset

6.5.3 Processing time of various methods

The proper comparison of algorithm efficiency is difficult because, in general, source code has not been made publicly available to allow testing on the same machine using the same conditions (e.g. operating system, MATLAB version where appropriate). One must then resort to using the information included in the published papers that have made use of the same images.

In this chapter, the average processing time of the method proposed by Bahadarkhan et al., [19], Bankhead et al., [20], Azzopardi et al., [17], Dai et al., [57], Vlachos and Dermatas [202], Zhao et al., [237], Mapayi et al., [140], Asad and Hassanien [14], and Memari et al., [143] we're obtained from Memari et al., [143].

The proposed method was run using Matlab version 2016a (Mathworks, Natick, CA) on a PC with a 3.6GHZ Intel Core i7 system and 16GB RAM.

Table 6.5 shows that the average processing time and the average accuracy of the proposed method against that of the aforementioned methods. The processing time of the proposed method is shorter than that of the method proposed by Bankhead et al., [20], Dai et al., [57], Asad and Hassanien [14], and Memari et al., [143] by 0.011%, 2.333%, 3.969%, and 0.222% respectively. Although, the average processing time of the proposed method is inferior to that of the method proposed by Bahadarkhan et al., [19], Azzopardi et al., [17], Vlachos and Dermatas [202], Zhao et al., [237], and Mapayi et al., [140] by 0.596%, 0.283%, 0.353%, 0.483%, and 0.539%, the value of the average accuracy achieved by the proposed method is higher than that of Bankhead et al., [20], Azzopardi et al., [17], Dai et al., [57], Vlachos and

Dermatas [202], Zhao et al., [237] and Mapayi et al., [140] by 1.8%, 0.8%, 1.4%, 2.4%, 0.6%, and 0.4%. Surprisingly, the proposed method achieves the same value of average accuracy (95.3%) as the method proposed by Bahadarkhan et al., [19].

But it is marginally inferior interms of the average accuracy, to the method proposed by Asad and Hassanien [14] and Memari et al., [143] by 0.1% and 0.3% respectively.

Method	Processing time per image (s)	Processing time per image (%)	Average accuracy	Computational resources	Development environment
BahadarKhan et al., [21]	1.5	0.0147	95.3	Intel Core i3 CPU running at 2.53 GHz coupled with 4 GB RAM	MATLAB
Bankhead et al., [22]	22.4	0.622	93.5	Intel Core i3 CPU running at 2.53 GHz coupled with 4 GB RAM	MATLAB
Azzopardi et al., [19]	11.8	0.328	94.5	Intel Core i3 CPU running at 2.53 GHz coupled with 4 GB RAM	MATLAB
Dai et al., [60]	106	2.944	93.9	Intel Core i3 CPU running at 2.53 GHz coupled with 4 GB RAM	MATLAB
Vlachos and Dermatas [217]	9.3	0.258	92.9	Intel Core i3 CPU running at 2.53 GHz coupled with 4 GB RAM	MATLAB
Zhao et al.[252]	4.6	0.128	94.7	Intel Core i3 CPU running at 3.1 GHz coupled with 8 GB RAM	MATLAB, C++
Mapayi et al. [150]	2.6	0.072	94.9	Intel Core i5 CPU running at 2.30 GHz coupled with 4 GB RAM	MATLAB
Asad and Hassaanien [16]	165	4.58	95.4	Intel Core i3 CPU running at 2.53 GHz coupled with 3 GB RAM	MATLAB
Memari et al., [153]	∼30	0.833	95.6	Intel Core i5 CPU running at 2.30 GHz coupled with 4 GB RAM	MATLAB
Proposed method	∼22	0.611	95.3	Intel Core i7 CPU running at 3.60GHz coupled with 16 GB RAM	MATLAB

Table 6.5: A comparison between the run-time of different retinal vessel segmentation methods

6.6 Chapter Discussion and Conclusion

This work has presented a 2D hybrid blood vessel segmentation method based on White top-hat scale-space Bilateral Hessian based Vessel Enhancement Filter, Hysteresis Thresholding and MATLAB Bwareaopen Operation. The 2D hybrid blood vessel segmentation method involves three stages including image and blood vessel enhancement for pre-processing, classification of pixels into blood vessels and background (non-blood vessels) for segmentation and blood vessel mask enhancement for post-processing. In the 2D hybrid method, White top-hat scale-space Bilateral Hessian based Vessel Enhancement Filter is used during image enhancement, Hysteresis Thresholding is used to group image pixels in to blood vessels and non-blood vessels, and MATLAB Bwareaopen Operation is used to enhance the resulting blood vessel mask for blood vessels segmentation in retinal images.

The performance of vessel segmentation method is evaluated against ten other methods (excluding human manual labelling) on both the STARE dataset and the DRIVE dataset. Table 6.1, and Table 6.4 show performance comparison in terms of the average sensitivity, specificity, and accuracy. According to these results, the proposed vessel segmentation algorithm reaches acceptable results and outperforms all other methods in terms of average sensitivity and accuracy on both STARE dataset and DRIVE dataset. In terms of the average specificity, the proposed method outperforms Bankhead et al., [22], Dai et al. [60], Bahadarkhan et al., [21], Martinez et al., [151], Soomro et al., [193], Akhavan et al., [8], Chatraborti et al., [47], Zhang et al., [248], and Nugroho et al., [163] on DRIVE dataset. On

STARE dataset, it performs better than Chatraborti et al., [47], Nugroho et al., [163], Dai et al. [60], Bankhead et al. [22], Asad and Hassaanien [16], Zhang et al., [248], Bahadarkhan et al., [21], and Martinez et al., [151]. But it achieves the same value of specificity as Memari et al., [153].

Nevertheless, the proposed method is marginally inferior to the methods presented by Zafer et al.[243], and Zhao et al.[252] on DRIVE, and Azzopardi et al., [19] on STARE. The proposed method incorporates the prior knowledge of blood vessels to perform the segmentation, and it can be applied to retinal images from multiple sources and under different conditions. This can be seen in the results achieved by this method on both the STARE and DRIVE datasets.

Figures 6.3, 6.4, 6.5 and 6.6 show a visual comparison between the segmentation performance of the proposed method and other state-of-the-art methods for a sample image 5 from the STARE and DRIVE datasets, respectively. As it can be seen, the proposed method can segment blood vessels of various sizes including small vessels irrespective of the image condition. Although the visual comparison is considered purely subjective, it can still emphasise the positive and negative points of various segmentation approaches in support of quantitative results.

Table 6.5 shows the average processing times among various vessel segmentation methods. The proposed method requires an average of $\sim 22sec$ to segment an image, making it comparable to most methods from the literature.

The proposed method addresses one of the main issues in medical image analysis, "lack of segmentation methods that can segment blood vessels of various sizes in 2D medical images." Since the blood vessels segmentation method fail to distinguish blood vessels from non-blood vessels due to image artefacts (such as noise, low contrast variation between the vessels and none vessels). Thus, the proposed method can be used during classification to calculate the number of blood vessels, vessel diameter and tortuosity, discriminating veins and arteries along with measuring the arteriovenous ratio. Furthermore, segmented blood vessels can be utilised as features for blood vessel disease classification and systematic disease (such as diabetes, stroke or hypertension) identification systems.

Chapter 7

An Automated Morphological Tool for Segmentation of Vessels

7.1 Chapter Overview

Plenty of research has been presented on blood vessel segmentation from histology images. Despite the advances in blood vessel segmentation that attain impressive results, there is a need for blood vessel segmentation methods that can segment blood vessel of various sizes from H&DAB (Haematoxylin and Diaminobenzidine) images. In this chapter, a fully automated morphological tool for segmentation and quantification of vessels in H&DAB stained histology mice brain image slides is presented. The morphological tool that exploits the capabilities of the stain normalisation method in [20], image saturation channel, ISODATA thresholding, MATLAB bwareaopen operation, Matlab erosion operation, Matlab dilation operation and morphometric approach during image stain standardisation, blood vessel segmentation, and blood vessel diameter quantification respectively. As pointed out in [39], this idea leads to successful image enhancement, blood vessel extraction and blood vessel quantification. Note: The work in this chapter was done to complement the efforts of clinical researchers engaged in research in Alzheimer's disease. The automated quantification results are compared against the manually obtained quantification results. The medical images and manually obtained quantification results were provided by clinical researchers (clinical researcher at Queen medical centre) who were part of the collaboration team.

7.2 Related Work

Automatic blood vessel segmentation from histology images, still face difficulty in extracting blood vessels from histology due to image artefacts (such as stain variation problem, specs, and stain leakage problem) in the images and the the complex nature of the vessels (blood vessels vary in size, shape, contrast distribution). A few methods have been applied to segmentation of blood vessels in histology images. A commonly used method is to segment blood vessels by manipulating colour in the image. This method can discriminate between objects with minimal effort. However, the performance depends on the colour model used during segmentation. For example, techniques that exploit RGB (Red Green Blue) colour model are associated with less accuracy as compared to techniques that utilise other colour models (such as HSV (Hue Saturation Value) colour space model, CIELAB colour space model) [3, 24, 211]. This is because RGB colour models are not perceptually uniform [3, 24]. Colour models such as HSV dissociates luminance information from the hue values thus providing a more consistent level of colour which enable accurate extraction of the region of interest [57, 175, 190, 189, 210]. However, techniques that exploit these models (such as HSV, Lab and LUV), struggles to detect objects due to colour variations, lighting conditions and staining artefacts [211]. For example, to extract vessels, Reyes-Aldasoro et al., [175], exploited distinctive hues of stained vascular endothelial, cell nuclei and background, to provide seeds for region growing method during object segmentation in 3D Hue Saturation Value (HSV) colour model. Then later post-processed the segmented objects that are extracted as microvessels by CD31 immunostaining by joining separate objects that are likely to belong to a single vessel, closing objects that have a narrow gap around their periphery, and splitting objects with multiple lumina into individual vessels. However, the segmentation results are not adequate as several objects in the images appeared to be linked as a single object due to colour variation. To deal with the fragmentation of intact vessels on the images and artefactual appearance of stain images. Xu et al., [233], proposed to reconstitute complete vessel walls by joining the topological skeletons of the blood vessel wall fragments, and then, removing artefactual fragments based on measured incoherence with neighbouring tissue in 3D. However, Xu et al., [233], manually delineated vessels yet manual intervention is prone to errors.

Unlike Reyes-Aldasoro et al., [175], Fernández-Carrobles et al., [74], utilised two image channels. Blood vessels in the RGB images are segmented by converting RGB images to HSV colour model. Then later, binary thresholding is applied to both saturation and hue channels using 30 and 20 respectively. A logical OR operator is applied to both images to extract vessels that are normally brown in colour. Small artefacts of the image are eliminated using Matlab erosion operation and Matlab dilation operation during post-processing. False positives are eliminated. Contours (that are mistaken to be small vessels) that are larger than 6 pixels are eliminated. The method is fast but fails to work on images with stain variation artefact [74, 211].

In the following sections, the problem of "lack of blood vessel segmentation methods that can segment blood vessels from H&DAB images" will be addressed by developing a morphological tool that can enhance the appearance of the histology images, segment the blood vessels and also quantify the blood vessel diameter of the blood vessel.

7.3 Methodology of the Fully Automated Morphological Tool for Segmentation and Quantification of Blood Vessels in Histology Images

The proposed morphological tool consists of three steps including image enhancement (also known as image pre-processing), segmentation, and quantification. The morphological tool exploits the stain normalisation method in [20] during stain normalisation to standardise the appearance of the image. In addition, it exploits only saturation channel and methods such as ISODATA thresholding, MATLAB bwareaopen operation, and Matlab dilation operation during segmentation of vessels to group image pixels in to blood vessels and non blood vessels. Since the accuracy of the segmentation determines the accuracy of the processes that come after segmentation, the performance of the segmentation results is evaluated based on the vessel quantification results. The morphological tool quantifies the blood vessel diameter following MATLAB region props operation steps. Unlike other

quantification methods [127, 209, 199], the diameter along the blood vessel traverse section and blood vessel longitudinal section are quantified separately. This is done to create a better understanding of image data. I used a morphometric approach to quantify the blood vessel diameter to detect morphological changes in vessels due to the presence of atheroma, thickening of blood vessels caused by the abnormal accumulation of material such as β-amyloid or fatty acid deposits in the inner layer of the wall of an artery.

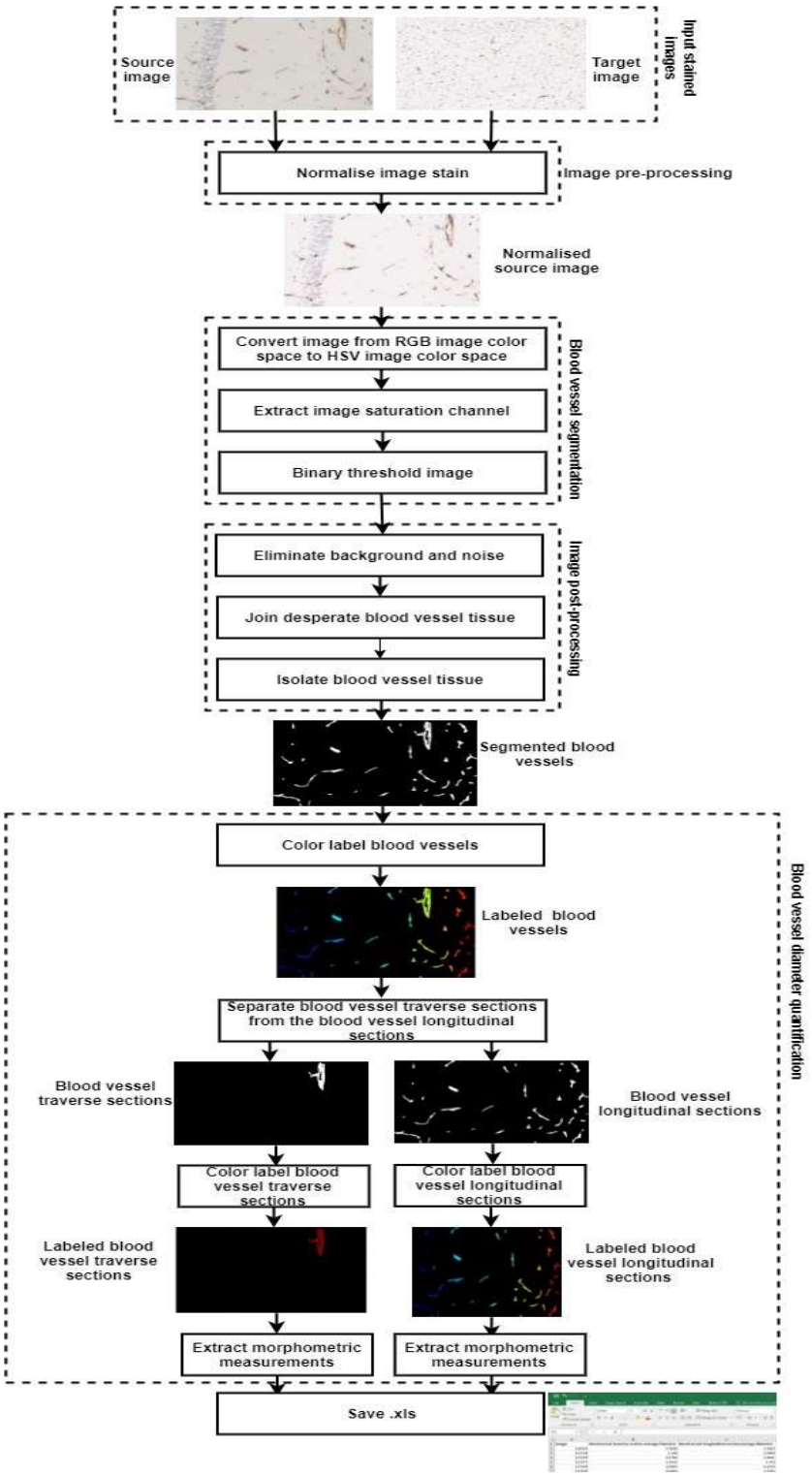

Figure 7.1: Block diagram showing the blood vessel segmentation procedure in histology images

7.3.1 Stain normalisation

A hybrid stain normalisation in [20], is used to standardise the stain and intensity in H& DAB images. The hybrid stain normalisation method normalises the stain following two stages that include the stain separation stage and colour transfer stage. It uses Octree colour

quantisation algorithm combined with Beer-Lambert law, and a modified blind source separation algorithm during the stain separation stage to computationally estimate the amount of stain in a histology image based on its chromatic and luminous response, and a modified colour transfer algorithm during the colour transfer stage to minimise the effect of varying staining and illumination. To the best of my knowledge, this is the first work to demonstrate that Beer-Lambert law applies to histology images with stains (such as Diaminobenzidine (DAB)) that are non-absorbers of light. In addition, compared to the original blind source separation method, the blind source separation method used in this work makes use of the Spatial-Spectral Schrodinger Eigenvectors and Eigenvalues rather than the ordinary Eigenvalues and Eigenvectors to incorporate texture and spatial information.

7.3.1.1 Stain separation

Stain separation is performed to computationally estimate the amount of stain in an histology image based on its chromatic and luminous response [177, 84, 173, 87]. Octree colour quantisation algorithm is combined with Beer-Lambert law, and a modified blind source separation algorithm are used during stain separation stage. The blind source separation method uses spatial-spectral Schrodinger-Eigen vectors and Eigen values during pre-whitening process to determine the set of stain vectors and stain matrix (3×3). By making use of Schrodinger-Eigen vectors, Iam able to incorporate texture and spatial information [42]. The Stain separation algorithm involves three steps that include,(a) Estimate stain, (b) Obtain the stain vectors, (c) Perform colour deconvolution. The three steps are described in the section below:-

A. Estimate stain

(a) Colour quantisation

Colour quantisation is the process of choosing M colours from image I to construct a quantised colour space, $\bar{I}$, where $\bar{I} = \bar{I}_j, j = \{1, 2, ..., M\}$ [190]. Colour quantisation is introduced due its ability to enhance the image [40, 100, 190, 112]. Octree quantisation algorithm that is highly non-uniform is employed to extract the classes [180] during colour quantisation. Octree quantisation algorithm quan-

tises the colour following the steps below: given an image I, every colour in the image is stored in an Octree of depth 8 (every leaf at depth 8 represents a distinct colour). A limit of M (in this case M = 256) leaves is placed on the tree. The colours are filtered basing on the limit of M leaves set. For example colour in the tree can result in two outcomes that include, (a) if there are less than M leaves the colour is filtered down the tree until either it reaches some leaf node that has an associated representative colour or it reaches the leaf node representing its unique colour, and (b) If there are greater than M leaves in the tree some set of leaves in the tree must be merged (their representative colours averaged) together and a new representative colour stored in their parent. Leaves are selected and merged following two criteria that include, (a) Reducible nodes that have the largest depth in the tree should be chosen first. They represent colours that lie closest together, and (b) If there is more than one group of leaves at the maximum depth the algorithm either merges leaves that represent the fewest number of pixels to keep the error small or reduce leaves that represent the most pixels. In this case large areas will be uniformly filled in a slightly wrong colour while maintaining detailed shadings.

Once the entire image has been processed, the colour in the image is quantised by simply filtering each colour down the tree until a leaf is hit.

(b) Convert the colour quantised image in to optical density space

$$Z = LOG(\ I_0)\ - LOG(\ I + 1) \tag{7.1}$$

where I_0 is the illuminating light on the quantised RGB Image I.

B. Obtain stain vector

The stain vector is obtained following steps below

(a) Pre-whiten data following the steps below.

Compute the correlation matrix using Equation 7.2:-

$$R = R_s \times \frac{R_s^{'}}{L_s} \tag{7.2}$$

where R_s is the received sigma. $R_s{}'$ is the conjugate transpose of R_s. L_s is the length of the sigma.

Obtain Eigen values U and Eigen vectors V using Schroedinger Potential in [42, 41].

Perform Eigen values decomposition using shur decomposition method in Equation 7.3. Shur decomposition method is expressed as [167], [79], [88], [186]:

$$\tilde{A}_{YY}^{(d)} = QUQ^{-1} \tag{7.3}$$

where Q is a unitary matrix, Q^{-1} is a conjugate transpose of Q. U is the diagonal matrix with real entries. Denoising the estimate $\tilde{A}_{YY}$ of $A_{YY} = E(YY^{-}1)$ is performed by estimating the noise variance. The noise variance is estimated by obtaining the average of the smallest Eigen values. The denoised image is obtained using equation below:-

$$\tilde{A}_{YY}^{(d)} = \tilde{A}_{YY} - \sigma_n^2 I_q \tag{7.4}$$

Given that ideally $\tilde{A}_{YY}^{(d)} = HH^{-1}$, the non-zero part of the matrix $LD^{\frac{1}{2}}$ equals H up to a unitary ambiguity matrix:

$$\tilde{L} = HU \tag{7.5}$$

where U is a unitary matrix. $\tilde{L}$ is constructed as a matrix containing p large norm. Column in $LD^{\frac{1}{2}}$.Then, the received signal is pre-filtered using:

$$\tilde{Y} = \tilde{L}\#Y \tag{7.6}$$

where # denote matrix pseudo-inverse.

(b) Perform multi-kurtosis maximisation

Multi user kurtosis (MUK) can be defined by $M_{q\times p}$ the following set of $q \times p$ complex matrices:

$M_{q\times p} = \{D \in C^{q\times p}\ such\ that\ D^H D = I_p\}$

MUK is performed following the steps below:-

Compute the gradient of $F(G)$ using the formula in Equation 7.7 with respect to W. Then later obtain an adaptive stochastic-gradient algorithm.

Let

$$\mathrm{F}(\ \mathrm{G}) = \sum_{j=1}^{p} \mathrm{sign}(\ K(\ z_j)\ )\ K(\ z_j)\ = \mathrm{sign}(\ K_a)\sum_{j=1}^{p}\left(E|z_j|^4 - 2E^2|z_j|^2 - \left|E\left(z_j^2\right)\right|^2\right)$$

And by invoking C2 with the assumption that symmetrical inputs

$(\ E(\ a^2(\ K)\ = 0)\ )$, the gradient of $F(\ G)$ with respect to W is given by:

$$\nabla(F(G)) = 4sign(K_a)\sum_{j=1}^{p}\left(E|z_j(k)|^2 z_j(k)Y^*(k)\right) \tag{7.7}$$

Update $W(k)$ in the direction of the instantaneous gradient using Equation (7.8).

$$W^{'}(k+1) = W\left(k\right) + \mu \mathrm{sign}(K_a)Y^*(k)Z\left(k\right) \tag{7.8}$$

where

$$\mathrm{Z}\ (k) = \left[|z_1\left(k\right)|^2 z_1\left(k\right)....|z_p\left(k\right)|^2 z_p\left(k\right)\right]$$

Satisfy the orthogonality constraint at the next iteration of the algorithm by utilising the unitary constraint using Gram-Schmidt orthogonalisation in Equation 7.9.

$$G{\in}M_{p\times p} \leftrightarrow G^H(k+1)G(k+1) = I_p \tag{7.9}$$

Undo the remaining unitary mixture which makes the equaliser W of size $p \times p$,

hence saving computational cost. Then, to satisfy the constraint in Equation 7.9, it suffices to satisfy $W\left(k+1\right) \in M_{p\times p}$, i.e.

$$W^{H}(k+1)W\left(k+1\right) = I_{p} \tag{7.10}$$

Since there is no guarantee that $W^{'}(k+1)$ will satisfy the constraint in (7.10), $W^{'}(k+1)$ has to be transformed into a unitary

$$W(k+1) = f\left(W^{'}\left(k+1\right)\right) \tag{7.11}$$

By treating $W(k+1)$ as a $p \times p$ matrix satisfying Equation 7.10 that is as close as possible to $W^{'}\left(k+1\right)$ in the Euclidean sense using the iterative procedure that satisfies the following criterion successfully for $j = 1, ..., p$:

$$\begin{cases} min_{W_j} \nabla(W_j) = \left(W_j - W_j^{'}\right)^{H}\left(W_j - W_j^{'}\right) \\ subject\ to: \ W_l^{H} W_j = \sigma_{ij}, l = 1, ..., j \end{cases} \tag{7.12}$$

where $\left\|X\right\|^{2} = X^{H}X$ is squared Euclidean norm of vector X, σ_{ij} is kronecker delta, $W_j^{'}$ is obtained from

$$W^{'} = \left[W_1^{'}, ..., W_p^{'}\right] \tag{7.13}$$

To solve (7.12), The Lagrangian of $\nabla(\ W_j)$ is first constructed using (7.14)

$$L_{\nabla}\left(W_j, \lambda_j, \mu, v\right) = \nabla\left(W_j\right) - \lambda_j\left(W_j^{H}W_j - 1\right) - \sum\nolimits_{l=1}^{j-1}\mu_{lj} Re\left(W_l^{H}W_j\right)$$

$$\text{-}\sum\nolimits_{l=1}^{j-1} V_{lj} Im\left(W_l^{H}W_j\right) \tag{7.14}$$

Where λ_j, $_{\iota}j$, and $V_l j$ are real scalar parameters. Setting the gradient of $L_{\nabla}(\ W_j, \lambda_j, \mu, v)$ with respect to W_j to zero $\frac{\partial L_{\nabla}}{\partial W_j = 0}$, The following equations are obtained for each j:

$$W_j - W_j^{'} - \lambda_j W_j - \sum\nolimits_{l=1}^{j-1} B_{lj} W_j = 0 \tag{7.15}$$

where $B_{lj} = \frac{1}{2}(\ \mu_l j + iV_{lj})$. From Equation 7.15, the equation below is formed

$$\begin{cases} \lambda_j = 1 - W_j^H W_j^{'} \\ B_{lj} = -W_l^H W_j^{'} \end{cases}$$

which gives

$$(1 - \lambda_j)\, W_j = W_j^{'} - \sum_{l=1}^{j-1} \left(W_l^H W_j^{'} \right) W_l \tag{7.16}$$

According to Equation 7.16

$$W_j \propto \left(W_j^{'} - \sum_{l=1}^{j-1} \left(W_l^H W_j^{'} \right) W_l \right)$$

C. Perform colour deconvolution

colour deconvolution scheme is used to transform quantised RGB channels of a histology image into density map for each stain.

(a) Determine stain concentration of individual stains:

$$C = W \times Z \tag{7.17}$$

where Z is the optical density map obtained in Equation 7.1, W is the stain matrix obtained in Equation 7.16.

The optical density maps of each stain are obtained by taking the columns of stain matrix W and taking rows of the stain concentration matrix using the equation below:

$$Y = WC \tag{7.18}$$

7.3.1.2 Colour transfer

Colour transfer procedure is performed to minimise the effect of varying staining and illumination [183]. I modified the colour transfer method in [213], [145],
[139] to achieve better stain normalisation results. This work introduces a weighting factor in the colour to easily adjust the contrast and brightness of the image tissue. The colour transfer involves 6 steps that include the following:

A. Let W be the stain matrix and C be the coefficient matrix from Equation 7.18.

$$Y_{source} = W_{source}C_{source}, Y_{target} = W_{target}C_{target} \tag{7.19}$$

B. Adjust the dynamic range of C_source so as it matches that of C_target to obtain a normalised source stains C_norm, by calculating the 95 percentile of each row of the C_{source} and C_{target} as $C_{s-extreme}(i)$ and $C_{T-extreme}(i)$ to obtain a scale matrix using Equation 7.20. The dynamic range is estimated with a pseudo maximum (95%) as it is robust.

$$D_{scale(\ i,1)} = \frac{C_{s\text{-}extreme(\ i)}}{C_{T\text{-}extreme(\ i)}} \tag{7.20}$$

where $i = 1, ..., r$ which is the row number in a coefficient matrix C.

C. Obtain the scale row of C_{source} using Equation 7.21.

$$C_{s-scaled(\ i,:)} = C_{target(\ i,:)}\ D_{scale(\ i,1)} \tag{7.21}$$

D. Colour transfer image in optical density space.

$$Y_{transferred} = W_{target}C_{s\text{-}scaled} \tag{7.22}$$

E. Apply a weighting factor to a colour transferred image

$$New_{Y_{transferred}} = T \times Y_{transferred} \tag{7.23}$$

Where $T \geq 1$, T can be adjusted to improve the brightness and contrast of the

normalised image. The default values of T for both H&DAB and H&E stain images is 1.

F. Convert the normalised image from optical density space to RGB colour space

$$I_{normalised} = I_0 exp(\ -New_{Y_{transferred}}) \tag{7.24}$$

where $I_0 = 255$

7.3.2 Blood vessel segmentation

Blood vessels are then extracted from the normalised images following the steps below:

1. Image conversion:- Normalised histology images are then converted from RGB colour space to HSV (hue, saturation and value) colour space to extract brown colour tissue (in this case the vessels).
   $I_{rgb} \longrightarrow I_{hsv}$
   where I_{rgb} is RGB image of dimension $N_r \times N_c \times 3$ with three colour channels (namely red, green and blue) and I_{hsv} is HSV image of dimensions $N_r \times N_c \times 3$ with three colour channels (namely hue, saturation and value). Hue is a circular property related to the wavelength of the colour. Saturation is a measure of purity of the colour or its departure from grey and value is a measure of the brightness.

2. Channel extraction:- saturation channel is extracted from the resulting HSV image since it contains all the brown tissue [74]. One channel is used to minimise computational time and memory usage [74]. To the best of our knowledge, no paper only utilises saturation during the segmentation of the whole vessels. Adams et al., [3], utilised saturation channel during edge detection rather than segmentation of the whole object.

3. Global thresholding:- global thresholding is applied to the saturation channel to obtain a binary image. This helps in eliminating the background and remaining with only image containing vessels. ISODATA thresholding method is utilised. The Iterative Self-Organizing Data Analysis Technique (Isodata) is an iterative technique that was

developed in 1978 by [1]. ISODATA algorithm aims at splitting non-homogeneous regions into two sub-regions (objects and background). According to Gonzalesbarron et al., [89], initially a guess is made at a possible value of a threshold. Then, the mean values of the two categories (objects and background) produced with this threshold are estimated. The threshold is moved to the middle of the distance between the two mean values. The procedure is repeated again and a new threshold is obtained. The process continues until the threshold stops changing its value.

4. A one-stage procedure that includes eliminating small artefacts such as pericytes that may be mistaken for vessels using MATLAB bwareaopen morphological operation. MATLAB bwareaopen morphological operation is used to remove all connected components (objects) that are fewer than 26 pixels from the binary image. MATLAB bwareaopen operation involves three steps that include (i) Determining connected components using Matlab bwconncomp operation. Matlab bwconncomp operation returns connected components (with a connectivity of 8 in the binary image), (ii) Computing the area of each component using Matlab region props operation. (iii) Removing small objects. All connected objects are labelled. ismember operation is used to remove all object with less than 300 pixels.

5. To deal with fragmentation of intact vessels on the images, and artefactual appearance of the vessel structures, Joining is performed using the Matlab dilation operation to join nearby vessel fragments [175, 74]. In segmentation, Matlab dilation operation is used to increases objects in image using the structuring element of a particular size. Matlab dilation operation is complementary operation of the Matlab erosion operation given by:-

$$A \oplus S = (A^C \ominus S)^C \tag{7.26}$$

Where $A \oplus S$ denotes Matlab dilation operation of the image A by structuring element S. A^c is the complement of pixels (i, j) in image A. Matlab dilation operation can also be given by:-

$$A \oplus S = \{z \mid (\hat{S})_z \bigcap A \neq \emptyset \tag{7.28}$$

Where $\hat{S}$ is the reflection of the structuring element S i.e. it is a set of pixel locations z, where reflected structuring element overlap with the foreground pixels in A when translated to z.

6. The artefactual fragments based on measured incoherence with neighbouring tissue are removed using Matlab erosion operation [74]. In segmentation, Matlab erosion operation is used to decreases objects in an image using structuring element of a particular size. Supposing A is the image consisting of pixels (i, j) and S is a structuring element. Then Matlab erosion of A by S is defined as a set of all pixel locations for which S placed at that pixel is contained within A. Matlab erosion can be applied on both binary image and grey-scale image. A Matlab erosion operation of A by S is denoted by $A \ominus S$ and is given by:-

$$A \ominus S = \{(i, j) : S_(i, j) \subset A\} \tag{7.30}$$

Note: The performance of the segmentation is evaluated based on the qualitative results as well as the quantification results. The automated quantification results are compared against the manually obtained quantification results.

7.3.3 Quantification of blood vessel diameter

In measuring blood vessel diameters, it is important to consider that depending on the plane of cut certain biological features can appear different. Blood vessels for instance may be cut along its longitudinal plane thus exposing the length of the vessel. Conversely, blood vessels may be cut in the transverse plane exposing the outer wall and the lumen. To create a better understanding of the data at hand, it is ideal to measure blood vessel diameters as they appear in both planes.

Compared to other researchers, this work obtains measurements of the traverse section and the longitudinal section of the vessels separately to get a better understanding of data. Regarding AD, β-amyloid plaques can accumulate in the vessel walls. Having a tool that can measure the outer and inner luminal walls of transverse cut vessels posits the possibility of quantifying vascular β-amyloid deposits. The diameters of the resulting blood vessels

are quantified following the steps below:-

1. The vessels are then labelled for proper quantification using Matlab bwlabel operation and jet colour map. Objects are labelled with different colours [97]:-
2. Two images (image containing vessel traverse section and an image containing vessel longitudinal section) are obtained from a labelled image. Through the help of Matlab region props operation, the method can distinguish between the traverse section of the vessels and the longitudinal section of the vessels. Vessels whose Euler number less than 1 are considered to be traverse section and vessels whose Euler number is equal to 1 are considered to be longitudinal section [175]. Euler number is calculated as the number of objects in the region minus the number of holes in those objects. MATLAB regionprops operation uses 8connectivity to compute the Euler number.
3. Vessels traverse section and vessel longitudinal section is colour labelled using the Matlab bwlabel operation respectively.
4. Morphometric measurements are used during the vessel quantification stage to detect changes in vessels. The measurements that are used include the ratio of the area of the vessel wall to the area of the blood vessel traverse section and the diameter of both the vessel traverse section and vessel longitudinal section. The diameter and the ratio of the area of the vessel wall to the area of the traverse section of the vessel have been long used in vascular medicine as it indicates the degree of stenosis and the type of vessel wall [159, 194, 11, 27]. The ratio of the area of the vessel wall to the area of the vessel lumen is calculated by following steps below:-

    - Find the area A_l of each vessel using Matlab regionprops operation. The area is the actual number of pixels in the region, returned as a scalar.
    - Fill the lumens of vessels using imfill operation.
    - Use Matlab regionprops operation to find the area A_f of each of the vessels. The area is the actual number of pixels in the region.
    - Find the ratio of the vessel wall to vessel lumen using 7.31:-

$$ratio = A_l \,./\, A_f \tag{7.31}$$

Note: the ratio that tends to 1 corresponds to a vessel with a small lumen and a ratio that tends to 0 corresponds to a vessel with a large lumen and a very thin wall.

The diameter of the vessels is obtained using Equation 7.33 following the steps below:-

- Find the area A_l of each vessel using Matlab regionprops operation. The area is the actual number of pixels in the region, returned as a scalar.
- Find the perimeter P_l of each vessel using Matlab regionprops operation. The perimeter is calculated as the distance around the boundary of the region returned as a scalar. Matlab regionprops operation computes the perimeter by calculating the distance between each adjoining pair of pixels around the border of the region.
- The diameter of each vessel is obtained by finding the ratio of area of each vessel to the perimeter of each vessel using Equation 7.33 [194, 11, 27]:-

$$V_{diameter} = A_l./P_l \tag{7.33}$$

Note: All measurements are performed for both traverse sections of the blood vessels and the longitudinal sections of blood vessels.

7.4 Experimental Evaluation

This section describes the evaluation of the proposed method on public and private image dataset. The image dataset used in this study includes H&DAB image dataset and H&E image dataset.

7.4.1 Evaluation Datasets

Two publicly available H&E datasets and one private H&DAB datasets were employed for the evaluation of the proposed segmentation method. In this section, a brief introduction to these datasets is presented, followed by an introduction to the evaluation metrics used in our experiments.

7.4.1.1 H&DAB image dataset

This dataset contains a total of 40 batches was used during the study. Each batch contained 40000 unique H&DAB cortical images of size 1920 × 1080 pixels. HDAB images were stained on different dates.

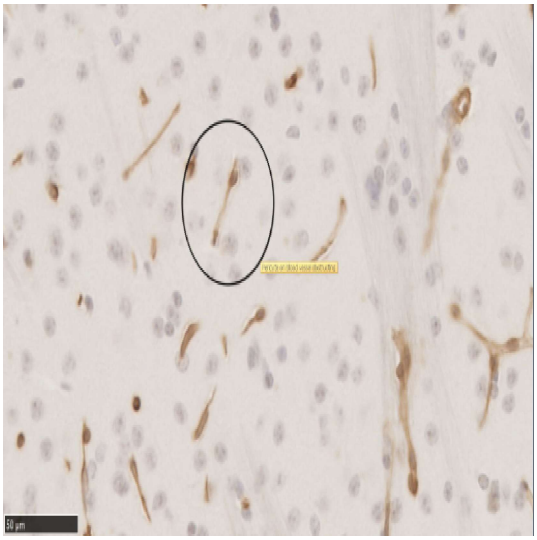

Figure 7.2: illustration of H&DAB image. circled is the blood vessel with pericytes on it

7.4.1.2 H&E image dataset

100 H&E stain images with dimensions of 1539×1376 pixels provided by Dr Abhishek Vahadane. I also used 22 H&E histology images with the dimension of 2000 × 2000 pixels of different datasets (i.e. breast dataset, colon dataset and lung dataset) provided by Alsubaie N et al. [15] under the support information section.H&E images came with ground truth. Please refer to Alsubaie N et al. [15] for more information about the ground truth. H&E images are from different scanners (Hamamatsu scanner and Aperio scanner).

7.4.2 Parameter selection for histology images

- A weighting factor W that lies between 1 and 3 is entered by the user.

7.4.3 Validation and evaluation of image preprocessing

In this thesis results from stain separation stage and the colour transfer stage are evaluated both qualitatively and quantitatively. The accuracy of stain separation is evaluated using the density maps. The density maps represent the amount of stain absorbed at each pixel. A similarity quality metric between the results obtained using the proposed method and the ground truth is used to evaluate the accuracy of the proposed method. Box plots are

used to compare stain separation obtained using the proposed stain normalisation method with that of other methods. Median is used for easy comparison. The quantitative results shown in Figure 7.3, show the superior performance of the proposed method over others. The accuracy of colour transfer is evaluated qualitatively as shown in Figure 7.5(f), Figure 7.6(f). The proposed stain normalisation method produces better results compared to other methods.

7.5 Experiments and Results

The performance results of the proposed stain normalisation method are compared with related methods. The performance of the vessel diameter quantification of the proposed method on H&DAB images is compared to the results of the clinical researcher expert.

7.5.1 Image pre-processing experimental results of the morphological method on H&DAB images

Table 7.1 show the performance comparision results interms of the average similarity index. The proposed method outperforms Alsubaie et al,. [15] by 4-13% for H for breast dataset, colon dataset, and the lung dataset. However Alsubaie's method [15] outperforms our method for E in only breast datasets. The proposed method still out performs Alsubaie's method [15] by 3-7% for E in colon and lung dataset. In comparison to Macenko's method [145], the proposed method outperforms Macenko's method [145] by 2-4% and 4-5% for H&E in all three datasets (breast and colon dataset).

The colour transfer stage is the final stage of stain normalisation process. The qualitative results of color transfer stage show that the proposed method can be applied on both H&E stain images and H&DAB images(Figure 7.5 and Figure 7.6). Khan's NMF method [125] and Macenko's SVD method [145] produces unrealistic stains when applied on H&DAB images. Khan's NMF method [125] and Macenko's SVD method [145] also introduces artefacts when applied on H&DAB images. Reinhards method produces slightly better results when applied on H&DAB but still not better than the proposed method. Compared to all methods, our method produces satisfactory results when applied on both H&DAB and H&E images. With the introduction of weighting factor in the colour transfer stage, the

contrast and brightness of the image tissue can be adjustment using the proposed method. The higher the weighting factor the brighter the image tissue (Figure 7.4). Note: The weighting factor is determined by trial and error but the default value usually provides a good starting point and users have not found this difficult.

Method	Breast Dataset		Lung Dataset		Colon Dataset		Median	
	H	E	H	E	H	E	H	E
Alsubaie N et al., [15]	0.697	0.879	0.722	0.797	0.714	0.758	0.705	0.811
Macenko et al., [145]	0.803	0.830	0.719	0.847	0.759	0.787	0.759	0.814
Proposed Method	0.827	0.878	0.764	0.825	0.763	0.829	0.770	0.838

Table 7.1: SSIM Index between the stain matrices and the ground truth. The last two columns show the median of SSIM index for all methods.

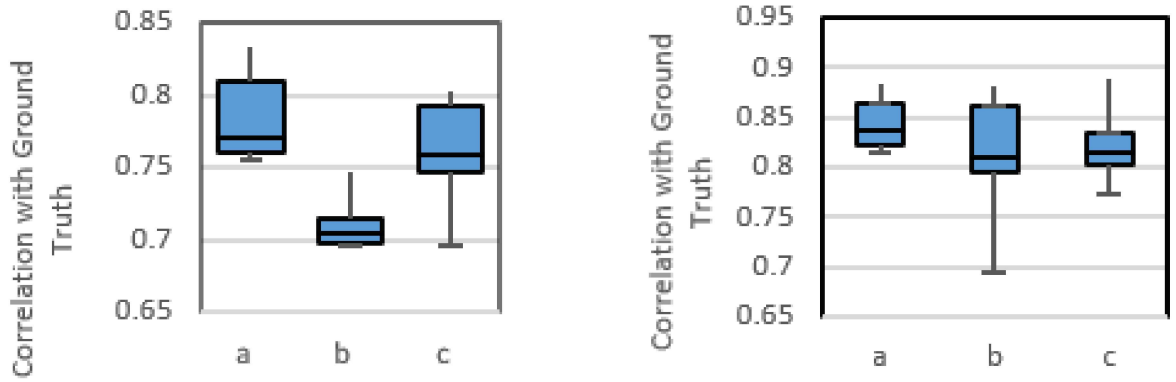

Figure 7.3: Correlation between the density maps and the ground truth with associated SSIM Index for each method with respect to H(Left) and E (right) stains in all three datasets (a) proposed method, (b) Alsubaie N et al. [15] and (c) Macenko et al. [145]

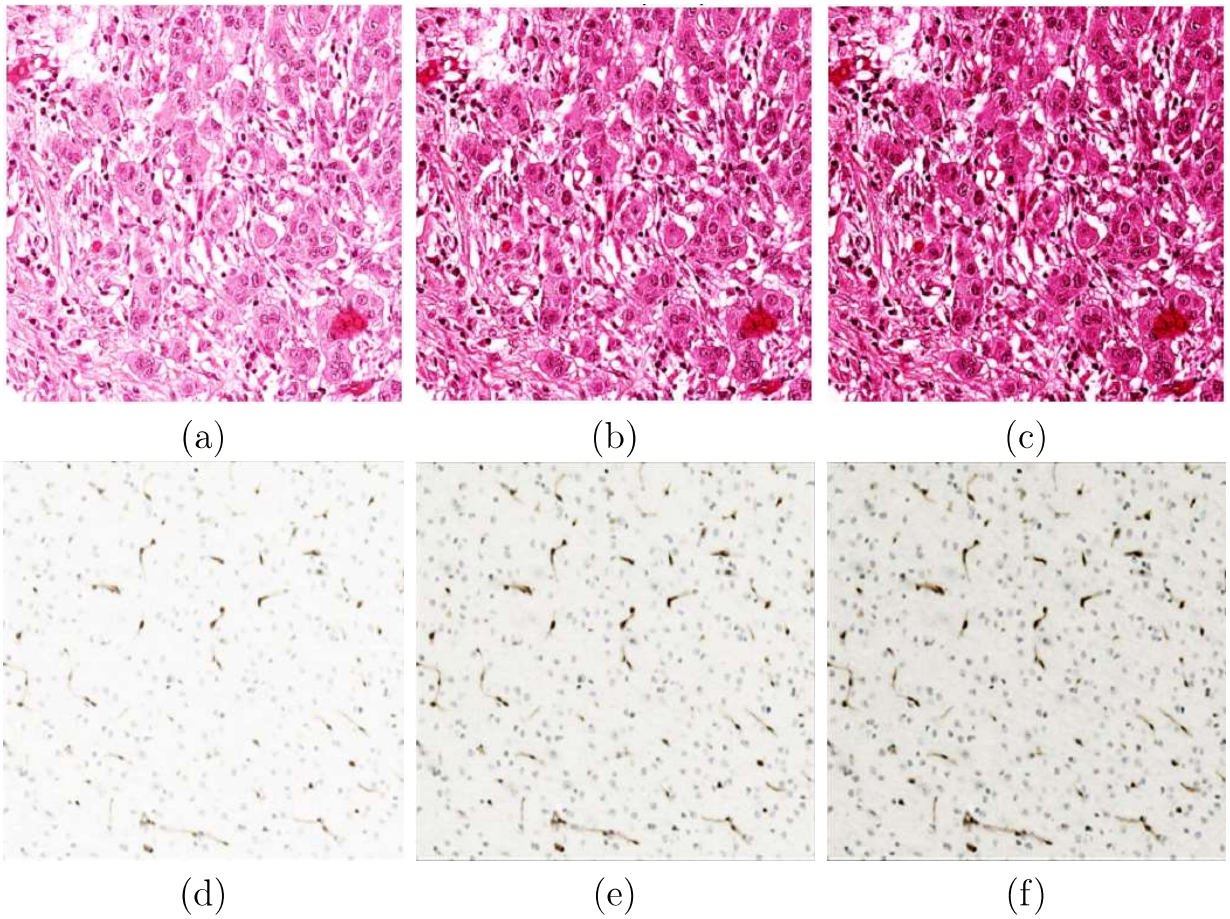

Figure 7.4: H&E and H&DAB normalised histology images at different weighting factors. First row are H&E stain images normalised at weighting factor 1, 2 and 3 respectively, and second row are H&DAB stain images normalised at weighting factors 1, 2, 3 respectively

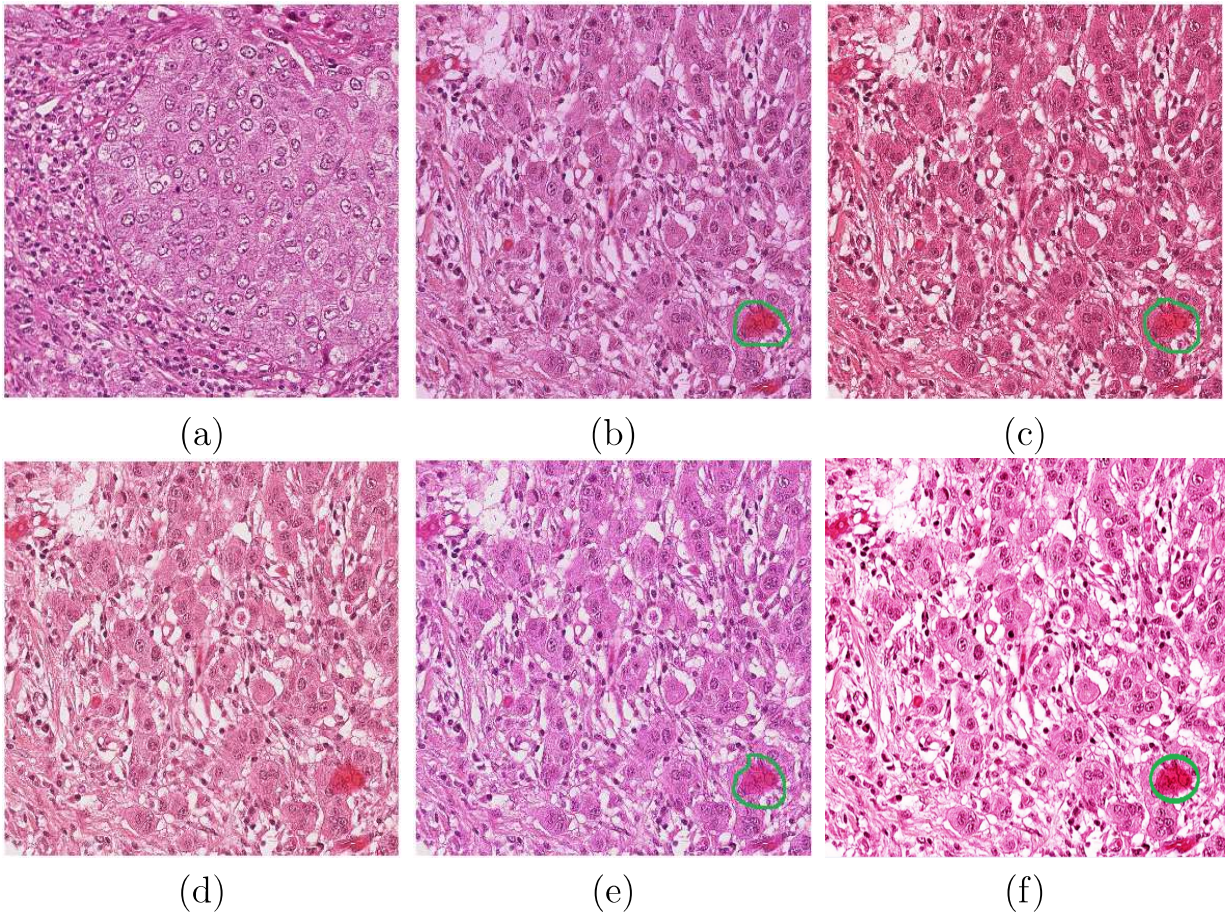

Figure 7.5: Comparison of different stain normalisation methods on H&E stain images.(a) target image,(d) source image, (b) Reinhard et al., [174],(c) Khan et al., [125], (e) Macenko et al., [145], (f) Proposed Method

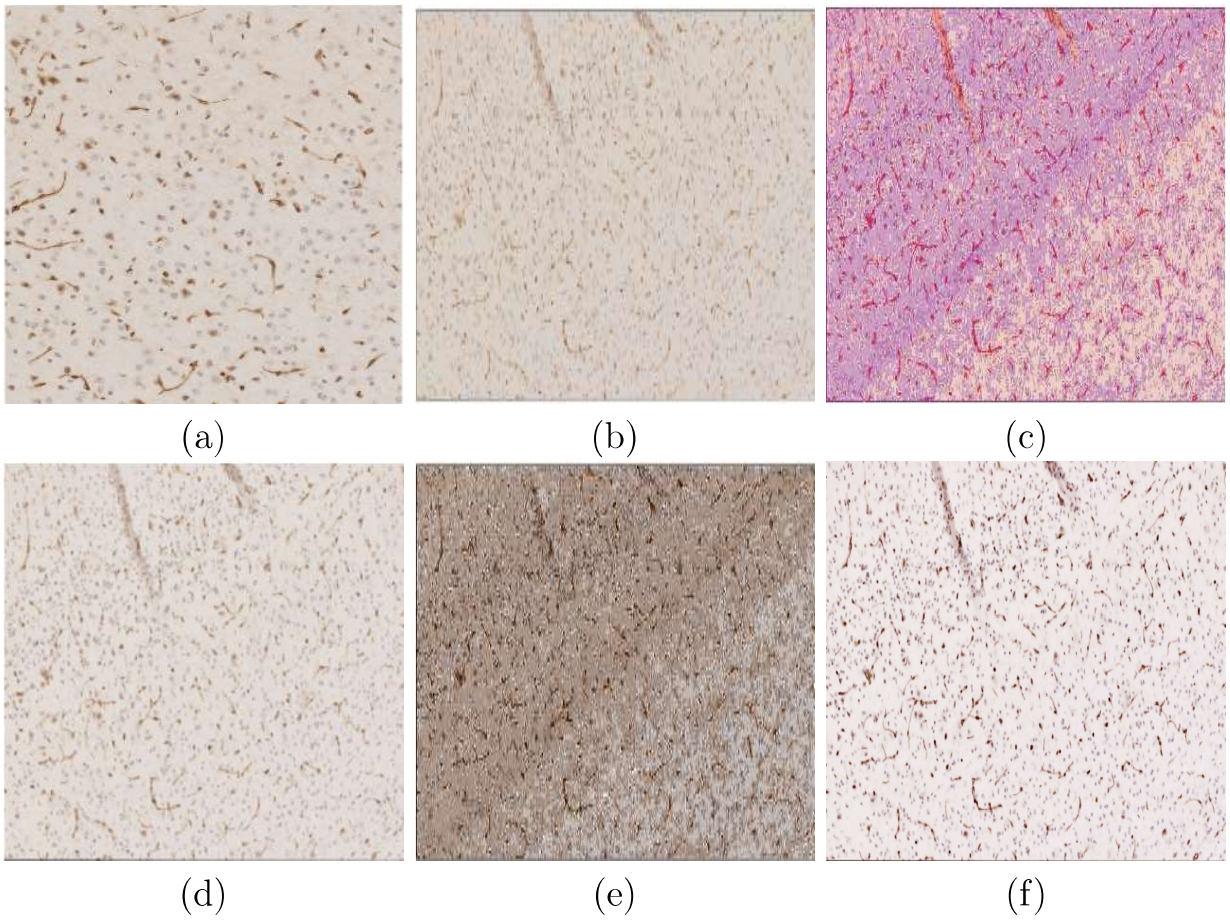

Figure 7.6: Comparison of different stain normalisation methods on H&DAB stain images.(a) target image, (d) source image, (b) Reinhard et al., [174],(c) Khan et al., [125], (e) Macenko et al., [145], (f) Proposed Method

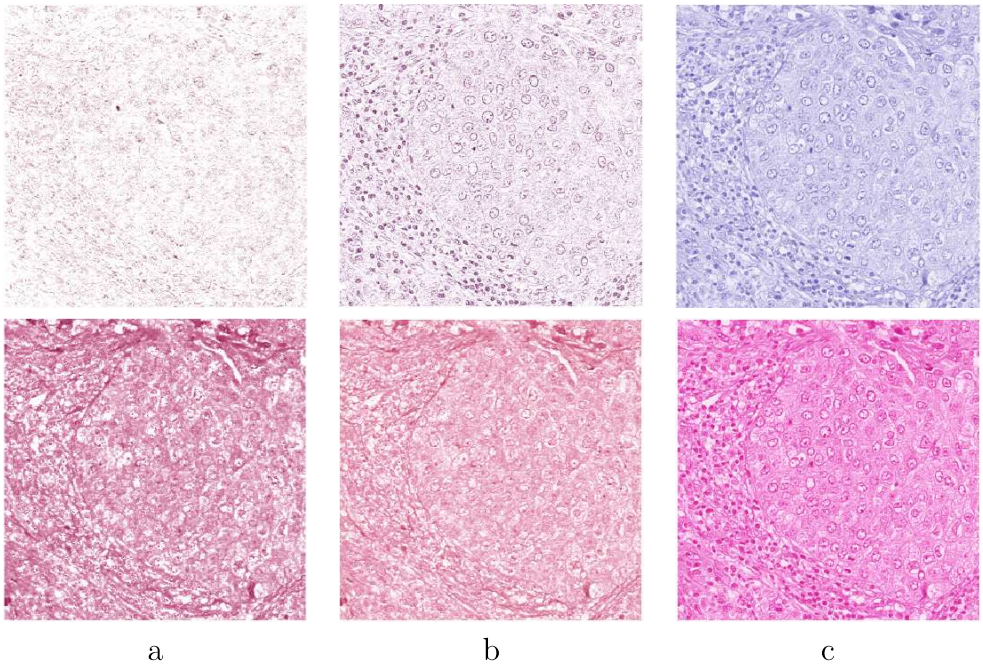

Figure 7.7: Stain separation after application of SVD, statistical blind source separation ICA and proposed method on H&E images. (a) statistical blind source separation ICA H&E images. (b) SVD H&E stains. (c) Proposed method

7.5.2 Blood vessel segmentation experimental results of the morphological method on H&DAB images

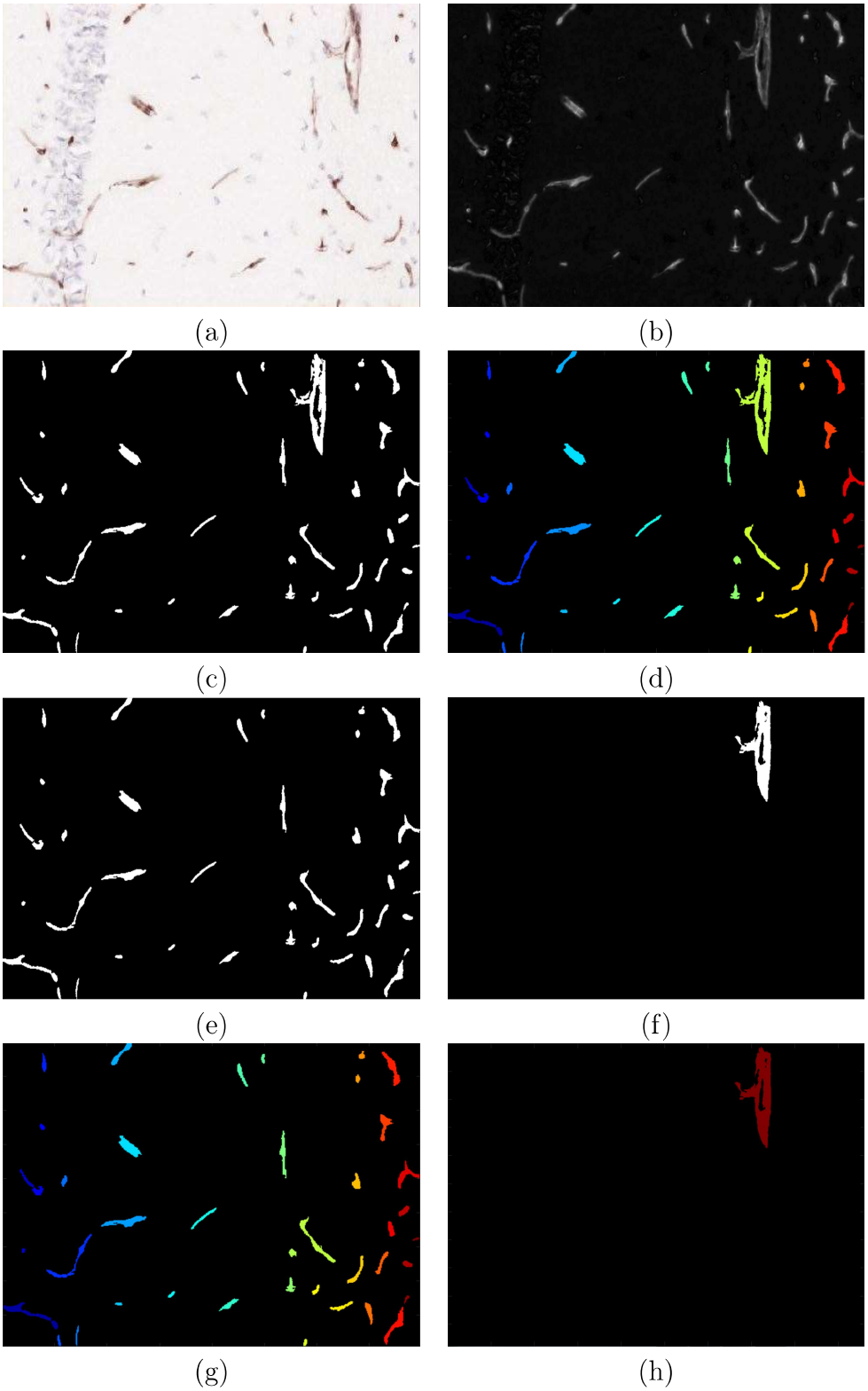

Figure 7.8: Results from each vessel segmentation step. (a) Original image; (b) Saturation channel extracted from HSV image colour space; (c) Binary vessel image; (d) Colour labelled vessel image; (e) Binary image containing vessel longitudinal sections; (f) Binary image containing vessel traverse sections; (g) Colour labelled vessel longitudinal section; (h) Colour labelled vessel traverse section

By using saturation, the ISODATA method, MATLAB dilation operation, the method can extract vessels in H&DAB stained histology images, and minimise computation time and use less memory during both segmentation and quantification. The method produces results in 120 seconds on a 250GB CPU.

7.5.3 Blood vessel diameter quantification results of the morphological method on the H&DAB stained images

The average blood vessel diameter obtained along the longitudinal (L) and traverse (T) sections of the blood vessels using the automated method are compared with the average blood vessel diameter obtained along the longitudinal and traverse section of the blood vessels, using the manual method by the human expert.

The human expert results [154] is considered as the target with an average diameter of $2.52\mu m$ and $3.23\mu m$ along the vessel longitudinal section and the vessel traverse section respectively for mice infected with wild type disease, average diameter of $2.55\mu m$ and $3.23\mu m$ along vessel longitudinal section and the vessel traverse section respectively for mice infected with Alzheimer disease, average diameter of $2.55\mu m$ and $3.45\mu m$ along the vessel longitudinal section and the vessel traverse section respectively for male mice, average diameter of $2.48\mu m$ and $2.97\mu m$ along the vessel longitudinal section and the vessel traverse section respectively for female mice, average diameter of $2.65\mu m$ and $3.23\mu m$ along the vessel longitudinal section and the vessel traverse section respectively after treatment A, average diameter of $2.56\mu m$ and $3.24\mu m$ along the vessel longitudinal section and the vessel traverse section respectively after treatment B, and average diameter of $2.38\mu m$ and $3.24\mu m$ along the vessel longitudinal section and the vessel traverse section respectively after treatment C. Table 7.2 shows the performance of the proposed method against the aforementioned human expert results on the H&DAB dataset. The proposed method achieves a similar average diameter of $2.97\mu m$ along the vessel traverse section for female mice. However, it needs an overall improvement of the average diameter of $0.28\mu m$ and $0.27\mu m$ along the vessel longitudinal section and the vessel traverse section respectively for mice infected with wild type disease, the average diameter of $0.51\mu m$ and $0.69\mu m$ along the vessel longitudinal section and the vessel traverse section respectively for mice infected with Alzheimer dis-

eased mice, the average diameter of $0.4\mu m$ and $0.76\mu m$ along the vessel longitudinal section and the vessel traverse section respectively for male mice, the average diameter of $0.43\mu m$ along the longitudinal section for female mice, the average diameter of $0.5\mu m$ and $0.5\mu m$ vessel longitudinal section and the vessel traverse section respectively after treatment A, the average diameter of $0.58\mu m$, $0.37\mu m$ along vessel longitudinal section and the vessel traverse section respectively after treatment B, and average diameter of $0.13\mu m$ and $0.39\mu m$ along vessel longitudinal section and the vessel traverse section respectively after treatment C. The reason why the morphological tool does not achieve similar results to the manual may be due to human error. It is widely known that manually obtained results are prone to errors. [155, 32].

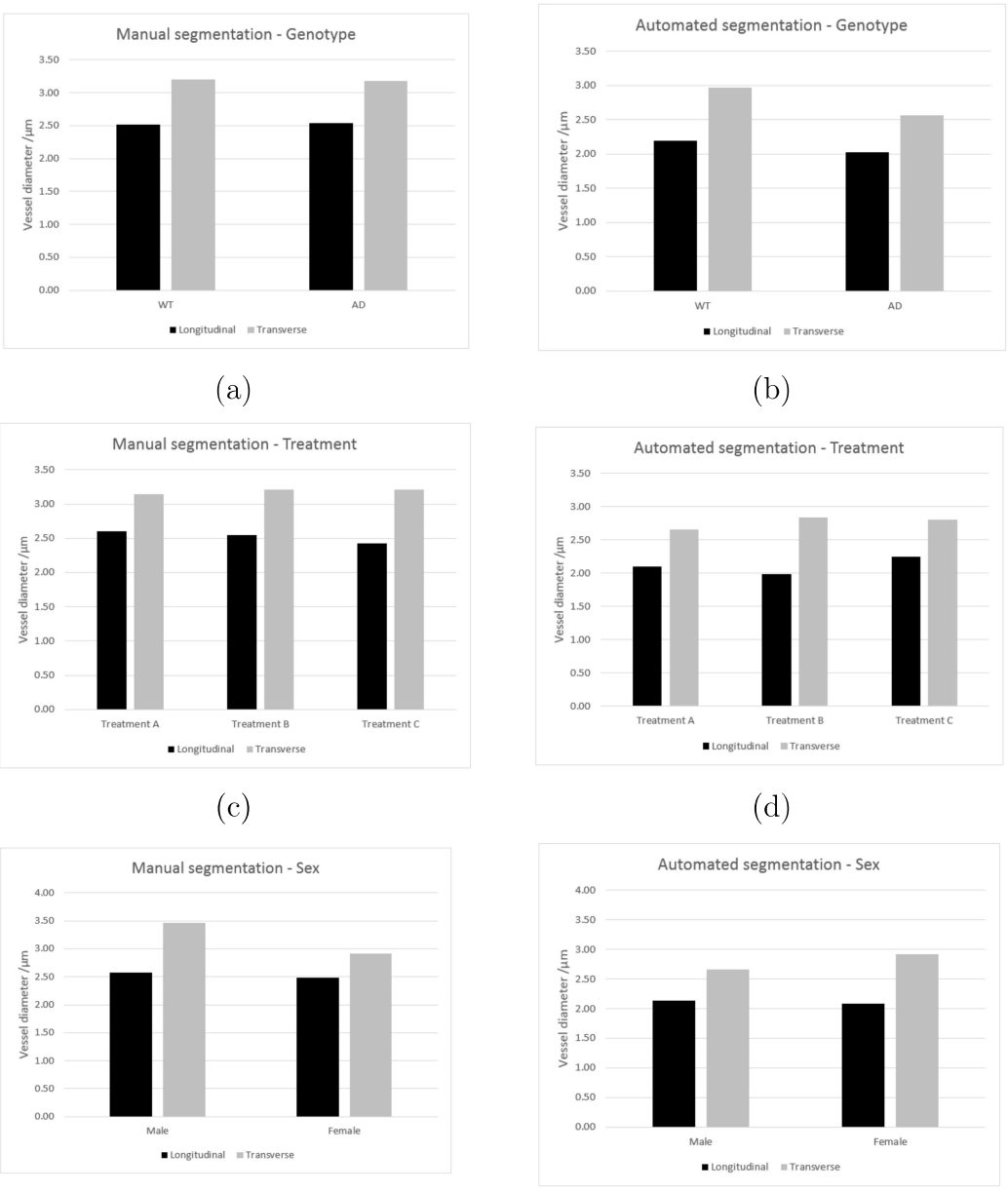

Figure 7.9: Comparison of vessel diameter quantification results using the manual quantification method and the proposed quantification method. (a) & (b) Vessel quantification results of Alzheimer's disease (AD) and wild type (WT) obtained using the manual quantification method and proposed method respectively; (c) & (d) Vessel quantification results of the three treatment groups obtained using the manual quantification method and the proposed method respectively; (e) & (f) Vessel quantification results of male and female mice obtained using the manual quantification method and the proposed method respectively.

Method type	Manual results													
Variables	Genotype				Gender				Treatment					
	WT		AD		M		F		A		B		C	
	L	T	L	T	L	T	L	T	L	T	L	T	L	T
Blood vessel diameter/μm	2.52	3.23	2.55	3.23	2.55	3.45	2.48	2.97	2.65	3.23	2.56	3.24	2.38	3.24
Method type	Automated results													
Variables	Genotype				Gender				Treatment					
	WT		AD		M		F		A		B		C	
	L	T	L	T	L	T	L	T	L	T	L	T	L	T
Blood vessel diameter/μm	2.24	2.96	2.04	2.54	2.15	2.69	2.05	2.97	2.15	2.73	1.98	2.87	2.25	2.85

Table 7.2: A comparison of average diameter values along the blood vessel longitudinal section and blood vessel traverse section between mice groups according to genotype, and gender, and treatment

7.6 Chapter Discussion and Conclusion

A morphological method for the blood vessel extraction and blood vessel quantification in H&DAB stained histology image slides is presented. The morphological method involves three steps including stain normalisation for the image enhancement stage, classification of pixels into blood vessel pixels and non-blood vessel pixels for segmentation and blood vessel diameter quantification for blood vessel quantification. The morphological method normalises histology images using the hybrid stain normalisation method in [20], segments the blood vessels using saturation channel, ISODATA thresholding, MATLAB bwareaopen operation, Matlab erosion and Matlab dilation operation, and quantifies the blood vessel diameter using the morphometric approach. The stain normalisation used image enhancement normalises the stain and enhances the brightness and contrast of the image. By using saturation, the ISODATA method, MATLAB dilation operation, the method can extract vessels in H&DAB stained histology images, and minimise computation time and use less memory during both segmentation and quantification. The method produces results in 120 seconds on a 250GB CPU. In the acquired images, as with any immunohistochemistry study, other biological features with similar characteristics may be mistaken for blood vessels. Figure 7.2 demonstrates the presence of many blood vessels but nestled amongst them are darker circular bulges known as pericytes. For accurate vascular measures to be taken, these pericytes must not be included in the extraction. Pericytes (in the background), along with other artefacts (such as specs), were eliminated by using MATLAB bwareaopen

operation and Matlab erosion operation during segmentation. In measuring blood vessel diameters, it is important to consider that depending on the plane of cut certain biological features can appear different. Blood vessels for instance may be cut along its longitudinal plane thus exposing the length of the vessel. Conversely, blood vessels may be cut in the transverse plane exposing the outer wall and the lumen. To create a better understanding of the data at hand, it is ideal to measure blood vessel diameters as they appear in both planes. Compared to other researchers, this work measures the diameter along the longitudinal and traverse of the blood vessel.

For blood vessel segmentation, Figure 7.8, show that the proposed method can segment blood vessels. More blood vessels are detected. Even though the visual comparison is considered purely subjective, it can still emphasise the positive and negative points of various segmentation approaches.

Note: since the accuracy of the segmentation determines the accuracy of the classification stage. This work evaluates the proposed segmentation method basing the blood vessel diameter quantification results. The results obtained using the morphological tool is compared against the results manually by the human expert results on the private H&DAB dataset. Table 7.2 shows the performance of the proposed method against the aforementioned human expert results on the H&DAB dataset. The proposed method achieves a similar average diameter (T=2.97μm) for female mice. However, it needs an overall improvement of average diameter along (L=0.28μm, T=0.27μm) for mice infected with wild type disease, average diameter along (L=0.51μm, T=0.69μm) for mice infected with Alzheimer disease, average diameter along (L=0.4μm, T=0.76μm) for male mice. Average diameter along (L=0.43μm) for female mice. average diameter along (L=0.5μm, T=0.5μm) after treatment A, average diameter along (L=0.58μm, T=0.37μm) after treatment B, and average diameter along (L=0.13, T=0.39) after treatment C. The reason why the morphological method does not achieve similar results may also be due to the pericytes nestled around the blood vessels. Pericytes on the blood vessels obstruct the quantification process.

Further work is needed to determine whether this segmentation and quantification method would work on images of whole mice brains without compromising computational speed and memory usage. In addition, when developing and designing the tools such as morphological

tool, it is essential to have some form of reference or expected performance target. The morphological tool has not been evaluated as there is no gold standard from the medical imaging literature on what should be an acceptable error measure. Validation of proposed manual tools typically involves inter-rater reliability (IRR) and concurrent validity tests. Furthermore, although the clinical researchers were involved from the beginning to the end of the development of the morphological tool, No proper investigation on the perception of clinical researchers on the use of an automatic morphological tool in Alzheimer disease research and cancer research was carried to explore the impact of using automated morphological tools in clinical research. Tools such as questionnaires could be used during the investigation.

Chapter 8

Conclusion and Future work

This chapter summarises the studies of the preceding chapters, highlights the thesis contribution, discusses the limitation of the proposed methods and outlines potential future work.

8.1 Summary of Thesis Achievements

This thesis has studied the application of automated techniques to the task of segmenting blood vessels of various sizes from both 2D and 3D medical images. To facilitate segmentation, two vessel enhancement filters were proposed. Novel methods for segmenting blood vessels of various sizes from 3D and 2D medical images have been proposed. Lastly, to facilitate research in histopathology, a morphological tool for stain normalisation and segmentation of blood vessels was developed. The achievements and the conclusions drawn from the associated studies will be presented in subsequent sections.

8.1.1 Developing a new blood vessel enhancement filter

Automatic blood vessel segmentation is currently limited by image artefacts (such as low contrast variation between blood vessel pixels and background, and noise) in the medical images. This study has introduced a new vessel enhancement filter that can correct illumination, enhance contrast and address noise of the image while maintaining strong sharp edged blood vessels to facilitate the segmentation of blood vessels in a wide range of medical images. Specifically, the capabilities of the White top-hat Morphological Transform and Bilateral Convolution have been integrated into the Frangi vessel enhancement filter to boost

the efficiency of the Frangi vessel enhancement filter by designing a new filter known as White top-hat scale-space Bilateral Hessian based Vessel Enhancement Filter (WBHVEF). Analysis of the WBHVEF filter on both the STARE dataset and DRIVE dataset indicate that indeed, the filter significantly boosts the efficiency of Frangi vessel enhancement filter. The WBHVEF filter is capable of enhancing blood vessels in retina images under all conditions. More vessels of strong edges are detected and tiny vessels rendered absent are detected. The results also reveal that WBHVEF filter gets rid of the unwanted tissue such as the optical disc. To demonstrate its potential for improving blood vessel segmentation, the WBHVEF filter has been utilised during the image enhancement stage of the 3D hybrid blood vessel segmentation method and 2D hybrid blood vessel segmentation method proposed in this thesis.

8.1.2 Developing a novel 3D hybrid blood vessel segmentation framework

A 3D hybrid blood vessel segmentation framework was developed for segmentation of blood vessels various sizes and evaluated on both 3D privately and publicly available medical image dataset using the 3D ground-truth data. The developed 3D hybrid blood vessel segmentation framework is able to simultaneously merge both outputs from two individual 3D medical images into a coherent segmentation result and, can post process the resulting blood vasculature to improve the quality of the resulting image. This is in contrast with the existing methods that obtain segmentation results using one image. In addition, by exploiting the capabilities of WHVEF and WBHVEF filter during the image enhancement stage, it has demonstrated that these filters have the potential for improving the performance of 3D hybrid blood vessel segmentation framework. Existing methods such as Multi-threshold Otsu, hysteresis thresholding and ISODATA thresholding are exploited during segmentation to classify the image voxels in to blood vessels and non-blood vessels. MATLAB bwareaopen operation is utilised during post processing to remove the unwanted objects (such as noise) from the resulting vasculature. Three 3D methods that adopt the same framework are developed and evaluated for comparison and validation purposes. In other words, the 3D hybrid method of WBHVEF filter combined with Hysteresis Thresh-

olding, Hysteresis Thresholding, Image Addition and Matlab Bwareaopen Operation, is quantitatively evaluated and compared to the existing blood vessel segmentation methods, including the method proposed by by Bhattacharya et al., [30], method proposed by Ding et al., [68] and a method proposed by Frangi et al., [77]. Evaluation of the method on private medical image dataset (including femoral dataset, CT pelvic arteriogram image dataset, heart dataset, mice brain dataset) from Queen medical Centre Nottingham.

The performance comparative results of the proposed method with the recent alternative methods shows the superiority of the proposed method over the existing ones in-terms of accuracy, specification, sensitivity, DICE and JAC on the carotid dataset. The proposed method outperforms the method proposed by Bhattacharya et al., [30], method proposed by Ding et al., [68] and a method proposed by Frangi et al., [77] with an average (sensitivity = 91.06%, specificity = 99.49%, accuracy = 99.41%, DICE = 74.53%, JAC = 59.40%).

Likewise, the comparison results of the proposed method with recent alternative methods demonstrate that the proposed method outperforms the existing methods in-terms of accuracy, sensitivity, DICE, and JAC on the femoral artery veins dataset. However, with the average specificity, the proposed method only outperforms Ding et al., [68] and is marginally inferior to the methods presented by Bhattacharya et al., [30] and Frangi et al., [77]. This may be due to the small ground-truth dataset used during evaluation. An overview of the experimental results on femoral dataset shows that the proposed method offers a reliable and robust segmentation solution for blood vessels. It is clearly observed that the proposed method reaches better performance in terms of the average sensitivity and accuracy.

The results of the proposed method are compared with those of the recent alternative methods in terms of sensitivity, specificity, accuracy, DICE, and JAC on the CT pelvic arteriogram image dataset. The proposed method achieves the highest average accuracy, specificity,DICE and JAC of 99.70%, 99.76%, 78.93%, and 65.20% respectively. However, considering the performance in terms of a sensitivity, the method proposed by Frangi et al., [77] reaches the highest average sensitivity value of 99.59% and performs better than all the other methods. This may be due to the small ground-truth dataset used during evaluation. As it can be seen in the visual comparison, the proposed method can segment blood vessels of various sizes including small vessels. Although the visual comparison is

considered purely subjective, it can still emphasise the positive and negative points of various segmentation approaches in support of quantitative results. Besides detecting the blood vessels of different sizes, the proposed method is capable of detecting abnormalities (such as blood vessel tortuosity, and blood vessel stenosis) in the blood vessels and therefore it can be used during early diagnosis. The method can be used to detect on both human and pets. This can be seen in the results achieved by this method on both the all datasets.

8.1.3 2D hybrid blood vessel segmentation method

A 2D hybrid blood vessel segmentation method was proposed for extraction of blood vessels of various sizes and evaluated on both 2D DRIVE dataset and STARE dataset using the publicly available ground truth data. To the best of the researcher's knowledge, this is the only segmentation method that employs White top-hat scale space Bilateral Hessian based Vessel Enhancement Filter during image enhancement. This is in contrast with other methods that apply other filters during the image enhancement stage. The 2D hybrid blood vessel segmentation method exploits a White top-hat scale space Bilateral Hessian based Vessel Enhancement Filter, hysteresis thresholding and Matlab bwareaopen operation during image enhancement, blood vessel segmentation and post processing respectively.

The performance comparison results of the proposed method with recent alternative methods in terms of sensitivity, specificity, and accuracy on the DRIVE dataset. **Note** that only the performance from previous studies who have reported their blood vessel segmentation results on STARE dataset and DRIVE dataset are included in the table for a fair comparison. Table 6.1 shows the performance of the proposed method against the aforementioned methods on the DRIVE dataset. The proposed method needs an overall improvement of 2.7% in-terms of sensitivity. On the other hand, with an average sensitivity of 74.9% and average accuracy of 95.4%, the proposed method achieves better performance than all the other methods with respect to the average sensitivity value and accuracy value. The average specificity achieved with the proposed method on a DRIVE dataset, outperforms Bankhead et al., [22], Dai et al. [60], Bahadarkhan et al., [21], Martinez et al., [151], Soomro et al., [193], Akhavan et al., [8], Chatraborti et al., [47], Zhang et al., [248], and Nugroho et al., [163]. But it is marginally inferior to the methods proposed by Zafer et al.[243], and Zhao et al.[252]. An overview of the testing results on DRIVE shows that the proposed method

offers a reliable and robust segmentation solution for blood vessels. It is clearly observed that the proposed method reaches better performance in terms of the average sensitivity and accuracy.

The performance comparison results of the proposed method with recent alternative methods in terms of sensitivity, specificity, and accuracy on the STARE dataset. In Table 6.4, the second human expert hand-labelled image is considered as the target performance level with average (sensitivity = 89.5%, specificity = 93.8% and accuracy = 93.4%), given the first human expert hand-labelled image as benchmark. Thus, the proposed method needs an overall improvement of 10.3% in average sensitivity. whereas Chatraborti et al., [47], Nugroho et al., [163], Dai et al. [60], Bankhead et al. [22], Azzopardi et al., [19], Asad and Hassaanien [16], Zhang et al., [248], Bahadarkhan et al., [21], Memari et al., [153], Martinez et al., [151] have a room of improvement of 21.6%, 14%, 11.8%, 13.7%, 12.3%, 14.7%, 17.8%, 13.7%, 11.3%, and 14.5% respectively. Considering the value of average sensitivity and the value of the average accuracy as performance measures, the proposed method reaches better performance than all the other methods. However, with the average specificity, the proposed method is only marginally inferior to the method presented by Azzopardi et al., [19]. and it has the same value of specificity as Memari et al., [153]. Compared to the results of the second expert hand labeled and methods proposed by Chatraborti et al., [47], Nugroho et al., [163], Dai et al. [60], Bankhead et al. [22], Asad and Hassaanien [16], Zhang et al., [248], Bahadarkhan et al., [21], Memari et al., [153], and Martinez et al., [151], the proposed method outperforms the average accuracy of these techniques. An overview of the testing results on STARE dataset shows that the proposed method offers a reliable and robust segmentation solution for blood vessels. It is clearly observed that the proposed method reaches better performance in terms of the average sensitivity and accuracy.

Figures 6.3, 6.4, 6.5 and 6.6 show a visual comparison between the segmentation performance of the proposed method and other state-of-the-art methods for a sample image from the STARE and DRIVE datasets, respectively. As it can be seen, the proposed method can segment blood vessels of various sizes including small vessels irrespective of the image condition. Although the visual comparison is considered purely subjective, it can still emphasise the positive and negative points of various segmentation approaches in support of

quantitative results.

8.1.4 Development of a morphological tool to segment blood vessels from histology images

The morphological tool was proposed for extraction and quantification of blood vessels in histology images. The morphological method involves three steps including stain normalisation for the image enhancement, classification of pixels into blood vessel pixels and non-blood vessel pixels for segmentation and blood vessel diameter quantification for blood vessel quantification.

For stain normalisation, Haemotoxylin and Diaminobenzidine (H&DAB) images are normalised following two steps including the stain separation stage and colour transfer stage. Octree colour quantisation algorithm combined with Beer-Lambert law and a modified blind source separation algorithm are exploited during the stain separation stage to computationally estimate the amount of stain in the histology images based on the chromatic and luminous response. A modified colour transfer algorithm is exploited during the colour transfer stage to minimise the effect of varying stain and illumination. The method can address the stain variation problem without distorting image tissue while maintaining brightness in the H&DAB images. To the best of my knowledge, this is the first work to demonstrate that Beer-Lambert law applies to histology images with stains (such as Diaminobenzidine (DAB)) that are non-absorbers of light. In addition, compared to the original blind source separation method, the blind source separation method used in this work makes use of the Spatial-Spectral Schrodinger Eigenvectors and Eigenvalues rather than the ordinary Eigenvalues and Eigenvectors to incorporate texture and spatial information. To demonstrate its potential in improving the blood vessel segmentation and quantification, the normalised images are used during segmentation and quantification.

For blood vessel segmentation, image pixels in the normalised image are grouped in to blood vessels and non-blood vessels using a saturation channel, ISODATA threshold method, MATLAB bwareaopen operation, MATLAB dilation operation. The proposed method can segment blood vessels. More blood vessels are detected. Even though the visual comparison is considered purely subjective, it can still emphasise the positive and negative points of

various segmentation approaches. To the best of my knowledge, this method uses only saturation channel during the segmentation of the whole blood vessel.

For blood vessel quantification, blood vessel diameter of the blood vessel traverse section and the blood vessel longitudinal sections are quantified separately to create a better understanding of the image data, following MATLAB region props operation steps. To the best of my knowledge, this is the first work to obtain diameter of traverse section and longitudinal section of the blood vessels separately.

Note: since the accuracy of the segmentation determines the accuracy of the classification stage. This work evaluates the proposed segmentation method basing the blood vessel diameter quantification results. The results obtained using the morphological tool is compared against the results manually obtained by the human expert results on the private H&DAB dataset. Table 7.2 shows the performance of the proposed method against the aforementioned human expert results on the H&DAB dataset. The proposed method achieves a similar average diameter of $2.97\mu m$ along the vessel traverse section for female mice. However, it needs an overall improvement of the average diameter of $0.28\mu m$ and $0.27\mu m$ along the vessel longitudinal section and the vessel traverse section respectively for mice infected with wild type disease, the average diameter of $0.51\mu m$ and $0.69\mu m$ along the vessel longitudinal section and the vessel traverse section respectively for mice infected with Alzheimer disease, the average diameter of $0.4\mu m$ and $0.76\mu m$ along the vessel longitudinal section and the vessel traverse section respectively for male mice, the average diameter of $0.43\mu m$ along the longitudinal section for female mice, the average diameter of $0.5\mu m$ and $0.5\mu m$ vessel longitudinal section and the vessel traverse section respectively after treatment A, the average diameter of $0.58\mu m$, $0.37\mu m$ along vessel longitudinal section and the vessel traverse section respectively after treatment B, and the average diameter of $0.13\mu m$ and $0.39\mu m$ along vessel longitudinal section and the vessel traverse section respectively after treatment C. The reason why the morphological method does not achieve similar results may also be due to the pericytes nestled around the blood vessels. Pericytes on the blood vessels obstruct the quantification process. Although, the proposed method can get rid of pericytes in the background, it fails to get remove pericytes on the blood vessels. For accurate vascular measurements, pericytes nestled around must not be included.

When developing and designing the tools such as the morphological tool, it is essential to involve users from the beginning to the end of the development to ensure the goal is met. Users were involved during development of the morphological tool and the resulting system is currently in use. However, the morphological tool was not evaluated as there is no gold standard from the medical imaging literature on what should be an acceptable error measure.

The morphological tool proposed in this thesis, is easy to use (Appendix A) and more valuable to clinician doing research in cancer and vascular diseases. The morphological tool can effectively normalise the stain and intensity in the stained medical image, segment blood vessels and quantify the blood vessel diameter.

8.2 Limitation and Future Work

Although this thesis has made a number of improvements to the state of the art in automatic blood vessel segmentation, there are still a number of areas in which the methods proposed could be improved

In chapter 4, it was noted that the White top-hat scale space Bilateral Hessian based Vessel Enhancement Filter (WBHVEF) is capable of enhancing the image and the blood vessels even in the presence of intensity inhomogeneity and noise. However, The methods was not evaluated quantitatively. Methods such as Pearson's correlation, Spearman rank correlation, and the root mean square error (RMSE) can be used to evaluate the performance of method in-terms of enhancing the image and blood vessel contrast. Methods such as Normalised root mean squared error and a signal-to-noise ratio, can be used to compare and rank the vessel enhancements filters.

In chapter 5, it is noted that a 3D hybrid method of White top-hat scale space Bilateral Hessian based Vessel Enhancement Filter combined with Hysteresis Thresholding, Hysteresis Thresholding, Image Addition and Matlab Bwareaopen Operation can segment blood vessels of various sizes from both MRI and CT scan images, however, a small ground-truth dataset was used to evaluate the method.

In chapter 7, the morphological tool developed in this thesis was not evaluated as there is no gold standard from the medical imaging literature on what should be an acceptable

error measure. Validation of proposed manual tools typically involves inter-rater reliability (IRR) and concurrent validity tests. Acceptable IRR performance is based on the definitions for the specific metric used. Metrics such as Pearson correlation coefficient could be used for this purpose. Furthermore, although the clinical researchers were involved from the beginning to the end of the development of the morphological tool, no proper investigation on the perception of clinical researchers on the use of an automatic morphological tool in a Alzheimer disease research and cancer research, was carried to explore the impact of using automated morphological tools in a clinical research. Tools such as questionnaire could be used during the investigation.

Appendix A

User manual for a morphological tool for blood vessel segmentation

A.1 Overview

The following MATLAB scripts and modules were developed using MATLAB 2016a on a Lenovo (Intel Core i7 CPU running at 3.60 GHz coupled with 16 GB RAM, 1TB hard disk. The MATLAB SCRIPT and functions for the White Top-Hat scale-space Hessian Based Vessel Enhancement Filter, White Top-Hat scale-space Bilateral Hessian based Vessel Enhancement Filter 2D blood vessel segmentation framework, 2D blood vessel segmentation framework and 2D blood vessel segmentation framework are provided on the repository.

A.2 User manual for a morphological tool for blood vessel segmentation

- Login to the application using the given username and password and Open the morphological tool GUI (Matlab code) file. This will launch a screen interface as shown in Figure A.1

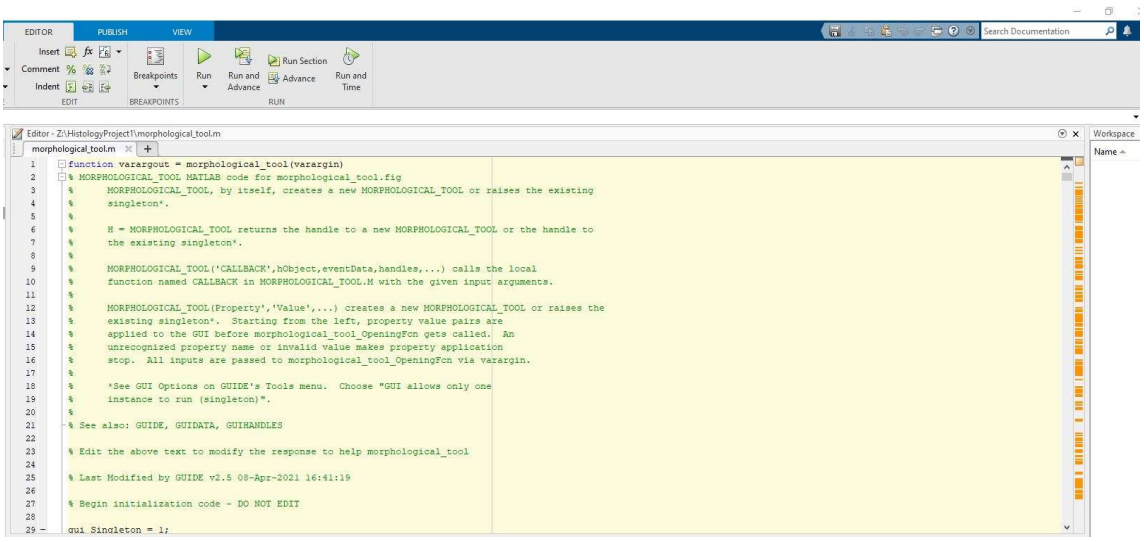

Figure A.1: Matlab code for the morphological tool

- Click on the green run button located at the top of the screen in Figure A.1. This will launch the screen interface shown in Figure A.2

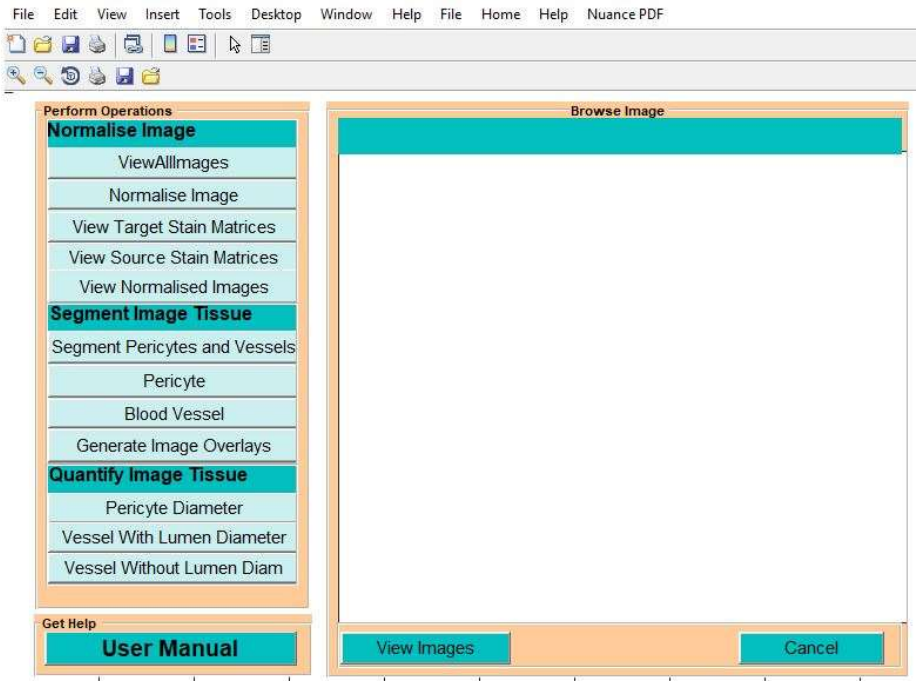

Figure A.2: Morphological tool interface

- On the menu, select '**Normalize image**' to standardise the stain in the source image. This will ask you to choose the target image and it will launch a window for you to choose the target image. After choosing the target image, the target image will be displayed as shown in Figure A.5

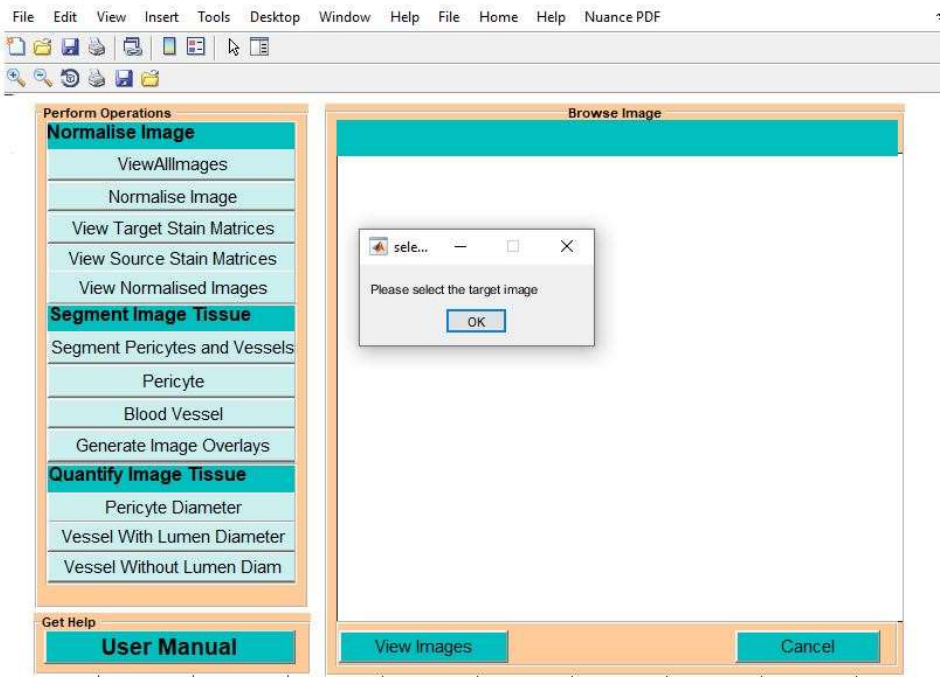

Figure A.3: Choose the target image

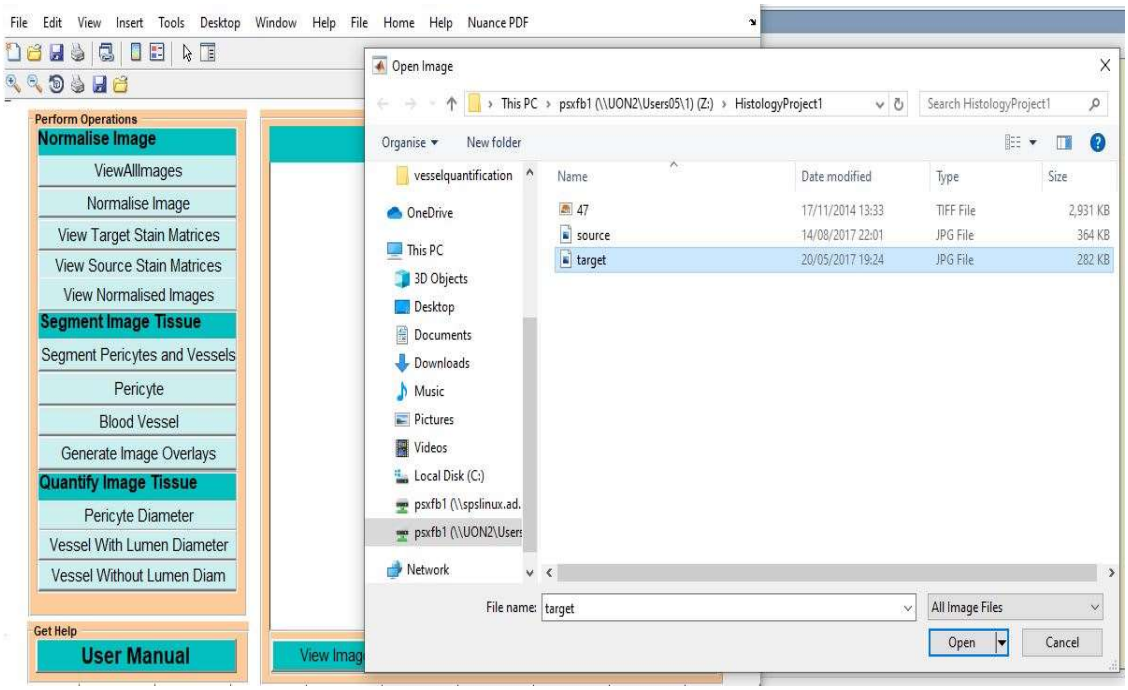

Figure A.4: Illustration of window to choose a target image

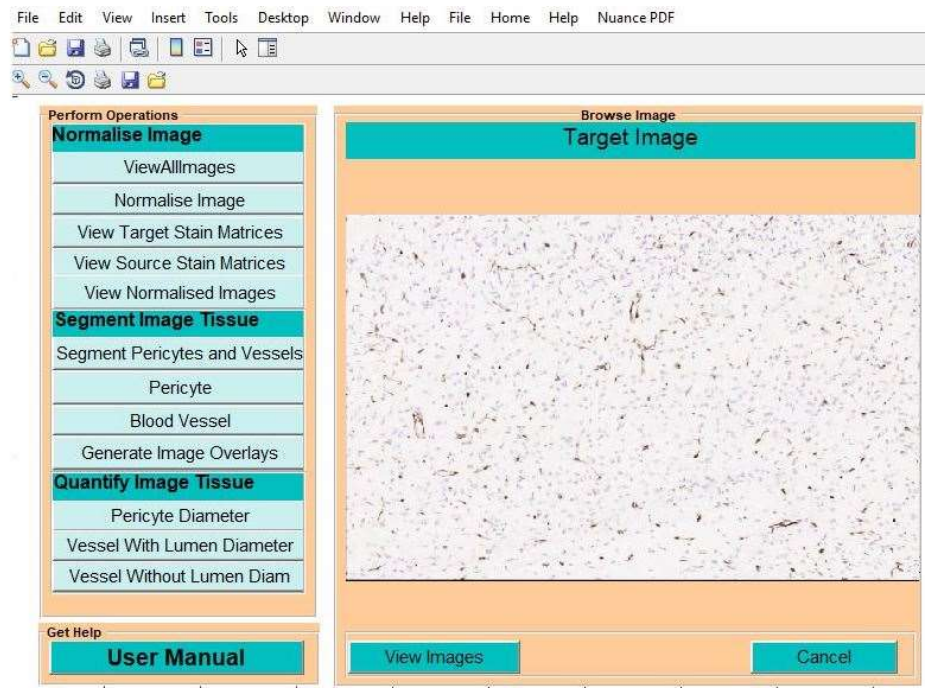

Figure A.5: Illustration of tool with a target image displayed

- After displaying the target image, it will ask you to enter the number of source images you want to normalise and it will launch a window for you to select the images you want to normalise.

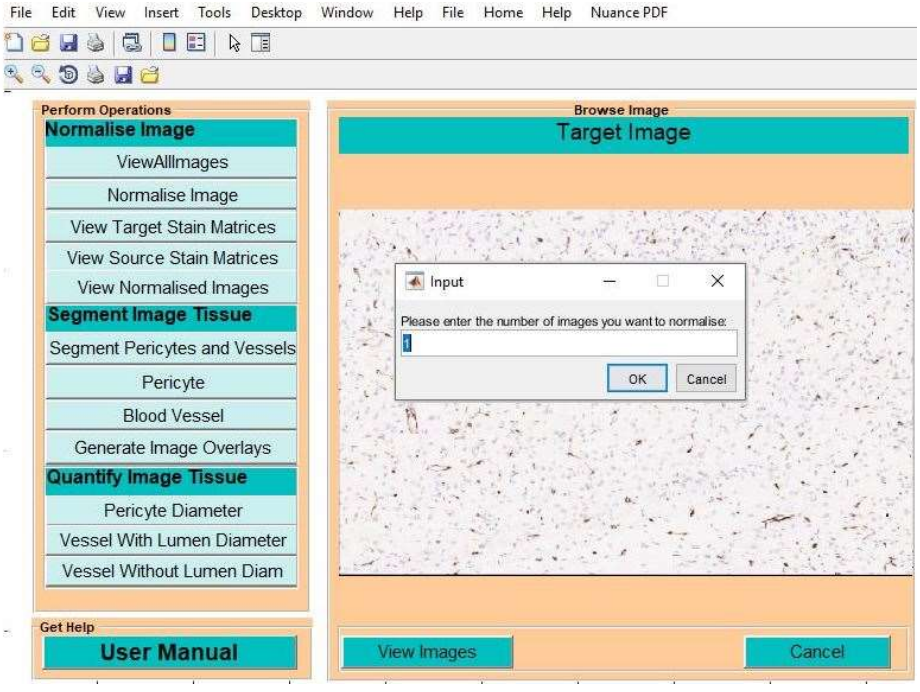

Figure A.6: Illustration of tool asking the user to enter the number of source images to normalise

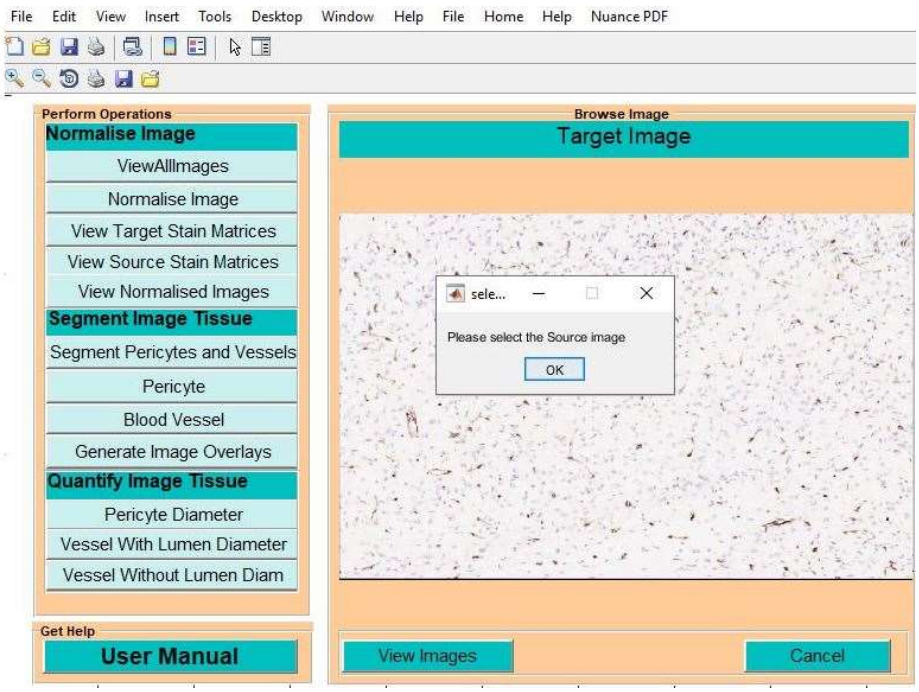

Figure A.7: Illustration of tool asking the user to choose the source image

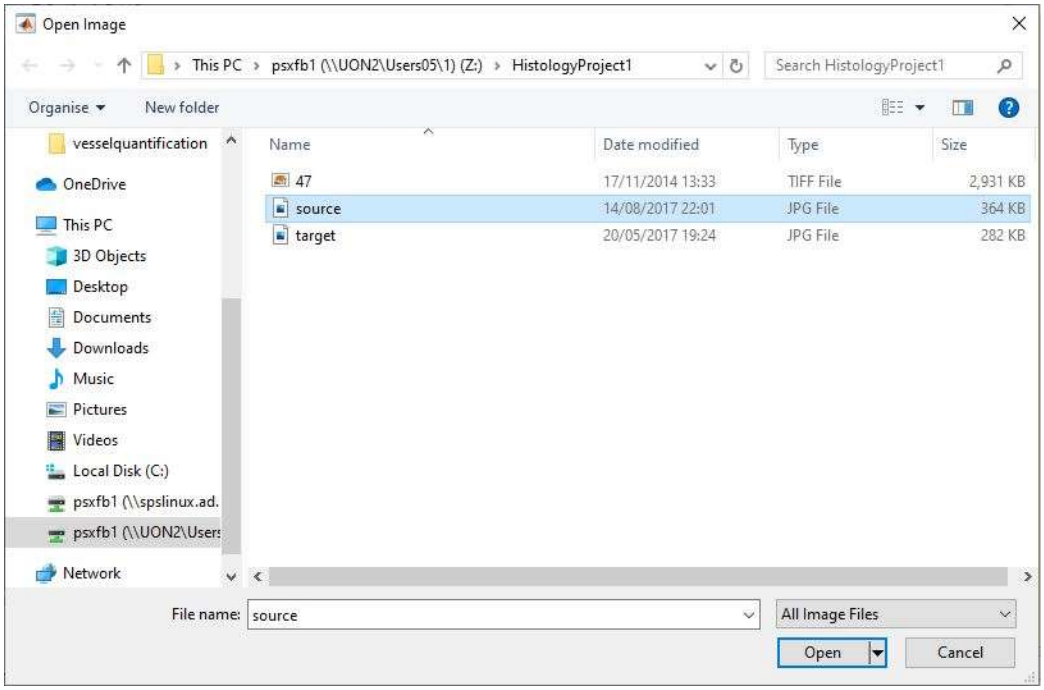

Figure A.8: Illustration of window to choose a source image

- After selecting the source image, it displays the source image (Figure A.9) and ask the user to enter the factor (Figure A.10).

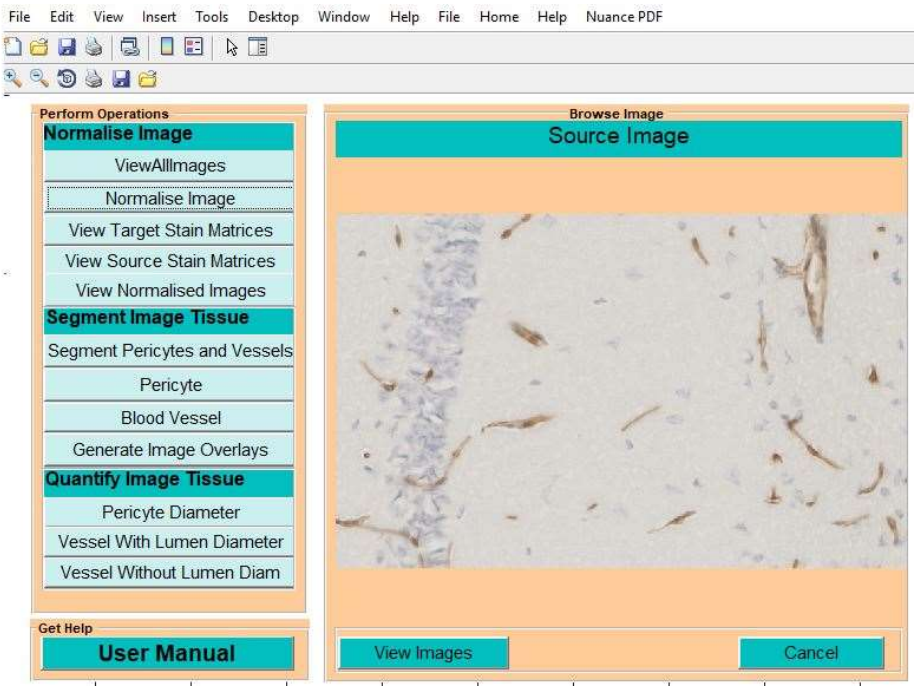

Figure A.9: Illustration of tool with a source image displayed

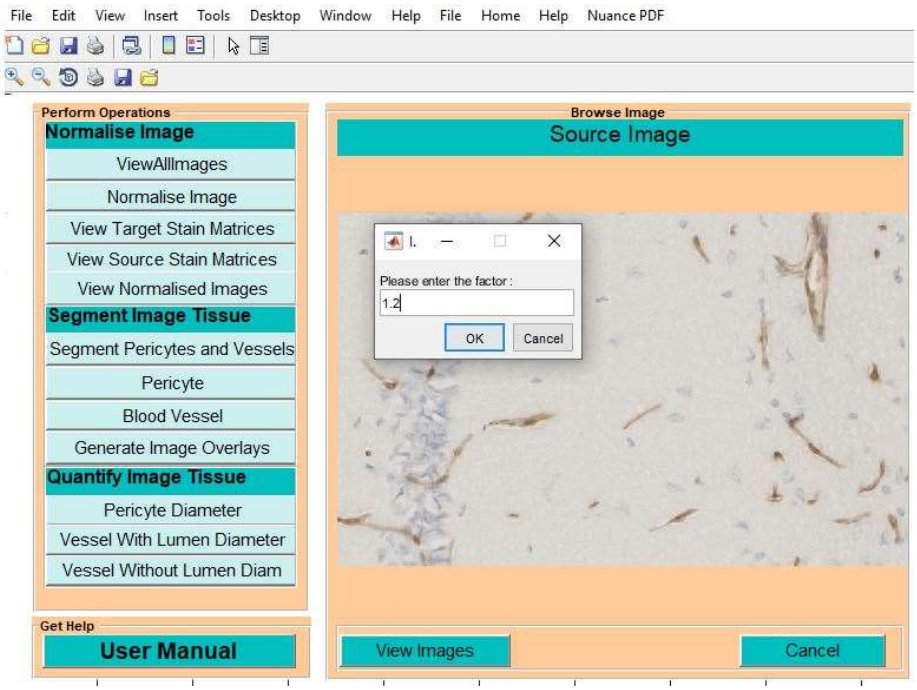

Figure A.10: Illustration of tool asking user to enter the factor

- After entering the factor, it will normalise the source image or sources images. After normalising the image, it will save and display the normalised image (Figure A.11). This will automatically create a folder and save the normalised image.

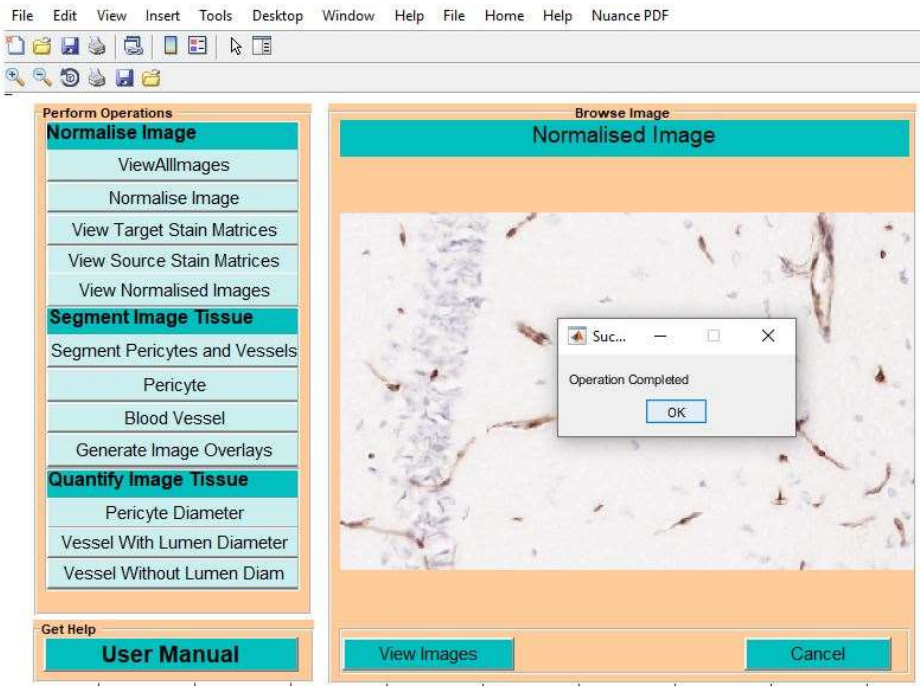

Figure A.11: Illustration of tool with a normalised image displayed

- To segment blood vessels, select **'Blood vessel'** option under **'Segment image tissue'**. This will ask the user the number of images he wants to segment and it will ask the user to choose the image. It then immediately launches the window for the user to choose the image. The user selects the image or images to be segmented. The tool automatically segments blood vessels and automatically creates a folder to save the files. The files are saved. It displays the segmentation results of the image you selected first.

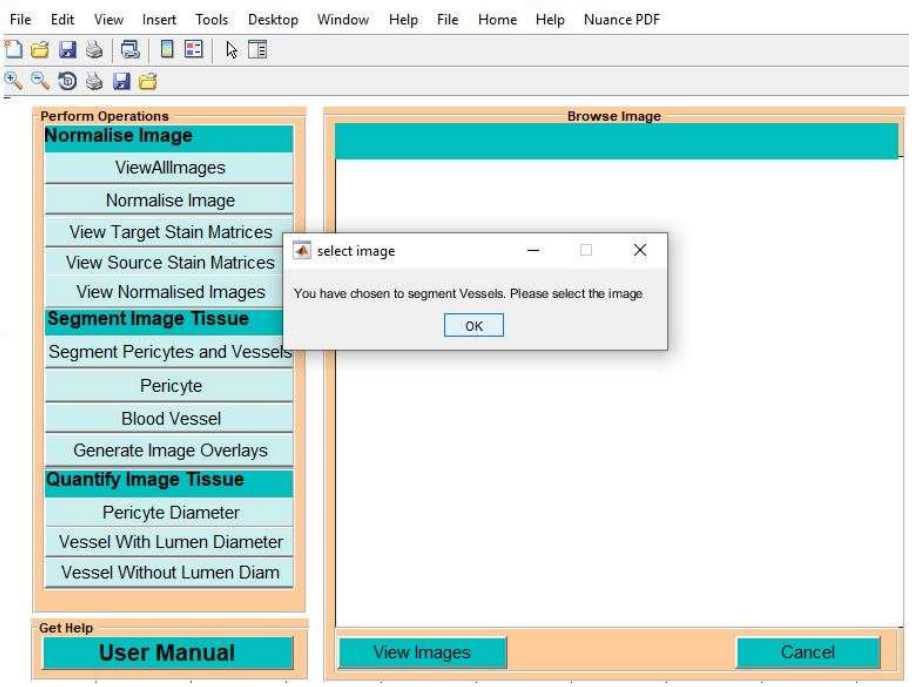

Figure A.12: Illustration of tool asking the user the number of images to segment

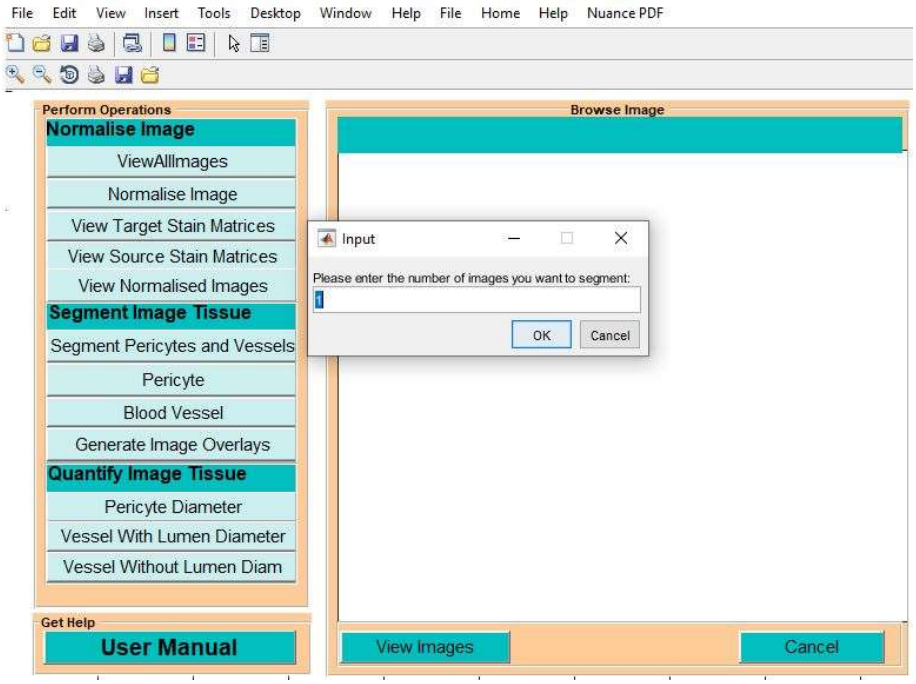

Figure A.13: Illustration of tool asking the user the choose the images to segment

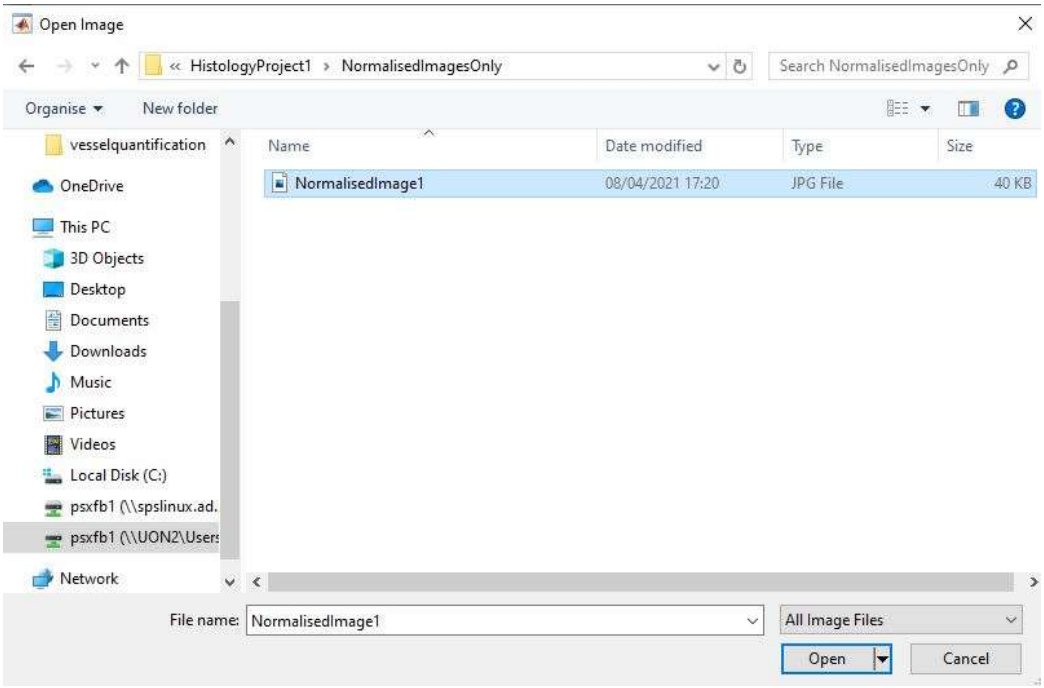

Figure A.14: Illustration of window for the user to choose the images to segment

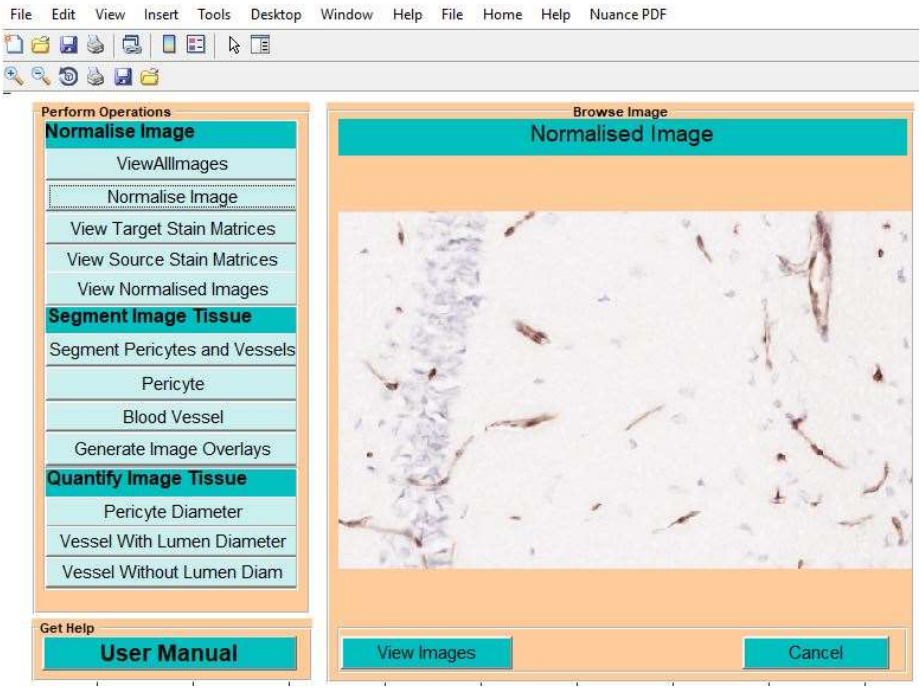

Figure A.15: Illustration of tool with normalised image to be segmented

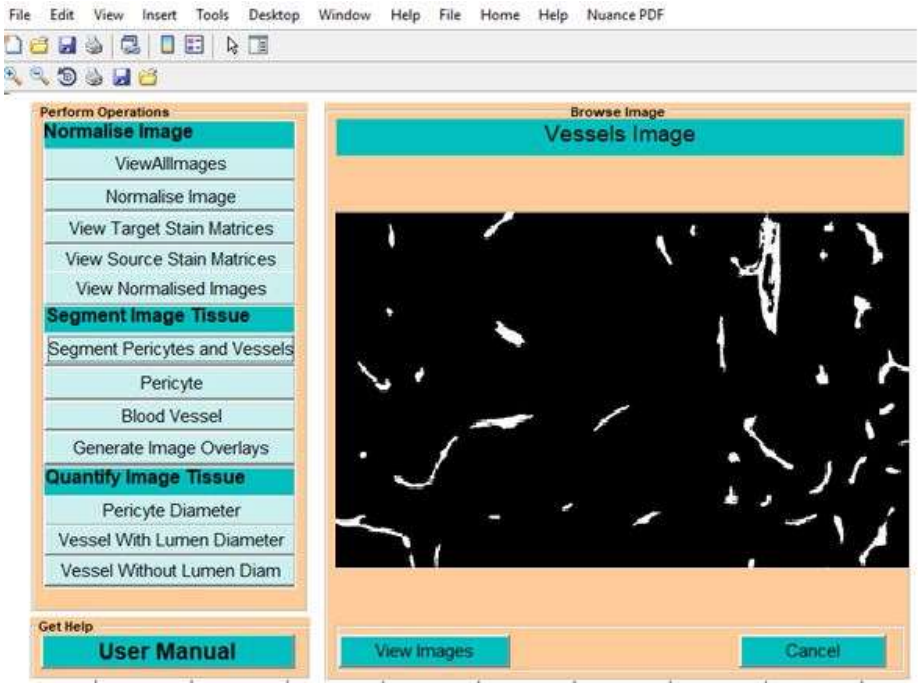

Figure A.16: Illustration of tool with blood vessels segmented

To quantify the blood vessels diameter of vessels with lumen, select the **"vessels with lumen"** option under the **"Quantify image Tissue"**. This displays the window for you to select the image or images with blood vessels with lumen. The tool will automatically quantify and save the image name and the average blood vessel diameter on a spreadsheet. **Note: The spreadsheet is saved in the same folder it saved the segmented images**.

To quantify the blood vessels diameter of the vessels without lumen, select the **'Vessels without lumen'** under the **"Quantify Image tissue"**. This displays the window for you to select the images with vessels without a lumen. This will quantify and save the diameter automatically on the spreadsheet.

Bibliography

[1] Picture thresholding using an iterative selection method. *IEEE Transactions on Systems, Man, and Cybernetics 8*, 8 (1978), 630–632.

[2] Abutaleb, A. S. Automatic thresholding of gray-level pictures using two-dimensional entropy. *Computer vision, graphics, and image processing 47*, 1 (1989), 22–32.

[3] Adams, A., Beach, C. L., Skubic, K., Van Deventer, L., and Young, G. Image segmentation of histology slides.

[4] Adapa, D., Joseph Raj, A. N., Alisetti, S. N., Zhuang, Z., and Naik, G. A supervised blood vessel segmentation technique for digital fundus images using zernike moment based features. *Plos one 15*, 3 (2020), e0229831.

[5] Adhikari, S. K., Sing, J. K., Basu, D. K., and Nasipuri, M. Conditional spatial fuzzy c-means clustering algorithm for segmentation of mri images. *Applied Soft Computing 34* (2015), 758–769.

[6] Ahmed, M. N., Yamany, S. M., Mohamed, N., Farag, A. A., and Moriarty, T. A modified fuzzy c-means algorithm for bias field estimation and segmentation of mri data. *IEEE transactions on medical imaging 21*, 3 (2002), 193–199.

[7] Ajam, A., Aziz, A. A., Asirvadam, V. S., Muda, A. S., Faye, I., and Gardezi, S. J. S. A review on segmentation and modeling of cerebral vasculature for surgical planning. *IEEE Access 5* (2017), 15222–15240.

[8] Akhavan, R., and Faez, K. A novel retinal blood vessel segmentation algorithm using fuzzy segmentation. *International Journal of Electrical and Computer Engineering 4*, 4 (2014), 561.

[9] Akram, F., Garcia, M. A., and Puig, D. Active contours driven by local and global fitted image models for image segmentation robust to intensity inhomogeneity. *PloS one 12*, 4 (2017), e0174813.

[10] Akram, M. U., Tariq, A., and Khan, S. A. Retinal image blood vessel segmentation. In *2009 International Conference on Information and Communication Technologies* (2009), pp. 181–192.

[11] Alam, M., Thapa, D., Lim, J. I., Cao, D., and Yao, X. Quantitative characteristics of sickle cell retinopathy in optical coherence tomography angiography. *Biomedical optics express 8*, 3 (2017), 1741–1753.

[12] Ali, E., Abd-El Rahman, A., El Sayed, A., et al. Automatic vessel extraction using particle swarming optimization for 3d medical images. *Current Medical Imaging Reviews 13*, 4 (2017), 471–477.

[13] Ali, S., and B, D. Segmentation model for noisy and intensity inhomogeneity images via logarithmic density function. *Journal of Applied Computational Mathematics* (2018).

[14] Almira, G. A., Harsono, T., Sigit, R., Bimantara, I. G. N. T. B., and Saputra, J. S. M. Performance analysis of gaussian and bilateral filter in case of determination the fetal length. *Knowledge Creation and Intelligent Computing (KCIC)* (2016).

[15] Alsubaie, N., Trahearn, N., Raza, S. E. A., Snead, D., and Rajpoot, N. M. Stain deconvolution using statistical analysis of multi-resolution stain colour representation. *PLOS ONE 12*, 1 (01 2017), 1–15.

[16] Asad, A. H., and Hassaanien, A.-E. Retinal blood vessels segmentation based on bio-inspired algorithm. In *Applications of Intelligent Optimization in Biology and Medicine*. Springer, 2016, pp. 181–215.

[17] Asl, M. E., Koohbanani, N. A., Frangi, A. F., and Gooya, A. Tracking and diameter estimation of retinal vessels using gaussian process and radon transform. *Journal of Medical Imaging 4*, 3 (2017), 034006.

[18] Avila-Montes, O. C., Kurkure, U., Nakazato, R., Berman, D. S., Dey, D., and Kakadiaris, I. A. Segmentation of the thoracic aorta in noncontrast cardiac ct images. *IEEE journal of biomedical and health informatics 17*, 5 (2013), 936–949.

[19] Azzopardi, G., Strisciuglio, N., Vento, M., and Petkov, N. Trainable cosfire filters for vessel delineation with application to retinal images. *Medical image analysis 19*, 1 (2015), 46–57.

[20] B, F. A hybrid approach for stain normalisation in digital histopathological images. *Multimedia tool and application* (2020).

[21] BahadarKhan, K., Khaliq, A. A., and Shahid, M. A morphological hessian based approach for retinal blood vessels segmentation and denoising using region based otsu thresholding. *PloS one 11*, 7 (2016), e0158996.

[22] Bankhead, P., Scholfield, C. N., McGeown, J. G., and Curtis, T. M. Fast retinal vessel detection and measurement using wavelets and edge location refinement. *PloS one 7*, 3 (2012), e32435.

[23] Baselice, F., Ferraioli, G., Pascazio, V., and Schirinzi, G. Enhanced wiener filter for ultrasound image denoising.

[24] Beevi, K. S., and Bindu, G. Analysis of nuclei detection with stain normalization in histopathology images. *Indian Journal of Science and Technology 8*, 23 (2015).

[25] Ben Abdallah, M., Malek, J., Krissian, K., and Tourki, R. An automated vessel segmentation of retinal images using multiscale vesselness. In *Eighth International Multi-Conference on Systems, Signals Devices* (2011), pp. 1–6.

[26] Beucher, S., and Meyer, F. The morphological approach to segmentation: the watershed transformation.

[27] Bevilacqua, V., Triggiani, M., Dimatteo, M., Bellantuono, G., Brunetti, A., Carnimeo, L., Marino, F., Telegrafo, M., and Moschetta, M. Computer assisted detection of breast lesions in magnetic resonance images. In *International Conference on Intelligent Computing* (2016), Springer, pp. 306–316.

[28] Bezdek, J. C. Objective function clustering. In *Pattern recognition with fuzzy objective function algorithms*. Springer, 1981, pp. 43–93.

[29] Bharkad, S. Automatic segmentation of blood vessels in retinal image using morphological filters. In *Proceedings of the 6th International Conference on Software and Computer Applications* (2017), pp. 132–136.

[30] Bhattacharya, M., Sharma, G., et al. Optimized coronary artery segmentation using frangi filter and anisotropic diffusion filtering. In *Computational and Business Intelligence (ISCBI), 2013 International Symposium on* (2013), IEEE, pp. 261–264.

[31] Boegel, M., Hoelter, P., Redel, T., Maier, A., Hornegger, J., and Doerfler, A. A fully-automatic locally adaptive thresholding algorithm for blood vessel segmentation in 3d digital subtraction angiography. In *Engineering in Medicine and Biology Society (EMBC), 2015 37th annual international conference of the IEEE* (2015), IEEE, pp. 2006–2009.

[32] Boitsov, V., Vatian, A., Egorov, N., Klochkov, A., Lobantsev, A., Markova, E., Gusarova, N., Shalyto, A., Zubanenko, A., Soldatov, R., et al. Software tools for manual segmentation of tomography images supporting radiologist's personal context. In *2019 25th Conference of Open Innovations Association (FRUCT)* (2019), IEEE, pp. 64–76.

[33] Buckeridge, D. L., Burkom, H., Campbell, M., Hogan, W. R., Moore, A. W., et al. Algorithms for rapid outbreak detection: a research synthesis. *Journal of biomedical informatics 38*, 2 (2005), 99–113.

[34] Bukenya, F., Awwad, A., Duan, J., Ehling, J., Faas, H., and Bai, L. Three-dimensional segmentation of blood vessels from intensity in-homogeneous medical images. In *2018 IEEE Symposium Series on Computational Intelligence (SSCI)* (Nov 2018), pp. 1508–1514.

[35] Bukenya, F., Awwad, A., Faas, H., Ding, J., Ehling, D., and Bai, L. Three-dimensional segmentation of vessels from intensity in-homogeneous medical images. *2016 IEEE Symposium Series on Computational Intelligence (SSCI)*.

[36] Bukenya, F., Bai, L., and Kiweewa, A. A review of blood vessel segmentation techniques. In *2018 1st International Conference on Computer Applications Information Security (ICCAIS)* (2018), pp. 1–10.

[37] Bukenya, F., Ehling, J., Kalema, A., Eyoh, I., Robert, J., and Bai, L. 3d segmentation of the whole heart vasculature using improved multi-threshold otsu and white top-hat scale space hessian based vessel filter. In *2016 IEEE Symposium Series on Computational Intelligence (SSCI)* (Dec 2016), pp. 1–7.

[38] Bukenya, F., Ehling, J., Kalema, A. K., Eyoh, I., Robert, J., and Bai, L. 3d segmentation of the whole heart vasculature using improved multi-threshold otsu and white top-hat scale space hessian based vessel filter. *IEEE Symposium Series on Computational Intelligence* (2016).

[39] Bukenya, F., Nerissa, C., Serres, S., Pardon, M.-C., and Bai, L. An automated method for segmentation and quantification of blood vessels in histology images. *Microvascular Research* (2019), 103928.

[40] Burns, P. D., and Berns, R. S. Quantization in multispectral color image acquisition. In *Color and Imaging Conference* (1999), vol. 1999, Society for Imaging Science and Technology, pp. 32–35.

[41] Cahill, N. D., Chew, S. E., and Wenger, P. S. Spatial-spectral dimensionality reduction of hyperspectral imagery with partial knowledge of class labels. In *Algorithms and Technologies for Multispectral, Hyperspectral, and Ultraspectral Imagery XXI* (2015), vol. 9472, International Society for Optics and Photonics, p. 94720S.

[42] Cahill, N. D., Czaja, W., and Messinger, D. W. Schroedinger eigenmaps with nondiagonal potentials for spatial-spectral clustering of hyperspectral imagery.

[43] Caio A. Palma, Fabio A.M. Cappabianco, J. S. I. P. A. M. Anisotropic diffusion filtering operation and limitations - magnetic resonance imaging evaluation.

[44] Cárdenes, R., de Luis-García, R., and Bach-Cuadra, M. A multidimensional segmentation evaluation for medical image data. *Computer methods and programs in biomedicine 96*, 2 (2009), 108–124.

[45] Carmeliet, P., and Jain, R. K. Angiogenesis in cancer and other diseases. *nature 407*, 6801 (2000), 249–257.

[46] Cervantes-Sanchez, F., Cruz-Aceves, I., Hernandez-Aguirre, A., Hernandez-Gonzalez, M. A., and Solorio-Meza, S. E. Automatic segmentation of coronary arteries in x-ray angiograms using multiscale analysis and artificial neural networks. *Applied Sciences 9*, 24 (2019), 5507.

[47] Chakraborti, T., Jha, D. K., Chowdhury, A. S., and Jiang, X. A self-adaptive matched filter for retinal blood vessel detection. *Machine Vision and Applications 26*, 1 (2015), 55–68.

[48] Challoob, M., and Gao, Y. Retinal vessel segmentation using matched filter with joint relative entropy. In *International Conference on Computer Analysis of Images and Patterns* (2017), Springer, pp. 228–239.

[49] Chandra, S., Tsogkas, S., and Kokkinos, I. Accurate human-limb segmentation in rgb-d images for intelligent mobility assistance robots. In *Proceedings of the IEEE International Conference on Computer Vision Workshops* (2015), pp. 44–50.

[50] Chaudhury, K. N., and Dabhade, S. D. Fast and provably accurate bilateral filtering. *IEEE Transactions on Image Processing 25*, 6 (2016), 2519–2528.

[51] Chen, B., Sun, Y., and Ong, S. H. Liver vessel segmentation using graph cuts with quick shift initialization. In *The 15th International Conference on Biomedical Engineering* (2014), Springer, pp. 188–191.

[52] Chen, C., Li, H., Zhou, X., and Wong, S. Constraint factor graph cut–based active contour method for automated cellular image segmentation in rnai screening. *Journal of microscopy 230*, 2 (2008), 177–191.

[53] Chen, K., Yin, Q., Jia, X., and Lu, M. Image enhancement based improved multi-scale hessian matrix for coronary angiography. *International Journal of Computer Applications 126*, 10 (2015).

[54] Chen, Q., and He, C. Variational segmentation model for images with intensity inhomogeneity and poisson noise. *EURASIP Journal on Image and Video Processing 2013*, 1 (2013), 28.

[55] Chen, Z., and Molloi, S. Automatic 3d vascular tree construction in ct angiography. *Computerized Medical Imaging and Graphics 27*, 6 (2003), 469–479.

[56] Cheng, D.-C., Billich, C., Liu, S.-H., Brunner, H., Qiu, Y.-C., Shen, Y.-L., Brambs, H. J., Schmidt-Trucksäss, A., and Schütz, U. H. Automatic detection of the carotid artery boundary on cross-sectional mr image sequences using a circle model guided dynamic programming. *Biomedical engineering online 10*, 1 (2011), 26.

[57] Cheng, J.-H., Sun, D.-W., Nagata, M., and Tallada, J. Quality evaluation of strawberry. In *Computer Vision Technology for Food Quality Evaluation (Second Edition)*. Elsevier, 2016, pp. 327–350.

[58] Chetan L Srinidhi, P. A. . J. R. Recent advancements in retinal vessel segmentation. *Journal of Medical Systems* (2017).

[59] Cui, H., Xia, Y., and Zhang, Y. 2d and 3d vascular structures enhancement via improved vesselness filter and vessel enhancing diffusion. *IEEE Access 7* (2019), 123969–123980.

[60] Dai, P., Luo, H., Sheng, H., Zhao, Y., Li, L., Wu, J., Zhao, Y., and Suzuki, K. A new approach to segment both main and peripheral retinal vessels based on gray-voting and gaussian mixture model. *PloS one 10*, 6 (2015), e0127748.

[61] Das, B., and Banerjee, S. Parametric contour model in medical image segmentation. In *Deformable Models*. Springer, 2007, pp. 31–74.

[62] Dash, J., and Bhoi, N. A thresholding based technique to extract retinal blood vessels from fundus images. *Future Computing and Informatics Journal 2*, 2 (2017), 103–109.

[63] De Momi, E., Caborni, C., Cardinale, F., Casaceli, G., Castana, L., Cossu, M., Mai, R., Gozzo, F., Francione, S., Tassi, L., et al. Multi-trajectories automatic planner for stereoelectroencephalography (seeg). *International journal of computer assisted radiology and surgery 9*, 6 (2014), 1087–1097.

[64] Dehkordi, M. T., Hoseini, A. M. D., Sadri, S., and Soltanianzadeh, H. Local feature fitting active contour for segmenting vessels in angiograms. *IET Computer Vision 8*, 3 (2014), 161–170.

[65] Demir, Ö. Computer-aided detection of polyps in ct colonography using regional textural features. In *Int'l Conference Proceedings* (2018), p. 119.

[66] Despotović, I., Goossens, B., and Philips, W. Mri segmentation of the human brain: challenges, methods, and applications. *Computational and mathematical methods in medicine 2015* (2015).

[67] Devi, H. Thresholding: A pixel-level image processing methodology preprocessing technique for an ocr system for the brahmi script. *Ancient Asia 1* (2006).

[68] Ding, Y., Ward, W., Wästerlid, T., Gowland, P., Peters, A., Yang, J., Nakagawa, S., and Bai, L. Three-dimensional vessel segmentation using a novel combinatory filter framework. *Physics in Medicine & Biology 59*, 22 (2014), 7013.

[69] Dunn, J. C. A fuzzy relative of the isodata process and its use in detecting compact well-separated clusters.

[70] Ecabert, O., Peters, J., Walker, M. J., Ivanc, T., Lorenz, C., von Berg, J., Lessick, J., Vembar, M., and Weese, J. Segmentation of the heart and

great vessels in ct images using a model-based adaptation framework. *Medical image analysis 15*, 6 (2011), 863–876.

[71] ECE, E. An efficient blood vessel detection algorithm for retinal images using local entropy thresholding. *International Journal of Engineering 1*, 4 (2012).

[72] Emrani, Zahra, S. B., and Rabbani, H. A new parallel approach for accelerating the gpu-based execution of edge detection algorithms. *Journal of Medical Signals and Sensors 7*, 1 (2017), 33–42.

[73] Esneault, S., Lafon, C., and Dillenseger, J.-L. Liver vessels segmentation using a hybrid geometrical moments/graph cuts method. *IEEE Transactions on Biomedical Engineering 57*, 2 (2010), 276–283.

[74] Fernández-Carrobles, M.-M., Tadeo, I., Noguera, R., García-Rojo, M., Déniz, O., Salido, J., and Bueno, G. A morphometric tool applied to angiogenesis research based on vessel segmentation. In *Diagnostic pathology* (2013), no. 1, BioMed Central, p. S20.

[75] Flasque, N., Desvignes, M., Constans, J.-M., and Revenu, M. Acquisition, segmentation and tracking of the cerebral vascular tree on 3d magnetic resonance angiography images. *Medical Image Analysis 5*, 3 (2001), 173–183.

[76] Fortier, A., Gullapalli, V., and Mirshams, R. A. Review of biomechanical studies of arteries and their effect on stent performance. *IJC Heart & Vessels 4* (2014), 12–18.

[77] Frangi, A. F., Niessen, W. J., Vincken, K. L., and Viergever, M. A. Multiscale vessel enhancement filtering. In *International Conference on Medical Image Computing and Computer-Assisted Intervention* (1998), Springer, pp. 130–137.

[78] Freiman, M., Frank, J., Weizman, L., Nammer, E., Shilon, O., Joskowicz, L., and Sosna, J. Nearly automatic vessels segmentation using graph-based energy minimization.

[79] G., Z. Horn, r. a.; johnson, c. r., matrix analysis. cambridge etc., cambridge university press 1985. xiii, 561 s., £ 35.00. isbn 0-521-30586-1. *ZAMM - Journal of Applied Mathematics and Mechanics / Zeitschrift für Angewandte Mathematik und Mechanik 67*, 3, 212–212.

[80] Gade, A., Vig, R., and Kulkarni, V. Segmentation of tumor region in mri images of brain using mathematical morphology. *International Journal of Image Processing (IJIP) 8*, 3 (2014), 95.

[81] Gamechi, Z. S., Bons, L. R., Giordano, M., Bos, D., Budde, R. P., Kofoed, K. F., Pedersen, J. H., Roos-Hesselink, J. W., and de Bruijne, M. Automated 3d segmentation and diameter measurement of the thoracic aorta on non-contrast enhanced ct. *European radiology 29*, 9 (2019), 4613–4623.

[82] Gao, J., Chen, G., and Lin, W. An effective retinal blood vessel segmentation by using automatic random walks based on centerline extraction. *BioMed research international 2020*.

[83] Gao, X., Bharath, A., Stanton, A., Hughes, A., Chapman, N., and Thom, S. A method of vessel tracking for vessel diameter measurement on retinal images. In *Proceedings 2001 International Conference on Image Processing (Cat. No. 01CH37205)* (2001), vol. 2, IEEE, pp. 881–884.

[84] Gavrilovic, M., Azar, J. C., Lindblad, J., Wählby, C., Bengtsson, E., Busch, C., and Carlbom, I. B. Blind color decomposition of histological images.

[85] GeethaRamani, R., and Balasubramanian, L. Retinal blood vessel segmentation employing image processing and data mining techniques for computerized retinal image analysis. *Biocybernetics and Biomedical Engineering 36*, 1 (2016), 102–118.

[86] Gharnali, B., and Alipour, S. Mri image segmentation using conditional spatial fcm based on kernel-induced distance measure. *Engineering, Technology & Applied Science Research 8*, 3 (2018), 2985–2990.

[87] Ghosh, B., Karri, S. P. K., Sheet, D., Garud, H., Ghosh, A., Ray, A. K., and Chatterjee, J. A generalized framework for stain separation in digital pathology applications. In *India Conference (INDICON), 2016 IEEE Annual* (2016), IEEE, pp. 1–4.

[88] Golub, G., and Van Loan, C. *Matrix Computations*. Johns Hopkins Studies in the Mathematical Sciences. Johns Hopkins University Press, 2013.

[89] Gonzales-Barron, U., and Butler, F. A comparison of seven thresholding techniques with the k-means clustering algorithm for measurement of bread-crumb features by digital image analysis. *Journal of Food Engineering 74*, 2 (2006), 268–278.

[90] Guedri, H., Abdallah, M. B., Nasri, F., and Belmabrouk, H. Computer method for tracking the centerline curve of the human retinal blood vessel. In *Engineering & MIS (ICEMIS), 2017 International Conference on* (2017), IEEE, pp. 1–6.

[91] Guha, I., Das, N., Rakshit, P., Nasipuri, M., Saha, P. K., and Basu, S. A semiautomatic approach for segmentation of carotid vasculature from patients' cta images. *Innovations in Systems and Software Engineering 13*, 4 (2017), 243–250.

[92] Guo, X., Huang, S., Fu, X., Wang, B., and Huang, X. Vascular segmentation in hepatic ct images using adaptive threshold fuzzy connectedness method. *Biomedical engineering online 14*, 1 (2015), 1–11.

[93] Hacihaliloglu, I., Abugharbieh, R., Hodgson, A. J., and Rohling, R. N. Automatic adaptive parameterization in local phase feature-based bone segmentation in ultrasound. *Ultrasound in medicine & biology 37*, 10 (2011), 1689–1703.

[94] Hacihaliloglu, I., Guy, P., Hodgson, A. J., and Abugharbieh, R. Volume-specific parameter optimization of 3d local phase features for improved extraction of bone surfaces in ultrasound. *The International Journal of Medical Robotics and Computer Assisted Surgery 10*, 4 (2014), 461–473.

[95] Haft-Javaherian, M., Fang, L., Muse, V., Schaffer, C. B., Nishimuraa, N., and Sabuncu, M. R. Deep convolutional neural networks for segmenting 3d

in vivo multiphoton images of vasculature in alzheimer disease mouse models. *arXiv preprint arXiv:1801.00880* (2018).

[96] Hao, D., Ding, S., Qiu, L., Lv, Y., Fei, B., Zhu, Y., and Qin, B. Sequential vessel segmentation via deep channel attention network. *Neural Networks 128* (2020), 172–187.

[97] Haralick, R. M., and Shapiro, L. G. *Computer and robot vision.* Addison-wesley, 1992.

[98] Hassan, G., El-Bendary, N., Hassanien, A. E., Fahmy, A., Snasel, V., et al. Retinal blood vessel segmentation approach based on mathematical morphology. *Procedia Computer Science 65* (2015), 612–622.

[99] Hassan, G., and Hassanien, A. E. Retinal fundus vasculature multilevel segmentation using whale optimization algorithm. *Signal, Image and Video Processing 12*, 2 (2018), 263–270.

[100] Hauta-Kasari, M., Parkkinen, J., Jääskeläinen, T., and Lenz, R. Multispectral texture segmentation based on the spectral cooccurrence matrix. *Pattern Analysis Applications 2* (1999), 275–284.

[101] Hawas, A. R., Ashour, A. S., and Guo, Y. 8 - neutrosophic set in medical image clustering. In *Neutrosophic Set in Medical Image Analysis*, Y. Guo and A. S. Ashour, Eds. Academic Press, 2019, pp. 167–187.

[102] He, X., Pan, Z., Dong, Q., and Wang, G. Veins segmentation and three-dimensional reconstruction from liver ct images using multilevel otsu method. In *Image and Graphics (ICIG), 2013 Seventh International Conference on* (2013), IEEE, pp. 248–251.

[103] Hernandez-Vela, A., Gatta, C., Escalera, S., Igual, L., Sabate, M., and Radeva, P. Accurate coronary centerline extraction, caliber estimation, and catheter detection in angiographies.

[104] Hochbaum, D. S., and Singh, V. An efficient algorithm for co-segmentation. In *2009 IEEE 12th International Conference on Computer Vision*, IEEE, pp. 269–276.

[105] Hofheinz, F., Langner, J., Beuthien-Baumann, B., Oehme, L., Steinbach, J., Kotzerke, J., and van den Hoff, J. Suitability of bilateral filtering for edge-preserving noise reduction in pet. *EJNMMI research 1*, 1 (2011), 23.

[106] Hou, Z. A review on mr image intensity inhomogeneity correction. *International journal of biomedical imaging 2006* (2006).

[107] Huang, D.-Y., and Wang, C.-H. Optimal multi-level thresholding using a two-stage otsu optimization approach. *Pattern Recognition Letters 30*, 3 (2009), 275–284.

[108] Ibragimov, B., Toesca, D., Chang, D., Koong, A., and Xing, L. Combining deep learning with anatomical analysis for segmentation of the portal vein for liver sbrt planning. *Physics in Medicine & Biology 62*, 23 (2017), 8943.

[109] Jaccard, P. The distribution of the flora in the alpine zone. 1. *New phytologist 11*, 2 (1912), 37–50.

[110] Jalba, A. C., Wilkinson, M. H., and Roerdink, J. B. Morphological hat-transform scale spaces and their use in pattern classification. *Pattern Recognition 37*, 5 (2004), 901–915.

[111] Jang, Y., Jung, H. Y., Hong, Y., Cho, I., Shim, H., and Chang, H.-J. Geodesic distance algorithm for extracting the ascending aorta from 3d ct images. *Computational and mathematical methods in medicine 2016* (2016).

[112] Jensen, E. C. Quantitative analysis of histological staining and fluorescence using imagej. *The Anatomical Record 296*, 3 (2013), 378–381.

[113] Jerman, T., Pernu, F., Likar, B., and Spiclin, Z. Beyond frangi: an improved multiscale vesselness filter. In *Medical Imaging 2015: Image Processing* (Mar. 2015), S. Ourselin and M. A. Styner, Eds., vol. 9413 of *Society of Photo-Optical Instrumentation Engineers (SPIE) Conference Series*, p. 94132A.

[114] Jiang, W., Baker, M. L., Wu, Q., Bajaj, C., and Chiu, W. Applications of a bilateral denoising filter in biological electron microscopy. *Journal of structural biology 144*, 1-2 (2003), 114–122.

[115] Jiang M, Ji Q, M. B. Model-based automated extraction of microtubules from electron tomography volume. *IEEE Trans Inf Technol Biomed.* (2006).

[116] Jin, J., Yang, L., Zhang, X., and Ding, M. Vascular tree segmentation in medical images using hessian-based multiscale filtering and level set method. *Computational and mathematical methods in medicine 2013* (2013).

[117] Joulin, A., Bach, F., and Ponce, J. Discriminative clustering for image co-segmentation. In *2010 IEEE Computer Society Conference on Computer Vision and Pattern Recognition* (2010), IEEE, pp. 1943–1950.

[118] Kainer, C. L. M. D. S. L. F. H. U. 3d microstructural evolution on solidifying mg–5nd–5 alloy observed via in situ synchrotron tomography.

[119] Kandil, H., Soliman, A., Ghazal, M., Mahmoud, A., Shalaby, A., Keynton, R., Elmaghraby, A., Giridharan, G., and El-Baz, A. A novel framework for early detection of hypertension using magnetic resonance angiography. *Scientific reports 9*, 1 (2019), 1–12.

[120] Kapade, S. D. Swarm intelligence based graph partitioning for image segmentation.

[121] Karl Krissian, Grégoire Malandain, N. A. R. V. Y. T. Model-based detection of tubular structures in 3d images. *Computer Vision and Image Understanding 80* (2000).

[122] Kasiri, K., Javad, D. M., Kazemi, K., Sadegh, H. M., and Kafshgari, S. Comparison evaluation of three brain mri segmentation methods in software tools. In *2010 17th Iranian Conference of Biomedical Engineering (ICBME)* (Nov 2010), pp. 1–4.

[123] Kekre, H., Sarode, T., Gharge, S., and Raut, M. K. Image segmentation of mri images using kmcg and kfcg algorithms. *International Journal of Computer Applications*, 4 (2011), 1–5.

[124] Khaled, K., Shalaby, M. A. W., and El Sayed, K. M. Automatic fuzzy-based hybrid approach for segmentation and centerline extraction of main coronary arteries. *Int. J. Adv. Comput. Sci. Appl 8*, 6 (2017), 258–264.

[125] Khan, A. M., Rajpoot, N., Treanor, D., and Magee, D. A nonlinear mapping approach to stain normalization in digital histopathology images using image-specific color deconvolution. *IEEE Transactions on Biomedical Engineering 61*, 6 (2014), 1729–1738.

[126] Kim, G., Xing, E. P., Fei-Fei, L., and Kanade, T. Distributed cosegmentation via submodular optimization on anisotropic diffusion. In *2011 international conference on computer vision* (2011), IEEE, pp. 169–176.

[127] Kim, N. T., Elie, N., Plancoulaine, B., Herlin, P., and Coster, M. An original approach for quantification of blood vessels on the whole tumour section. *Analytical cellular pathology 25*, 2 (2003), 63–75.

[128] Kotte, S., Kumar, P. R., and Injeti, S. K. An efficient approach for optimal multilevel thresholding selection for gray scale images based on improved differential search algorithm. *Ain Shams Engineering Journal* (2016).

[129] Kumar, J. H., Seelamantula, C. S., Narayan, N. S., and Marziliano, P. Automatic segmentation of common carotid artery in transverse mode ultrasound images. In *2016 IEEE International Conference on Image Processing (ICIP)* (2016), IEEE, pp. 389–393.

[130] Kurkure, U., Avila-Montes, O. C., and Kakadiaris, I. A. Automated segmentation of thoracic aorta in non-contrast ct images. In *Biomedical Imaging: From Nano to Macro, 2008. ISBI 2008. 5th IEEE International Symposium on* (2008), IEEE, pp. 29–32.

[131] Kurugol, S., Estepar, R. S. J., Ross, J., and Washko, G. R. Aorta segmentation with a 3d level set approach and quantification of aortic calcifications in non-contrast chest ct. In *Engineering in Medicine and Biology Society (EMBC), 2012 Annual International Conference of the IEEE* (2012), IEEE, pp. 2343–2346.

[132] lathen, G., Jonasson, J., and Borga, M. Blood vessel segmentation using multi-scale quadrature filtering. *Pattern Recognition Letters 31*, 8 (2010), 762–767.

[133] Lavanya, R., Mohanaiah, P., and Kishore, P. A hybrid approach to visual vessel extraction with segmentation. *Materials Today: Proceedings 5*, 1 (2018), 287–293.

[134] Lebre, M.-A., Vacavant, A., Grand-Brochier, M., Rositi, H., Abergel, A., Chabrot, P., and Magnin, B. Automatic segmentation methods for liver and hepatic vessels from ct and mri volumes, applied to the couinaud scheme. *Computers in biology and medicine 110* (2019), 42–51.

[135] Leena, C., and Sreedevib, A. A multi-objective enhancement technique for poor contrast magnetic resonance images of brain glioblastomas. *Third International Conference on Computing and Network Communications* (2020).

[136] Li, C., Kao, C.-Y., Gore, J. C., and Ding, Z. Minimization of region-scalable fitting energy for image segmentation. *IEEE transactions on image processing: a publication of the IEEE Signal Processing Society 17*, 10 (2008), 1940.

[137] Li, X., Jiang, D., Shi, Y., and Li, W. Segmentation of mr image using local and global region based geodesic model. *Biomedical engineering online 14*, 1 (2015), 8.

[138] Liang, Y., Wang, F., Treanor, D., Magee, D., Roberts, N., Teodoro, G., Zhu, Y., and Kong, J. A framework for 3d vessel analysis using whole slide images of liver tissue sections. *International journal of computational biology and drug design 9*, 1-2 (2016), 102–119.

[139] Lingdao Sha, Dan Schonfeld, A. S. Color normalization of histology slides using graph regularized sparse nmf, 2017.

[140] Liu, M., Zhang, J., Yap, P.-T., and Shen, D. View-aligned hypergraph learning for alzheimer's disease diagnosis with incomplete multi-modality data. *Medical image analysis 36* (2017), 123–134.

[141] Liu, S., and Peng, Y. A local region-based chan–vese model for image segmentation. *Pattern Recognition 45*, 7 (2012), 2769–2779.

[142] Livne, M., Rieger, J., Aydin, O. U., Taha, A. A., Akay, E. M., Kossen, T., Sobesky, J., Kelleher, J. D., Hildebrand, K., Frey, D., et al. A u-net deep learning framework for high performance vessel segmentation in patients with cerebrovascular disease. *Frontiers in neuroscience 13* (2019), 97.

[143] Lu, J., Xu, Y., Chen, M., and Luo, Y. A coarse-to-fine fully convolutional neural network for fundus vessel segmentation. *Symmetry 10*, 11 (2018), 607.

[144] Lu, P., Xia, J., Li, Z., Xiong, J., Yang, J., Zhou, S., Wang, L., Chen, M., and Wang, C. A vessel segmentation method for multi-modality angiographic images based on multi-scale filtering and statistical models. *Biomedical engineering online 15*, 1 (2016), 120.

[145] Macenko, M., Niethammer, M., Marron, J. S., Borland, D., Woosley, J. T., Guan, X., Schmitt, C., and Thomas, N. E. A method for normalizing histology slides for quantitative analysis. In *Biomedical Imaging: From Nano to Macro, 2009. ISBI'09. IEEE International Symposium on* (2009), IEEE, pp. 1107–1110.

[146] Mahmood, M. T., Khan, A., and Choi, T.-S. Shape from focus based on bilateral filtering and principal component analysis. In *Applications of Soft Computing*. Springer, 2009, pp. 453–462.

[147] Manjunath, K., Prabhu, K. G., and Siddalingaswamy, P. A knowledge based approach for colon segmentation in ct colonography images. In *2015 IEEE International Conference on Signal and Image Processing Applications (ICSIPA)* (2015), IEEE, pp. 65–70.

[148] Manniesing, R., Viergever, M., and Niessen, W. Vessel enhancing diffusion: a scale space representation of vessel. *Medical Image Analysis - MED IMAGE ANAL* (01 2006).

[149] Manniesing, R., Viergever, M. A., and Niessen, W. J. Vessel axis tracking using topology constrained surface evolution. *IEEE Transactions on Medical Imaging 26*, 3 (2007), 309–316.

[150] Mapayi, T., Viriri, S., and Tapamo, J.-R. Adaptive thresholding technique for retinal vessel segmentation based on glcm-energy information. *Computational and mathematical methods in medicine 2015*.

[151] Martinez-Perez, M. E., Hughes, A. D., Thom, S. A., Bharath, A. A., and Parker, K. H. Segmentation of blood vessels from red-free and fluorescein retinal images. *Medical image analysis 11*, 1 (2007), 47–61.

[152] Meijs, M., Patel, A., van de Leemput, S. C., Prokop, M., van Dijk, E. J., de Leeuw, F.-E., Meijer, F. J., van Ginneken, B., and Manniesing, R. Robust segmentation of the full cerebral vasculature in 4d ct of suspected stroke patients. *Scientific reports 7*, 1 (2017), 1–12.

[153] Memari, N., Saripan, M. I. B., Mashohor, S., Moghbel, M., et al. Retinal blood vessel segmentation by using matched filtering and fuzzy c-means clustering with integrated level set method for diabetic retinopathy assessment. *Journal of Medical and Biological Engineering 39*, 5 (2019), 713–731.

[154] Mendonca, A., and Campilho, A. Segmentation of retinal blood vessels by combining the detection of centerlines and morphological reconstruction. *IEEE Transactions on Medical Imaging 25*, 9 (2006), 1200–1213.

[155] Moccia, S., De Momi, E., El Hadji, S., and Mattos, L. S. Blood vessel segmentation algorithms—review of methods, datasets and evaluation metrics. *Computer methods and programs in biomedicine 158* (2018), 71–91.

[156] Moghimirad, E., Rezatofighi, S. H., and Soltanian-Zadeh, H. Multi-scale approach for retinal vessel segmentation using medialness function. In *2010 IEEE International Symposium on Biomedical Imaging: From Nano to Macro* (2010), pp. 29–32.

[157] Mukherjee, L., Singh, V., and Peng, J. Scale invariant cosegmentation for image groups. In *CVPR 2011* (2011), IEEE, pp. 1881–1888.

[158] Mumford, D., and Shah, J. Optimal approximations by piecewise smooth functions and associated variational problems. *Communications on pure and applied mathematics 42*, 5 (1989), 577–685.

[159] Nakagawa, D., Shojima, M., Yoshino, M., Kin, T., Imai, H., Nomura, S., Saito, T., Nakatomi, H., Oyama, H., and Saito, N. Wall-to-lumen ratio of intracranial arteries measured by indocyanine green angiography.

[160] Nguyen, U., Bhuiyan, A., Park, L., and Ramamohanarao, K. An effective retinal blood vessel segmentation method using multi-scale line detection. *Pattern Recognition 46* (01 2012), 703–.

[161] Niu, S., Chen, Q., De Sisternes, L., Ji, Z., Zhou, Z., and Rubin, D. L. Robust noise region-based active contour model via local similarity factor for image segmentation. *Pattern Recognition 61* (2017), 104–119.

[162] Noothout, J. M., De Vos, B. D., Wolterink, J. M., and Išgum, I. Automatic segmentation of thoracic aorta segments in low-dose chest ct. In *Medical Imaging 2018: Image Processing* (2018), vol. 10574, International Society for Optics and Photonics, p. 105741S.

[163] Nugroho, H. A., Aras, R. A., Lestari, T., and Ardiyanto, I. Retinal vessel segmentation based on frangi filter and morphological reconstruction. In *2017 International Conference on Control, Electronics, Renewable Energy and Communications (ICCREC)* (2017), IEEE, pp. 181–184.

[164] Nungsanginla, L., Kumar, M., and Saxena, R. Contrast enhancement techniques using histogram equalization: A survey. *International Journal of Current Engineering and Technology 4* (6 2014).

[165] Odstrcilik, J., Kolar, R., Budai, A., Hornegger, J., Jan, J., Gazarek, J., Kubena, T., Cernosek, P., Svoboda, O., and Angelopoulou, E. Retinal vessel segmentation by improved matched filtering: evaluation on a new high-resolution fundus image database. *IET Image Processing 7*, 4 (2013), 373–383.

[166] Otsu, N. A threshold selection method from gray level histograms. *IEEE T. Syst. Man Cy. C 9* (1979), 62–66.

[167] Papadias, C. B. Globally convergent blind source separation based on a multiuser kurtosis maximization criterion. *IEEE Transactions on Signal Processing 48*, 12 (Dec 2000), 3508–3519.

[168] Pepe, A., Li, J., Rolf-Pissarczyk, M., Gsaxner, C., Chen, X., Holzapfel, G. A., and Egger, J. Detection, segmentation, simulation and visualization of aortic dissections: A review. *Medical image analysis 65* (2020), 101773.

[169] Perona, P., and Malik, J. Scale-space and edge detection using anisotropic diffusion. *IEEE Transactions on pattern analysis and machine intelligence 12*, 7 (1990), 629–639.

[170] Pham, D. L., and Prince, J. L. An adaptive fuzzy c-means algorithm for image segmentation in the presence of intensity inhomogeneities. *Pattern recognition letters 20*, 1 (1999), 57–68.

[171] Qiu, C., Xiao, J., Yu, L., Han, L., and Iqbal, M. N. A modified interval type-2 fuzzy c-means algorithm with application in mr image segmentation. *Pattern Recognition Letters 34*, 12 (2013), 1329–1338.

[172] Qu, Z., and Zhang, L. Research on image segmentation based on the improved otsu algorithm. In *Intelligent Human-Machine Systems and Cybernetics (IHMSC), 2010 2nd International Conference on* (2010), vol. 2, IEEE, pp. 228–231.

[173] Rabinovich, A., Agarwal, S., Laris, C., Price, J. H., and Belongie, S. J. Unsupervised color decomposition of histologically stained tissue samples. In *Advances in neural information processing systems* (2004), pp. 667–674.

[174] Reinhard, E., Adhikhmin, M., Gooch, B., and Shirley, P. Color transfer between images. *IEEE Computer graphics and applications 21*, 5 (2001), 34–41.

[175] Reyes-Aldasoro, C. C., Williams, L. J., Akerman, S., Kanthou, C., and Tozer, G. M. An automatic algorithm for the segmentation and morphological analysis of microvessels in immunostained histological tumour sections. *Journal of Microscopy 242*, 3 (2011), 262–278.

[176] Roth, H. R., Shen, C., Oda, H., Oda, M., Hayashi, Y., Misawa, K., and Mori, K. Deep learning and its application to medical image segmentation. *Medical Imaging Technology 36*, 2 (2018), 63–71.

[177] Ruifrok, A. C., Johnston, D. A., et al. Quantification of histochemical staining by color deconvolution. *Analytical and quantitative cytology and histology 23*, 4 (2001), 291–299.

[178] Saiyam, T., and Singh, S. Non linear image enhancement. *INTERNATIONAL JOURNAL OF ENGINEERING RESEARCH TECHNOLOGY (IJERT) 2* (2013), 254–261.

[179] Samantaa, S., Dey, N., Das, P., Acharjee, S., and Chaudhuri, S. S. Multilevel threshold based gray scale image segmentation using cuckoo search. *arXiv preprint arXiv:1307.0277* (2013).

[180] Sampath, R., and Biros, G. A parallel geometric multigrid method for finite elements on octree meshes. *SIAM Journal on Scientific Computing 32*, 3 (2010), 1361–1392.

[181] Sangsefidi, N., Foruzan, A. H., and Dolati, A. Balancing the data term of graph-cuts algorithm to improve segmentation of hepatic vascular structures. *Computers in biology and medicine 93* (2018), 117–126.

[182] SARAN, A. N., NAR, F., AND SARAN, M. Vessel segmentation in mri using a variational image subtraction approach. *Turkish Journal of Electrical Engineering & Computer Sciences 22*, 2 (2014), 499–516.

[183] SARASWAT, M., AND ARYA, K. Automated microscopic image analysis for leukocytes identification: A survey. *Micron 65* (2014), 20 – 33.

[184] SARI, S., ASAHRORI, S., ROSLAN, H., AND IBRAHIM, N. Gabor edge detection method based on bilateral filter and otsu threshold for noisy ultrasound image.

[185] SATO, Y., NAKAJIMA, S., SHIRAGA, N., ATSUMI, H., YOSHIDA, S., KOLLER, T., GERIG, G., AND KIKINIS, R. Three-dimensional multi-scale line filter for segmentation and visualization of curvilinear structures in medical images. *Medical image analysis 2*, 2 (1998), 143–168.

[186] SCHOTT, J. R. *Matrix analysis for statistics*. John Wiley & Sons, 2016.

[187] SELVALAKSHMI, V., AND DEVI, S. N. Segmentation and 3d visualization of liver, lesions and major blood vessels in abdomen cta images. *Biomedical Research 28*, 16 (2017), 7206–7212.

[188] SELVARAJ, D., AND DHANASEKARAN, R. Mri brain image segmentation techniques-a review.

[189] SERTEL, O., KONG, J., CATALYUREK, U. V., LOZANSKI, G., SALTZ, J. H., AND GURCAN, M. N. Histopathological image analysis using model-based intermediate representations and color texture: Follicular lymphoma grading. *Journal of Signal Processing Systems 55*, 1-3 (2009), 169.

[190] SERTEL, O., KONG, J., LOZANSKI, G., SHANA'AH, A., CATALYUREK, U., SALTZ, J., AND GURCAN, M. Texture classification using nonlinear color quantization: Application to histopathological image analysis. In *Acoustics, Speech and Signal Processing, 2008. ICASSP 2008. IEEE International Conference on* (2008), IEEE, pp. 597–600.

[191] Shang, Y., Deklerck, R., Nyssen, E., Markova, A., de Mey, J., Yang, X., and Sun, K. Vascular active contour for vessel tree segmentation. *IEEE Transactions on Biomedical Engineering 58*, 4 (2011), 1023–1032.

[192] Sofka, M., and Stewart, C. V. Retinal vessel centerline extraction using multiscale matched filters, confidence and edge measures. *IEEE Transactions on Medical Imaging 25*, 12 (2006), 1531–1546.

[193] Soomro, T. A., Gao, J., Lihong, Z., Afifi, A. J., Soomro, S., and Paul, M. Retinal blood vessels extraction of challenging images. In *Australasian Conference on Data Mining* (2018), Springer, pp. 347–359.

[194] Sozio, F., Rossi, A., Weber, E., Abraham, D. J., Nicholson, A. G., Wells, A. U., Renzoni, E. A., and Sestini, P. Morphometric analysis of intralobular, interlobular and pleural lymphatics in normal human lung. *Journal of anatomy 220*, 4 (2012), 396–404.

[195] Starck, J.-L., Fadili, J., and Murtagh, F. The undecimated wavelet decomposition and its reconstruction. *IEEE Transactions on Image Processing 16*, 2 (2007), 297–309.

[196] Sthitpattanapongsa, P., and Srinark, T. An equivalent 3d otsu's thresholding method. In *Pacific-Rim Symposium on Image and Video Technology* (2011), Springer, pp. 358–369.

[197] Sultan, M. S., Martins, N., Ferreira, M. J., and Coimbra, M. T. Segmentation of bones & mcp joint region of the hand from ultrasound images. In *Engineering in Medicine and Biology Society (EMBC), 2015 37th Annual International Conference of the IEEE* (2015), IEEE, pp. 3001–3004.

[198] Sun, X., Xu, Q., and Zhu, L. An effective gaussian fitting approach for image contrast enhancement. *IEEE Access PP* (01 2019), 1–1.

[199] Swiderska-Chadaj, Z., Markiewicz, T., Cierniak, S., and Koktysz, R. Automatic quantification of vessels in hemorrhoids whole slide images. In *Computa-*

tional Problems of Electrical Engineering (CPEE), 2016 17th International Conference (2016), IEEE, pp. 1–4.

[200] Swiebocka-Wiek, J. Skull stripping for mri images using morphological operators. 172–182.

[201] Taha, A. A., and Hanbury, A. Metrics for evaluating 3d medical image segmentation: analysis, selection, and tool. *BMC medical imaging 15*, 1 (2015), 29.

[202] Tan, L., and Jiang, J. Chapter 13 - image processing basics. 649–726.

[203] Tankyevych, O., Talbot, H., and Dokládal, P. Curvilinear morpho-hessian filter. *2008 5th IEEE International Symposium on Biomedical Imaging: From Nano to Macro* (2008), 1011–1014.

[204] Tetteh, G., Efremov, V., Forkert, N. D., Schneider, M., Kirschke, J., Weber, B., Zimmer, C., Piraud, M., and Menze, B. H. Deepvesselnet: Vessel segmentation, centerline prediction, and bifurcation detection in 3-d angiographic volumes. *arXiv preprint arXiv:1803.09340* (2018).

[205] Thakur, K., Damodare, O., and Sapkal, A. Poisson noise reducing bilateral filter. *Procedia Computer Science 79* (12 2016), 861–865.

[206] Tian, Y., Pan, Y., Duan, F., Zhao, S., Wang, Q., and Wang, W. Automated segmentation of coronary arteries based on statistical region growing and heuristic decision method. *BioMed research international 2016* (2016).

[207] Toennies, K. D. *Guide to medical image analysis.* Springer.

[208] Tomasi, C., and Manduchi, R. Bilateral filtering for gray and color images. In *Computer Vision, 1998. Sixth International Conference on* (1998), IEEE, pp. 839–846.

[209] Tonar, Z., Egger, G. F., Witter, K., and Wolfesberger, B. Quantification of microvessels in canine lymph nodes. *Microscopy research and technique 71*, 10 (2008), 760–772.

[210] Tosta, T. A. A., Neves, L. A., and do Nascimento, M. Z. Segmentation methods of h&e-stained histological images of lymphoma: a review. *Informatics in Medicine Unlocked 9* (2017), 35–43.

[211] Tsou, C.-H., Lu, Y.-C., Yuan, A., Chang, Y.-C., and Chen, C.-M. A heuristic framework for image filtering and segmentation: Application to blood vessel immunohistochemistry. *Analytical Cellular Pathology 2015*.

[212] V, M., and Singh, J. F. Contrast limited fuzzy adaptive histogram equalization for enhancement of brain images. *International journal of imaging systems and technology* (3 2017).

[213] Vahadane, A., Peng, T., Sethi, A., Albarqouni, S., Wang, L., Baust, M., Steiger, K., Schlitter, A. M., Esposito, I., and Navab, N. Structure-preserving color normalization and sparse stain separation for histological images. *IEEE transactions on medical imaging 35*, 8 (2016), 1962–1971.

[214] van Bemmel, C. M., Spreeuwers, L. J., Viergever, M. A., and Niessen, W. J. Level-set based carotid artery segmentation for stenosis grading. In *International Conference on Medical Image Computing and Computer-Assisted Intervention* (2002), Springer, pp. 36–43.

[215] Vicente, S., Kolmogorov, V., and Rother, C. Cosegmentation revisited: Models and optimization. In *European Conference on Computer Vision* (2010), Springer, pp. 465–479.

[216] Vignati, A., Giannini, V., Carbonaro, L., Bertotto, I., Martincich, L., Sardanelli, F., and Regge, D. A new algorithm for automatic vascular mapping of dce-mri of the breast: Clinical application of a potential new biomarker. *Computer methods and programs in biomedicine 117*, 3 (2014), 482–488.

[217] Vlachos, M., and Dermatas, E. Multi-scale retinal vessel segmentation using line tracking. *Computerized Medical Imaging and Graphics 34*, 3 (2010), 213–227.

[218] Volonghi, P., Tresoldi, D., Cadioli, M., Usuelli, A. M., Ponzini, R., Morbiducci, U., Esposito, A., and Rizzo, G. Automatic extraction of three-dimensional thoracic aorta geometric model from phase contrast mri for morphometric and hemodynamic characterization. *Magnetic resonance in medicine 75*, 2 (2016), 873–882.

[219] Vovk, U., Pernus, F., and Likar, B. A review of methods for correction of intensity inhomogeneity in mri. *IEEE transactions on medical imaging 26*, 3 (2007), 405–421.

[220] Wang, C., Wang, Q., and Smedby, Ö. Automatic heart and vessel segmentation using random forests and a local phase guided level set method. In *Reconstruction, Segmentation, and Analysis of Medical Images*. Springer, 2016, pp. 159–164.

[221] Wang, L., Chang, Y., Wang, H., Wu, Z., Pu, J., and Yang, X. An active contour model based on local fitted images for image segmentation. *Information sciences 418* (2017), 61–73.

[222] Wang, L., Duan, H., and Wang, J. A fast algorithm for three-dimensional otsu's thresholding method. In *IT in Medicine and Education, 2008. ITME 2008. IEEE International Symposium on* (2008), IEEE, pp. 136–140.

[223] Wang, L., Li, C., Sun, Q., Xia, D., and Kao, C.-Y. Active contours driven by local and global intensity fitting energy with application to brain mr image segmentation. *Computerized medical imaging and graphics 33*, 7 (2009), 520–531.

[224] Wang, L., You, S., and Neumann, U. Supporting range and segment-based hysteresis thresholding in edge detection.

[225] Wang, M., Zheng, S., Li, X., and Qin, X. A new image denoising method based on gaussian filter. In *2014 International Conference on Information Science, Electronics and Electrical Engineering* (2014), vol. 1, pp. 163–167.

[226] Waqqas-ur Rehman, B., Servin, M., and Pause, M. Object detection in digital images under non-standardized conditions using illumination and shadow filtering. *International Journal of Computer and Information Engineering* (2017).

[227] Weber, T. F., Müller, T., Biesdorf, A., Wörz, S., Rengier, F., Heye, T., Holland-Letz, T., Rohr, K., Kauczor, H.-U., and von Tengg-Kobligk, H. True four-dimensional analysis of thoracic aortic displacement and distension using model-based segmentation of computed tomography angiography. *The international journal of cardiovascular imaging 30*, 1 (2014), 185–194.

[228] Weickert, J. *Anisotropic diffusion in image processing*, vol. 1.

[229] Wörz, S. 3d model-based segmentation of 3d biomedical images. In *International Doctoral Workshop on Mathematical and Engineering Methods in Computer Science* (2014), Springer, pp. 40–46.

[230] Wu, C.-H., Agam, G., and Stanchev, P. A general framework for vessel segmentation in retinal images. In *2007 International Symposium on Computational Intelligence in Robotics and Automation* (2007), pp. 37–42.

[231] Xian, Z., Wang, X., Yan, S., Yang, D., Chen, J., and Peng, C. Main coronary vessel segmentation using deep learning in smart medical. *Mathematical Problems in Engineering 2020* (2020).

[232] Xie, Y., Padgett, J., Biancardi, A. M., and Reeves, A. P. Automated aorta segmentation in low-dose chest ct images. *International journal of computer assisted radiology and surgery 9*, 2 (2014), 211–219.

[233] Xu, Y., Pickering, J. G., Nong, Z., and Ward, A. D. Segmentation of digitized histological sections for vasculature quantification in the mouse hind limb. In *Medical Imaging 2015: Digital Pathology* (2015), vol. 9420, International Society for Optics and Photonics, p. 942003.

[234] Xu, Y., Pickering, J. G., Nong, Z., and Ward, A. D. Segmentation of digitized histological sections for quantification of the muscularized vasculature in the mouse hind limb. *Journal of microscopy 266*, 1 (2017), 89–103.

[235] Yang, M.-S. A survey of fuzzy clustering. *Mathematical and Computer modelling 18*, 11 (1993), 1–16.

[236] Yang, X., Do Yang, J., Hwang, H. P., Yu, H. C., Ahn, S., Kim, B.-W., and You, H. Segmentation of liver and vessels from ct images and classification of liver segments for preoperative liver surgical planning in living donor liver transplantation. *Computer methods and programs in biomedicine 158* (2018), 41–52.

[237] Yang, X., Jin, J., Xu, M., Wu, H., He, W., Yuchi, M., and Ding, M. Ultrasound common carotid artery segmentation based on active shape model. *Computational and mathematical methods in medicine 2013*.

[238] Yang, X., Wang, L.-J., Qin, J.-W., and Zuo, H. A fast decomposed three-dimensional otsu algorithm based on cuckoo search for image segmentation. *Journal of Applied Science and Engineering 21* (2018), 447–454.

[239] Ye, C., Tao, D., Song, M., Jacobs, D. W., and Wu, M. Sparse norm filtering. *arXiv preprint arXiv:1305.3971* (2013).

[240] Yeh, C.-H., Lin, C.-Y., Muchtar, K., Lai, H.-E., and Sun, M.-T. Three-pronged compensation and hysteresis thresholding for moving object detection in real-time video surveillance. *IEEE Transactions on Industrial Electronics 64*, 6 (2017), 4945–4955.

[241] Yu, C., Dian-ren, C., Yang, L., and Lei, C. Otsu's thresholding method based on gray level-gradient two-dimensional histogram. In *Informatics in Control, Automation and Robotics (CAR), 2010 2nd International Asia Conference on* (2010), vol. 3, IEEE, pp. 282–285.

[242] Yuan, X., Martínez, J.-F., Eckert, M., and López-Santidrián, L. An improved otsu threshold segmentation method for underwater simultaneous localization and mapping-based navigation. *Sensors 16*, 7 (2016), 1148.

[243] Zafer, Y., and Kose, C. Blood vessel extraction in colour retina fundus images with enhancement filter and unsupervised classification. *Journal of healthcare engineering* (2017).

[244] Zaitoun, N. M., and Aqel, M. J. Survey on image segmentation techniques. *Procedia Computer Science 65* (2015), 797–806.

[245] zhan Zeng, Y., qian Zhao, Y., hui Liao, S., Liao, M., Chen, Y., and yao Liu, X. Liver vessel segmentation based on centerline constraint and intensity model. *Biomedical Signal Processing and Control 45* (2018), 192 – 201.

[246] Zhang, J., Tang, Z., Gui, W., and Liu, J. Retinal vessel image segmentation based on correlational open active contours model. In *2015 Chinese Automation Congress (CAC)* (2015), pp. 993–998.

[247] Zhang, K., Zhang, L., Lam, K.-M., and Zhang, D. A level set approach to image segmentation with intensity inhomogeneity. *IEEE transactions on cybernetics 46*, 2 (2016), 546–557.

[248] Zhang, L., Li, Q., You, J., and Zhang, D. A modified matched filter with double-sided thresholding for screening proliferative diabetic retinopathy. *IEEE Transactions on Information Technology in Biomedicine 13*, 4 (2009), 528–534.

[249] Zhang, R., Zhou, Z., Wu, W., Lin, C.-C., Tsui, P.-H., and Wu, S. An improved fuzzy connectedness method for automatic three-dimensional liver vessel segmentation in ct images. *Journal of Healthcare Engineering 2018* (2018).

[250] Zhao, F., Chen, Y., Hou, Y., and He, X. Segmentation of blood vessels using rule-based and machine-learning-based methods: a review. *Multimedia Systems* (Dec 2017).

[251] Zhao, S., Tian, Y., Wang, X., Xu, P., Deng, Q., and Zhou, M. Vascular extraction using mra statistics and gradient information. *Mathematical Problems in Engineering 2018*.

[252] Zhao, Y., Liu, Y., Wu, X., Harding, S. P., and Zheng, Y. Retinal vessel segmentation: An efficient graph cut approach with retinex and local phase. *PloS one 10*, 4 (2015), e0122332.

[253] Zhao, Y., Rada, L., Chen, K., Harding, S. P., Zheng, Y., et al. Automated vessel segmentation using infinite perimeter active contour model with hybrid region information with application to retinal images. *IEEE Trans. Med. Imaging 34*, 9 (2015), 1797–1807.

[254] Zhao, Y., Zheng, Y., Liu, Y., Zhao, Y., Luo, L., Yang, S., Na, T., Wang, Y., and Liu, J. Automatic 2-d/3-d vessel enhancement in multiple modality images using a weighted symmetry filter. *IEEE transactions on medical imaging 37*, 2 (2018), 438–450.

[255] Zhao, Z., Chang, W., and Jiang, Y. Fuzzy local means clustering segmentation algorithm for intensity inhomogeneity image. In *Image and Signal Processing (CISP), 2015 8th International Congress on* (2015), IEEE, pp. 453–457.

[256] Zheng, X., Tang, Y., and Hu, W. Image thresholding based on gray level-fuzzy local entropy histogram. *IEEJ Transactions on Electrical and Electronic Engineering 13*, 4 (2018), 627–631.